

Track reconstruction in the LHCb experiment

Track reconstruction in the LHCb experiment

ACADEMISCH PROEFSCHRIFT

TER VERKRIJGING VAN DE GRAAD VAN DOCTOR
AAN DE UNIVERSITEIT VAN AMSTERDAM
OP GEZAG VAN DE RECTOR MAGNIFICUS
PROF. MR. P.F. VAN DER HEIJDEN
TEN OVERSTAAN VAN EEN DOOR HET COLLEGE VOOR PROMOTIES
INGESTELDE COMMISSIE, IN HET OPENBAAR TE VERDEDIGEN
IN DE AULA DER UNIVERSITEIT
OP VRIJDAG 13 SEPTEMBER 2002, TE 12:00 UUR

door

Rutger Mark van der Eijk

geboren te Breukelen

Promotor: Prof. Dr W.Hoogland
Co-Promotor: Dr. M.H.M.Merk

Faculteit der Natuurwetenschappen, Wiskunde en Informatica

ISBN 90-6488-022-0

The work described in this thesis is part of the research programme of 'het Nationaal Instituut voor Kernfysica en Hoge-Energie Fysica' (NIKHEF) in Amsterdam, the Netherlands. The author was financially supported by the 'Stichting Fundamenteel Onderzoek der Materie' (FOM).

Aan mijn ouders

Contents

Introduction	1
1 Theoretical context	5
1.1 CP violation	5
1.2 CP violation in the Standard Model	6
1.3 Neutral B mesons	9
1.4 B decays in LHCb	11
1.4.1 $B_d \rightarrow \pi^+ \pi^-$	11
1.4.2 $B_s \rightarrow D_s^\pm K^\mp$	12
1.5 B meson production	14
2 The LHCb experiment	19
2.1 The Large Hadron Collider	19
2.2 The LHCb detector	24
2.2.1 Vertex detector system	24
2.2.2 RICH detectors	26
2.2.3 Calorimeters	29
2.2.4 Muon detector	32
2.3 LHCb main tracking system	32
2.3.1 Magnet	33
2.3.2 Inner Tracker	36
2.3.3 Outer Tracker	38
2.4 LHCb trigger	42
3 LHCb Outer Tracker straw detector	45
3.1 Operation principle	45
3.1.1 Creation of ionisation clusters	45
3.1.2 Drift of electrons and ions in gases	46
3.1.3 Gas amplification	49
3.1.4 Signal development and time measurement	49
3.2 Drift gas selection	50
3.3 Outer Tracker prototypes	52
3.4 Material selection	56
3.5 Conclusions	57

4 Outer Tracker prototype tests	59
4.1 Test beam setup	59
4.1.1 Particle beam	59
4.1.2 Magnet	60
4.1.3 Electronics	60
4.2 Software	62
4.2.1 Low level data acquisition	62
4.2.2 Online monitoring and control	63
4.2.3 Event reconstruction	63
4.2.4 Simulation with Garfield	66
4.3 Drift time	66
4.4 Distance-drift time relation	70
4.5 Efficiency	72
4.6 Resolution	74
4.7 Noise and cross-talk	79
4.8 Summary and conclusions	80
5 Track fitting	85
5.1 Event simulation	85
5.1.1 Event generation	86
5.1.2 Particle tracking	86
5.1.3 Detector response	87
5.2 Track fitting procedure	88
5.2.1 Kalman filter	89
5.2.2 Measurements	93
5.2.3 Track parameter propagation	97
5.2.4 Multiple scattering and energy loss	100
5.2.5 Kalman smoother	101
5.3 Track fitting performance	102
5.3.1 Resolution and pulls	102
5.3.2 Tuning the fit	104
5.3.3 Momentum dependence	107
5.4 Conclusions	109
6 Pattern recognition	111
6.1 Particle rates and detector occupancies	112
6.2 Track seeding	119
6.2.1 Track segment finding	119
6.2.2 Track seed initialisation	121
6.3 Track following	123
6.3.1 Inter station following	123
6.3.2 Intra station search	125
6.4 Pattern recognition performance	127
6.4.1 Track seeding	128
6.4.2 Track following	128

6.4.3 Combined track seeding and following	130
7 Tracking performance	135
7.1 $B_s \rightarrow D_s^\pm K^\mp$	135
7.1.1 Event selection	135
7.1.2 Background rejection	136
7.1.3 Mass resolution	137
7.2 $B_d \rightarrow \pi^+ \pi^-$	137
7.2.1 Event selection	137
7.2.2 Background rejection	138
7.3 Pattern recognition performance	140
7.4 Event yields	141
7.5 Comparison	144
7.6 Outlook	146
Bibliography	147
Summary	153
Samenvatting	157
Acknowledgement	161

Introduction

Almost all human beings wonder why things are the way they are. The scientific method is the process by which scientists, collectively and over time, endeavour to construct an accurate (that is, reliable, consistent and non-arbitrary) representation of the world[1]. Physicists have been very successful in applying this method to the physical world around us. When it comes to the basic constituents of matter and the forces acting between them a theory emerged in the past decades, called the Standard Model, that is able to successfully describe the physics at a length scale of 10^{-16} in terms of a limited, but still unsatisfactory large, number of fundamental parameters. The theory of the elementary constituents of matter is intimately linked to cosmological questions and in particular to the evolution of our universe after its creation.

One of the still unsolved questions is why our universe consist of matter while anti-matter is very rare.. It is common scientific knowledge that a particle and its anti-particle can annihilate and for instance produce two photons, and reversely a particle anti-particle pair can materialise out of photons. Just after the big bang a dynamic equilibrium between these reactions kept the number of particles, anti-particles and photons equal. About 10^{-8} s after the big bang the temperature of the universe dropped below the threshold for the particle anti-particle pair reaction, i.e. the energy of the photons ceased to be sufficient to generate a particle anti-particle pair. Therefore, particles and anti-particles disappeared by annihilation into photons.

At present practically no free anti-particles are observed. Furthermore, there is an overwhelming abundance of photons (about 1 billion photons for each matter particle). In 1967 the Russian physicist Andrei Sakharov listed three necessary requirements for any theory that attempts to explain this remarkable fact[2]. One of these requirements is violation of the *CP* symmetry. The combined *Charge* and *Parity* operation transforms a particle state into a anti-particle state. Hence, in case the laws of nature are not invariant under the *CP* operation particles behave differently from anti-particles.

CP violation was first observed[3] in the decay of neutral kaons in 1964. Measurements shows this asymmetry to be at a per mille level ($\epsilon = 2.3 \cdot 10^{-3}$)[4]. The Standard Model incorporates *CP* violation by the complex phase in the Cabibbo-Kobayashi-Maskawa (CKM) matrix, which links the weak eigenstates of quarks to the mass eigenstates. This parametrisation does, however, not provide a deeper understanding of the origin of the asymmetry, nor does it explain the magnitude of the matter anti-matter asymmetry in the universe. One of the remaining challenges of high energy physics is to find an explanation for *CP* violation.

The parametrisation does predict *CP*-violating effects to occur for *B* mesons. Furthermore, due to the interference between the mixing and decay amplitudes in the

decay of neutral B mesons the CP asymmetries are expected to be large. Recent experiments[5, 6] indeed show a large CP asymmetry in the decay of B_d ; $\sin 2\beta \sim 0.78$. CP violation is expected in many more B decays. These are, however, expected to have small branching ratios ($10^{-4} - 10^{-5}$). Therefore, also taking into account experimental (i.e. trigger, reconstruction and tagging) inefficiencies, a copious source of B mesons is needed. The Large Hadron Collider (LHC), the new proton-proton collider at CERN, produces B mesons at a high rate.

The LHCb-detector is designed to study CP violation in the B meson system at the LHC. It aims to study B physics with unprecedented statistics. By making precision measurements on many different B meson decay channels, LHCb will be able to test the internal consistency of the Standard Model, and look for physics beyond the model.

The subject of this thesis is the reconstruction of particle trajectories in the LHCb experiment. The thesis contains three components:

- a study on the design of the outer tracker, one of the LHCb detector sub-systems that measures the charged particle trajectories,
- a study of the reconstruction of the particle trajectories from the detector measurements,
- a study on the implications of the track reconstruction efficiency and resolution on the measurements of CP violation in B decays.

The outline of this thesis is as follows.

Chapter 1 gives an overview of CP violation and how it is incorporated in the Standard Model. Aspects of the neutral B meson system are described.

Chapter 2 provides an introduction to the LHCb experiment. It starts with a description of the LHC, i.e. the accelerator at which the LHCb detector is situated. All LHCb sub-detector components are shortly described, with a particular emphasis on the tracking system as it is the main subject of this thesis. The chapter concludes with an outline of the LHCb trigger system.

Chapter 3 describes the underlying physics processes of the operation of the LHCb outer tracker straw detector. Furthermore, the selection of the drift gas and the detector material is discussed. Four prototype outer tracker modules are presented.

Chapter 4 is devoted to the outer tracker prototype tests in a particle beam at CERN. After describing the experimental setup and the software, the analysis and results are presented. These measurements were used to design the final outer tracker modules as described in chapter 2.

Chapter 5 describes the procedure to fit trajectories through the measurements of the LHCb tracking detectors. The obtained track parameter resolutions are presented.

Chapter 6 starts with an overview of the expected particle fluxes and the detector occupancies in the LHCb experiment. A possible solution to the pattern recognition task involved in reconstructing the particle trajectories is presented. The chapter is concluded by presenting the performance of these pattern recognition algorithms.

Chapter 7 summarises the overall performance of the LHCb tracking system using two benchmark decay modes. A discussion is given of the (in)efficiency in the event reconstruction due to the pattern recognition algorithms of chapter 6. The expected event

yields in a year of data-taking are presented and compared with an earlier, less detailed, study presented in the LHCb technical proposal[7]. An estimate of the resolutions on measuring some CP violating parameters is presented. Finally, a brief outlook is given on possible pattern recognition algorithm improvements and on a recently started study re-optimising the LHCb detector.

Chapter 1

Theoretical context

In this thesis a study of the track reconstruction in the LHCb detector is described. The LHCb detector is optimised for the measurement of B meson production and decay at the LHC, in particular the observation and measurement of CP asymmetries in specific B meson decays. In this chapter the theoretical context for these measurements is discussed. It is, however, not intended to give a full theoretical description of CP violation in neutral B meson decays. For more detailed descriptions the reader is referred to excellent publications and textbooks[7, 8, 9, 10].

Section 1.1 describes the concept of CP violation. Section 1.2 explains how CP violation is incorporated in the Standard Model. Section 1.3 describes the neutral B meson system. Section 1.4 discusses two B decay channels which for the LHCb experiment are used as benchmark channels for track reconstruction. Section 1.5 describes production characteristics of B mesons at the LHC.

1.1 CP violation

The violation of CP symmetry implies that the laws of nature are not invariant under the combined Charge and Parity transformation. Parity P is the inversion of space coordinates (exchange of left and right handedness). Charge conjugation C changes the sign of the “internal” quantum numbers such as charge and baryon number.

For a long time physics was assumed to be invariant under the parity transformation, i.e. the mirror image of any physical process obeys the same physical laws as the original process. However, in 1957 an experiment[11] showed that the electrons emitted in the beta decay of ^{60}Co are predominantly produced in the direction opposite to the spin of the cobalt nucleus. The mirror image of an electron decay opposite to the spin direction is a decay along the spin direction. After the alignment of the spins the observation of a top/down asymmetry in the experiment immediately implies the violation of parity.

Later, it was observed that in the decay $\pi^+ \rightarrow \mu^+ \nu_\mu$ the neutrino always emerges left handed. Again, parity is violated as the mirror process, i.e. with the neutrino right handed, does not occur. However, the charge conjugate of the mirror process, i.e. $\pi^- \rightarrow \mu^- \bar{\nu}_\mu$ with the anti-neutrino right handed, was observed. Therefore, it seemed that the symmetry is restored under the combined operation of C and P .

fermion	family			q/e
	I	II	III	
lepton	e	μ	τ	-1
	ν_e	ν_μ	ν_τ	0
quark	u	c	t	2/3
	d	s	b	-1/3

Table 1.1: The three families of elementary fermions in the Standard Model, i.e. the leptons and quarks.

However, in 1964 also CP symmetry was demonstrated to be violated in the decay of neutral kaons[3]. An interesting aspect of neutral kaons is the ability for a K^0 to transform into the anti-particle \bar{K}^0 and vice versa (see section 1.3 for the similar underlying mechanism for neutral B mesons in the Standard Model). It turned out that the particles observed in nature (the *mass eigenstates*) are not K^0 and \bar{K}^0 , but linear combinations of these states. Two states are observed with quite distinct lifetimes; K_S with $\tau = 0.89 \times 10^{-10}$ s and K_L with $\tau = 5.2 \times 10^{-8}$ s. The experiment in 1964 showed the K_L to be composed of the $CP = -1$ eigenstate K_2 with a small admixture of the $CP = +1$ eigenstate K_1 , i.e.

$$|K_L\rangle = \frac{1}{\sqrt{1+|\epsilon|^2}} (|K_1\rangle + \epsilon |K_2\rangle) . \quad (1.1)$$

Experimentally ϵ is found to be $(2.271 \pm 0.017) \times 10^{-3}$ [4] demonstrating violation of CP symmetry in the mixing of K^0 and \bar{K}^0 . The next section shows how CP violation is incorporated in the standard model.

1.2 CP violation in the Standard Model

The Standard Model provides an accurate theoretical framework for the description of the interactions between the fundamental constituents of matter. Matter is thought to be made out of two types of fundamental fermions (spin $\frac{1}{2}$ particles): quarks and leptons. Interactions are described by the exchange of spin 1 bosons. The interactions described by the Standard Model are the electromagnetic-, weak- and strong-force. Gravitation, the fourth fundamental interaction, is not incorporated in the model.

The fundamental fermions of the Standard Model are divided into three families with similar properties but increasing mass. Each family contains a lepton with an associated lepton-neutrino as well as an up- and down-type quark (see table 1.1). Together with the corresponding anti-particles the Standard Model incorporates 24 fundamental fermions¹. With the recent[12] direct observation of the tau neutrino all fermions of the Standard Model are experimentally observed.

Quantum Electro Dynamics (QED) gives the quantum field description of electromagnetic interactions between charged fermions. The corresponding electromagnetic

¹Each quark can in addition occur in three colour states.

current is mediated by the exchange of photons. In the sixties Glashow, Weinberg and Salam [13, 14, 15] developed a theory combining the electromagnetic and weak interactions. They predicted the existence of three mediators of the weak interaction, i.e. the Z , W^+ and W^- . These massive bosons were found in 1983[16, 17]. The theory of the strong interactions, Quantum Chromo Dynamics (QCD), describes an interaction that acts only between quarks. The strong interaction is mediated by 8 gauge bosons collectively called gluons.

The charged current weak interaction (mediated by the exchange of W^\pm bosons) is known to maximally violate P . The violation is explained by the sum of a vector and axial-vector in the hadronic charged current of this interaction², i.e. it has the form:

$$j_u^{cc} = (\bar{u}, \bar{c}, \bar{t}) \gamma_u (1 - \gamma_5) V_{\text{CKM}} \begin{pmatrix} d \\ s \\ b \end{pmatrix} , \quad (1.2)$$

where γ_u are the Dirac matrices, $1 - \gamma_5$ the projection operator to left handed states and V_{CKM} the 3×3 unitary Cabibbo-Kobayashi-Maskawa matrix[18, 19]

$$V_{\text{CKM}} = \begin{pmatrix} V_{ud} & V_{us} & V_{ub} \\ V_{cd} & V_{cs} & V_{cb} \\ V_{td} & V_{ts} & V_{tb} \end{pmatrix} . \quad (1.3)$$

The CKM matrix relates the flavour eigenstates of the down type quarks (d, s, b) to the weak interaction eigenstates (d', s', b'), i.e.

$$\begin{pmatrix} d' \\ s' \\ b' \end{pmatrix} = V_{\text{CKM}} \begin{pmatrix} d \\ s \\ b \end{pmatrix} . \quad (1.4)$$

The elements of V_{CKM} express the relative strength of the couplings between the up and down type quarks. The requirement of unitarity of the matrix, i.e. $V_{\text{CKM}} \cdot V_{\text{CKM}}^\dagger = \mathbb{1}$, introduces constraints between the elements. In general three real parameters and six phases can be defined for a unitary 3×3 matrix. Five can however be removed by appropriate re-phasing of the quark fields without changing the physically observable quantities. A popular parametrisation is due to Wolfenstein[20] expressed in powers of the sine of the Cabibbo angle[18] $\lambda = 0.222 \pm 0.002$ [4]:

$$V_{\text{CKM}} = \begin{pmatrix} 1 - \lambda^2/2 & \lambda & A\lambda^3(\rho - i\eta) \\ -\lambda & 1 - \lambda^2/2 & A\lambda^2 \\ A\lambda^3(1 - \rho - i\eta) & -A\lambda^2 & 1 \end{pmatrix} + \mathcal{O}(\lambda^4) , \quad (1.5)$$

with A , ρ and η real numbers. The phase, i.e. the imaginary component $i\eta$, is the source of CP violation in the Standard Model.

The unitarity relation of the CKM matrix that is most relevant for B mesons decays is:

$$\sum_i V_{id} V_{ib}^* = V_{ud} V_{ub}^* + V_{cd} V_{cb}^* + V_{td} V_{tb}^* = 0 , \quad (1.6)$$

²A vector changes sign under the parity operation whereas an axial vector does not.

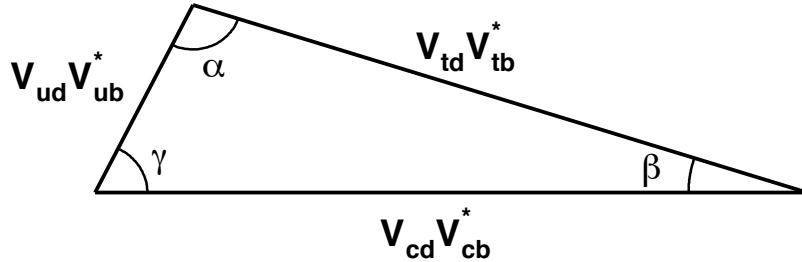


Figure 1.1: The unitarity triangle with the angles α , β and γ .

The three complex quantities $V_{id}V_{ib}^*$ form a triangle in the complex plane as shown in figure 1.1. The angles of this *unitarity triangle* are defined by:

$$\begin{aligned}\alpha &\equiv \arg\left(-\frac{V_{td}V_{tb}^*}{V_{ud}V_{ub}^*}\right) \\ \beta &\equiv \arg\left(-\frac{V_{cd}V_{cb}^*}{V_{td}V_{tb}^*}\right) \\ \gamma &\equiv \arg\left(-\frac{V_{ud}V_{ub}^*}{V_{cd}V_{cb}^*}\right)\end{aligned}. \quad (1.7)$$

Recently, the experiments BaBar and Belle made direct measurements of the angle β using B_d meson decays. The BaBar result is[5]:

$$\sin 2\beta = 0.75 \pm 0.09(\text{stat}) \pm 0.04(\text{syst}) \quad . \quad (1.8)$$

The Belle result is[6]:

$$\sin 2\beta = 0.82 \pm 0.12(\text{stat}) \pm 0.05(\text{syst}) \quad . \quad (1.9)$$

The area of the unitarity triangle is a measure of the amount of CP violation, i.e. in case no CP violation would exist the triangle would collapse into a line[21]. The BaBar and Belle results thus show the existence of CP violation in B meson decays.

In order to test if the Standard Model provides the full explanation of the observed CP violation additional measurements are required. If the sides and angles of the unitarity triangle(s) are independently measured the triangle becomes over-constrained. LHCb aims to test the internal consistency of the Standard Model by making precision measurements on many different B meson decay channels.

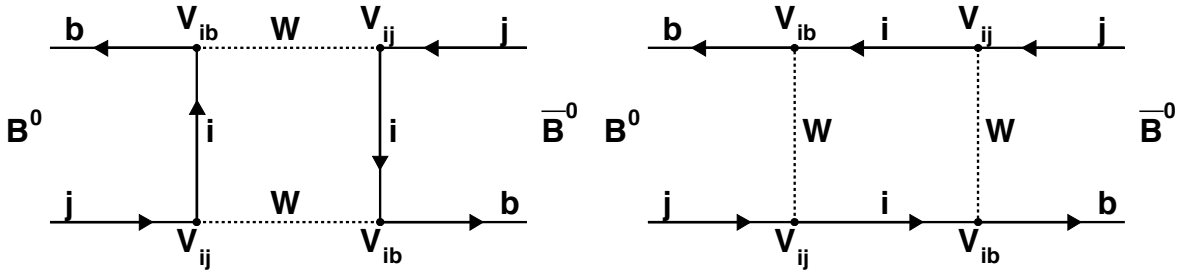


Figure 1.2: Feynman box diagrams for neutral B^0 - \bar{B}^0 oscillations. The index i represents one of the up-type quarks u, c, t . The index j represents a d or s quark making up the B_d respectively B_s meson.

1.3 Neutral B mesons

Neutral B meson decays are interesting to study CP violation for several reasons:

- Due to the large b quark mass, Heavy Quark Effective Theory (HQET)[22] provides a framework to calculate hadronic effects. Hence the theoretical uncertainties in these calculations are much smaller than for the kaon system.
- Due to the existence of B^0 - \bar{B}^0 oscillations, two interfering amplitudes (i.e. the direct decay $B^0 \rightarrow f$ and the decay via mixing $B^0 \rightarrow \bar{B}^0 \rightarrow f$) with possibly different phases contribute to the decay of a neutral B meson. Because these amplitudes are expected to be of the same order the CP asymmetry is expected to be large.

In this section the physics of the neutral B meson system is described. The symbols B^0 and \bar{B}^0 are used to represent the particle and anti-particle states of both B_d^0 as B_s^0 .

B^0 - \bar{B}^0 oscillations (mixing) occur in the Standard Model through the exchange of two W bosons via the box diagrams shown in figure 1.2. The dominant diagrams are the ones that exchange two top quarks (i.e. $i = t$). This is due to the high top quark mass (compared to charm and up quarks) and because the diagrams are Cabibbo favoured[23].

The time dependent wave function for neutral B mesons can be written as the superposition:

$$\Psi(t) = a(t) |B^0\rangle + b(t) |\bar{B}^0\rangle . \quad (1.10)$$

The time evolution of this system is described by the Schrödinger equation:

$$i\hbar \frac{\partial \Psi}{\partial t} = H\Psi = \left(M - i\frac{\Gamma}{2} \right) \Psi , \quad (1.11)$$

with M and Γ the 2×2 mass and decay matrices. Normalising and diagonalising H results in the two mass eigenstates B_L and B_H expressed in terms of the flavour

eigenstates B^0 and \bar{B}^0 :

$$\begin{aligned} |B_L\rangle &= \frac{1}{\sqrt{p^2 + q^2}} (p|B^0\rangle + q|\bar{B}^0\rangle) \\ |B_H\rangle &= \frac{1}{\sqrt{p^2 + q^2}} (p|B^0\rangle - q|\bar{B}^0\rangle) \quad . \end{aligned} \quad (1.12)$$

They have a simple exponential evolution in time, i.e.

$$\begin{aligned} |B_L(t)\rangle &= e^{-(\Gamma_L/2+iM_L)t} |B_L(0)\rangle \\ |B_H(t)\rangle &= e^{-(\Gamma_H/2+iM_H)t} |B_H(0)\rangle \quad . \end{aligned} \quad (1.13)$$

It then follows that the evolution of an initially ($t = 0$) pure B^0 (or \bar{B}^0) is given by:

$$\begin{aligned} |B_{\text{phys}}^0(t)\rangle &= g_+(t)|B^0\rangle + (q/p)g_-(t)|\bar{B}^0\rangle \\ |\bar{B}_{\text{phys}}^0(t)\rangle &= (p/q)g_-(t)|B^0\rangle + g_+(t)|\bar{B}^0\rangle \quad , \end{aligned} \quad (1.14)$$

with

$$g_{\pm}(t) = \frac{1}{2} (e^{-(\Gamma_L/2+iM_L)t} \pm e^{-(\Gamma_H/2+iM_H)t}) \quad . \quad (1.15)$$

What is measured experimentally are the decay rates of particles into final states. The time-dependent rates for initially pure B^0 and \bar{B}^0 states decaying into final state f at time t are given by:

$$\begin{aligned} R_f(t) \equiv |\langle f | B_{\text{phys}}^0(t) \rangle|^2 &= \frac{|A_f|^2}{2} e^{-\Gamma t} (I_+(t) + I_-(t)) \\ \bar{R}_f(t) \equiv |\langle f | \bar{B}_{\text{phys}}^0(t) \rangle|^2 &= \frac{|A_f|^2}{2} \left| \frac{p}{q} \right|^2 e^{-\Gamma t} (I_+(t) - I_-(t)) \quad , \end{aligned} \quad (1.16)$$

where Γ is the average decay width of the two mass eigenstates, and with $A_f \equiv \langle f | B^0 \rangle$, i.e. the instantaneous decay amplitude for a flavour eigenstate B^0 into final state f . The functions $I_+(t)$ and $I_-(t)$ are given by:

$$\begin{aligned} I_+(t) &= (1 + |\lambda|^2) \cosh \frac{\Delta\Gamma}{2} t - 2\text{Re}(\lambda) \sinh \frac{\Delta\Gamma}{2} t \\ I_-(t) &= (1 - |\lambda|^2) \cos \Delta m t - 2\text{Im}(\lambda) \sin \Delta m t \quad , \end{aligned} \quad (1.17)$$

with $\Delta\Gamma$ and Δm the mass and decay width differences of the mass eigenstates. The complex parameter λ is given by:

$$\lambda = \frac{q}{p} \frac{\bar{A}_f}{A_f} \quad , \quad (1.18)$$

with $\bar{A}_f \equiv \langle f | \bar{B}^0 \rangle$, i.e. the instantaneous decay amplitude $\bar{B}^0 \rightarrow f$.

The above equations hold in general for all neutral B decays. The components of the decay rate formulae express the time dependence due to the oscillations. The specifics for a certain decay, i.e. the difference in decay amplitudes, is expressed in the single

parameter λ . A similar set of equations for the time-dependent rates $R_f(t)$ and $\bar{R}_{\bar{f}}(t)$ of the B^0 and \bar{B}^0 states decaying into final state \bar{f} is obtained by replacing $A_f \rightarrow \bar{A}_{\bar{f}}$, $\bar{A}_f \rightarrow A_{\bar{f}}$ and interchanging p and q in equations 1.16-1.18. The parameter λ then transforms into $\bar{\lambda} = \frac{p}{q} \frac{A_{\bar{f}}}{A_f}$.

CP violation is studied by measuring the decay-rate asymmetry between particles and anti-particles. In the time dependent decay-rate asymmetries

$$\begin{aligned}\mathcal{A}_f(t) &= \frac{R_f(t) - \bar{R}_f(t)}{R_f(t) + \bar{R}_f(t)} \\ \mathcal{A}_{\bar{f}}(t) &= \frac{R_{\bar{f}}(t) - \bar{R}_{\bar{f}}(t)}{R_{\bar{f}}(t) + \bar{R}_{\bar{f}}(t)}\end{aligned}\quad (1.19)$$

acceptance effects of the detector are cancelled since the asymmetries are built from identical particles. In case the final state is a CP eigenstate $f = \bar{f}$ and the rate asymmetries $\mathcal{A}_f(t)$ and $\mathcal{A}_{\bar{f}}(t)$ are identical. This asymmetry is a CP asymmetry and can directly be used to demonstrate CP violation. If in addition the decay is dominated by a single CKM phase and under the assumption³ $|q/p| = 1$ the parameter $|\lambda| = 1$. Combining equation 1.16 and 1.17 into equation 1.19, and assuming $\Delta\Gamma \cong 0$, the CP asymmetry simplifies to:

$$\mathcal{A}_{CP}(t) = -\text{Im}(\lambda) \sin \Delta mt \quad . \quad (1.20)$$

The term $\sin(\Delta mt)$ expresses the $B^0 - \bar{B}^0$ oscillations, the amplitude $\text{Im}(\lambda)$ is the amount of CP violation.

$$\Delta\Gamma \cong 0$$

1.4 B decays in LHCb

Many different decay modes of the B_d and B_s exist. However, most of the decay modes interesting for the study of CP violation have small branching ratios. Therefore, an efficient reconstruction of these decays is essential. As is discussed in section 2.4 the selection of generic B decay events in LHCb is done at trigger level 1. To select the interesting B meson decays from the large B sample, the full B decay needs to be reconstructed. Hence, all stable decay products need to be efficiently and precisely reconstructed by the tracking system. In this thesis the reconstruction of two benchmark decay modes is investigated. Selected are a decay into two final state particles, i.e. $B_d \rightarrow \pi^+ \pi^-$ and a decay into four particles, i.e. $B_s \rightarrow D_s^\pm K^\mp$ followed by $D_s^\pm \rightarrow K^+ K^- \pi^\pm$.

1.4.1 $B_d \rightarrow \pi^+ \pi^-$

The decay $B_d \rightarrow \pi^+ \pi^-$ is interesting because the final state is a CP eigenstate. The decay rate asymmetries $\mathcal{A}_f(t)$ and $\mathcal{A}_{\bar{f}}(t)$ in equation 1.19 are therefore CP asymmetries. Assuming the $\bar{b} \rightarrow \bar{u} + W(u\bar{d})$ tree diagram in figure 1.3 (left) is the dominant Feynman

³This is expected to be a very good approximation for neutral B mesons.

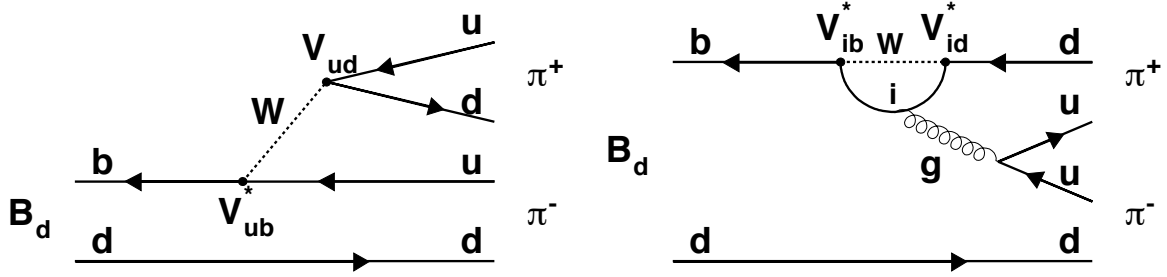


Figure 1.3: The tree(left) and penguin(right) Feynman diagrams for the decay $B_d \rightarrow \pi^+ \pi^-$. The index i represents one of the up-type quarks u, c, t .

diagram contributing to this decay and using $\lambda = |\lambda| e^{i\phi}$ it can be shown that $\phi = 2\alpha$ and hence $\text{Im}(\lambda) = \sin 2\alpha$. Therefore (using equation 1.20), the CP asymmetry is given by:

$$\mathcal{A}_{\pi\pi} = -\sin 2\alpha \sin \Delta mt \quad . \quad (1.21)$$

This channel can thus be used to measure the angle α of the unitarity triangle⁴.

The B_d meson has an average lifetime of 1.56×10^{-12} s. It will travel on average about one cm (seen from the LHCb lab-frame) before it decays (see figure 1.4). The decay is therefore characterised by a displaced vertex made up by two oppositely charged tracks (pions). The resulting momentum vector points to the primary vertex. The existence of a B meson decay vertex a few mm apart from the primary interaction vertex is a general characteristic of B events. The LHCb experiment relies on the existence of these secondary vertices to trigger on B events (see trigger section 2.4).

1.4.2 $B_s \rightarrow D_s^\pm K^\mp$

Another relevant channel is the decay of a B_s meson into a D_s meson and a kaon. Both decays $B_s \rightarrow D_s^- K^+$ and that of $B_s \rightarrow D_s^+ K^-$ are possible. The leading order Feynman diagram for the channel $B_s \rightarrow D_s^- K^+$ is indicated in the left plot of figure 1.5. The decay is determined by the $\bar{b} \rightarrow \bar{c} + W(u\bar{s})$ transition. The channel $B_s \rightarrow D_s^+ K^-$ proceeds through the right diagram in figure 1.5, i.e. via a $\bar{b} \rightarrow \bar{u} + W(c\bar{s})$ transition. The conjugate diagrams hold for the decay of the \bar{B}_s .

The rate asymmetries $\mathcal{A}_{D_s^- K^+}(t)$ and $\mathcal{A}_{D_s^+ K^-}(t)$ are expected to be large. From these

⁴In case the penguin diagram of figure 1.3 (right) contributes significantly (which seems to be the case[24]) the approximation leading to equation 1.20 does not hold. It can be shown that the CP asymmetry is then given by:

$$\mathcal{A}_{\pi\pi} = a \cos \Delta mt + b \sin \Delta mt \quad , \quad (1.22)$$

where a and b depend on the ratio of the contribution of the penguin and tree diagrams and on the strong phase difference between these diagrams[7].

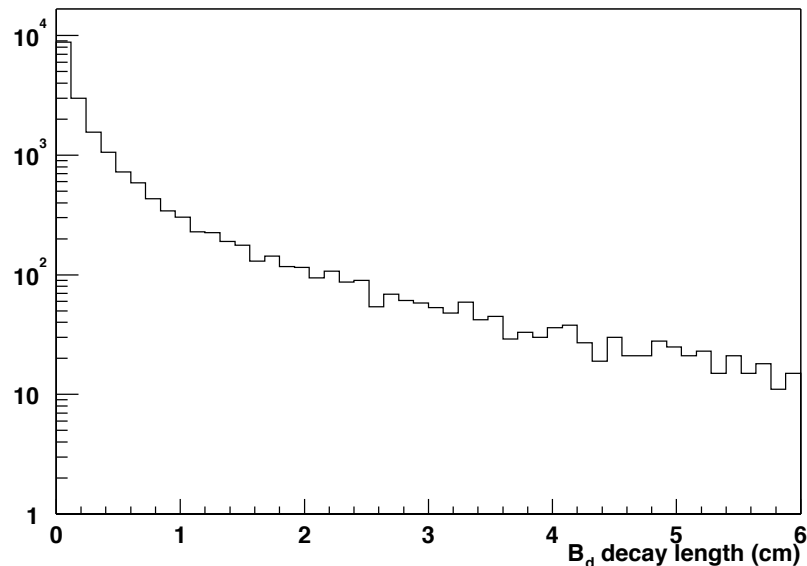


Figure 1.4: The simulated decay length of the B_d meson in $B_d \rightarrow \pi^+\pi^-$ events.

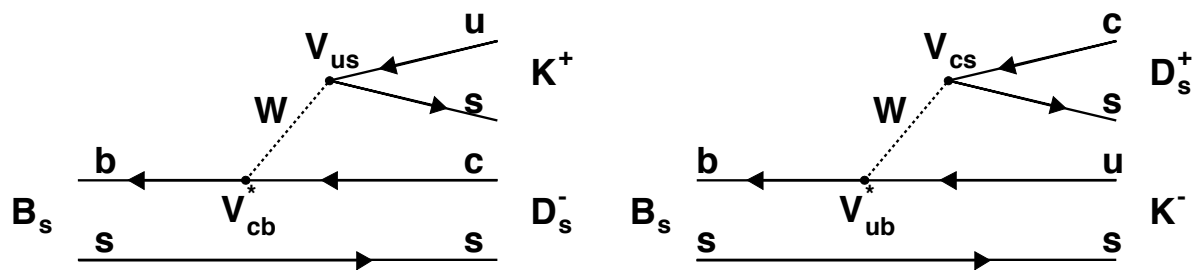


Figure 1.5: Feynman diagrams of the decay of a B_s into a $D_s^- K^+$ and into a $D_s^+ K^-$ pair.

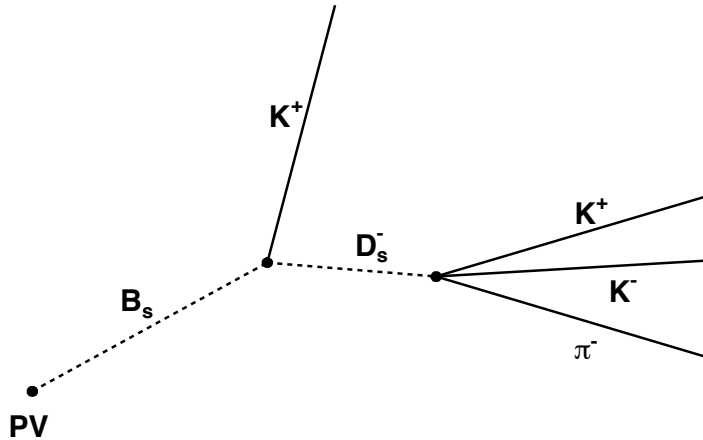


Figure 1.6: The kinematics of the decay $B_s \rightarrow D_s^- K^+$.

rate asymmetries $|\lambda|$ and ϕ can be extracted. It can be shown[7] that:

$$\begin{aligned}\phi = \arg \lambda &= -\gamma' + \Delta \\ \bar{\phi} = \arg \bar{\lambda} &= \gamma' + \Delta\end{aligned}, \quad (1.23)$$

where the weak angle $\gamma' = \gamma - 2\delta\gamma$. The angle $\delta\gamma$ is a small phase in the B_s mixing and γ is defined in equation 1.7. Δ is the strong-phase difference between the $b \rightarrow c + W(u\bar{s})$ and $b \rightarrow u + W(\bar{c}s)$ transition diagrams. By measuring both time dependent decay asymmetries the angle γ' can thus be extracted.

B_s mesons have an average lifetime of 1.6×10^{-12} s, and will, similarly to B_d , travel in the LHCb lab-frame typically 1 cm. The D_s has a lifetime (0.46×10^{-12} s) and will travel a few mm. In this thesis the decay of the D_s into $KK\pi$ is discussed⁵. The decay is kinematically characterised by two oppositely charged kaons with an additional pion forming a vertex displaced from the primary vertex. The resulting momentum vector points to the B_s decay vertex, which is made of this D_s together with an additional kaon (see figure 1.6).

1.5 B meson production

The calculation of the B meson production cross sections in proton-proton collisions at the LHC are complicated due to non perturbative QCD effects as well as the fact that protons are composite particles. Heavy flavour production in a hadron collider is

⁵The branching ratio for the D_s decay into these particles is about 5 %. Most other decays can not be fully reconstructed because they contain neutrinos and neutral particles.

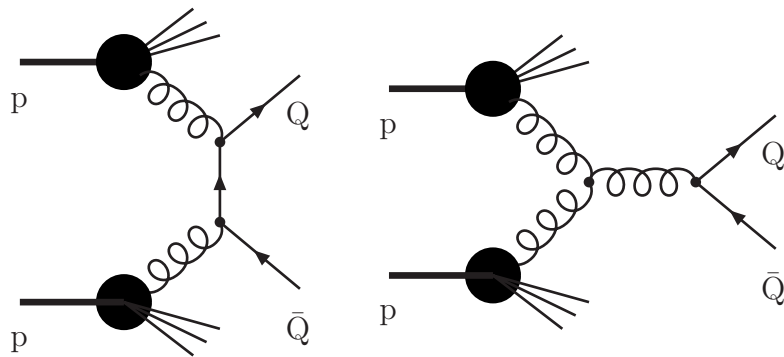


Figure 1.7: Feynman diagrams of the dominant first order production mechanisms of heavy quarks at the LHC.

usually described by splitting the interaction in a *hard* (high momentum transfer) part and in a *soft* part. The hard part describes the strong interaction of constituent partons forming heavy flavour quarks in terms of elementary processes such as the diagrams shown in figure 1.7. Calculations of the cross section for heavy flavour production have been performed to next-to-leading order precision (see e.g. [8] and references therein). The calculations are quantitatively in good agreement with experimental data for t quarks. However, for the lighter b quarks large discrepancies between calculations and measurements are observed. Large uncertainties exist due to higher order effects. As in reference[7] it is assumed that the cross section for inelastic proton-proton collisions is 80 mb, the $b\bar{b}$ cross section is taken to be 0.5 mb.

In the strong interaction b quarks will always be produced in $b\bar{b}$ -pairs. Figure 1.8 shows the relation between the polar angle (i.e. the angle with respect to the beam axis) of a B meson and \bar{B} meson produced in the same B event as obtained with the event generator PYTHIA[25]. The figure shows that the polar angle of the b quark and that of the \bar{b} quark have a strong positive correlation. In addition, the figure shows that the B meson production is peaked at small (~ 0 rad) and high ($\sim \pi$ rad) θ , i.e. along the beam. The fact that both B mesons are produced in the same forward region has led to the single arm forward geometry of the LHCb detector (see section 2.2). As can be seen from figure 1.9 the LHCb angular acceptance of 10 mrad to 250 mrad covers a large fraction of the phase-space of produced B mesons.

In LHCb we are interested in studying specific B meson decays and hence in the efficient reconstruction of the stable decay products of these mesons. In addition to the B mesons many other particles are produced in the proton-proton collision. The tracks from the underlying event, i.e. all produced particles not directly associated with the B , need in principle⁶ not to be reconstructed. Figure 1.10 shows the primary charged particle multiplicity within the LHCb acceptance for $B \rightarrow \pi^+\pi^-$ events. In addition, the figure shows the primary particle multiplicity for *minimum bias*⁷ inelastic interactions.

⁶The current RICH (global) pattern recognition algorithm assumes most particles traversing the detector volume to be efficiently reconstructed.

⁷A minimum bias event is an event obtained with a random trigger, i.e. no selection(bias) on the type of interaction is applied.

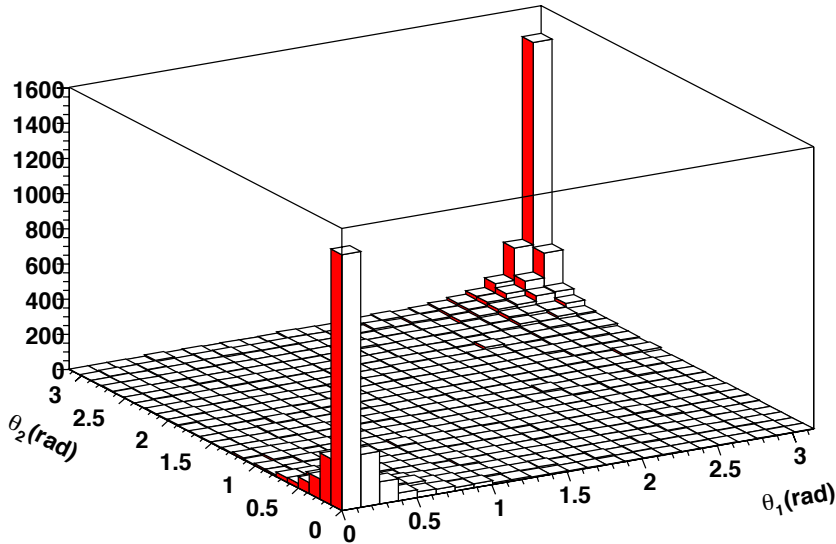


Figure 1.8: Simulated correlation between the polar angle θ of a B meson and of a \bar{B} meson simultaneously produced in a single event.

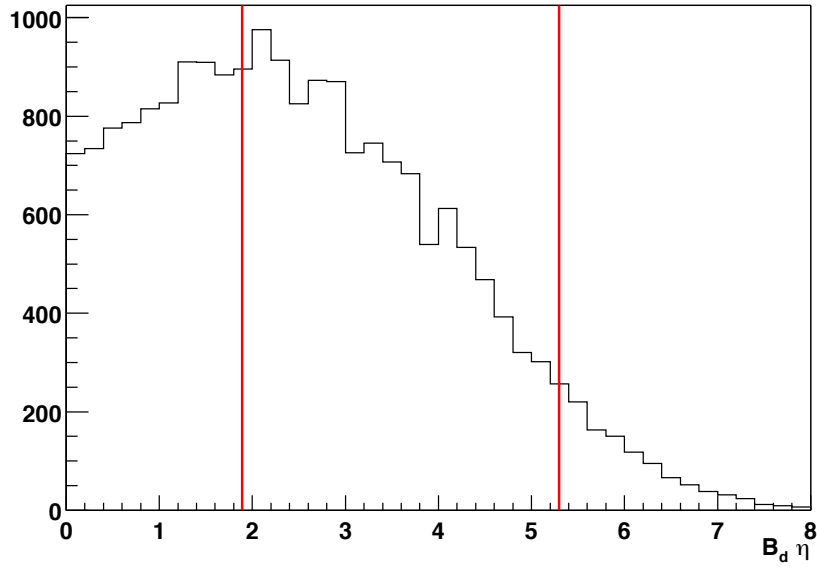


Figure 1.9: Simulated pseudo-rapidity distribution ($\eta = -\log(\tan(\theta/2))$) for B mesons produced at the LHC. The lines indicate the LHCb detector geometrical acceptance.

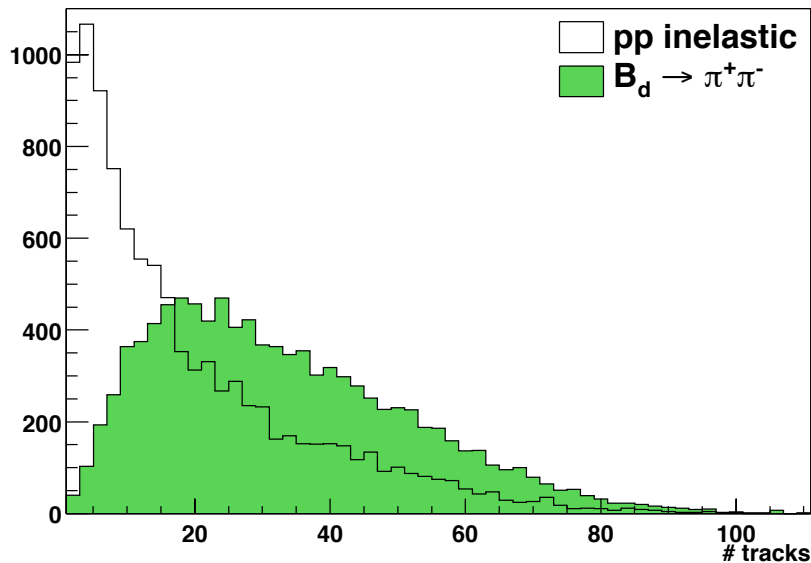


Figure 1.10: The simulated primary charged particle multiplicity in the LHCb geometric acceptance for $B \rightarrow \pi^+\pi^-$ events and inelastic interactions.

These distributions show that the particle multiplicities for B events are expected to be higher than for minimum bias inelastic interactions.

Chapter 2

The LHCb experiment

This chapter gives an overview of the experimental aspects of the LHCb experiment. LHCb will be situated at one of the interaction points of the new accelerator facility, the Large Hadron Collider (LHC) [26], at CERN. Section 2.1 gives a description of the main properties of the LHC accelerator. The LHCb detector and the various type of detection systems are described in section 2.2. A detailed description of the LHCb main tracking system, a vital ingredient for the reconstruction of the particle trajectories, is given in section 2.3. In section 2.4 the LHCb trigger scheme is discussed.

2.1 The Large Hadron Collider

After 11 years of running in November 2000 CERN’s main accelerator facility LEP[27] was closed to be replaced by a new generation accelerator; the Large Hadron Collider (LHC). The LHC is a circular collider of 26.66 km circumference colliding two proton beams rotating in opposite directions with a centre of mass energy of $\sqrt{s} = 14$ TeV. The high energy and luminosity of the LHC allow the study of new fields of physics.

To reach the high centre of mass collision energy in the LHC a chain of accelerators is used. Existing accelerators at CERN will be upgraded[26] to reach the performance required for the LHC. The chain starts with a linear proton accelerator (Linac) accelerating bunches of 10^{11} particles to an energy of 50 MeV. These bunches will be boosted to 1.4 GeV by the PS Booster (PSB) and transmitted to the Proton Synchrotron (PS). The PS accelerates the protons further to 26 GeV and injects them into the Super Proton Synchrotron (SPS). The SPS accelerates the bunches to 450 GeV and finally injects them clockwise and counter-clockwise into the LHC-ring. A total of about seven minutes is needed to fill both LHC rings. When the rings are filled the LHC further accelerates the protons to an energy of 7 TeV. See figure 2.1 for a schematic layout of the accelerator chain.

The cross sections of the interesting physics processes at the LHC energy are typically small (range $\mathcal{O}(\text{pb})\text{-}\mathcal{O}(\text{nb})$ [8]). Therefore, to gather enough statistics to be sensitive to these phenomena collisions with a high luminosity are required. The luminosity in terms of machine parameters is given by:

$$\mathcal{L} = \frac{N_1 N_2 k_b f \gamma}{4\pi \varepsilon_n \beta^*} F \quad , \quad (2.1)$$

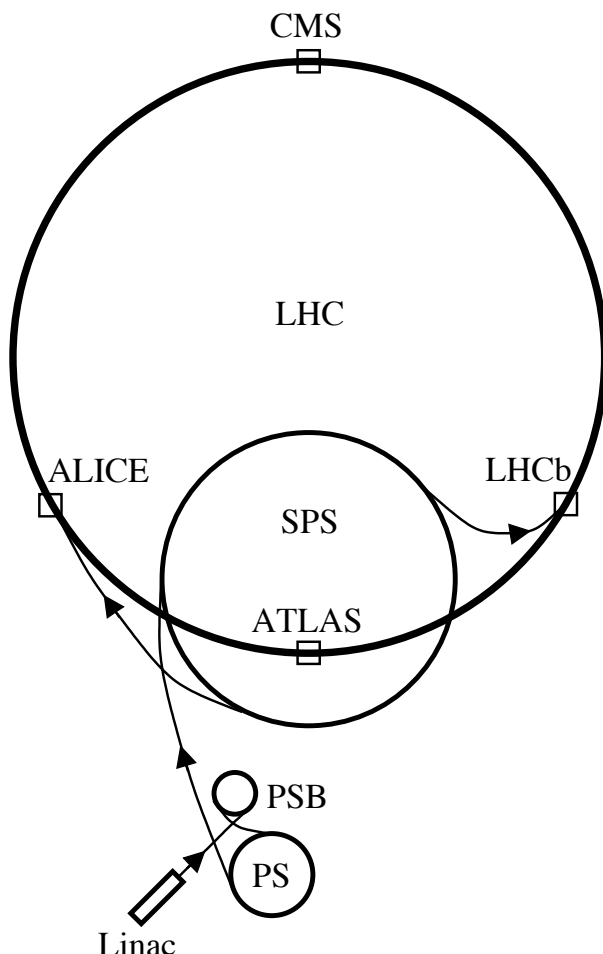


Figure 2.1: Schematic layout of the accelerator complex at CERN. Shown is the accelerator chain supplying the Large Hadron Collider (LHC) of protons. It consists of the 50 MeV proton linac, the 1.4 GeV PS booster(PSB), the 26 GeV PS and the SPS injecting the protons at 450 GeV into the LHC. Also shown are the locations along the LHC of the four experiments Alice, ATLAS, CMS and LHCb.

energy	14 TeV
circumference	26.66 km
N	1.05×10^{11}
k_b	2622
f	11245.5 Hz
γ	7460.6
ε_n	$3.75 \mu\text{m} \cdot \text{rad}$
β^*	0.5 m
F	0.9
fill lifetime	10 h

Table 2.1: LHC parameters[26] at the nominal design luminosity of $10^{34}\text{cm}^{-2}\text{s}^{-1}$.

where N_1 and N_2 are the average number of protons per bunch for the two beams, k_b the number of filled bunches, f the revolution frequency, γ the relativistic factor $1/\sqrt{1 - \beta^2}$, ε_n the normalised transverse emittance, β^* the value of the betatron function at the interaction point, and F a factor taking into account that the two beams cross under an angle of 200 μrad [26]. The betatron function describes transverse oscillations the particles make around their central orbit. It is determined by the arrangement of quadrupoles. At the interaction point the beam is focused, which is expressed by a small betatron value at the vertex. With the nominal values listed in table 2.1, the LHC design luminosity of $10^{34}\text{cm}^{-2}\text{s}^{-1}$ is obtained.

After the beams have been filled the number of particles will decrease due to interactions and other beam losses. The expected luminosity lifetime is 10 h. The total integrated luminosity per year (10^7 s) is 10^{41}cm^{-2} .

Bunches are spaced by 25 ns, corresponding to 3564 bunches in the ring and a bunch crossing rate of 40 MHz. However, due to a non-integer ratio of the PS, SPS and LHC revolution frequencies not all bunches are filled therefore “bunch-trains” separated by a group of empty bunches will circulate in the rings. Along the ring there will be four interaction regions occupied by the main LHC experiments Alice[28], ATLAS[29], CMS[30] and LHCb[7]. LHCb will be situated 100 meter under the surface in the cavern called “pit8” (IP8). At the LHCb interaction region 73 % of the beam crossings will actually contain protons in both bunches. The start of the LHC is scheduled for the year 2007[31].

At the design luminosity of $10^{34}\text{cm}^{-2}\text{s}^{-1}$ on average 27 proton-proton interactions will occur per beam crossing. These interactions will take place in an interaction region, which has a size of 5.3 cm ($= 1\sigma$) along the beam direction. Therefore, a multiple of primary interactions with possible associated secondary vertices will take place that can not be separated in time. Matching secondary decay-vertices to the corresponding primary interaction vertices, both at trigger time and off-line, can therefore often not be done unambiguously. This is the reason why LHCb, which is designed to study the production of B particles and their subsequent decay, has chosen to run at a lower luminosity. In addition a dedicated trigger (the “pile-up veto”[32]) will reject multiple interactions at the lowest trigger level (level 0).

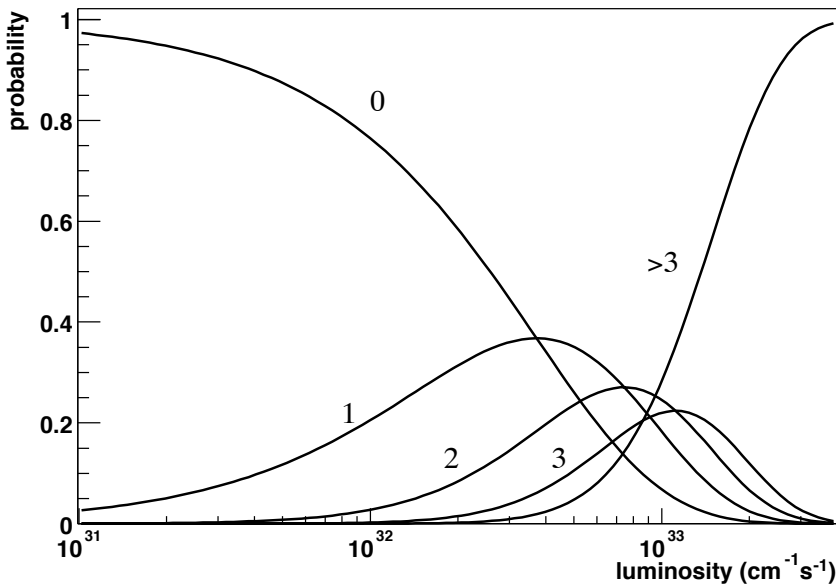


Figure 2.2: The probability distributions for empty, single, double, triple and multiple interactions per beam crossing, as a function of the luminosity.

A lower luminosity in comparison to the other interaction points can be achieved by increasing the betatron value β^* of the beam. At LHCb β^* can be varied from 0.5 m up to 12 m[26].

Figure 2.2 shows the expected probability for zero, single, double, triple or more interactions per beam crossing as a function of the luminosity, assuming a 80 mb inelastic proton-proton cross section (see section 1.5). It shows the maximum single event probability to be obtained for a luminosity of $4 \times 10^{32} \text{ cm}^{-2}\text{s}^{-1}$. This, however, is not the optimal luminosity from the point of view of maximising the number of single B meson events selected by the LHCb trigger. An optimisation study[32], taking into account the trigger efficiency for single B event bunch crossings as a function of luminosity, shows this maximum to be achieved for a luminosity of $3 \times 10^{32} \text{ cm}^{-2}\text{s}^{-1}$. The single B event rate distribution is, however, rather flat in the range $2 - 5 \times 10^{32} \text{ cm}^{-2}\text{s}^{-1}$.

Another advantage of a low luminosity is a relatively low particle rate in the detectors. Hence, the radiation damage will be less a problem and detector occupancies will be relatively low. Taking all above points into account, the nominal luminosity of the LHCb experiment is chosen to be $2 \times 10^{32} \text{ cm}^{-2}\text{s}^{-1}$ [7]. The detectors are designed to withstand a maximum luminosity of $5 \times 10^{32} \text{ cm}^{-2}\text{s}^{-1}$. At the nominal luminosity, after applying the pile-up veto, the event rate is approximately 10 MHz, with more than 90 % containing a single interaction. Assuming a $b\bar{b}$ production cross section of 0.5 mb, this represents $5.6 \times 10^{11} b\bar{b}$ pairs per year (10^7 s) occurring in single interactions[33].

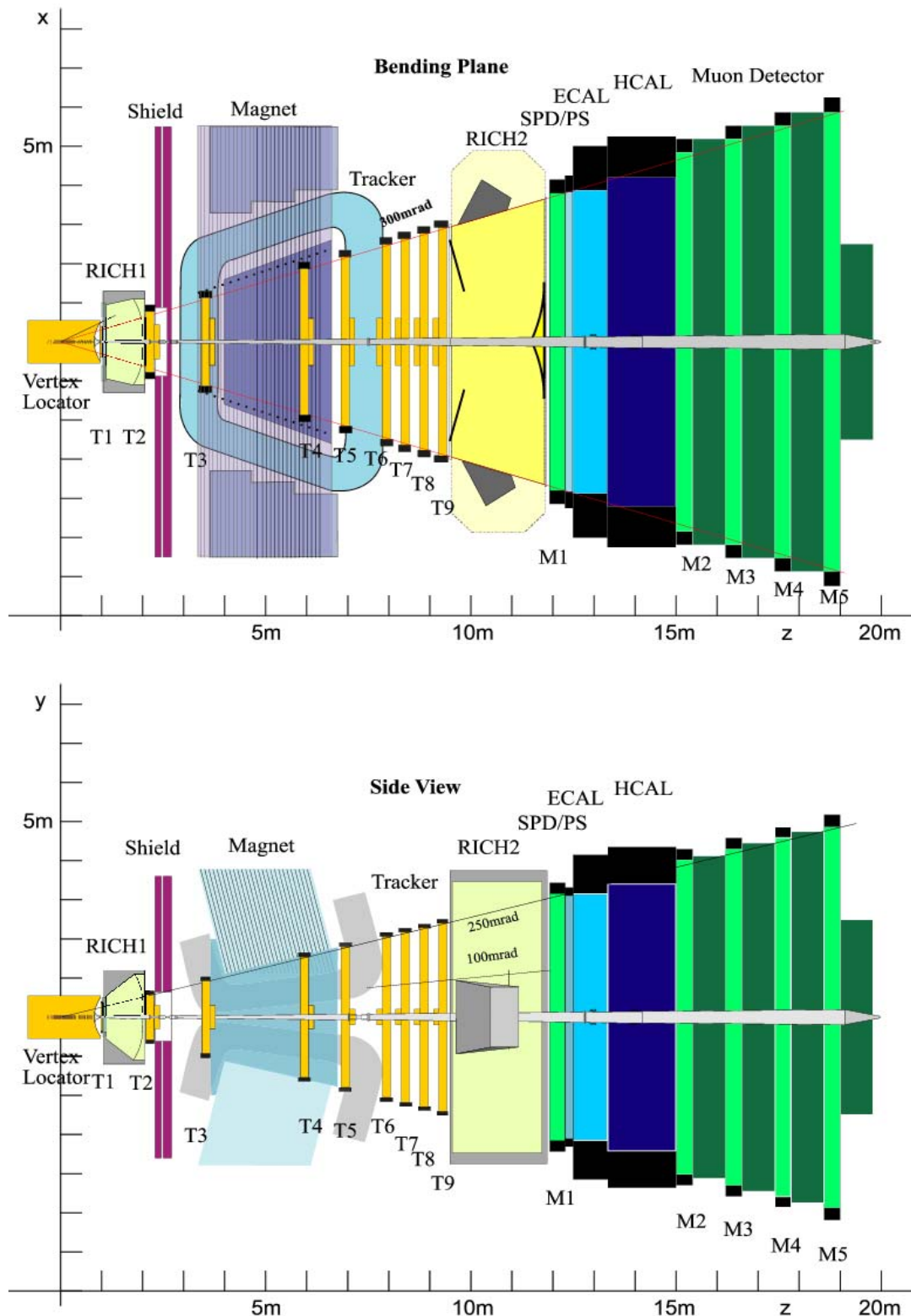


Figure 2.3: Cross sections of the LHCb detector. The top figure is the cross section of the detector in the bending plane of the magnet, i.e. the top view. The bottom figure is the cross section of the detector in the non-bending plane, i.e. the side view. All detector sub-systems of the spectrometer are indicated.

2.2 The LHCb detector

The fact that both B hadrons are predominantly produced in the same forward cone (see section 1.5) is exploited in the layout of the LHCb detector. The LHCb detector is a single arm forward spectrometer with a polar angular coverage from 10 mrad to 300(250) mrad in the horizontal(vertical) plane. The asymmetry between the horizontal and vertical plane is determined by a large dipole magnet with the main component in the vertical direction. In figure 2.3 the layout of the LHCb spectrometer is shown. The top figure shows the cross section of the detector in the bending plane (of the magnet), i.e. the top view. The bottom figure shows the cross section of the detector in the non-bending plane, i.e. the side view. LHCb uses a right-handed coordinate system with y pointing upwards, x horizontal and pointing to the outside of the LHC-ring and the z -axis along the beam. The proton-proton collisions take place around $z = 0$ located at the left side in the figures.

The vertex detector is built around the proton interaction region. It is used to measure the particle trajectories close to the interaction point in order to precisely separate primary and secondary vertices. Directly after the vertex detector RICH-1 (a Ring Imaging CHerenkov detector) is located. It is used for particle identification of low momentum tracks. The main tracking system is partly placed in the dipole magnet. It is used to reconstruct the trajectories of charged particles and to measure their momenta. Following the tracking system is RICH-2. It allows the identification of the particle type of high momentum tracks. The electromagnetic and hadronic calorimeters provide measurements of the energy of electrons, photons and hadrons. These measurements are used at trigger level to identify high p_t particles. The muon system is used to trigger on muons in the event. The beam-pipe has a conical shape and is made out of an aluminium-beryllium alloy.

The following sections outline the main aspects of the detector sub-systems. The vertex detector system is described in section 2.2.1, the RICH detectors in section 2.2.2, the calorimeters in section 2.2.3, and the muon detector in section 2.2.4. The main tracking system, consisting of the outer tracker, the inner tracker and the dipole-magnet, is described in more detail in section 2.3.

2.2.1 Vertex detector system

The LHCb vertex locator (VELO) consists of 25 stations of silicon strip detectors placed perpendicular to the beam. The VELO measures the particle trajectories close to the interaction region. The high resolution of the coordinate measurements of the track allows the reconstruction and separation of the primary interaction vertex from the secondary decay vertices of B mesons. To realize this high precision the detector must be placed as close as possible to the interaction point. This is achieved by placing the whole vertex detector inside a secondary vacuum. Each station is split in an upper and lower half. This enables the retraction of the detectors by 3.0 cm from their operation position to allow a safe injection and acceleration of a new “fill” of proton bunches in the LHC. The sensors are encapsulated in a thin aluminium box. This is to provide adequate wake field suppression, to shield the detectors from excessive RF pick-up noise

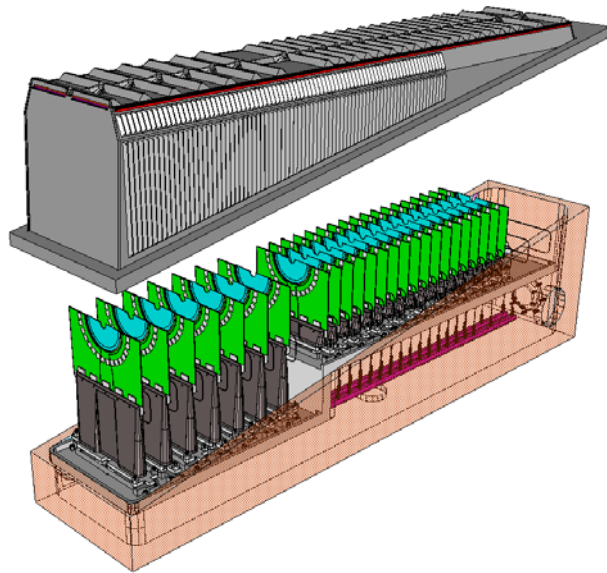


Figure 2.4: View of one half of the LHCb vertex detector. Shown are the 25 detection stations with their basic support structure. Also shown is the aluminium box used to provide wake field suppression and minimise RF pick-up noise in the detectors[34].

and to separate the primary vacuum from the secondary vacuum[35]. See figure 2.4 for a technical drawing of one half of the vertex detector system.

Each upper or lower station contains two half-disc detectors separated by 2 mm. One disc has radial strips measuring the ϕ coordinate, the other disc has circular strips measuring r (see figure 2.5). The discs have a radial coverage from 8 mm to 42 mm and are $300\mu\text{m}$ thick. Both the R and ϕ detectors are divided in an inner and outer region. The strip to strip distance (pitch) in the inner region of the R detectors is $40 \mu\text{m}$. In the outer region the pitch is gradually increased to a maximum pitch of $92 \mu\text{m}$ at a radius of 42 mm. The minimum strip pitch in the ϕ detector is $37 \mu\text{m}$ increasing up to a maximum $98 \mu\text{m}$ in the outer region of the silicon wafer. The system has a total of 204800 channels. A detailed description of the LHCb vertex detector system is given in the VELO technical design report [34].

The vertex detector provides information at several stages in the trigger. Two dedicated silicon stations, placed at the opposite side of the interaction region as the LHCb spectrometer, are used in the Level-0 trigger to reject events with multiple proton-proton interactions. The remaining VELO detectors are used in the Level-1 trigger to select B events by detecting displaced secondary vertices. The higher trigger levels (2 and 3) use the full vertex detector information to reconstruct and precisely measure a full decay chain. The LHCb trigger scheme is described in more detail in section 2.4.

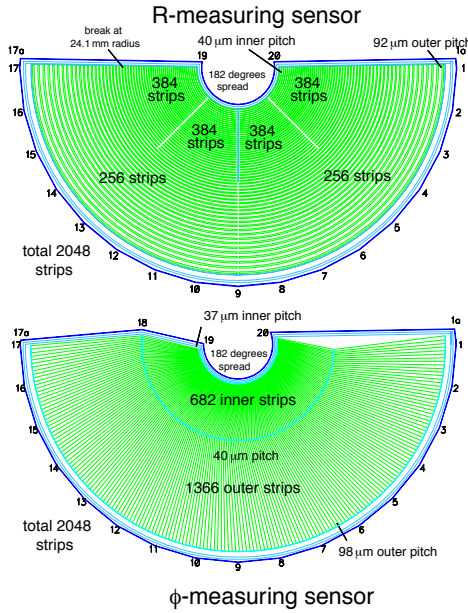


Figure 2.5: Schematic layout of the R and ϕ vertex detector half discs. The R detector has circular strips, the ϕ detector radial strips tilted under an angle of 20 degrees in the inner region and -10 degrees in the outer region[34].

2.2.2 RICH detectors

LHCb uses two Ring Imaging CHerenkov (RICH) detectors. RICH-1 is placed directly downstream of the vertex detector and before the main tracking system. RICH-2 is positioned after the tracking stations and in front of the calorimeters (see figure 2.3). RICH detectors measure the Cherenkov angle[36] of light emitted when a charged particle traverses a medium with a velocity higher than the speed of light in that medium. These measurements are used, together with the momentum measurements by the main tracking system, to perform particle identification of charged tracks.

The operation principle of the RICH detectors is based on the Cherenkov effect[36]. When a charge track traverses a medium with a velocity v higher than the speed of light in that medium electromagnetic radiation is emitted along the trajectory. This Cherenkov radiation is emitted under a unique angle θ_c with respect to the particle direction, i.e.

$$\cos\theta_c = \frac{c}{vn} \quad , \quad (2.2)$$

where n is the refractive index of the medium. Particles can therefore be identified when their momentum and the opening angle of the Cherenkov radiation cone are known. The Ring Imaging CHerenkov (RICH) detector of LHCb measures θ_c by focusing the emitted light with a spherical mirror on a plane of photo-detectors. The photons emitted along the trajectory of the traversing particles will then form a ring on the photo-detector plane, with the radius proportional to θ_c . Figure 2.6 shows the angle θ_c as a function of momentum for π^- and K^- mesons for CF_4 as the radiator medium.

Distinguishing pions from kaons is essential for increasing the signal to background

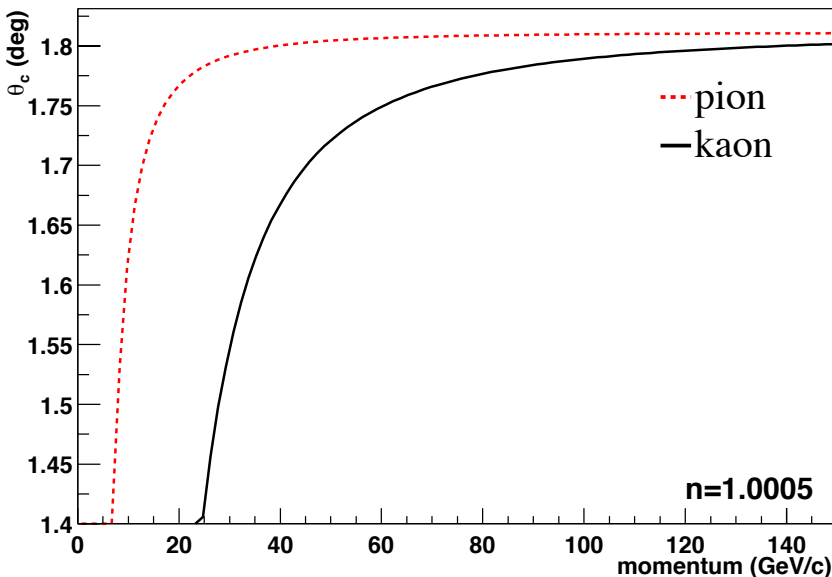


Figure 2.6: Cherenkov angle θ_c as a function of momentum for pions and kaons in the CF_4 ($n = 1.0005$) radiator medium.

ratio of various important CP-violating B decays (e.g. for the decays $B_s \rightarrow D_s^\pm K^\mp$ of section 1.4.2). The LHCb RICH detectors have to provide identification of charged particles over a wide momentum range, i.e. from 1 GeV/c up to a momentum of about 150 GeV/c. In order to achieve this, several radiator materials with different refractive indices are used. Figure 2.7 shows the layout of the two RICH detectors, RICH-1 and RICH-2.

RICH-1 is used to perform particle identification of “low” momentum tracks over the full LHCb angular acceptance, i.e from 10 to 300 mrad (250 mrad) in the horizontal (vertical) plane. There are two radiators in RICH-1. The first radiator is a 5 cm thick aerogel layer with a refractive index $n = 1.03$. It provides pion-kaon separation up to about 10 GeV/c. The second radiator in RICH-1 is a volume filled with C_4F_{10} gas providing 85 cm path length with refractive index $n = 1.0014$.

The RICH-2 detector is used to perform particle identification of high momentum tracks. This requires a lower refractive index, but a longer path length for the particles to traverse to collect sufficient Cherenkov photons. It has a reduced outer angular acceptance of 120 mrad (100 mrad) in the horizontal (vertical) plane. This is possible because most high momentum tracks are produced under small angles as can be seen from figure 2.8. RICH-2 contains CF_4 gas providing 167 cm path length with refractive index $n = 1.0005$.

The information from both RICH detectors has to be correlated with the tracking and momentum information from the main tracking system to provide particle identification. The angular resolution of the reconstructed Cherenkov angle has several contributions. The error due to the reconstructed track parameters (especially the angle of the track)

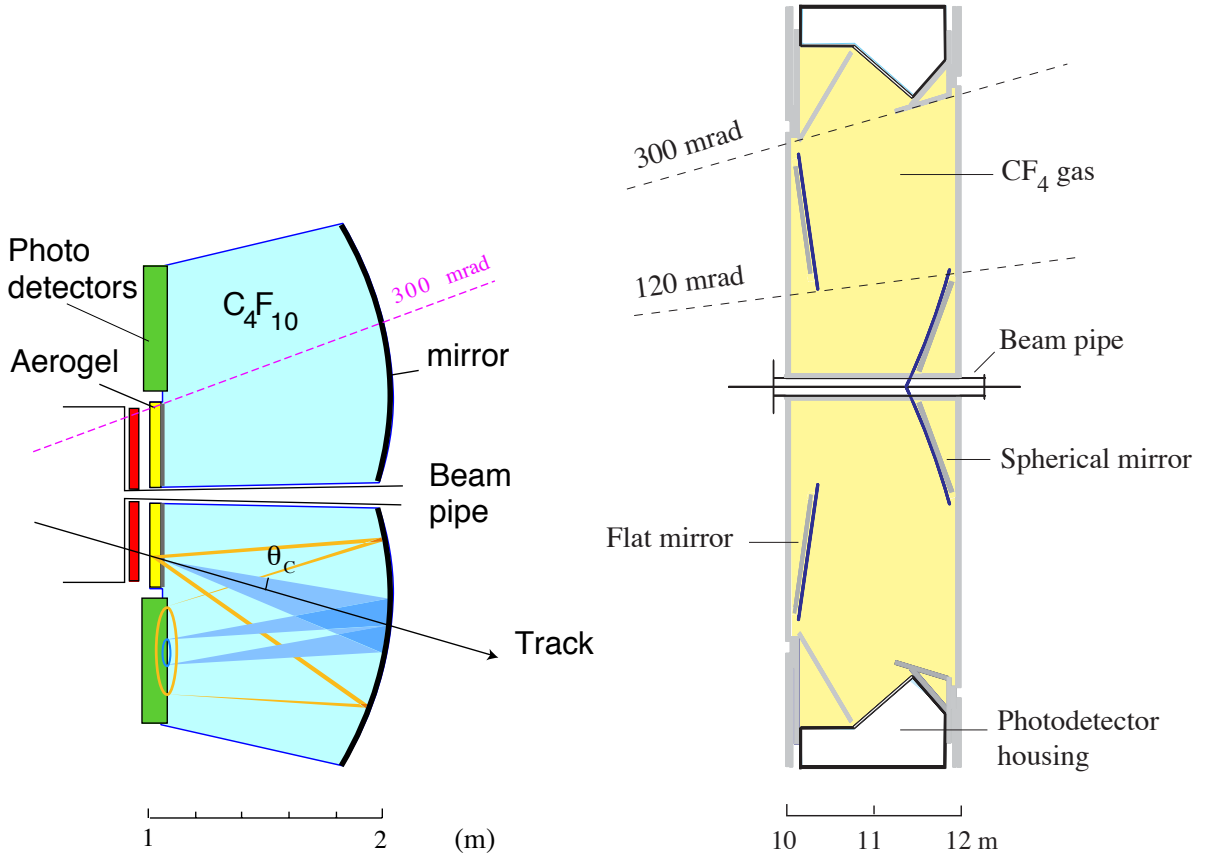


Figure 2.7: Schematic layout of both RICH detectors. The left drawing shows a top view of RICH-1. Illustrated is the focusing on the photo-detectors of Cherenkov light created along a track passing through the detector volumes. For a straight track, the light produced in the two radiators (Aero-gel and C_4F_{10}) has a different angle, but results in two Cherenkov rings on the photo-detector plane with the same centre[37]. The right drawing shows the top view of RICH-2. The flat mirrors deflect the light on photo-detectors that are placed outside of the LHCb acceptance.

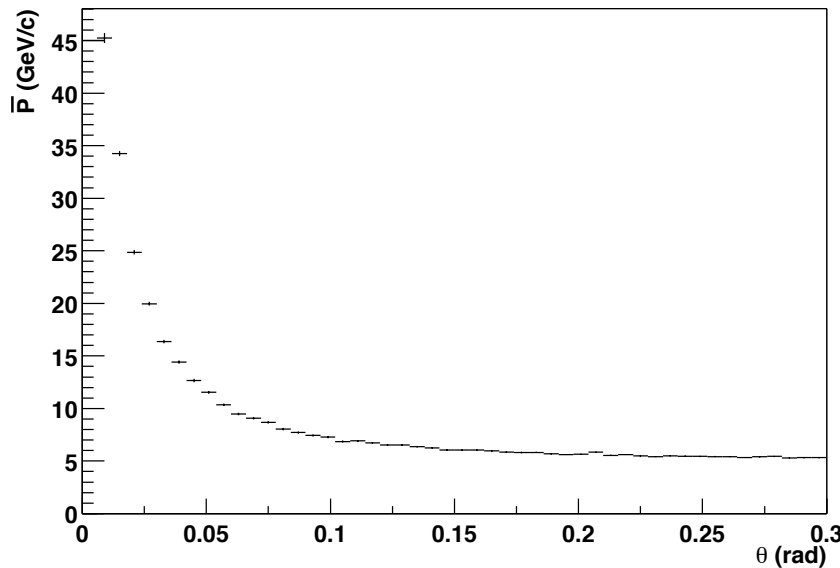


Figure 2.8: The average charged track momentum as a function of the production angle θ .

is required to contribute only a small fraction to the total resolution of the Cherenkov angle. Studies show[37, 38] the reconstructed track angle resolutions (see chapter 5) to be indeed sufficiently small.

Figure 2.9 gives for true pions the separation, in units of the standard deviation σ , between the pion and kaon hypothesis. A better than 3σ separation between kaons and pions is achieved for momenta between 2 and 100 GeV/c. For a detailed description of the LHCb RICH detector system see the RICH technical design report [37].

2.2.3 Calorimeters

The LHCb calorimetry consists of an electromagnetic calorimeter(ECAL) and a hadron calorimeter(HCAL). The complete system is positioned downstream of RICH-2, directly behind ($z = 12.3$ m) the first muon station M1 extending up to $z = 15.0$ m where the other muon stations start. The HCAL is positioned directly after the ECAL. Two special detection layers, the SPD and PS, are placed in front of the ECAL for charged particle and pre-shower detection. The calorimeters provide a measurement of the energy and the impact position of particles. These measurements are used at trigger level to identify hadrons, electrons and photons. In particular the calorimeter measurements are used to trigger on high p_t hadrons and electrons originating from a B decay (see section 2.4 for the LHCb trigger system).

The LHCb calorimeters are sampling calorimeters, i.e. they are constructed out of a sequence of layers of passive absorbing material alternated by active detection layers. An incident particle is stopped in the calorimeters by a cascade of decays and interactions

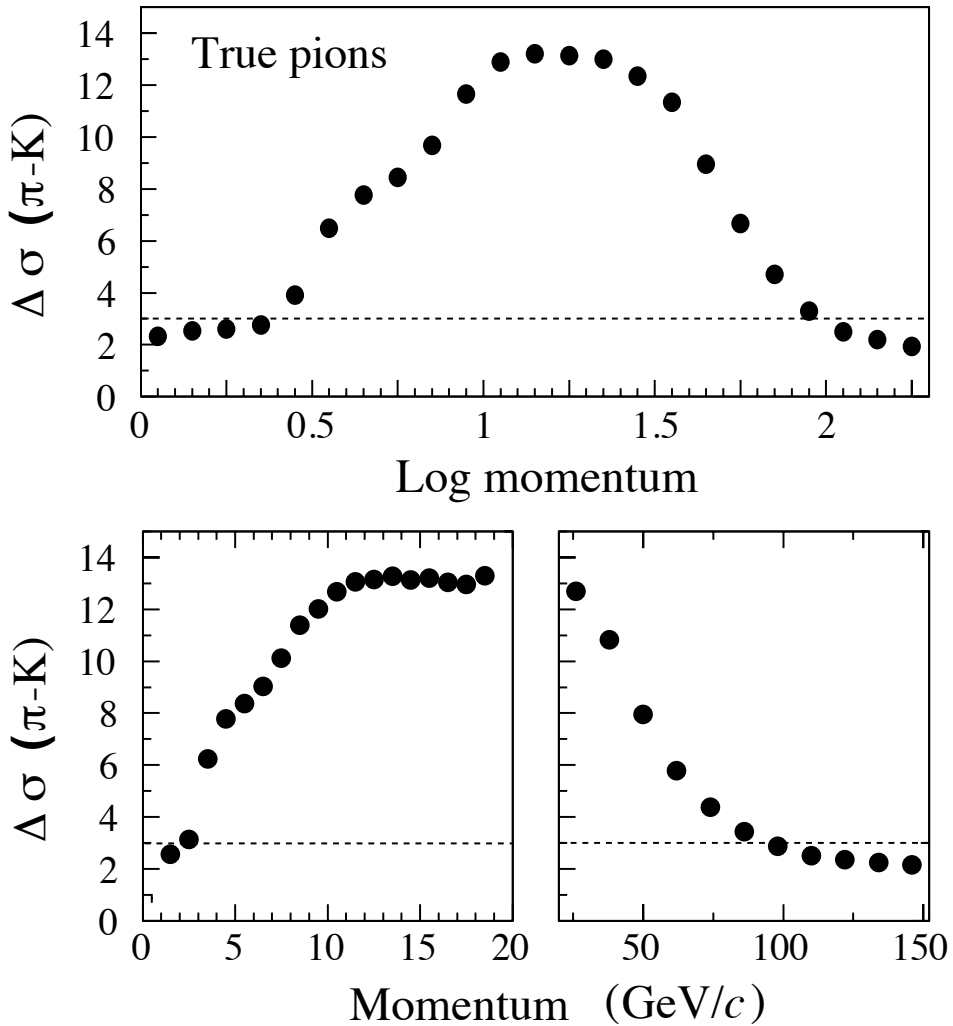


Figure 2.9: Number of σ separation between the pion and kaon hypothesis for true pions as a function of momentum[37]. The top figure shows a logarithmic momentum scale. The Bottom figure a linear momentum scale. The dotted line indicates the 3σ level.

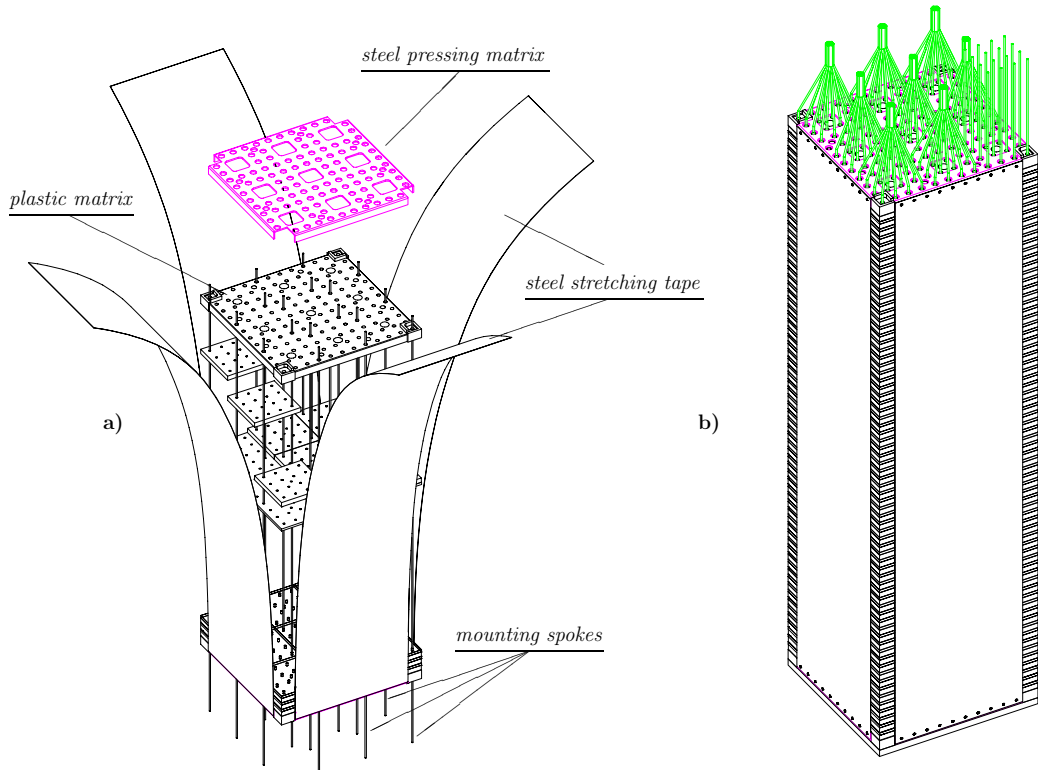


Figure 2.10: a) The assembly of a single ECAL “Shashlik” module from layers of lead and scintillator. b) The assembled module with inserted WLS-fibres. [39]

into progressively lower energy particles. This is called a shower. The signal produced in the active layers is a measure for the total amount of deposited energy. As active material scintillating plastics interwoven by wavelength-shifting(WLS) fibres are used. These fibres collect the light emitted in the scintillators and transfer it onto photomultiplier tubes. The passive absorption material is different for the two calorimeters.

The pad/pre-shower detector consists of a 15 mm thick layer of scintillator pads(SPD), a 12 mm lead radiator plate corresponding to about 2 radiation lengths(X_0) followed by another 15 mm thick scintillator pad layer(PS). The SPD is used to detect charged particles¹. The lead layer will likely cause electromagnetic particles (photons, electrons and positrons) to radiate causing an early shower that can be detected by the pre-shower(PS) layer. This is used for the identification of photons.

The electromagnetic calorimeter (ECAL) has a “Shashlik” geometry. It is built from individual modules of 66 alternating layers of 2 mm thick lead and 4 mm thick scintillating tiles, corresponding to a total depth of $25 X_0$ (see figure 2.10). The main use of the ECAL is the measurement of electromagnetic showers allowing, in combination

¹Neutral particles will not cause scintillators to fire. As neutral particles (like e.g. photons from π^0 's) will decay further downstream in the calorimeter system (causing charged particles that will be detected), the SPD layer can be used to distinguish charged from neutral particles.

with SPD and PS, the discrimination of electrons, photons and $\pi^0(\rightarrow 2\gamma)$'s, and a measurement of their energy. The energy resolution is $\sigma(E)/E = 10\%/\sqrt{E} \oplus 1.5\%$ with E in GeV.

The hadron calorimeter (HCAL) has a scintillating-tile geometry, with the tiles running parallel to the beam axis. The HCAL is made out of two halves each consisting of 26 stacked-up modules. A module is made out of 8 submodules. A submodule is constructed out of 26 identical 20 mm thick scintillator/steel sampling structures. One single HCAL module is 1.6 m long and weighs 9.5 tons corresponding to a depth of 7.3 interaction lengths (λ_I). The energy resolution of the HCAL is $\sigma(E)/E = 80\%/\sqrt{E} \oplus 5\%$.

For a detailed description of the LHCb calorimeters see the calorimeter technical design report [39].

2.2.4 Muon detector

The LHCb muon detector system is positioned at the far downstream end of the detector (see figure 2.3). It is used to trigger and, off-line, to identify muons relying on their penetrative power (compared to electrons/positrons and hadrons). The muon system consists of four detection stations M2-M5 after the calorimeters and one station M1 just before the pre-shower detector. The stations M2-M5 are interleaved with 0.8 m thick steel plates. These muon shields together with the shielding of the ECAL and HCAL gives a total absorber-thickness of 20 λ_I .

The chamber technology of the stations is determined by the expected particle rate. Resistive plate chambers (RPC)[40] are used in the outer regions of stations M4 and M5, where the particle rate is below $1 \text{ kHz cm}^{-2} \sim 48\%$ of the total area. Multi-wire proportional chambers (MWPC)[41, 42] are used for the coverage of ($\sim 52\%$) the remaining area. The technology for the inner part of station M1 (less than 1 % of total area), where rates of up to 400 kHz cm^{-2} are expected, is still to be selected. The total muon system has about 26000 readout channels. For a detailed description of the LHCb muon system see the muon system technical design report [43].

2.3 LHCb main tracking system

The reconstruction of particle trajectories in LHCb is the topic of this thesis. This section gives an overview of the LHCb main tracking detectors i.e. the outer tracker and the inner tracker. The description corresponds to the detector as presented in the LHCb outer tracker technical design report[44]. It is commonly referred to as *LHCb-classic*². The studies presented in this thesis have led to this design, in particular to that of the outer tracker³.

The main task of the LHCb tracking system is the efficient reconstruction of charged tracks in the spectrometer. The reconstructed particle trajectory is used to link the

²Recently new studies have started to reduce the amount of material in the detector (see section 7.6). The new design is referred to as *LHCb-light*.

³The inner tracker detector design is still being studied, and subject to changes. The detector presented in section 2.3.2 is the status of the detector at the time of the outer tracker technical design report[44].

measurements of the VELO, RICH-1 and RICH-2, the calorimeters and the muon system to the same particle. The measured deflection of the particle by the magnetic field gives the particle momentum.

The system consists of nine stations of tracking chambers (T1-T9) located between the vertex detector and RICH-2. The main function of the individual stations is as follows (see figure 2.3 for the positioning of the stations).

- Station T1 provides a link between the main tracking system and the vertex detector. Furthermore, it is used, together with station T2, to provide a precise prediction of the track direction through RICH-1. Station T2 is also vital in the precise measurement of the track momentum.
- Stations T3, T4 and T5 are used for “following” the track through the magnetic field. These stations are not directly required for the momentum measurement in the track fit. They are however valuable for the pattern recognition by allowing the matching of the track measurements before and after the magnet. Station T3 is also used in the downstream tracking to link the low-field region and the region where there is a magnetic field.
- Stations T6, T7, T8 and T9 are used for finding tracks. They provide an initial track seed for the reconstruction algorithm. In this low-field region particles approximately follow straight line trajectories making track finding relatively easy. In addition these stations provide the track link towards the detector systems downstream of the tracking system. Tracking information is in particular needed for the pattern recognition algorithms in RICH-2.

Figure 2.11 shows the charged particle rate in a (x, y) -plane in the magnet. Close to the beam the rate is high. Furthermore, due to the bending of charged particles in the magnetic field the particles are more spread along the x -axis. To cover the full acceptance two detector technologies are used. The regions of high track density (small r) are covered by an inner tracker based on silicon technology. The inner tracker has a “cross-shaped” geometry. It is further described in section 2.3.2. The outer tracker covers the remaining part of the angular acceptance. The stations have dimensions increasing from $141\text{ cm} \times 116\text{ cm}$ in T2 till $582\text{ cm} \times 481\text{ cm}$ in T9. Station T1 contains only inner tracker modules. The outer tracker is further described in section 2.3.3.

Each station consists of four detection planes, each measuring a 2-D point on the track. The most precise measurements are required in the bending plane (x, z) since these provide the momentum measurement. Therefore, the wire/strip orientation of the detectors is vertical (X -layer) or under a stereo-angle of $\pm 5^\circ$ with respect to the vertical (U -layer and V -layer).

2.3.1 Magnet

LHCb uses a conventional dipole magnet, placed relatively close to the interaction region in order to keep the size affordable. The aperture of the magnet corresponds to the LHCb acceptance of 300 mrad horizontally and 250 mrad vertically. This leads to an aperture

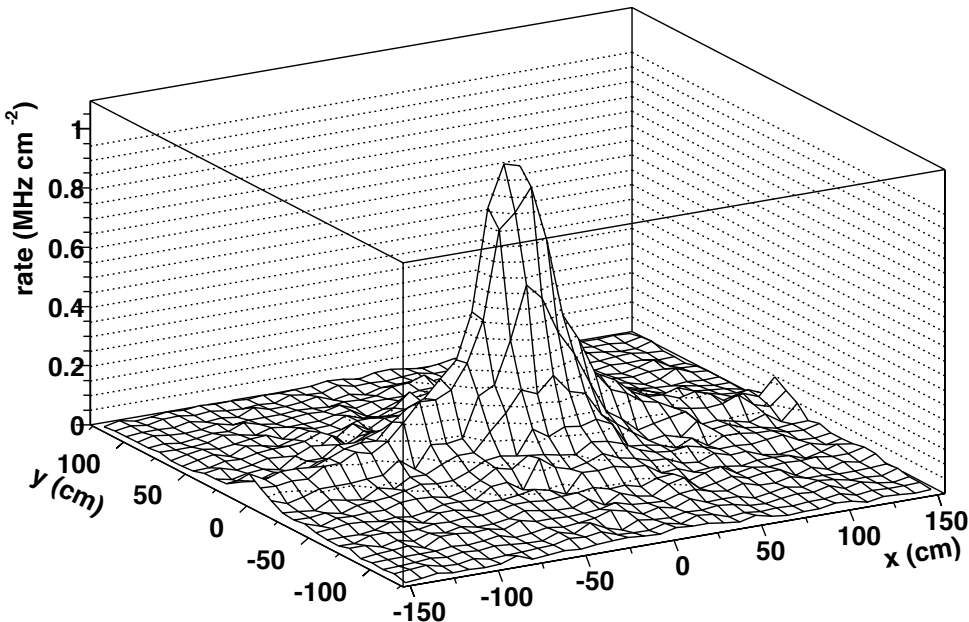


Figure 2.11: Charged particle rate in the (x, y) -plane at $z = 480$ cm.

of $260\text{ cm} \times 220\text{ cm}$ at the lower z position of the magnet increasing to $420\text{ cm} \times 350\text{ cm}$ at the high z side. A magnetic shield, just behind RICH-1, protects this detector against the stray field of the magnet.

The magnetic field has the main component along the vertical axis (B_y) and has the maximum field strength at the edges of the acceptance. The top plot in figure 2.12 shows the field components B_x , B_y and B_z as a function of z at the line $x = y = 0$. One sees that the vertical component of the field increases after the magnetic shielding, rising to ~ 1.0 T at $z = 5$ m and decreasing below 0.1 T above $z \sim 9$ m. The total field integral is approximately 4 Tm. The bottom plot in figure 2.12 shows the field components along a line originating at $x = y = z = 0$ under an angle $\theta_x = \theta_y = 100$ mrad. It shows a significant B_z component. Figure 2.13 shows the vertical component of the magnetic field in a (x, y) -plane in the magnet. One sees that the field is stronger near the magnet poles.

The non uniformity of the magnetic field integral has a maximum of about 5 %[45]. Hence, particles experience, depending on the their line of flight through the magnet, different integral fields and therefore deflections. Therefore, the full magnetic field map has to be taken into account in the trajectory reconstruction. For a detailed description of the LHCb magnet see the magnet technical design report[45].

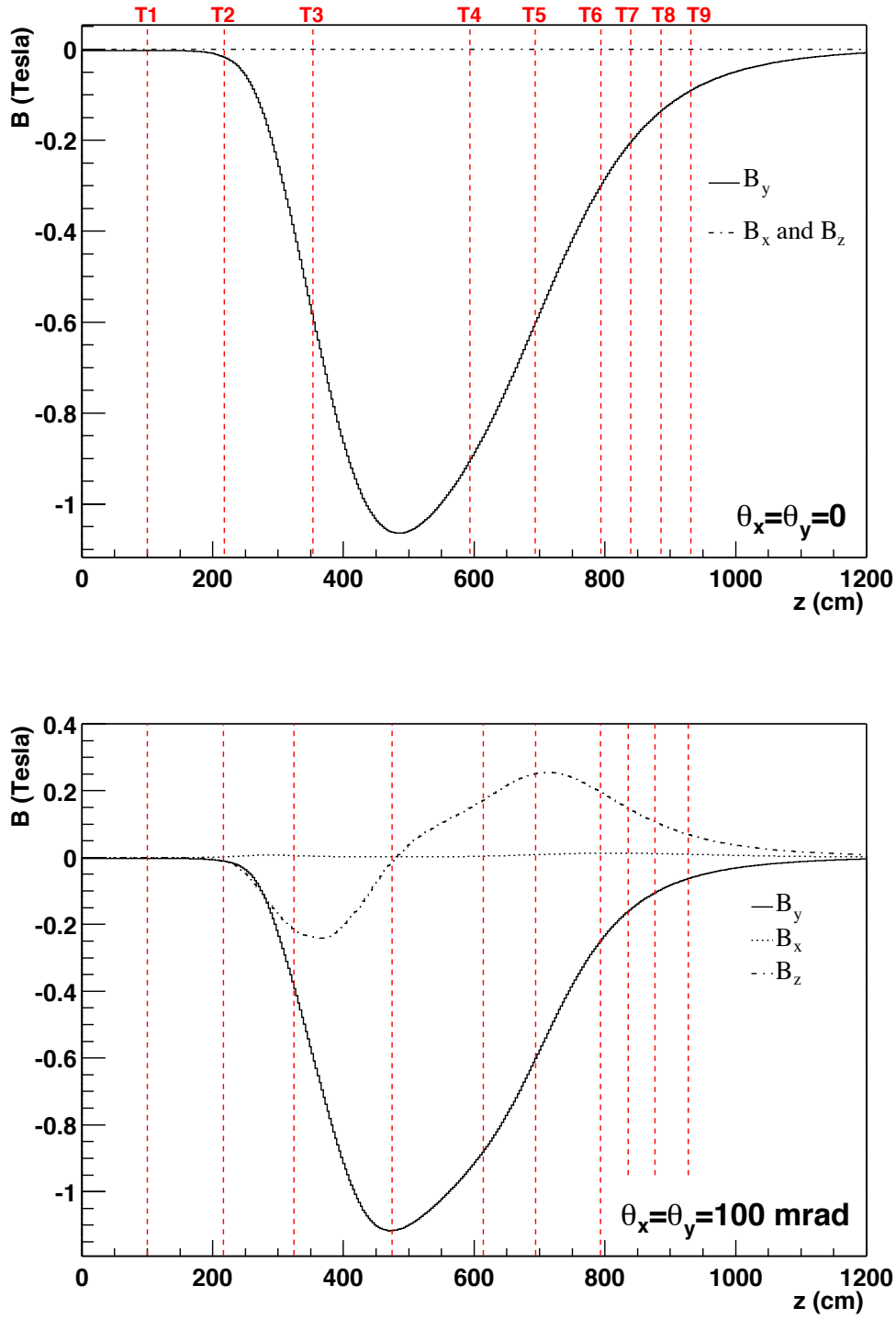


Figure 2.12: The top plot shows the magnetic field components B_x , B_y and B_z as a function of z along the z -axis ($\theta_x = \theta_y = 0$). The bottom plot shows the components along a line under an angle $\theta_x = \theta_y = 100$ mrad. The dashed vertical lines indicate the positions of the tracking stations.

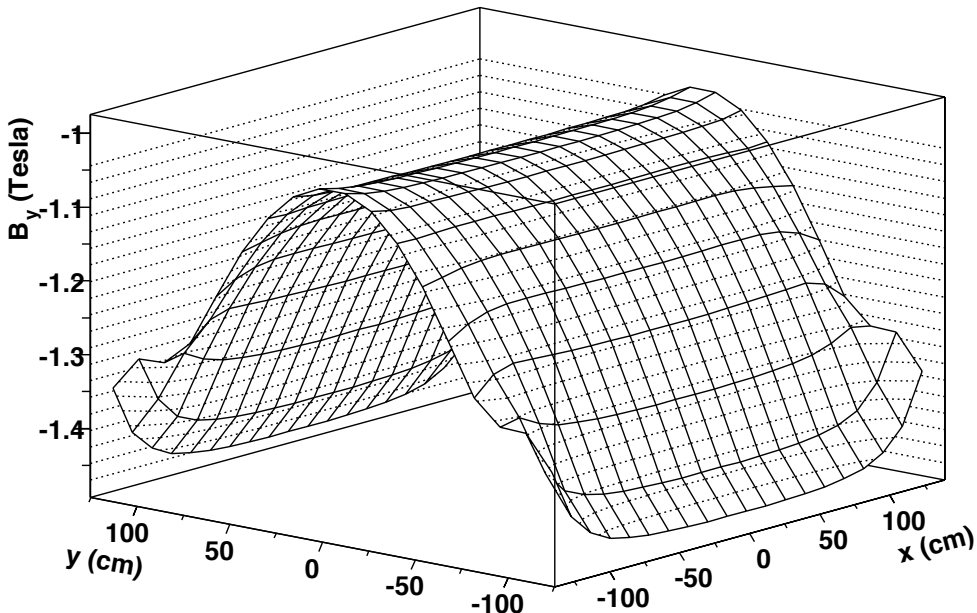


Figure 2.13: Vertical magnetic field component B_y in the (x, y) -plane at $z = 450$ cm.

2.3.2 Inner Tracker

The LHCb inner tracker consists of nine stations (T1-T9) of silicon strip detectors. The inner tracker detectors measure the particle trajectories in the high flux region close to the beam-pipe. The inner most dimensions of the inner tracker stations are determined by the outer radius of the beam-pipe. Because of the conical shaped beam-pipe the layout differs from station to station.

The outer dimensions of the inner tracker stations result from a simulation study of the outer tracker occupancy (see section 6.1). To keep the surface of the relatively expensive inner tracker technology as small as possible, the inner tracker covers a cross-shaped area around the beam-pipe, reflecting the particle rate distribution as in figure 2.11.

Each inner tracker station consists of four rectangular ‘‘boxes’’, one above, one below and one on each side of the beam-pipe. In figure 2.14 the layout of an inner tracker station 4 layer is shown. All stations are assembled from standard silicon sensors of $300\ \mu\text{m}$ thick. The sensors have a fixed size of $11\ \text{cm} \times 7.8\ \text{cm}$. Two options exist for the pitch of the sensors; or a pitch of $237.5\ \mu\text{m}$ resulting in 320 strips per sensor, or a pitch of $197.9\ \mu\text{m}$ resulting in 384 strips per sensor. Measurements[46] on prototype sensor show a single hit resolution of $50\ \mu\text{m}$.

From the silicon sensors ladders are formed. The silicon ladders consist of either one or two sensors connected by a read-out hybrid at one side of the ladder (see figure 2.15). These ladders are grouped forming a cross-shaped layer of the inner tracker as shown in figure 2.14. Each station consists of four of these layers, i.e. a x, u, v , and x -layer.

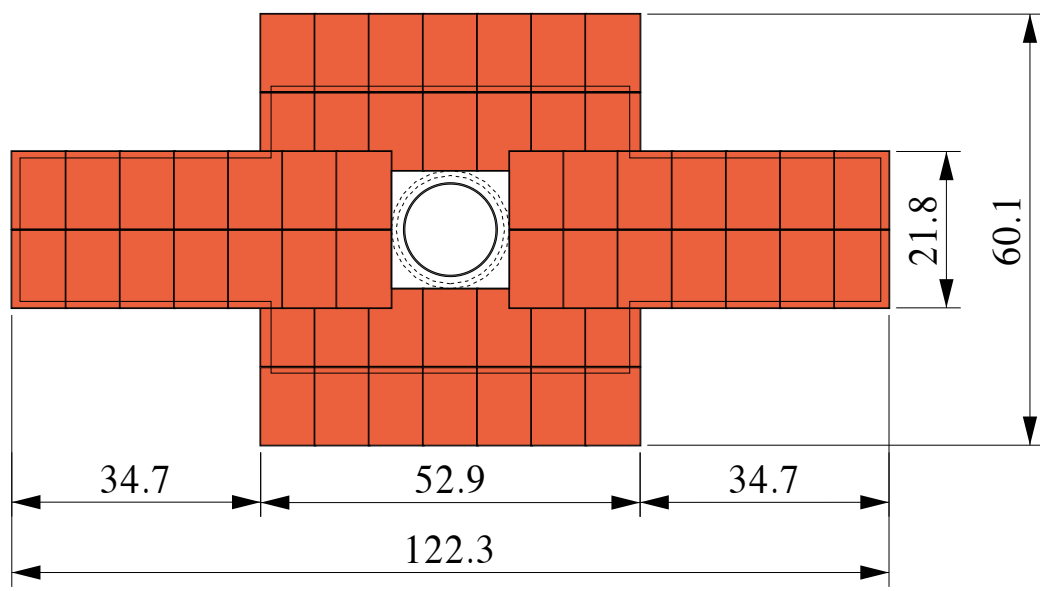


Figure 2.14: Layout of an inner tracker x -layer of station 4[46].

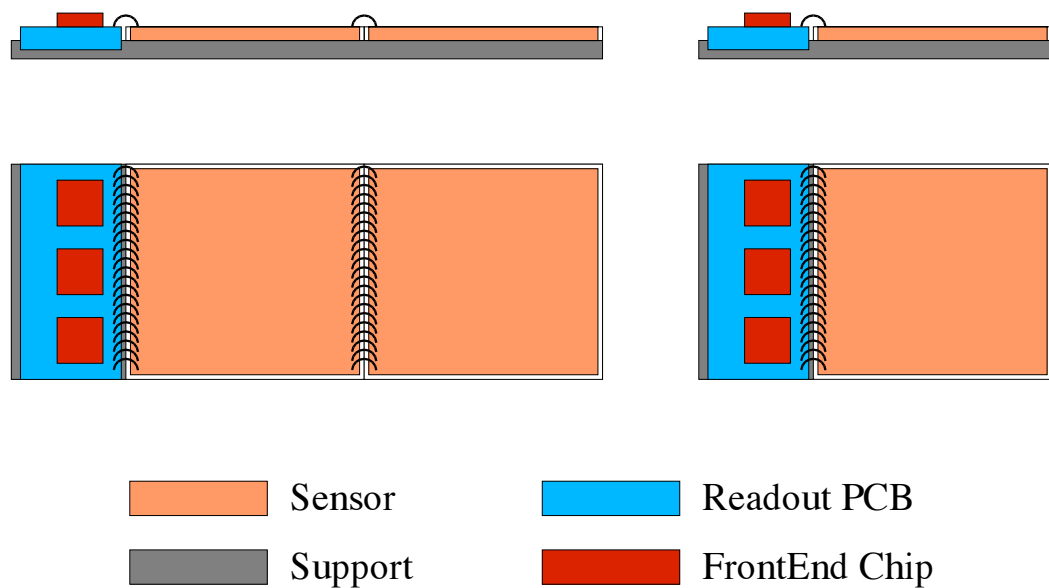


Figure 2.15: Layout of two-sensor and one-sensor inner tracker ladders[47].

cell shape	straw tube
cathode material	40 μm Kapton-XC + 25 μm aluminium
anode material	gold-tungsten
anode diameter	25 μm
cell size	5 mm
wire pitch	5.25 mm
# cells/layer	64
support structure	Nomex
module thickness	0.7 % X_0

Table 2.2: Material and geometry properties of the LHCb outer tracker detector.

efficiency	97.2 %
resolution	205 μm
t_{\max} in 0.0 T	32.5 ns
t_{\max} in 1.4 T	40.9 ns
cross talk	6 %
primary ionisations	30 cm^{-1}

Table 2.3: Performance parameters of an outer tracker prototype module in the default gas mixture $\text{Ar}(75)/\text{CF}_4(15)/\text{CO}_2(10)$ at the start of the efficiency plateau.

Adding up all layers of all stations gives a total area of $\sim 14 \text{ m}^2$ silicon. Depending on the sensor pitch the inner tracker constitutes a total of 344 k or 287 k read-out channels.

2.3.3 Outer Tracker

The LHCb outer tracker consists of eight stations (T2-T9) of straw tube detectors. This thesis describes the prototype tests and the design considerations leading to the outer tracker layout as presented in the outer tracker technical design report[44]. This section summarises the final layout. Table 2.2 lists the main material and geometry properties. For a description of the outer tracker electronics and gas system the reader is referred to the technical design report[44].

Drift cells are chosen with a straw tube geometry. The straw cathode is produced out of two staggered layers as indicated in figure 2.16. The inner layer is a 40 μm thick *Kapton-XC*⁴ foil, having a 25 % doping of carbon. The outer layer of the cell is a 25 μm thick layer of aluminium. The tubes have a diameter of 5 mm and a maximum length of 240 cm in station T9. A gold-tungsten wire of 25 μm is used as anode. To position the wire in the centre of the straw wire locators are placed typically every 70-80 cm for straws longer than 1 m.

In order to have a maximum signal latency of less than 50 ns (corresponding to

⁴Kapton-XC is a product name for carbon doped polyimide foils.

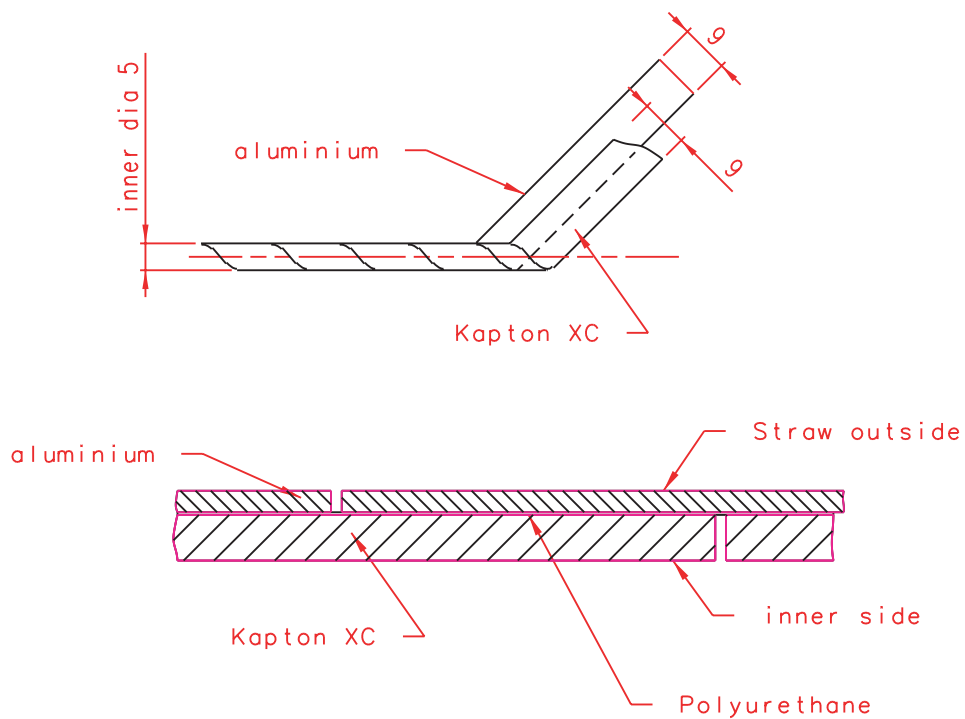


Figure 2.16: Winding pattern of the straw tubes. The two layers are wound from 9 mm wide strips of Kapton-XC and aluminium foil, staggered by half a winding cycle[44].

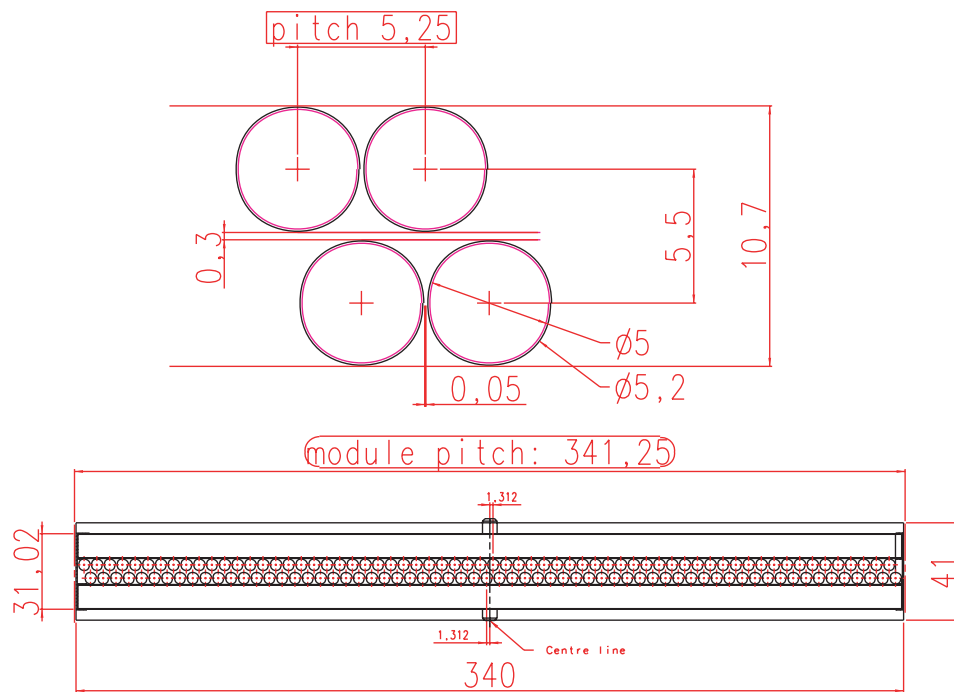


Figure 2.17: Cross section of an outer tracker straw tube module[44].

station	z_{end} (cm)	active area		channels
		x_{max} (cm)	y_{max} (cm)	
2	227.5	70.4	58.1	4.3 k
3	363.5	112.5	92.9	6.8 k
4	603.5	186.7	154.1	11.4 k
5	703.5	217.6	179.6	13.1 k
6	803.8	248.6	205.2	15.1 k
7	849.7	262.8	217.0	16.0 k
8	895.6	277.0	228.7	16.8 k
9	941.5	291.2	240.4	17.5 k
				101.0 k

Table 2.4: Outer dimensions and numbers of active readout channels for the outer tracking detector stations.

two bunch-crossings) a fast drift gas is needed⁵. The measurements and simulations presented in chapter 4 show this is achieved for a gas mixture containing a small fraction of CF_4 (15 %). The chosen default gas is the mixture $Ar/CF_4/CO_2$ in the volume ratio 75/15/10. In table 2.3 the performance of a full scale prototype, as measured in the test beam is summarised.

The drift tubes are grouped into modules. One standard module⁶ contains two staggered layers of straw tubes, with 64 tubes per layer. The wire pitch within a mono-layer is 5.25 mm. The distance between two mono-layers is 5.5 mm. The two mono-layers are sandwiched between two panels, each consisting of a 10 mm thick layer of *Nomex*⁷ between a 0.1 mm thick carbon facing and a 25 μm thick aluminium foil. The straws are directly glued on the aluminium foil, which acts as a ground foil. It also allows a controlled straight positioning of the tubes over their full length. Each module forms a gas tight box and is a self-contained detector unit. See figure 2.17 for a cross section of a standard LHCb outer tracker module. One module corresponds to 0.7 % of a radiation length.

Modules are grouped together forming a complete double layer as shown in figure 2.18. Each outer tracker station contains four of these double layers. The number of modules depends on the outer dimensions of the station. Table 2.4 gives the position, outer dimensions and number of readout channels per outer tracker station. In total the outer tracker constitutes ~ 100 k readout channels.

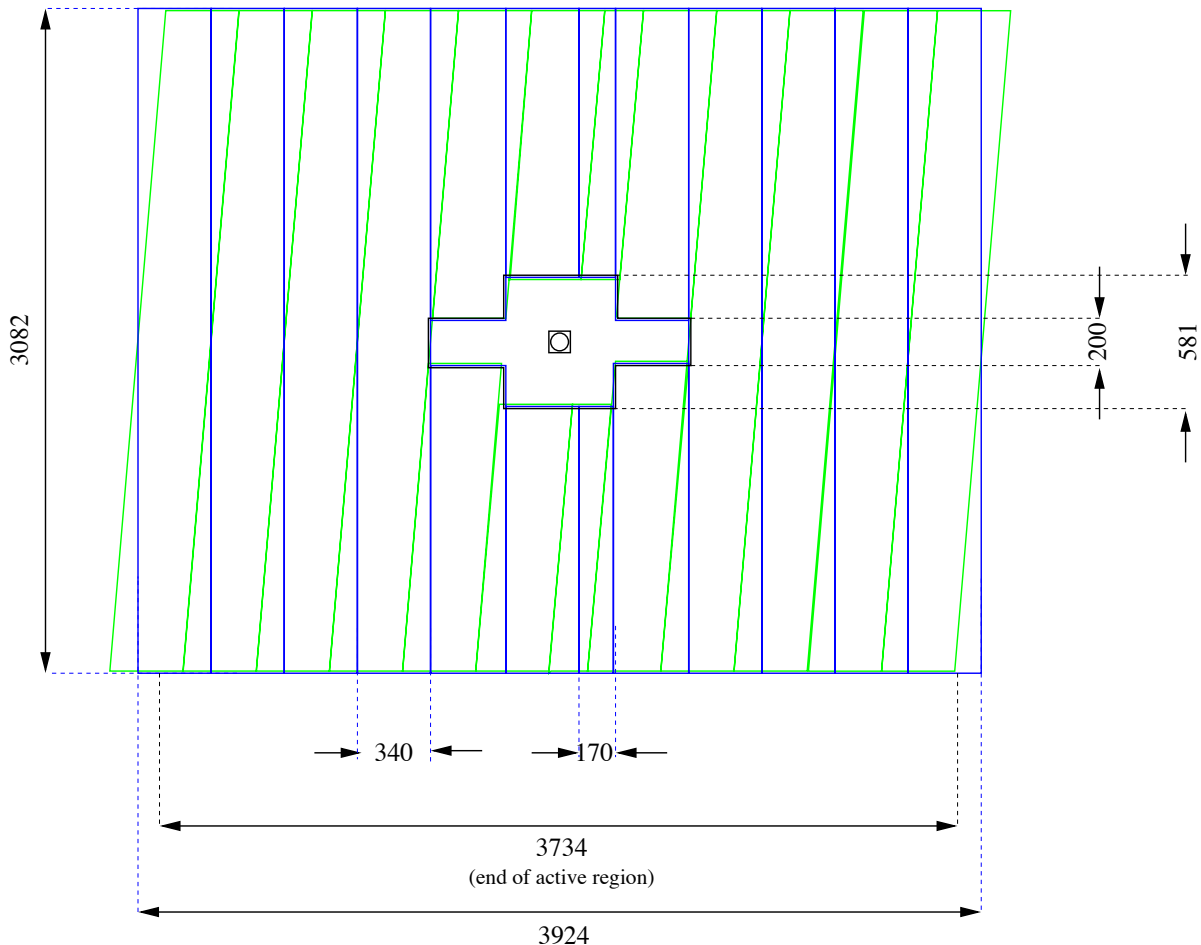


Figure 2.18: Subdivision into modules of station T4[44].

level	output rate	latency	characteristics
0	1 MHz	4.0 μ s	high p_t tracks + pile-up veto
1	< 40 kHz	< 2048 μ s	vertex topology (secondary vertex)
2	5 kHz	~10 ms/event	level-1 refinement with p -information
3	200 Hz	variable	fully reconstructed B hadrons

Table 2.5: Summary of the LHCb four level(Level-0 to Level-3) trigger scheme. Shown are the output rate, latency and main characteristics of the trigger levels.

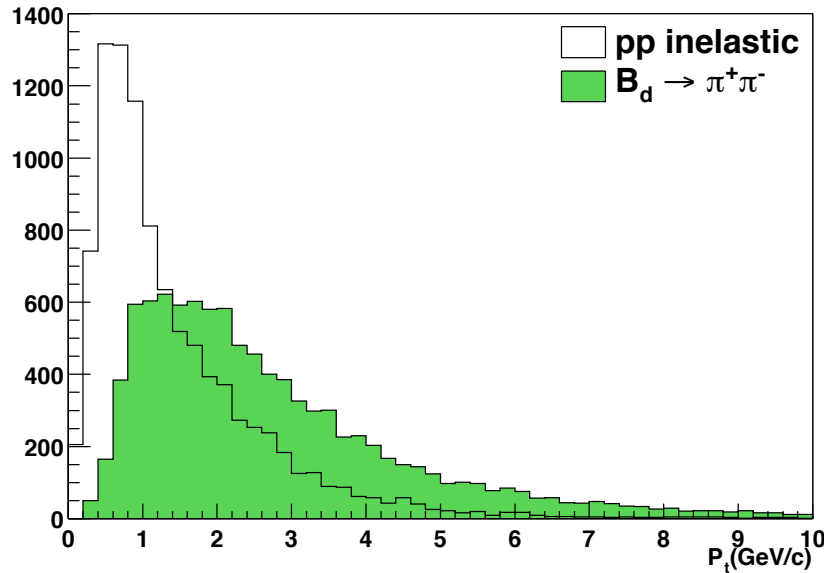


Figure 2.19: The p_t distribution of the charged hadrons with the highest p_t in the event, for pp inelastic events and $B_d \rightarrow \pi^+\pi^-$ events[7].

2.4 LHCb trigger

The total event rate at the LHCb interaction point is about 16 MHz. Only a small fraction of these events contain B hadrons, and even a smaller fraction have decays which are interesting for the study of CP-violation. Furthermore, the storage capacity of the data collection system limits the output rate to about 200 Hz. To achieve this enormous rate reduction a sophisticated trigger scheme is required. LHCb has a four level (Level-0 to Level-3) trigger system. The main aspects are summarised in table 2.5. Below an overview of these trigger levels is given. For a detailed description see the LHCb technical proposal[7].

Use is made of the fact that the decay products of B hadrons have a relatively large transverse momentum, p_t , compared to the particles produced in minimum bias events. Figure 2.19 shows the p_t distribution of the highest p_t charged hadrons in an event, for pp inelastic events and for $B_d \rightarrow \pi^+\pi^-$ events. The **Level-0** trigger exploits this characteristic by triggering on high p_t tracks. The trigger combines four high p_t particle triggers. The calorimeter system provides the input for a photon, electron and hadron high p_t trigger. The muon system provides a high p_t muon trigger. In addition the Level-0 trigger contains a pile-up veto to suppress bunch crossings with more than one

⁵If events of more bunch-crossings would overlap the track reconstruction pattern recognition presented in chapter 6 would become much more complicated.

⁶In the magnet stations some modules in the border region have a reduced size because of limited space.

⁷Nomex is a product name for honeycomb structured carbon plates.

decay mode	trigger efficiency
$B_d \rightarrow \pi^+ \pi^-$	0.17
$B_d \rightarrow J/\psi K_s$	0.19
$B_d \rightarrow \bar{D}^0 K^{*0}$	0.13
$B_s \rightarrow D_s^- \pi^+$	0.16
$B_s \rightarrow D_s^- K^+$	0.16
$B_s \rightarrow J/\psi \phi$	0.23

Table 2.6: Summary of the trigger efficiency for various B meson decays[7].

proton-proton interaction⁸. The pile-up veto detector determines the number of primary vertices. The Level-0 trigger has a fixed output rate of 1 MHz and a fixed latency of 4.0 μs [48].

The LHCb **Level-1** trigger relies on the existence of secondary vertices in B events. As input the hit-clusters from the vertex detector are used. These hits are combined to form track segments from which a primary vertex is reconstructed. Tracks with a significant impact parameter with respect to this vertex are selected and used in a search for secondary vertices. From this a probability for the event to be a non B event is calculated. Events with a high probability are rejected by the trigger. The Level-1 trigger reduces the data rate to below 40 kHz in a maximum latency of 2048 μs .

The **Level-2** trigger is basically a refinement of the Level-1 trigger by adding momentum information. Low momentum tracks can have relatively large kinks due to multiple scattering. These kinks can cause an artificially large impact parameter faking a displaced secondary vertex. By using the momenta for the tracks found in the Level-1 trigger the error on the impact parameter can be computed properly. This information can be used to reject fake secondary vertices[7]. The Level-2 trigger reduces the rate to approximately 5 kHz. It is estimated that a latency of \sim 10 ms/event can be achieved.

The last trigger level, **Level-3**, uses combined event information of several detector systems to perform a full or partial reconstruction of B hadron final states. Four topological classes of B hadron decays with distinct signals are reconstructed.

- **Charged two body decays** with the vertex mass compatible with the B meson mass (e.g. $B \rightarrow \pi\pi$, $B \rightarrow K\pi$, $B \rightarrow KK$ and $B \rightarrow \mu\mu$).
- **Dilepton decays** with the lepton vertex compatible with a displaced vertex from a J/ψ (e.g. $B \rightarrow J/\psi K_s$, $B \rightarrow J/\psi \phi$ and $B \rightarrow J/\psi K^*$).
- **Low multiplicity decays with neutrals.** Two track decay vertices giving, with the addition of a π^0 or photon, the B meson mass (e.g. $B \rightarrow \rho^+ \pi^-$, $B \rightarrow \rho^0 \pi^0$ and $B \rightarrow K^* \gamma$).

⁸Events with two interactions cause two primary vertices and roughly double the amount of hits in the detectors. The presence of primary vertices introduces an ambiguity in assigning the secondary (B) vertex to the primary vertex at trigger time. Furthermore, too many hits in the detectors makes the pattern recognition difficult. Therefore, bunch crossings with multiple interactions are rejected.

- **Decays with D mesons**, i.e. B decays where a combination of tracks make up the mass of a D meson (e.g. $B_s \rightarrow D_s \pi$ or $B_s \rightarrow D_s^\pm K^\mp$).

A fifth class is reserved for reconstructing non B events. In reconstructing the events of these classes similar cuts are applied as in the full off-line reconstruction but now with looser criteria. The final output rate at the Level-3 trigger is 200 Hz. This trigger level will likely be realized by using the reconstruction power of computer farms. A maximum latency is not yet specified as one can easily add more CPU power to achieve the required processing time. The events selected by the Level-3 trigger are stored on tape. The amount of minimum bias events in this sample is estimated to be smaller than 1 %[7]. See table 2.6 for a summary of the performance of the LHCb trigger for various decay channels.

Chapter 3

LHCb Outer Tracker straw detector

The LHCb outer tracker is built out of gas filled drift tubes. The subject of this chapter is the physics of drift tubes. Section 3.1 gives a theoretical overview of the operation principle of gas filled drift detectors. Section 3.2 discusses the selection of the gas mixture for the LHCb tracker. The various prototypes of the outer tracker that have been constructed are discussed in section 3.3. These prototypes have been tested in a particle beam at CERN. Chapter 4 describes these tests in detail. Section 3.4 discusses the selection of the detector material. Section 3.5 summarises the decisions made.

3.1 Operation principle

Fast gas filled chambers to detect ionising particles have become a standard technique in particle physics experiments since 1968 when the first multi-wire proportional chamber was operated[49]. The research[50] on gas detectors from then is still relevant to date. This section briefly reviews the operation principle of the drift tubes used for the outer tracker in LHCb.

3.1.1 Creation of ionisation clusters

A charged particle traversing a gaseous medium will undergo electromagnetic interactions with the gas constituents. These interactions will slightly deflect the particle from the original trajectory and cause it to lose energy. If the energy transferred in the interaction is higher than the ionisation potential of the gas constituent ($\mathcal{O}(10 \text{ eV})$), electron-ion pairs can be liberated. In case these ejected primary electrons have enough energy they can cause further ionisation by producing secondary electron-ion pairs. These ionisations will usually occur close to the primary ionisation resulting in clusters of ionisation. The cluster size, i.e. the number of ionisations per primary electron, depends on the energy transfer in the primary collision. It ranges from one ionisation to more than 20[51].

In a gas, the number of primary interactions per unit length is relatively small. As they are independent the primary ionisation follows Poisson statistics, i.e. the proba-

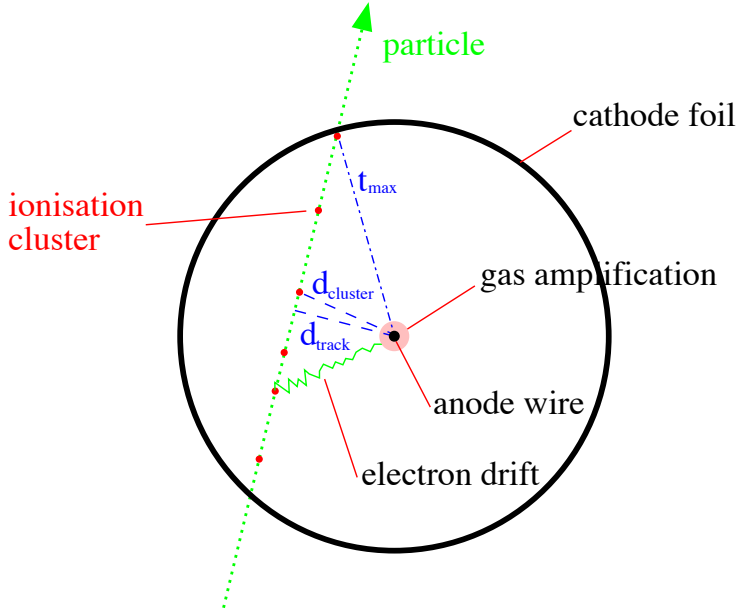


Figure 3.1: A particle traversing a gas filled drift tube at a distance d_{track} from the wire. It causes Poisson distributed clusters of electron-ion pairs along the trajectory. Under the influence of the electric field the electrons drift towards the anode wire. Close to the anode wire gas amplification takes place.

bility $P(n; l)$ to find n primary ionisations for a particle traversing a length l is:

$$P(n; l) = \frac{(\frac{l}{\lambda})^n \exp(-\frac{l}{\lambda})}{n!} , \quad (3.1)$$

where λ is the average distance between subsequent ionisations. With the default outer tracker gas mixture $Ar(75)/CF_4(15)/CO_2(10)$ (see chapter 4), a minimum ionising particle creates on average about 30 primary ionisations per cm[50, 52], corresponding to $\lambda \sim 0.33\text{mm}$. A typical event inside the LHCb straw is schematically depicted in figure 3.1.

3.1.2 Drift of electrons and ions in gases

The liberated electrons will scatter off the gas constituents with their direction randomised at every collision. In case no (electromagnetic) force is applied the electrons move randomly with an average energy of $\frac{3}{2}kT$, i.e. the thermal energy. Under normal conditions this corresponds to a velocity (v) of about 10^7 cm s^{-1} .

In case an electric field E is applied the charge carriers will experience a force causing them to drift towards the anode wire. On a macroscopic scale the scattering of the electrons and ions with the gas constituents can be modelled as a frictional force

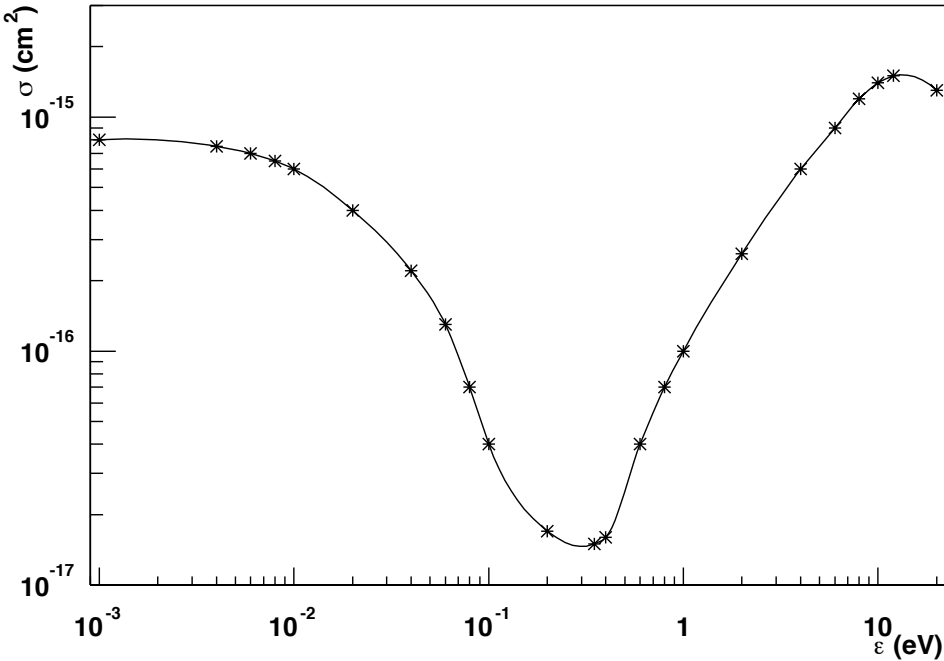


Figure 3.2: Effective momentum transfer cross section as a function of the electron energy ε for argon[53].

proportional to the velocity. The equation of motion then is:

$$m \frac{du}{dt} = eE - Ku \quad , \quad (3.2)$$

where u is the macroscopic drift velocity, K a characteristic constant for the frictional force and e and m the charge and mass of the charge carrier. Solving equation 3.2 for u gives:

$$u = \frac{eE}{K} \left(1 - e^{-\frac{Kt}{m}}\right) \quad , \quad (3.3)$$

The ratio $\frac{m}{K}$ defines the characteristic time τ . Because of the small mass electrons will quickly reach the asymptotic value for $t \gg \tau$, i.e.

$$u = \frac{eE\tau}{m} \quad . \quad (3.4)$$

A maximum drift time of 40 ns corresponds in an 2.5 mm outer tracker straw tube to an average macroscopic drift velocity u of $6 \cdot 10^6 \text{ cm s}^{-1}$.

On a microscopic scale τ can be seen as the average time between two collisions. This time depends on the cross section σ for collisions of the electrons with the gas constituents, the number of constituents N , and the average fractional energy loss per collision η [54], i.e.

$$\tau \sim \frac{\sqrt{\eta}}{N\sigma} \quad . \quad (3.5)$$

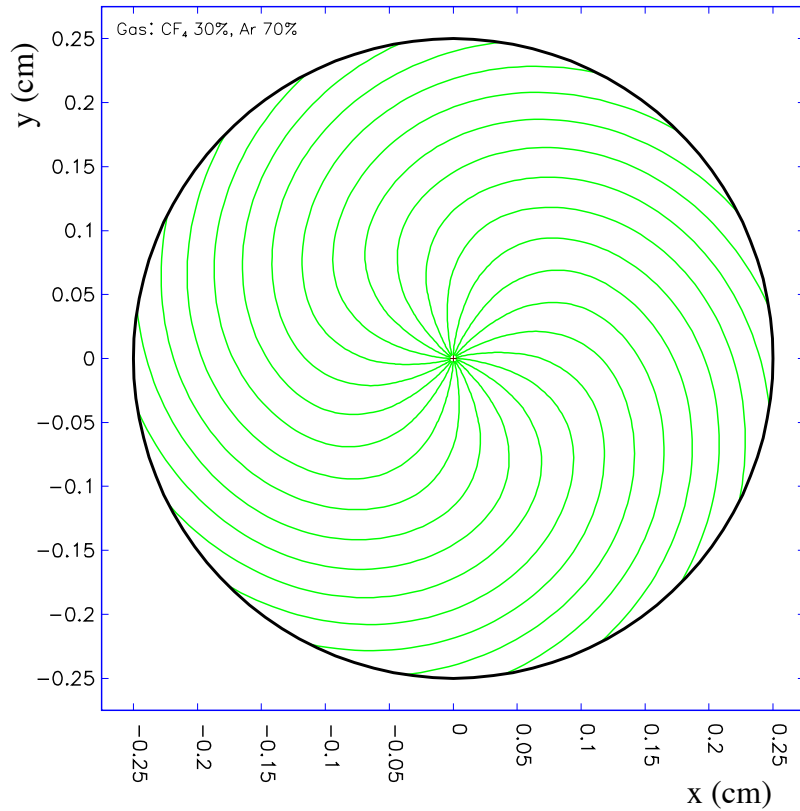


Figure 3.3: Simulated drift lines in a 5 mm radius straw tube in the fast gas mixture $Ar(70)/CF_4(30)$ in a 1.6 T magnetic field along the wire. The drift lines spiral around the anode.

The interaction cross section σ for a particular gas molecule is usually not a constant as it depends on the excitation levels of the molecule as well as the electron energy. A discussion of the calculation or determination of these cross sections is beyond the scope of this thesis. Figure 3.2 shows the cross section as a function of the electron energy for argon.

When a magnetic field B is applied perpendicular to the electric field E the electron will move under an angle with respect to the electric field lines. This angle α_L , called the *Lorenz angle*, is defined by the ratio of the velocity perpendicular(u_\perp) and parallel(u_\parallel) to the electric field. Modifying the equation of motion 3.2 to include a magnetic field component $e[u \times B]$, it can be shown that the Lorenz angle is given by[54]:

$$\tan \alpha_L \equiv \frac{u_\perp}{u_\parallel} = \frac{eB\tau}{m} = \omega\tau \quad . \quad (3.6)$$

The magnitude of the macroscopic velocity, in the presence of a magnetic field, u_B is given by[54]:

$$u_B = \frac{eE\tau}{m\sqrt{1 + \omega^2\tau^2}} = \frac{u}{\sqrt{1 + \tan^2 \alpha_L}} = u \cos \alpha_L \quad , \quad (3.7)$$

which shows that the presence of a magnetic field reduces the drift velocity. This effect is larger for gases with a large τ , i.e. for gases which are fast without a magnetic field. Moreover, a drift gas with a large Lorenz angle causes the electrons to spiral around the anode as can be seen in figure 3.3. Hence, the effective drift distance is larger with consequently a larger drift time. These effects are taken into account in selecting a fast outer tracker gas mixture, since part of the detector will operate in over one Tesla magnetic field.

The drift process of the ions is different from that of the electrons. The ions will drift towards the cathode with a velocity that is smaller than that of the electrons (typically a factor 1000). This is mainly due to the fact that the ions are heavier which prevents them from reaching the asymptotic value of the macroscopic drift velocity u (see equation 3.3). In gas mixtures an interesting charge transfer process takes place between the ions. All ions will transfer the energy in a few collisions to the gas constituents with the lowest ionisation potential. The result of these reactions is that the positive charge is mainly carried by the gas component with the lowest ionisation potential, which for the LHCb tracker is CO_2 ($I_0 = 13.7$ eV).

3.1.3 Gas amplification

If the electric field E is high enough drifting electrons will gain sufficient energy to ionise new gas molecules. This property is exploited in drift tubes in which the radial electric field is given by:

$$E(r) = \frac{V}{d \ln \frac{d_b}{d_a}} , \quad (3.8)$$

where V is the applied voltage, d_a and d_b the radii of anode wire and cathode tube and d a distance from the wire. As an electron moves towards the anode wire the electric field, and hence the energy of the electron, will increase. Close to the wire the energy will be high enough to cause ionisation. This process will quickly repeat itself for the liberated electrons resulting in an avalanche of ionisations. The net effect is an enormous increase of the number of charges contributing to the signal development. This process, called gas amplification, can result in signal gains of up to 10^6 . At standard operation conditions the LHCb outer tracker drift tubes operate at a modest average gas gain of 2×10^4 [55].

3.1.4 Signal development and time measurement

The pulse shape of the electrical signal induced on the wire is important as it determines the drift time measurement. Figure 3.4 shows the current signal produced in a 166 cm long Kapton-XC straw tube by a ^{55}Fe radiation source. The ^{55}Fe produces a cloud of about 200 electrons at a small “point” in the straw volume. Therefore, the signal produced is equivalent to the signal produced by a very large single ionisation cluster. It can therefore be used as a calibration source.

The signal from the ^{55}Fe source contains two superimposed components. The electrons created in the avalanche drift towards the anode in a fraction of a nanosecond creating a steep small pulse. The ions drift to the cathode in the order of a microsecond

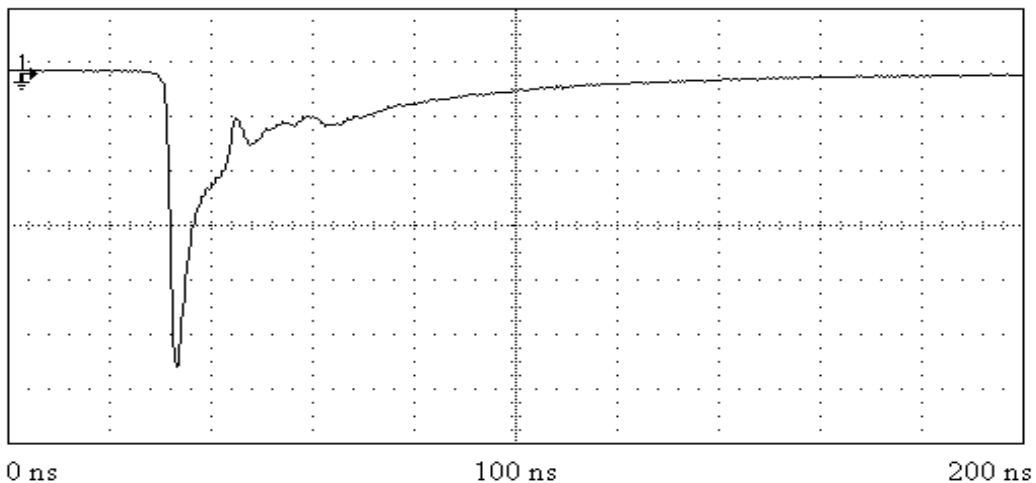


Figure 3.4: Current signal produced in a 166 cm long Kapton-XC straw tube by a ^{55}Fe radiation source[56]. The gas mixture used is $\text{Ar}(65)/\text{CF}_4(30)/\text{CO}_2(5)$. The spikes at the falling edge are superimposed reflected signals caused by improper termination of the straw tube.

causing a signal with a long tail. The steep leading edge of the signal forms an excellent signature to trigger the measurement of the (drift-)time. Electronically this is achieved by measuring the time at which the signal amplitude passes a certain threshold.

The signal produced by a traversing particle is a super-position of the signals created by the individual cluster arriving in the avalanche region. A single electron amplified by the average outer tracker gas gain of 2×10^4 leads to a deposited charge of 3 fC. The cluster with the shortest distance to the wire arrives first. The arrival time of this cluster provides the measurement of the track position. Therefore, the outer tracker electronics triggers on the leading edge of an induced signal surpassing a threshold of 2 fC.

3.2 Drift gas selection

Important considerations for the selection of the gas mixture are, the signal gain, the maximum signal collection time and stable detector operation. The following summarises these considerations.

signal gain

Firstly, the signal gain should be sufficient in order to efficiently detect and measure a traversing particle. In principle, avalanche multiplication occurs in all gases. However, in noble gases multiplication is known to occur at already modest electric fields compared to polyatomic molecules. Polyatomic molecules have many rotation and vibration modes that can absorb the energy of the electrons[50]. This energy is not used to ionise a molecule. Consequently, multiplication is less likely to occur in a collision with a poly-

atomic molecule. LHCb uses argon as noble gas because of the high ionisation potential¹ and relatively low cost compared to for example xenon or krypton.

signal collection time

A second important requirement on the outer tracker drift gas is that it must be fast enough to keep the maximum signal collection time below 50 ns (corresponding to two bunch crossings). Adding CF_4 to an argon based drift gas is known to increase the drift velocity [57]. This can be explained in the following way. From figure 3.2 it can be seen that the cross section σ for electrons to interact with argon is small for energies around ~ 0.3 eV. Furthermore, because argon is a noble gas, the fractional energy loss per collision η is small up to the energy needed for ionisation. As can be seen from equation 3.5 in combination with 3.4, a low interaction cross section results in a high macroscopic drift velocity u . In the drift region of the straw tubes it is therefore an advantage to keep the energy of electrons in argon below ~ 0.5 eV. CF_4 has a large electron scattering cross section for energies > 0.5 eV, and a significantly higher η [57, 54]. “High” energy electrons interacting with CF_4 will therefore lose a large fraction of their energy, moving them into the low cross section region around ~ 0.3 eV. The overall result is that the average electron cross section is smaller, and hence the average drift velocity u higher. Accordingly LHCb has decided to use CF_4 together with argon.

The use of CF_4 also has a drawback. CF_4 is strongly electronegative². Consequently, drifting electrons have a significant probability to be captured by a CF_4 molecule. Hence, not all electrons liberated by the traversing particle will reach the anode³. This has a direct effect on the detection efficiency as the signal size is reduced. Furthermore, it effects the resolution as the electronics trigger on the leading edge of the signal (see section 3.1.4) created by the avalanche of the first arriving cluster. As depicted in figure 3.1 this is the cluster nearest to the wire. Capturing of the electron(s) in this cluster therefore affects the resolution. The test-beam measurements described in chapter 4 show that the consequences of the above mentioned effects are acceptable.

stable operation

The third requirement for the drift gas is that stable operation conditions are ensured at high particle rates. The excited atoms of a noble gas only returns to the ground state by emitting photons with an energy corresponding to the ionisation potential or higher. These photons can cause excitation of electrons from e.g. the cathode. These new electrons in turn can cause a secondary avalanche. This process can repeat itself making the detector unstable. To prevent this from happening often a *quencher* is added to the gas mixture to absorb the emitted photons. The existence of many energy dissipation modes in polyatomic molecules make them good quenchers. Often used quenchers are CH_4 and CO_2 . Aging studies have been performed with both quenchers

¹A high ionisation potential prevents argon ionisation before the multiplication region.

²At electron energies of a few eV the cross section for electron capture is large: $\sim 10^{-18}$ cm²[57].

³Another process which eliminates the electrons is the recombination of electrons with the created ions. Because the ions have a relatively long lifetime space charge builds up at high rates. Measurement[58] show that at rates of about 1 MHz cm⁻¹ this effect starts to contribute.

characteristics	9002-9005	6030-6034	0604 + 2004	5
# cells/layer	32	16	32	64
cathode material	¹⁾	²⁾	^{2) OR 3)}	³⁾
wire material	⁴⁾	⁴⁾	⁴⁾	⁴⁾
wire diameter	25 μm	25 μm	25 μm	25 μm
length	0.3 m	0.3 m	2.0 m	2 \times 1.6 m
cell shape	honeycomb	straw tube	straw tube	straw tube
cell size	8.0 mm	5.0 mm	5.0 mm	5.0 mm
pitch	9.0 mm	6.0 mm	6.0 mm	5.25 mm

1) Pokalon-C; 2) double Kapton-XC; 3) Kapton-XC + aluminium; 4) gold-tungsten

Table 3.1: Characteristics of LHCb outer tracker prototypes.

together with argon and CF_4 . These studies indicate that the combination of CF_4 with CH_4 damages the cathode surface and causes aging of the anode wire[44, 58]. Therefore, LHCb has chosen to use CO_2 as quencher.

3.3 Outer Tracker prototypes

The use of small drift tubes for the LHCb outer tracker was inspired by the R&D work on the Honeycomb Strip Chamber[51] for the ATLAS muon detector and by the drift chambers used in HERA-B[59]. A common property of these drift tubes is the use of small drift cells (order 1 cm) with a cathode made out of a thin folded foil⁴. Since 1998 several prototype drift cell modules for LHCb have been built. Both prototypes with a honeycomb-like cell geometry as well as prototypes with a straw geometry have been constructed. Other parameters that have been varied are the cell size, wire to wire distance (pitch), cathode material, electrical shielding and module length. The main characteristics of the most relevant prototype modules are presented in table 3.1. They are described below.

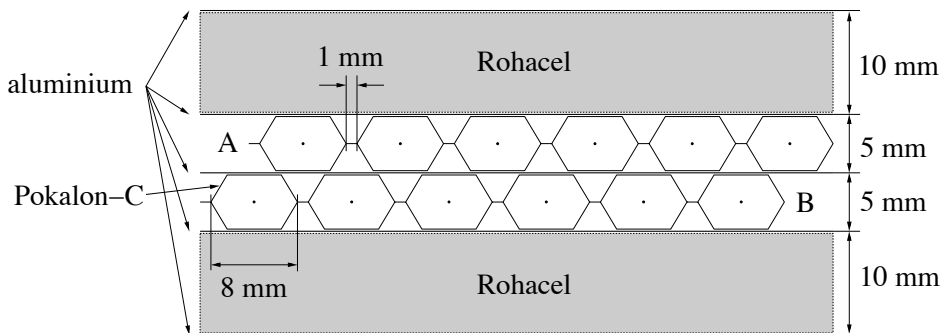


Figure 3.5: Cross section of 8 mm honeycomb prototype modules 9002-9005.

⁴The use of MWPC[41] is not a sensible option because the electric field configuration prevents drift time measurements with a good resolution.

- The honeycomb **modules 9002-9005** contain two staggered mono-layers of 32 drift cells each. The mono-layers are mounted directly on top of each other and sandwiched between two 10 mm thick layers of Rohacell foam. The drift cells are constructed out of a *Pokalon-C*⁵ foil. By means of a folding machine[51] the foils are folded forming a half honeycomb structure. Two of these foils are glued on top of each other forming a full honeycomb. A honeycomb cell is 5 mm thick and 8 mm wide. The wire pitch inside a mono-layer is 9 mm, leaving 1 mm for gluing the foils. Every drift cell contains a 30 cm long gold plated tungsten wire with a diameter of 25 μm . Figure 3.5 shows a cross section of a module.

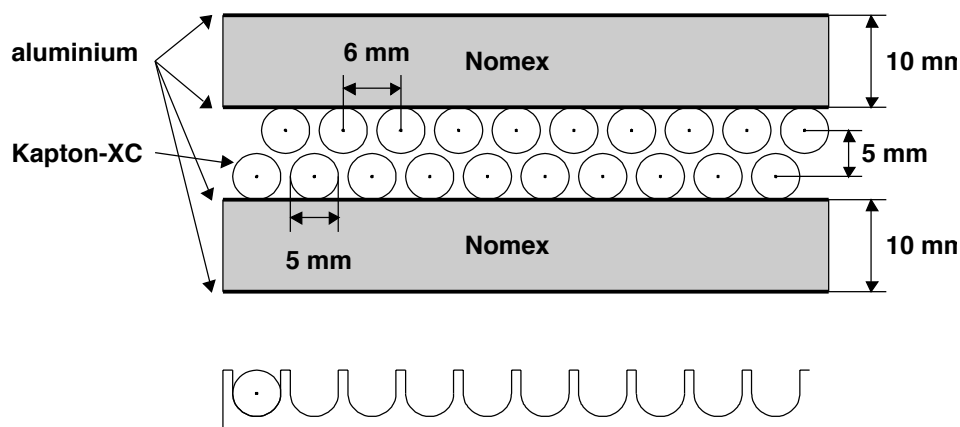


Figure 3.6: Cross section of 5 mm straw tube prototype modules 6030-6034. The cross section of the combs to support the tubes is also shown.

- The straw tube **modules 6030-6034** contain two staggered mono-layers of 16 drift cells each. The two mono-layers are sandwiched between two 10 mm thick layers of *Nomex*. Straw tubes made out of *Kapton-XC* are used as the cathode of the drift cells. The straw positions are fixed by placing them in aluminium combs at the edges of the module. The straws have a 5 mm diameter, the wire to wire pitch is 6 mm inside a mono-layer. Every drift cell contains a 30 cm long gold plated tungsten anode wire with a diameter of 25 μm . Figure 3.6 shows a cross section of the modules and the combs.
- The straw tube **modules 2004 and 0604** are similar to the modules 6030-6034. They are also made out of two mono-layers of 5 mm straw tubes sandwiched between two 10 mm thick supporting layers of *Nomex*. The main difference is the larger spacing between the mono-layers as well as between the mono-layers and support structure. The mono-layers in the modules contain 32 straw tubes

⁵Pokalon-C is a product designation for a carbon-loaded polycarbonate.

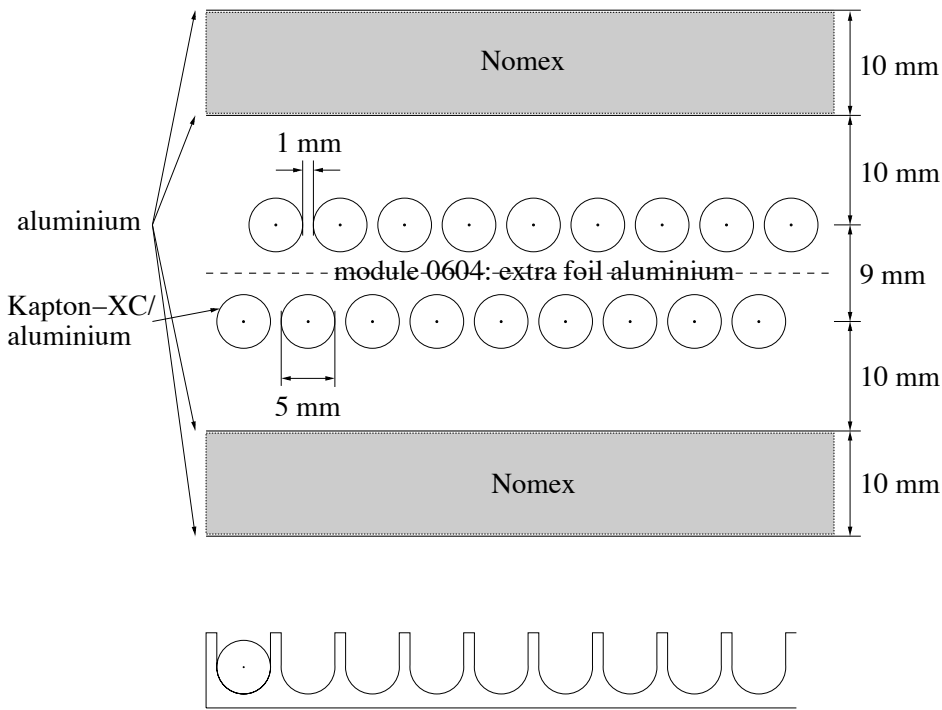


Figure 3.7: Cross section of 5 mm straw tube prototype modules 2004 and 0604. The cross section of the combs to support the tubes is also shown.

and are 2 m long. In order to test the electrical properties two types of straws are used. Half of the straw tubes in each mono-layer consist of double Kapton-XC windings. The other half of the straws contain a Kapton-XC winding on the inside and an aluminium winding on the outside. In addition module 0604 has an extra aluminium foil positioned between the two mono-layers to improve electrical shielding in order to reduce cross talk between straws in different layers.

To guarantee sufficient mechanical precision the straws are supported by aluminium combs at the edges and at 66 cm from the edges of the module. The 25 μm diameter gold-tungsten wires are supported by wire-locators in the combs at 66 cm. See figure 3.7 for a cross section of the modules and the combs. Figure 3.8 shows a photograph of module 2004 when it was constructed.

- Straw tube **module 5** is a full scale prototype of the outer tracker. It is 3.2 m long consisting of two 1.6 m long half-modules. Each half-module consists of two staggered mono layers sandwiched between two 10 mm thick supporting Nomex panels. A single mono-layer contains 64 straw tubes with an inner diameter of 5.0 mm and a cathode consisting of a 40 μm thick inner winding of Kapton-XC and a 25 μm thick aluminium outer winding. The outer aluminium winding is used to improve electrical shielding in order to reduce cross talk between straws. The tubes are directly mounted on an aluminium grounding foil that is attached to the Nomex panels. The 25 μm diameter gold-tungsten wires are supported by

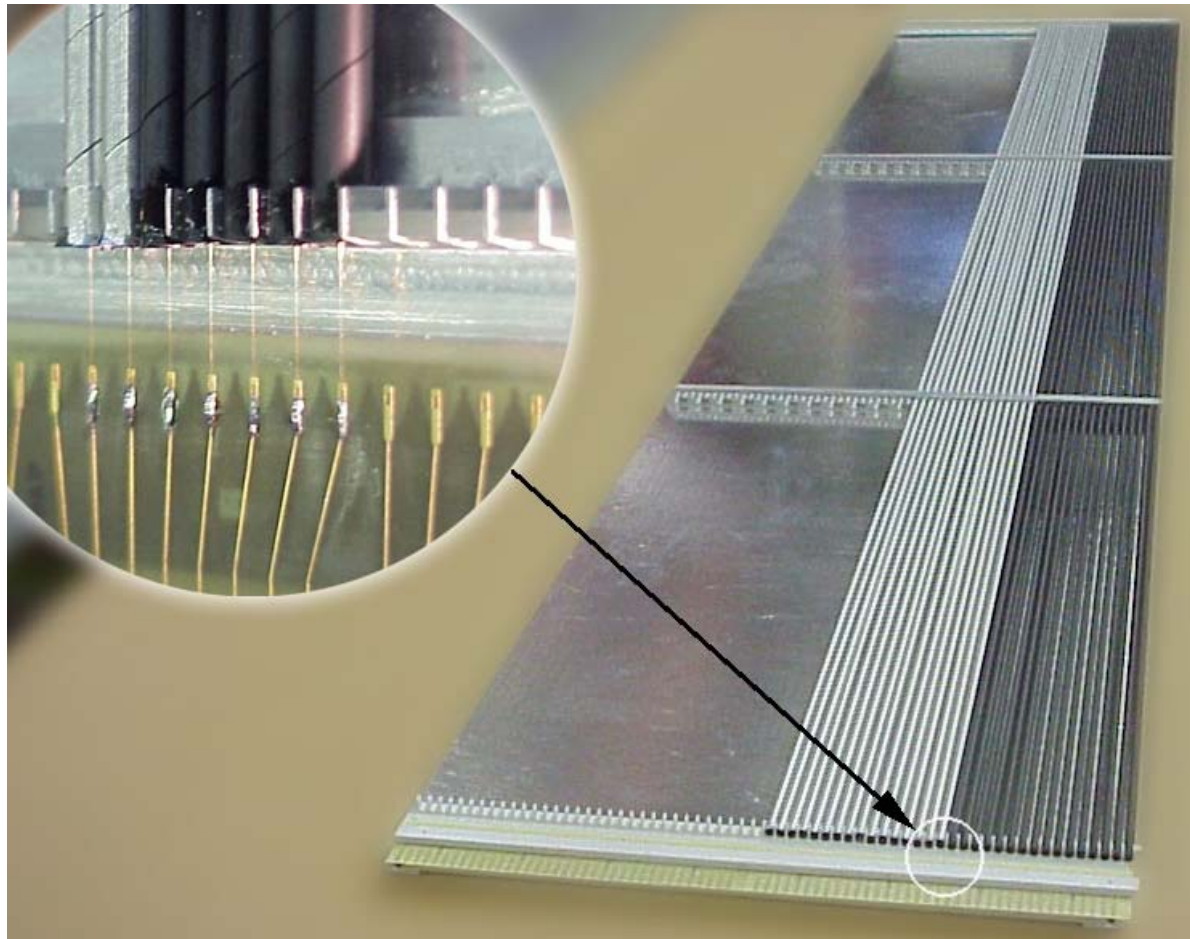


Figure 3.8: Photograph of one half of module 2004 during construction. Shown is a single layer of double Kapton-XC (dark, right) and the Kapton-XC/aluminium (light, left) straws mounted in the straw support combs. The combs are attached to the Nomex layer. The zoom (see the inset) shows the mounting of the wires on the read-out board.

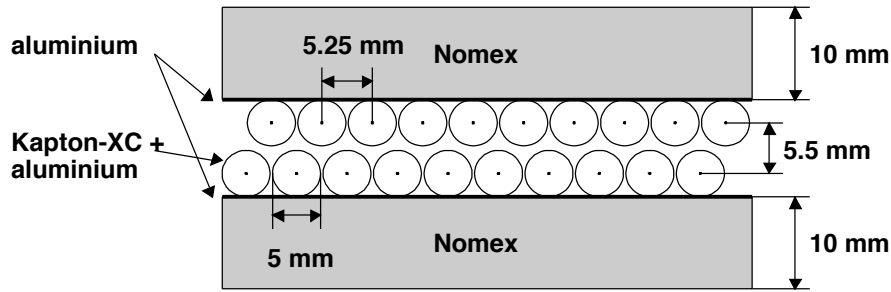


Figure 3.9: Cross section of 5 mm straw tube prototype module 5.

wire-locators in the centre of each tube and at both ends of the wire. The wires of both half modules are not connected and not electrically terminated. See figure 3.9 for a cross section of the module.

3.4 Material selection

The selection of the cathode material is based on an optimisation between the following factors:

- thin and low Z (to minimise radiation length)
- good electrical conductivity
- resistant to high rates (i.e. no aging)
- low cost per detection cell
- easy to manufacture.

Extensive aging studies have been performed on different kinds of cathode materials[60, 58, 44]. In addition prototype modules have been tested for their electrical properties[56]. The following briefly summarises these studies.

Free fluorine radicals created by CF_4 dissociation are known to aggressively react with various materials. This is shown to be the case for aluminium and copper[60]. For this reason several carbon doped polymers have been tested as cathode material. Adding carbon is done to increase conductivity. Polycarbonate foil *Pokalon-C* is used as cathode material in the HERA-B honeycomb drift cells. The LHCb prototype modules 9002-9005 (see previous section) also use Pokalon-C. Hera-B has experienced aging problems with Pokalon-C and has decided to coat the foils with a gold layer [61]. Together with the fact that Pokalon-C is no longer produced by the manufacturer⁶ it is chosen not to use this material. Measurement on Kapton-XC[44] show it to be sufficiently radiation hard for the LHCb environment and is therefore chosen to be used for the outer tracker.

⁶Restarting the production would imply rebuilding the production facility with considerable costs.

Due to the fact that folding Kapton-XC requires an impractical high temperature of about 400 C the honeycomb construction method is not used. Kapton-XC can be wound to form straw tubes (see figure 2.16). Straw tubes have the additional advantage compared to honeycombs that they are electrically symmetric⁷. Therefore, it is decided to build straw tube drift cells. A detailed study of the electrical properties[56] shows that having an outer layer of aluminium significantly improves conductivity and reduces cross talk. The reduction of cross talk is confirmed by the test-beam measurements in section 4.7.

3.5 Conclusions

The LHCb outer tracker is built out of layers of gas filled drift tubes. The main component of the gas mixture is argon. To obtain a sufficiently fast drift gas the mixture contains a significant CF_4 component. CO_2 is used as a quencher. The exact gas mixture can be varied to match the operation criteria (i.e. maximum drift time, resolution, efficiency and cost) required. Chapter 4 shows drift time measurements for different gas mixtures.

The disadvantage of using CF_4 is that it is strongly electronegative, i.e. free electrons can be captured by the CF_4 molecules forming fluorine radicals. Furthermore, created fluorine radicals can cause aging of the detector materials. Extensive aging test have been performed on various cathode materials with various gas mixtures. The polymer Kapton-XC is shown to be radiation tolerant in the chosen gas mixture at the expected particle rates. Studies on the electrical properties of the drift tubes show that the addition of an aluminium layer significantly improves conductivity and reduces cross talk. Therefore, it is chosen to produce straw tube drift cells with a cathode constructed out of an inner layer of Kapton-XC covered by a layer of aluminium.

Various outer tracker prototype modules have been built. The next chapter shows measurements performed on these prototypes in a test beam. These test beam measurements together with the conclusions presented here and with the occupancy considerations of chapter 6 have lead to the final outer tracker module design as presented in section 2.3.3.

⁷In the corners of the honeycombs the electrical field is badly defined causing ionisations in this area to take a unacceptable long time to drift towards the anode.

Chapter 4

Outer Tracker prototype tests

From 1998 until 2001 several of the prototypes described in section 3.3 have been tested in a particle beam. The short prototype modules 9002-9005 and 6030-6034 were used to measure drift cell properties for varying drift gas, high voltage and magnetic field. Properties measured are the maximum drift time, drift time spectra, efficiency, resolution and cross talk. The full scale modules 0604, 2004 and 5 were studied to test if similar performance is achieved for full scale modules and to verify uniform operation over the full length of the drift cells.

This chapter describes these tests. In section 4.1 the experimental setup is described. In section 4.2 the software is described. In sections 4.3 till 4.7 the analysis and results are presented. In section 4.8 the results are summarised and conclusions are drawn. Some of the results are as well presented in LHCb notes [55, 62, 63].

4.1 Test beam setup

All tests are performed in a pion beam at the CERN PS accelerator complex. A typical¹ test setup is shown in figure 4.1. The setup consists of stations of prototype modules, a large bending magnet, scintillators and readout- and data acquisition- electronics. The magnet is used to test the performance of the prototypes in a magnetic field. The scintillators trigger the passage of particles. The following subsections describe the particle beam, magnet and electronics used in the test beams.

4.1.1 Particle beam

The PS accelerates protons up to an energy of 25 GeV. Part of these protons are extracted from the PS into the “East Area” where, via targets, secondary beams are produced. The PS operates with a “super-cycle” of 14.4 seconds delivering 1 to 3 spills of particles with a duration of 300 to 500 ms on these secondary beam production targets. The maximum number of protons in a spill is $2 \cdot 10^{11}$. The LHCb outer tracker tests are performed at the secondary beam called T7. Beam magnets and slits allow the controlling of the content, intensity and shape of the T7 beam. In most of the

¹The exact configuration of the prototypes into stations was different in each test beam period.

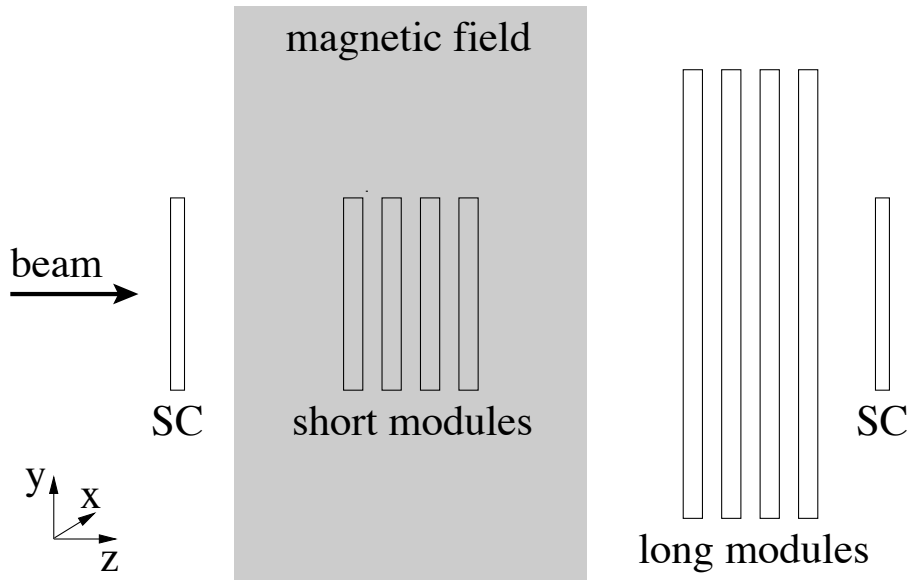


Figure 4.1: Typical test beam setup. The particles travel from left to right. Some prototypes are placed in a magnetic field, others are in a field free region. Two scintillators (SC) trigger the passage of a particle.

tests a 9.5 GeV π^- beam is used. The beam intensity can be varied from a minimum instantaneous rate of about 20 kHz, i.e. ~ 6000 particles in a spill of 300 ms, up to a rate of a few MHz.

4.1.2 Magnet

To test the detector behaviour in a magnetic field the conventional CERN magnet MN22 is used. This magnet has a maximum field of 1.37 T within a gap volume of $1.0 \times 1.0 \times 0.5 \text{ m}^3$ between the coils.

4.1.3 Electronics

A block-diagram of the data acquisition electronics used in the test setup is shown in figure 4.2. The individual components are briefly described below. A more detailed description can be found elsewhere[64].

ASDBLR

Directly connected to the detector modules is a board supplying the high voltage to the detector and performing the first step in the signal readout. On the board ASDBLR(**A**mplifier **S**haper **D**iscriminator with **B**ase **L**ine **R**estoration) chips[65] are mounted. The input to these chips is the analog signals from the detector wires. The output is a digital signal, i.e. information on the pulse height and shape is not stored.

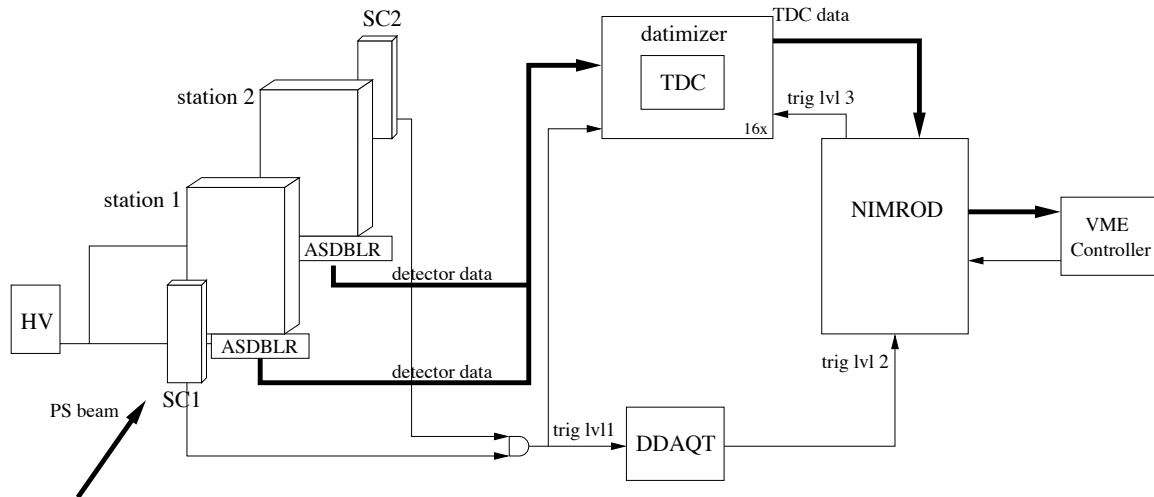


Figure 4.2: Block-diagram of electronics used in the test beams. The detector setup is schematically depicted on the left side. On the right side the DAQ components are shown.

Every ASDBLR chip handles 8 readout channels. A study on the operational properties of the chip used in the LHCb outer tracker is presented elsewhere[66].

TDC

The digital output of the ASDBLRs is further processed by the *datimizer* boards [67]. The most important component of a datimizer board is the TDC chip. The 32 channel TDC32 chip[68] developed at CERN is used. This chip provides a time to digital conversion with a binning of 0.78 ns, and contains, apart from the TDC, a data buffer of 256 words deep. It is highly configurable for the needs of specific experiments via a JTAG[69] interface. The TDC is operated in “data-driven” mode and triggers on the leading edge of the signal from the ASDBLRs. To improve the quality of the data, from 2000 onwards the tests were done with gated TDC inputs, reducing the input trigger rate of the TDC.

NIMROD

The NIMROD[70] is a VME module. It receives a clock and a clock synchronised trigger from the DDAQT module (see below) and distributes this to the TDCs. The TDC data of a maximum of 16 datimizer boards are combined to an event by a single event builder NIMROD module².

²The NIMROD (**NIKHEF MDT Read Out Driver**) was originally designed for the ATLAS muon chambers(MDT) to collect the data from a maximum of 16 Front End Links (in our case the datimizers) and to send these data via a high speed link to a higher level data acquisition module.

VME controller

The VME controller is a Motorola processor running a real time Lynx OS system. On the processor a data acquisition program is running steering the various VME components (see section 4.2.1 for a brief description of this software). The main task is to communicate parameter settings with the NIMROD and to read out the event data. The data is read out via the VME bus and stored on disk.

DDAQT

The coincidence of the signal of two scintillators, one placed before and one after the stations, is used as a primary trigger. This primary trigger signal is fed into the trigger processor unit called DDAQT[71]. The DDAQT has the possibility to reduce the trigger rate by outputting every n^{th} trigger of the input triggers, i.e. pre-scaling. This secondary trigger signal serves as input for the NIMROD. These secondary triggers are given with a resolution of 25 ns corresponding to the (NIMROD) clock. Since the timing of the trigger pulse should be known with a higher precision, the primary trigger is fed into a dedicated TDC channel on a datimizer board to provide a precision time *measurement* (in steps of $25/32 = 0.78$ ns) of the trigger signal.

4.2 Software

For the prototype tests both *online* and *offline* software is used. The online software is used to control the data acquisition hardware and for monitoring the data taking. The online software consists of the LLDAQ software described in section 4.2.1 and the monitoring and control software described in section 4.2.2.

The offline software consists of three components, *event reconstruction*, *analysis* and *simulation*. The event reconstruction is essentially the reconstruction of the particle trajectories (section 4.2.3). Several modules have been developed for the analysis of the test beam data. The analysis algorithms are briefly described together with the presentation of the test beam results in sections 4.3 to 4.7. *Simulation* software was used to compare the detector measurements with theory.

4.2.1 Low level data acquisition

The **Low Level Data AQquisition** (LLDAQ) software directly steers the hardware modules (the NIMROD, DDAQT and VME controller) of the test beam electronics. It initialises the modules at the start of data taking and does the readout of the event data from the NIMROD into software buffers. This data is subsequently written to disk. At the same time the buffers can be accessed by external processes to perform online analysis. The LLDAQ software is based on software used by the L3+Cosmics experiment[72] for their (similar) electronics modules.

4.2.2 Online monitoring and control

Online monitoring and control software is especially developed for the LHCb outer tracker tests. It is written in C++ within a ROOT[73] framework. Interaction with the user mainly occurs via Graphical User Interfaces (GUI). Three of these interfaces are briefly described below. A more detailed description is given elsewhere[74].

The **run controller** is used to start and stop a data taking run. Via pop-up windows the settings of the run can be entered, which are then communicated to the LLDAQ software. Furthermore, the run settings are stored into log files. During data taking it provides statistics on the data acquisition, e.g. number of events processed, data acquisition errors, etc.

The second GUI is the online **event display**. It allows a display of events in text as well as graphical form. In text form the hit wires with corresponding measured TDC values in the event are displayed. The graphical representation gives a 3D view of the test beam setup. The wires hit in the event can be overlayed. See figure 4.3 (top) for a picture of the event display. Shown are the wires in a station hit by a passing particle.

A third GUI is the **histogram display**. It enables the online gathering and display of statistical information on the event data. Especially useful histograms are a wire map (to look for dead or tripping channels) and drift time spectra. See figure 4.3 (bottom) for a picture of the histogram display.

4.2.3 Event reconstruction

Before analysing the drift cell properties, e.g. the efficiency, resolution and cross talk, the events must be reconstructed. Tracks are reconstructed using the measurements of the prototype detector planes, i.e. no external high precision tracking system is used. Tracks are found using a pattern recognition algorithm based on an idea of Tolsma[51]. The algorithm consists of the following steps:

- Make a list of all hit combinations between hits in different detector layers. For each combination there are 4 “hit pairs” corresponding to the left/right ambiguities as illustrated in figure 4.4.
- All hit pairs are used as track seeds. The seed with the longest lever-arm is considered first, forming an initial track candidate. The *residuals* (see section 4.6) of all hits with respect to the line joining the two hits of the track candidate are calculated. If a residual is smaller than 4σ (where σ is the calculated error), with a minimum of 0.5 mm, the hit is added to the candidate. In case of a left/right ambiguity the combination with the smallest residual is chosen.
- A track candidate is required to consist of a minimum of 3 hits.
- Hit pairs contained within the track candidate are removed from the list of seeds. The above procedure is repeated on the remaining seeds until no seeds are left.
- Some of the track candidates found will have hits in common. To prevent this double counting, hits are required to be only used by one candidate. This is

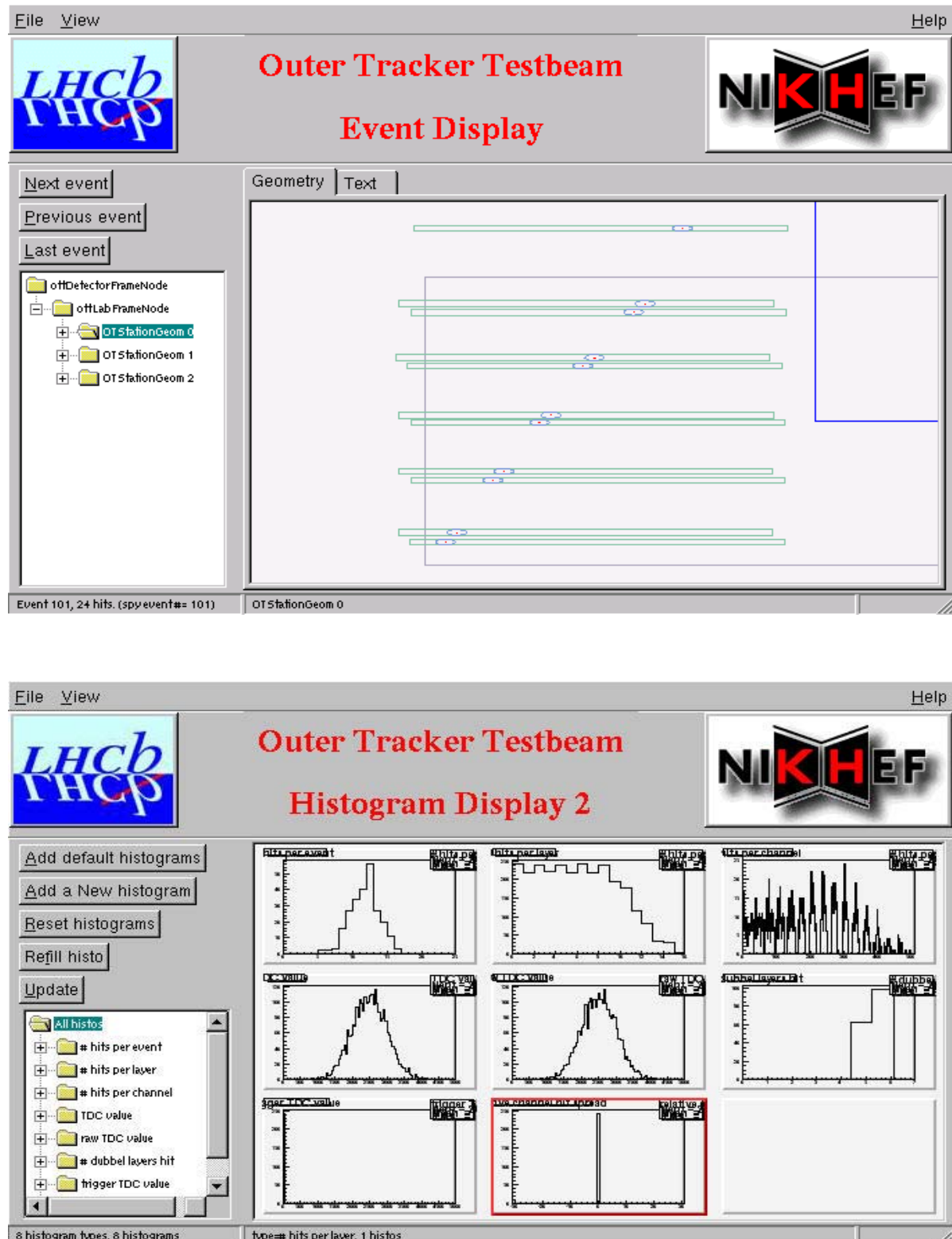


Figure 4.3: Pictures of the online event display (top) and histogram display (bottom) used in the test beams.

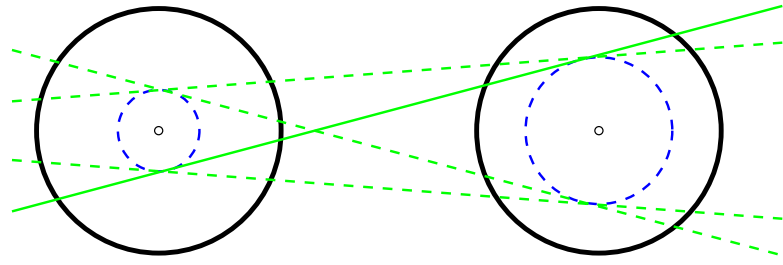


Figure 4.4: The measured drift time corresponding to a particle traversing a drift cell can be represented by a circle of constant drift distance around the wire. From a single cell it is unknown at which “side” of the wire the particle traversed, i.e. it has a left/right ambiguity. Shown is a particle (solid line) traversing two drift cells and circles of constant drift distance (dashed circles) corresponding to the resulting drift time. The dashed lines corresponds to the three additional hit pairings that can be made due to the left/right ambiguity at reconstruction time.

achieved by fitting the candidates and selecting the track with the highest quality Q defined as:

$$Q = N - w \sum \chi_i^2 , \quad (4.1)$$

with N the number of hits on the track, χ_i^2 the contribution of hit i and w a weight factor³ set to 0.1. All hits used by this track are removed from the other candidates.

- If more than one track candidate with at least 3 hits remains, the next highest quality candidate is selected and the above selection procedure is repeated on (possible) remaining candidates.

The track fit is performed in the time domain, i.e. a χ^2 minimisation is performed of:

$$\chi^2 = \sum \left(\frac{t_{\text{hit}} - T(d_{\text{reco}})}{\sigma_t} \right)^2 , \quad (4.2)$$

where t_{hit} is the measured drift time, T the drift time-distance relation (see section 4.4) that converts the fitted shortest distance to the wire d_{reco} to a time, and σ_t the resolution of the measurement t_{hit} (see section 4.6). To determine the drift time-distance relation and the resolution an iterative approach is followed using the fitted tracks. This approach is shown to converge in a few iterations, resulting in a good fit (average reduced χ^2 of 1.3)[62].

The modules are aligned using a software alignment procedure described elsewhere[62]. An alignment precision better than 50 μm is obtained.

³A selection based on a total χ^2 criterium only tends to bias for the selection of tracks with a small number of hits. The quality criterium mentioned above does not have this problem[75].

4.2.4 Simulation with Garfield

To compare measurements with theory the computer program Garfield[76] is used. Garfield is a program used to make detailed simulations of drift chambers. It interfaces to the Magboltz program[77] for the computation of electron transport properties in arbitrary gas mixtures. An interface to the Heed program[78] is used to simulate ionisation of gas molecules by particles traversing a chamber.

Garfield can be used to calculate and plot a wide variety of quantities relating to drift chambers. In this thesis Garfield is used to simulate the response of individual drift cells of the outer tracker prototypes to the passage of an ionising particle. Simulated are the creation of ionisation clusters along the trajectory, the drift of the charge carriers, the avalanche near the anode including attachment, the induction of a signal on the anode wire, the shaping of this signal corresponding to the ASDBLR, and finally the measurement of the drift time defined by the moment that the signal exceeds a threshold. These simulations are used to obtain the electron drift trajectories and drift time spectra. From the drift time spectra the maximum drift time is extracted. The dependency on gas mixture, high voltage and magnetic field is studied for several cell geometries.

4.3 Drift time

An important measurement characterising the behaviour of a drift cell is the drift time spectrum, i.e. the distribution of measured drift times for a uniformly irradiated cell. The shape of such a spectrum is determined by the cell geometry, gas mixture, the magnetic field and the applied high voltage. The left plot in figure 4.5 shows a measured drift time spectrum for the short 5 mm straw tube drift cells of module 6033 in the gas mixture $Ar(80)/CO_2(20)$. The right plots in figure 4.5 show the measured drift time spectra in the gas mixture $Ar(65)/CF_4(30)/CO_2(5)$ for different values of the magnetic field.

Comparison of the left and right plots shows three things. Firstly, the spectrum for the gas mixture without CF_4 is broader. This is due to the slower drift velocity in this gas mixture. Secondly, the right plot shows the widening of the spectra due to an increase in magnetic field. The latter is caused by the longer drift path in case of a magnetic field as discussed in section 3.1.2. Finally, the spectra in the fast gas mixture contain a 'shoulder' for small drift times. This shape of the drift time spectrum is rather well reproduced by the simulation program Garfield as is shown in figure 4.6 (right figure).

The shoulder in the spectrum can be understood qualitatively by a combination of two things: the dependence of the drift velocity on the distance to the anode wire and the electron attachment due to CF_4 . In figure 4.6 (left) the drift velocity dependency according to Garfield/Magboltz is shown. At very small distances the velocity is high, causing the steep edge in the drift time spectrum for small drift times. The dip in the drift velocity around $0.4 \text{ cm } \mu\text{sec}^{-1}$ corresponds to the shoulder in the drift time distribution of figure 4.5. Electron attachment can prevent the closest cluster from reaching the avalanche region, causing a more distant cluster to pass the threshold with consequently a longer drift time. This distance is larger for tracks passing near the

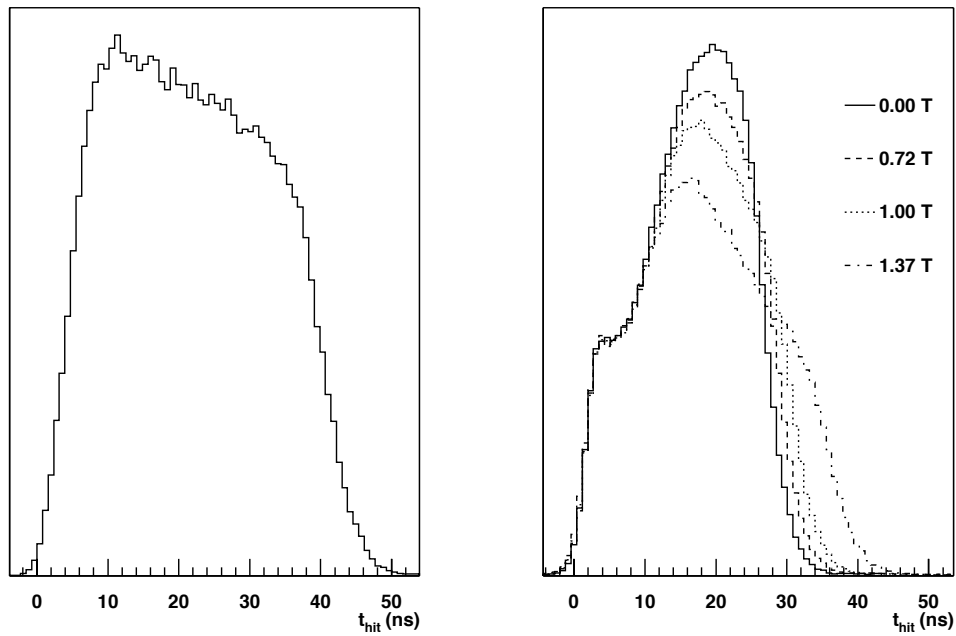


Figure 4.5: Drift time spectra in a 5 mm straw tube drift cell of module 6033. left) In the gas mixture $\text{Ar}(80)/\text{CO}_2(20)$ with no magnetic field. right) In the gas mixture $\text{Ar}(65)/\text{CF}_4(30)/\text{CO}_2(5)$ with different values for the magnetic field.

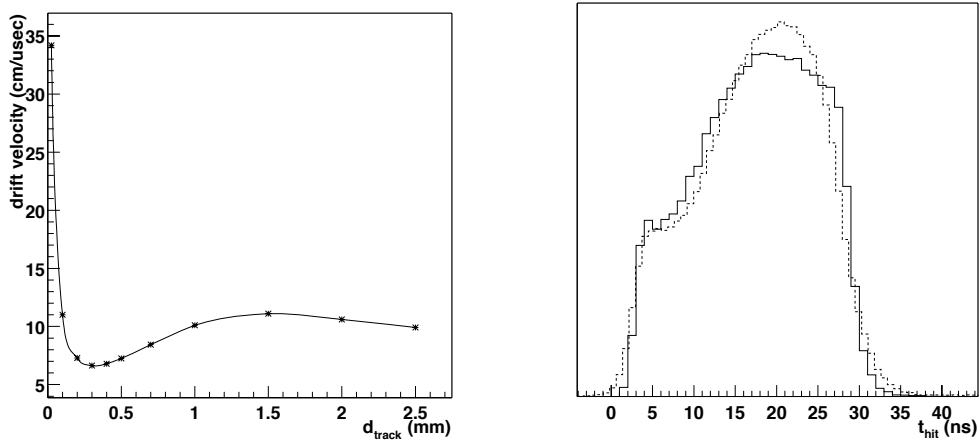


Figure 4.6: left) Electron drift velocity versus d_{track} in 5 mm straw tubes in a $\text{Ar}(65)/\text{CF}_4(30)/\text{CO}_2(5)$ gas mixture and an applied voltage of 1800 V obtained with Garfield[76]. right) Simulated (solid line) and measured (dashed line) drift time spectrum in these tubes under the same conditions.

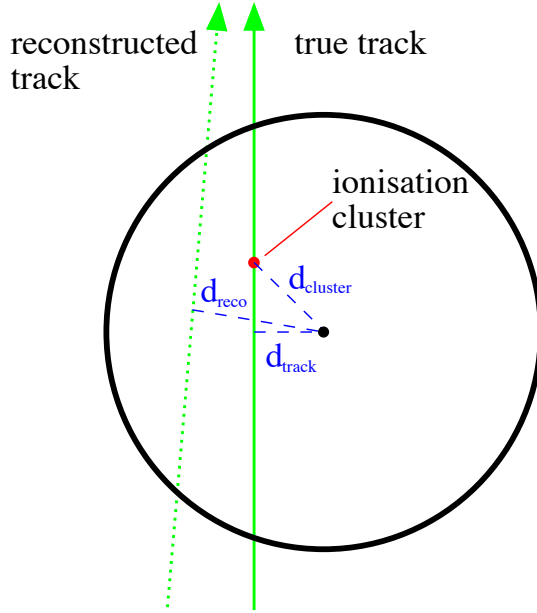


Figure 4.7: A particle traversing a gas filled drift tube at a distance d_{track} from the wire causes the closest ionisation cluster at a distance d_{cluster} . The closest distance of the reconstructed track to the wire is d_{reco} .

wire (see figure 4.7), causing a shift of these hits to larger drift times in the drift time spectrum.

An important quantity that can be directly extracted from a drift time spectrum is the maximum drift time (t_{\max}) in the cell. The total signal collection time, i.e. drift time in the tube plus signal propagation time along the tube, for an LHCb drift cell is required to be within two LHC bunch crossings (50ns). The signal propagation time is $\sim 3.8 \text{ ns/m}$ [56]. This requirement has the consequence that the limits on the maximum drift time range from $\sim 45 \text{ ns}$ in the small magnet stations down to $\sim 35 \text{ ns}$ in the large stations in the track seeding region. As discussed in section 3.1.2 a magnetic field increases the drift time and hence t_{\max} . Fortunately, in LHCb only the small chambers (with consequently a small signal propagation time) will be positioned in a large magnetic field. The maximum drift time t_{\max} is defined as the time interval containing 98 % of the signals, with 1 % of the signals arriving before the beginning and 1 % after the end of the interval.

Table 4.1 shows the maximum drift time in 8 mm honeycomb cells for various gas mixtures without and with a 1.0 T magnetic field along the wire direction. Both measured t_{\max} values on the prototype modules 9002-9005 in a test beam as well as simulated values with Garfield are shown. Due to problems with the test beam electronics⁴ [62] the amount of valuable data is limited. Within the limited statistics available, measurements

⁴These problems occurred in the 1998 and to a smaller extent in the 1999 test beam periods. The problems were solved in the test beams of 2000 and 2001.

$Ar/CF_4/CO_2$ mixture		t_{\max} (ns)	
		B = 0.0 T	B = 1.0 T
80 / 0 / 20	test beam	110	110
	Garfield	110	125
88 / 7 / 5	test beam	70	90
	Garfield	70	88
81 / 14 / 5	test beam	60	90
	Garfield	64	80
68 / 27 / 5	test beam	55	65
	Garfield	60	60
71 / 29 / 0	test beam	45	110
	Garfield	40	120

Table 4.1: Simulated and measured maximum drift times t_{\max} in the 8 mm honeycomb cells of modules 9002-9005 for various gas mixtures and magnetic fields along the wire direction. The measurement accuracy is estimated to be 20 %.

B (T)	0.0	0.5	0.72	0.8	1.0	1.2	1.37	1.6	1.8	2.0
t_{\max} (ns)	26.9	27.4	28.4	29.1	30.4	32.8	35.4	39.7	44.2	49.6

Table 4.2: Simulated maximum drift times t_{\max} for 5 mm straw tube in a $Ar(65)/CF_4(30)/CO_2(5)$ gas mixture for various magnetic field values along the wire.

and simulation agree.

Only the gas mixture without CO_2 (i.e. 71% argon and 29% CF_4) stays within the required maximum of 45 ns drift time in case no magnetic field is applied. However, if the field is turned on the increase in drift time is large; it is even larger than for relatively slow drift gases. This is caused by the increased Lorentz angle resulting in a longer effective drift distance as explained in section 3.1.2. The maximum drift time in 8 mm honeycomb cells is too large to be used for the outer tracker. Therefore, drift cells with a smaller cell size are required.

Table 4.2 shows *simulated* maximum drift times in a 5 mm straw tube in the gas mixture $Ar(65)/CF_4(30)/CO_2(5)$ for various magnetic field values along the wire. It is seen that straw tubes up to a field of ~ 1.8 T are expected to stay within the required 45 ns for the small magnet stations. The long stations are expected to stay within the required 35 ns up to ~ 1.4 T.

Measurements of t_{\max} have been performed on the short 5 mm straw tubes of modules 6030-6034 for a wide variety of conditions, e.g. gas mixture, high voltage and magnetic field. Table 4.3 summarises measured t_{\max} values for several gas mixtures at four values of the magnetic field. The simulated t_{\max} with Garfield (see table 4.2) and the measured t_{\max} in the test-beam for the gas mixture $Ar(65)/CF_4(30)/CO_2(5)$ are in good agreement (measured values are 1-2 ns larger). As expected the maximum drift time decreases as the amount of CF_4 in the gas mixture is increased. These measurements show that

mixture $Ar/CF_4/CO_2$	t_{\max} (ns)			
	B = 0 T	B = 0.72 T	B = 1.0 T	B = 1.37 T
80 / 0 / 20	41.2	43.2	44.8	49.1
65 / 5 / 30	39.0	40.5	42.2	45.1
75 / 15 / 10	32.5	34.5	36.3	40.9
75 / 20 / 5	31.4	33.1	35.1	40.8
70 / 20 / 10	31.4	33.0	35.2	39.3
70 / 25 / 5	29.2	30.9	32.8	37.5
65 / 30 / 5	28.2	30.1	32.0	36.0

Table 4.3: Measured maximum drift times t_{\max} in the 5 mm straw tube cells of modules 6030-6034 for various gas mixtures and magnetic fields along the wire.

5 mm straw tubes, with a $Ar/CF_4/CO_2$ gas mixture containing 15 % of CF_4 are fast enough to meet the LHCb timing requirements in all stations.

4.4 Distance-drift time relation

An outer tracker drift cell measures the *time* between a particle traversing a cell and the arrival of the first electron clusters in the avalanche region near the wire. Particle trajectories are, however, described in space coordinates making the shortest *distance* at which the particle past the wire interesting. Therefore, a relation between the measured drift time and the shortest distance of approach is needed.

This relation in general depends on many variables and parameters, e.g. gas mixture, cell geometry, applied high voltage and magnetic field. Due to the statistical nature of the energy loss process involved the time measured (t_{hit}) for particles traversing at the same minimum distance d_{track} will fluctuate. As the number of created clusters along the trajectory is limited (about 30 per cm), the distance of the closest cluster to the wire d_{cluster} is not equal to the particle distance of closest approach d_{track} (see figure 4.7). The relative difference between these distances is largest for particles passing near the wire.

Two distance-time relations can be identified:

- A $T(d)$ -relation is used to describe the behaviour of a drift cell. It gives the best estimate of the expected drift time for an ionisation cluster created at a distance d_{cluster} .
- A $D(t)$ -relation is used to give the best estimated distance d_{hit} of the distance of closest approach d_{track} of a traversing particle given a drift time measurement t_{hit} .

Because of the mentioned effects these relations are not the inverse of each other. Especially at small distances/times they do not coincide. This chapter describes the behaviour of the drift tubes. Hence, the deduction of the $T(d)$ -relation is described. A $D(t)$ relation is obtained in a similar way.

A $T(d)$ relation can be obtained from a theoretical model by simulating it with a computer program like Garfield. However, to be certain that the calculated relation matches reality one should always verify it by measurements. There are several methods to determine a $T(d)$ -relation from data.

A **first** way to determine a $T(d)$ -relation is to *measure* it by using an external high precision reference tracker, e.g. a silicon detector telescope. With such a system the trajectory of a traversing particle and hence the distance of closest approach d_{track} is precisely measured. The detection cell provides a measured drift time t_{hit} corresponding to that distance. The $T(d)$ -relation is obtained by fitting it to a sample of data points $(t_{\text{hit}}, d_{\text{track}})$. This method has the disadvantage that a precise reference tracking system has to be present. In LHCb there is no external system to provide this.

A **second** method obtains the $T(d)$ -relation by integrating the drift time spectrum. The integral of the drift time spectrum up to a drift time t_{hit} corresponds to the number of particles which results in a drift time smaller than this time. The integral of the *distance* distribution corresponds to the same number of particles but now as a function of the drift distance. If a cell is uniformly irradiated the drift distance distribution will be flat. Consequently, integration leads to a linear function of the distance. Therefore, a number of particles in the integrated drift time spectrum directly maps to a distance. Hence, a normalised integrated drift time spectrum gives an approximate $T(d)$ -relation.

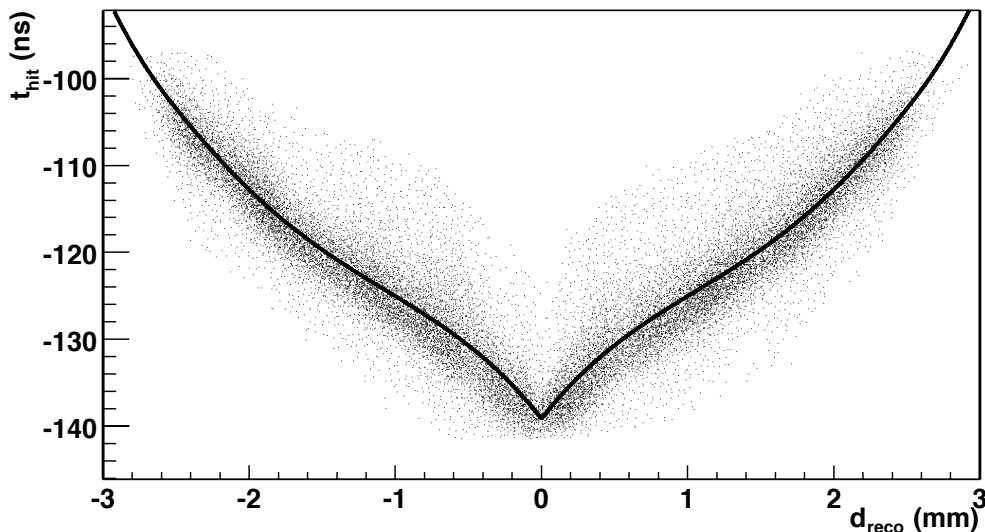


Figure 4.8: Scatter plot of measured drift time t_{hit} in straw tubes of module 6033A versus predicted distance to wire from reconstructed tracks d_{reco} in the remaining layers of the modules 6030-6034. A high voltage of 1800 V and a magnetic field of $B = 1.37$ T is applied. An $\text{Ar}(65)/\text{CF}_4(30)/\text{CO}_2(5)$ gas mixture is used. The superimposed curve is the fitted $T(d)$ relation.

Several effects limit the precision of this method. Firstly, due to the statistical nature of the processes involved the drift spectrum will be smeared. Secondly, the

method assumes the cell efficiency to be independent of the distance. Finally, the cell irradiation is never completely uniform.

A **third** more accurate method uses the result of the second method as an input. Studies[51] have shown that an accurate measurement of the distance drift time relation can be achieved by using the data from the drift tubes itself. The method is based on the assumption that the track parameters resulting from a fit through the individual detector hits will provide a better estimate of the distance between a track and the wire than the individual hits. This method named *auto-calibration* is an iterative method. It starts with an initial estimate of the $T(d)$ -relation using the previous method and using this relation to determine the hit positions. With these hit positions a track fit is done. The tracks are used to predict the distance d_{track} at which the track passed the wire. The reconstructed d_{track} is defined as d_{reco} . The difference between $t_{\text{reco}} = T(d_{\text{reco}})$ and the measured drift time t_{hit} is used to correct the $T(d)$ -relation. This is done by minimising the χ^2 function

$$\chi^2 = \sum_i \left(\frac{T(d_{\text{reco},i}) - t_{\text{hit},i}}{\sigma_{t,i}} \right)^2$$

for a large set of tracks with respect to the parameters describing the $T(d)$ -relation. A 3^d order spline function with 6 parameters is used to describe the $T(d)$ -relation. With the corrected $T(d)$ -relation the tracks are refitted, and the procedure is repeated. After a few iterations this procedure converges to a stable relation.

Because there is no external high precision reference tracker in the prototype tests it is decided to use the third method to determine the $T(d)$ relation. Figure 4.8 shows the measured drift time in straw tubes of module 6033A versus the predicted distance to the wire for tracks reconstructed from hits in all other layers of the modules 6030-6034. The superimposed curve is the fitted $T(d)$ -relation.

4.5 Efficiency

Efficient track reconstruction in LHCb requires a high efficiency of individual detection cells. The hit efficiency is defined by the probability that an ionising particle traversing a detection cell is observed, i.e. causes a hit. The efficiency is determined by calculating the ratio of the number of observed hits (N_{hit}) over the number of expected hits (N_{reco}) in a given cell from the track fit, i.e.

$$\varepsilon = \frac{N_{\text{hit}}}{N_{\text{reco}}} \quad . \quad (4.3)$$

To determine the efficiency tracks are reconstructed using all layers except the layer under consideration. From the reconstructed track a prediction is obtained for the track position in the test layer and accordingly a distance to the wire of the closest cell. If an actual hit is recorded in that cell it is said to be efficient for that distance.

In the ideal case of no electron attachment and a fully efficient readout electronics the single cell efficiency is given by:

$$\epsilon(l) = 1 - P(0; l) = 1 - \exp\left(\frac{-l}{\lambda}\right) \quad , \quad (4.4)$$

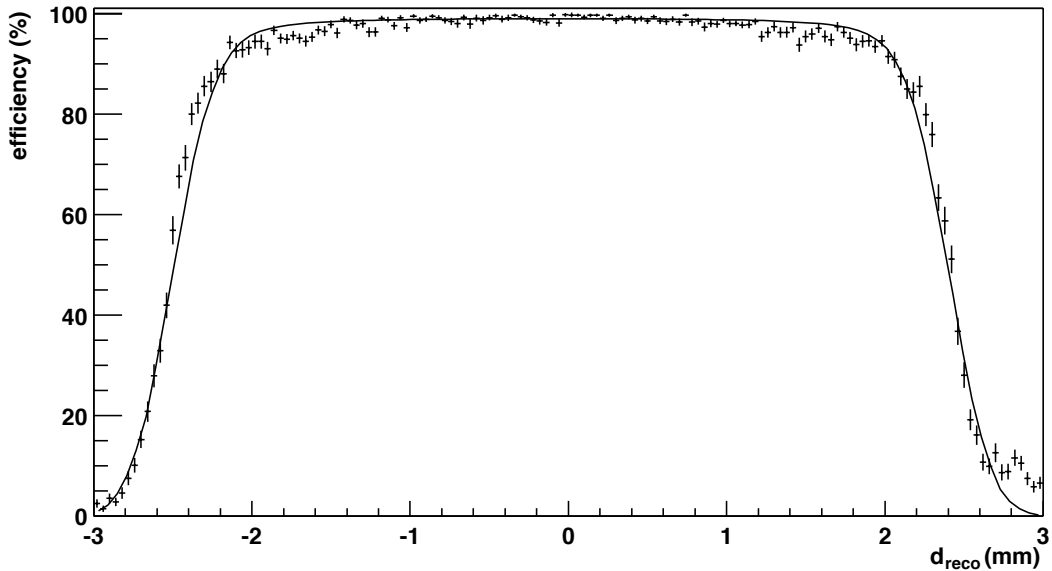


Figure 4.9: Drift cell efficiency as a function of predicted distance between track and wire, for the gas mixture $Ar(65)/CF_4(30)/CO_2(5)$ at $HV=1800$ V in module 6033. The fitted curve is explained in the text.

where l is the length of the trajectory in the cell, and λ the average ionisation distance. $P(0; l)$ represents the probability that no cluster is created as given by equation 3.1. The track segment l in the cell is short for particles traversing a cell close to the boundary. The shorter the track segment the smaller the number of primary ionisation clusters created, hence the lower the detection efficiency.

Figure 4.9 shows the efficiency in a drift tube of module 6033 as a function of reconstructed distance d_{reco} between track and wire. The figure shows that for a large part of the drift tube the efficiency is close to 100 %. The error on the predicted position of the track in the cell results in an apparent non-zero efficiency outside the cell boundary. It also tends to hide the shape predicted by equation 4.4. The shown curve is the results of a χ^2 -fit to the data, taking into account the parametrisation of the efficiency as a function of l , the distance traversed in the drift cell, i.e.

$$\epsilon(l) = \epsilon_0 \left(1 - \exp\left(\frac{-l}{\lambda}\right)\right) . \quad (4.5)$$

The distance l is related to the nominal distance to the track d_{track} by:

$$l = 2\sqrt{R^2 - d_{track}^2} . \quad (4.6)$$

Because of the error in d_{reco} a convolution is done with a Gaussian centred at d_{reco} with variance σ^2 . The fit of this toy model is reasonable and results in⁵ $\epsilon_0 = 99.2\%$,

⁵Due to misalignment the centre of the efficiency plot slightly deviates from zero. This offset is fitted to be 49 μm.

$\lambda = 835 \mu\text{m}$ and $\sigma = 198 \mu\text{m}$. The fitted λ is roughly a factor 3 larger than the 0.3 mm expected for $\text{Ar}(65)/\text{CF}_4(30)/\text{CO}_2(5)$ (see section 3.1.1). A possible explanation for this is given by the loss of electrons due to attachment. This effectively reduces the number of used clusters, which corresponds to an increased average ionisation distance λ . This is roughly in agreement with the attachment coefficient for this gas mixture of about 4 [44].

The average efficiency over the cell range of -2.5 mm to +2.5 mm is calculated from the average efficiency determined from curves as figure 4.9 multiplying it with a geometrical correction factor for the dead area between two cells. For the short 5 mm straw tubes of modules 6030-6034, which have a pitch of 6 mm, this correction factor is 6/5. This leads to an average efficiency of 96.4 % in figure 4.9.

Figure 4.10 shows the average efficiencies as function of the high voltage for five gas mixtures in the straw tubes of these short modules. The region where the efficiency as function of the voltage is (almost) constant is called the efficiency plateau. Gas detectors are usually operated at such a plateau because it ensures stable and uniform operation under small variations in conditions. The arrows point to the beginning of the plateau, which is taken as the lowest high voltage at which the efficiency exceeds 95 % (in steps of 50 V). In the summary table 4.4 on page 80 the corresponding high voltage is given.

The full scale prototype module 5 is tested in the gas mixture $\text{Ar}(75)/\text{CF}_4(15)/-\text{CO}_2(10)$. Figure 4.11 shows the dependence of the efficiency on high voltage for these chambers. An average efficiency of 97 % is obtained at 1600 V. The prototype is tested at 10 points along the length of the wire. Figure 4.12 shows the efficiency as a function of position along the tube at 1600 V. A slight increase of efficiency is observed towards the centre of the module at $x = 0$. This is explained by the fact that the wires are not electrically terminated at the centre of the module. This causes signals to be reflected at the wire end. Both the direct and reflected components of the signal will contribute to the signal on the ASDBLR. Signal from the centre of the module will have a maximum amplitude because both components will arrive at the same time, hence the efficiency is higher.

4.6 Resolution

A track is reconstructed by fitting a line through the measured hits. To properly weigh the measurements of the drift cells in the track reconstruction a prediction of the precision of the measurements is required. As for the drift-time distance relation one can define a resolution in the time and in the distance domain. In accordance with common practise we report here on the coordinate resolution.

The error on the measured distance $d_{\text{hit}} = D(t_{\text{hit}})$ is given by the *residual*:

$$r_{\text{track}} = d_{\text{hit}} - d_{\text{track}} , \quad (4.7)$$

where d_{track} is the closest distance of approach of a particle to the wire. On average the residual is zero. The coordinate resolution $\sigma_{d_{\text{hit}}}$ is given by the square root of the variance on the residual.

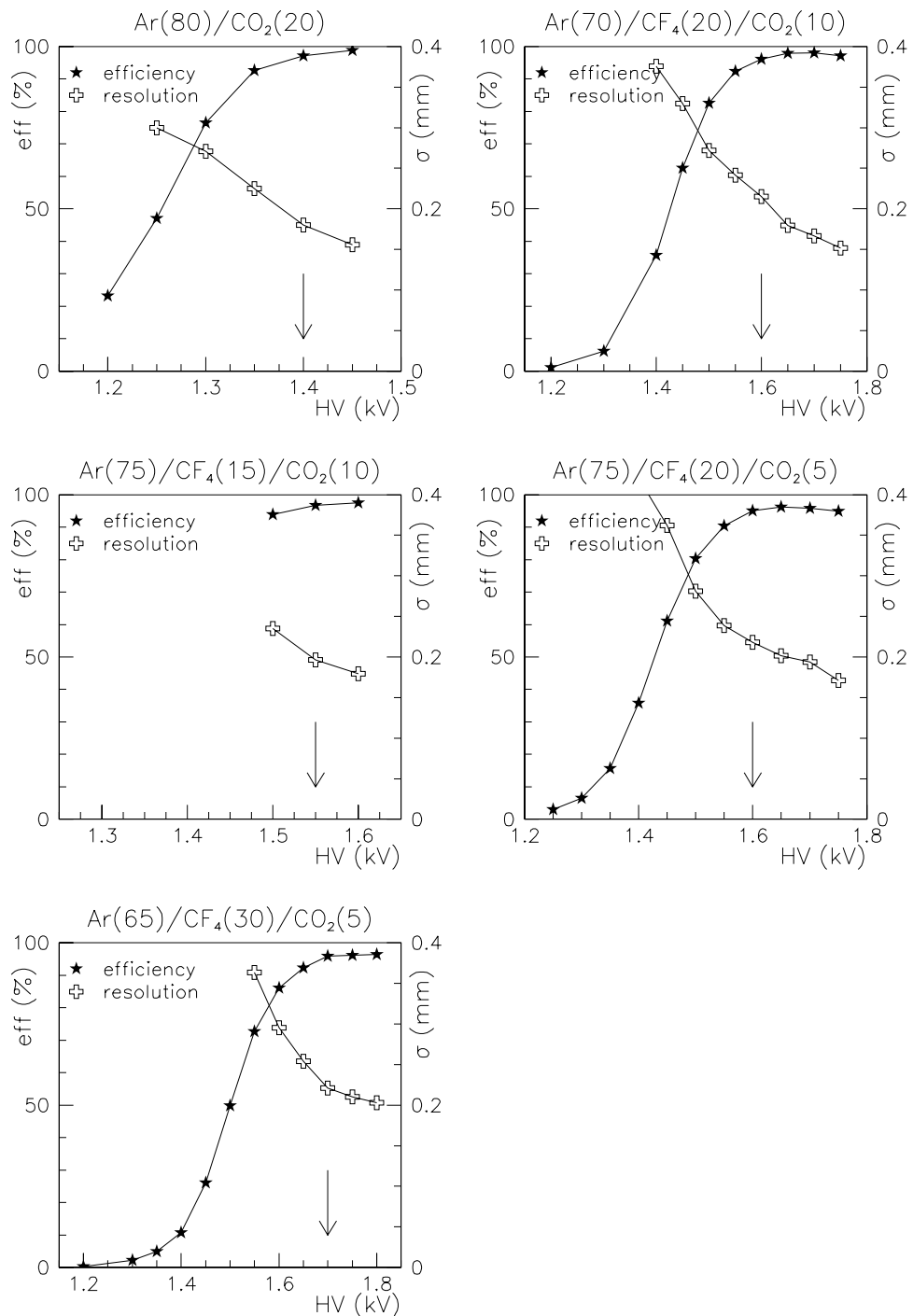


Figure 4.10: Efficiency and coordinate resolution as a function of high voltage for various gas mixtures in straw tubes of module 6033. The left axis shows the efficiency, the right axis shows the resolution.

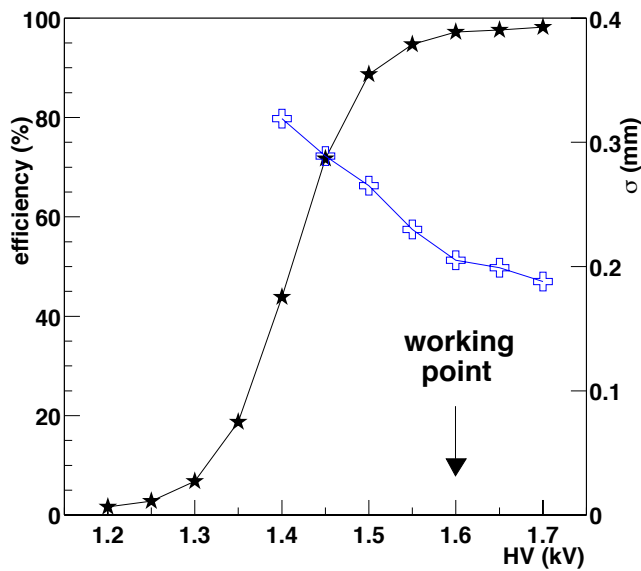


Figure 4.11: Efficiency and resolution as a function of high voltage for straw tubes of module 5 in the gas mixtures $Ar(75)/CF_4(15)/CO_2(10)$.

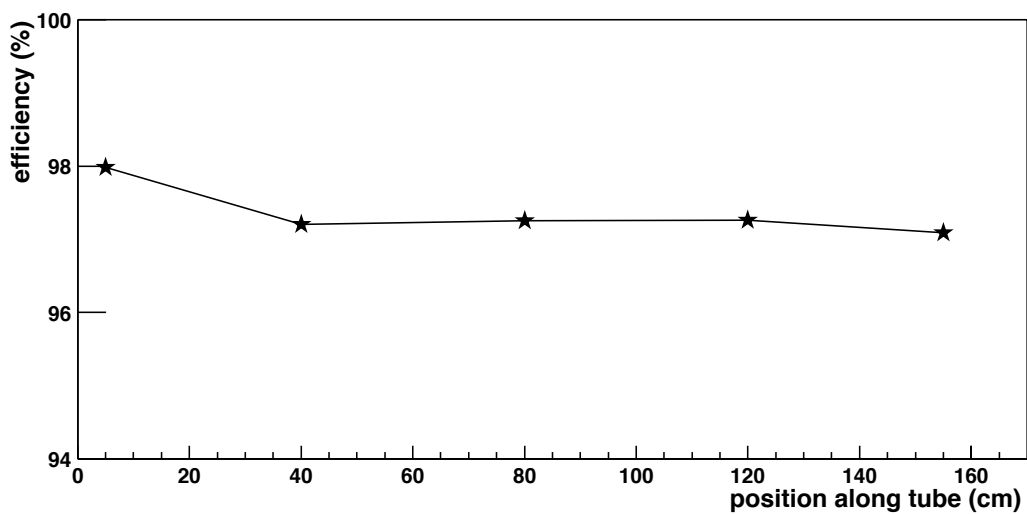


Figure 4.12: Efficiency as a function of position along the straw tubes in one half-module 5 in the gas mixtures $Ar(75)/CF_4(15)/CO_2(10)$.

In the test-beams no external high precision tracking system was available to determine d_{track} with an accuracy much better than the resolution of the drift cells. Therefore, a track is reconstructed from the measurements of the drift cells, resulting in a reconstructed distance d_{reco} (see figure 4.7). The error on d_{reco} depends on the geometrical configuration of the setup, the number of measurements and their assumed precision. If the measurement precision is assumed constant over the whole cell the precision of the reconstructed distance is proportional to the measurement precision, i.e.

$$\sigma_{d_{\text{reco}}} = f \cdot \sigma_{d_{\text{hit}}} , \quad (4.8)$$

The factor f is a constant which follows from the geometry of the setup and the number of hits on the track. Because f is independent of $\sigma_{d_{\text{hit}}}$ it can be determined by fitting a track with an arbitrary assumption on this measurement precision.

The residual can be determined as:

$$r_{\text{reco}} = d_{\text{hit}} - d_{\text{reco}} . \quad (4.9)$$

The variance of the residual is the sum of two contributions, one due to the error of the measured distance, the other due to the error in the distance calculated from the reconstructed track, i.e.

$$\begin{aligned} \sigma_{r_{\text{reco}}}^2 &= \sigma_{d_{\text{hit}}}^2 + \sigma_{d_{\text{reco}}}^2 \\ &= \sigma_{d_{\text{hit}}}^2 \cdot \left(1 + \frac{\sigma_{d_{\text{reco}}}^2}{\sigma_{d_{\text{hit}}}^2}\right) \\ &= \sigma_{d_{\text{hit}}}^2 \cdot (1 + f^2) , \end{aligned} \quad (4.10)$$

where the geometrical factor f defined in equation 4.8 is used. To determine $\sigma_{d_{\text{hit}}}$ the *scaled residual* is defined as:

$$r_{\text{scaled}} = \sqrt{1/(1 + f^2)} \cdot r_{\text{reco}} . \quad (4.11)$$

The scaling factor $1 + f^2$, typically 1.1-1.2, depends on the number of hits on the track. The variance of the scaled residual will be equal to $\sigma_{d_{\text{hit}}}^2$. Therefore, the coordinate resolution can be obtained from the scaled residual distribution.

Figure 4.13 shows the average scaled residual distribution for a 5 mm straw tube. The fitted curve is a Gaussian with a constant background term over the range ± 1.0 mm. The non-Gaussian background is less than 3% of the total distribution. Therefore, the resolution is defined as the σ of the Gaussian. Figure 4.10 shows the average resolution for different gas mixtures as a function of the applied high voltage. In all cases the resolution improves with high voltage. This is mainly due to the increased efficiency for detecting the closest ionisation cluster(s). The resolutions determined at the start of the efficiency plateau are summarised in table 4.4.

Also for the full scale prototype module 5 the resolution is determined. Figure 4.11 shows the dependence of the resolution on high voltage for this prototype in the gas mixture $Ar(75)/CF_4(15)/CO_2(10)$. A resolution of 205 μm is obtained at 1600 V. Figure 4.14 shows the resolution as a function of position along the tube at 1600 V. A slight improvement of resolution is observed towards the centre of the module at $x = 0$. This is explained by the fact that at this position, the signal amplitude has a maximum due to the non electrical termination of the wires.

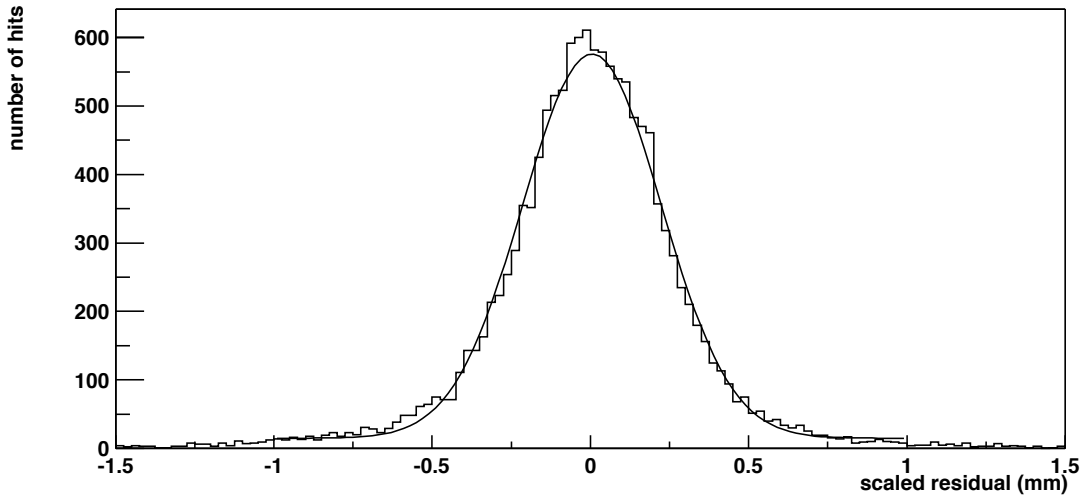


Figure 4.13: The scaled residual distribution averaged over a 5 mm straw tube in the gas mixture $Ar(65)/CF_4(30)/CO_2(5)$ with no magnetic field and a high voltage of 1700 V. The shown curve is a fitted Gaussian with a constant background term.

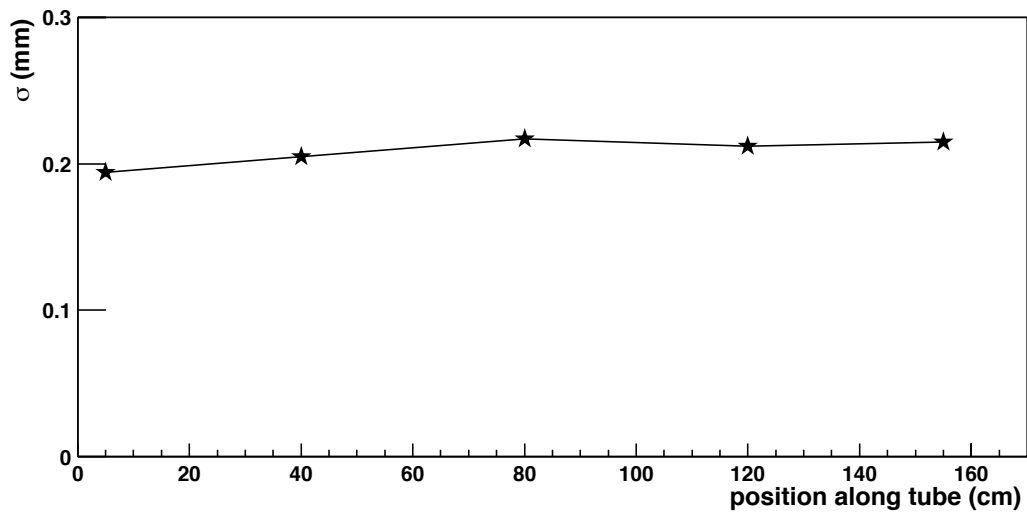


Figure 4.14: Resolution as a function of position along the straw tubes in one half-module 5 in the gas mixtures $Ar(75)/CF_4(15)/CO_2(10)$.

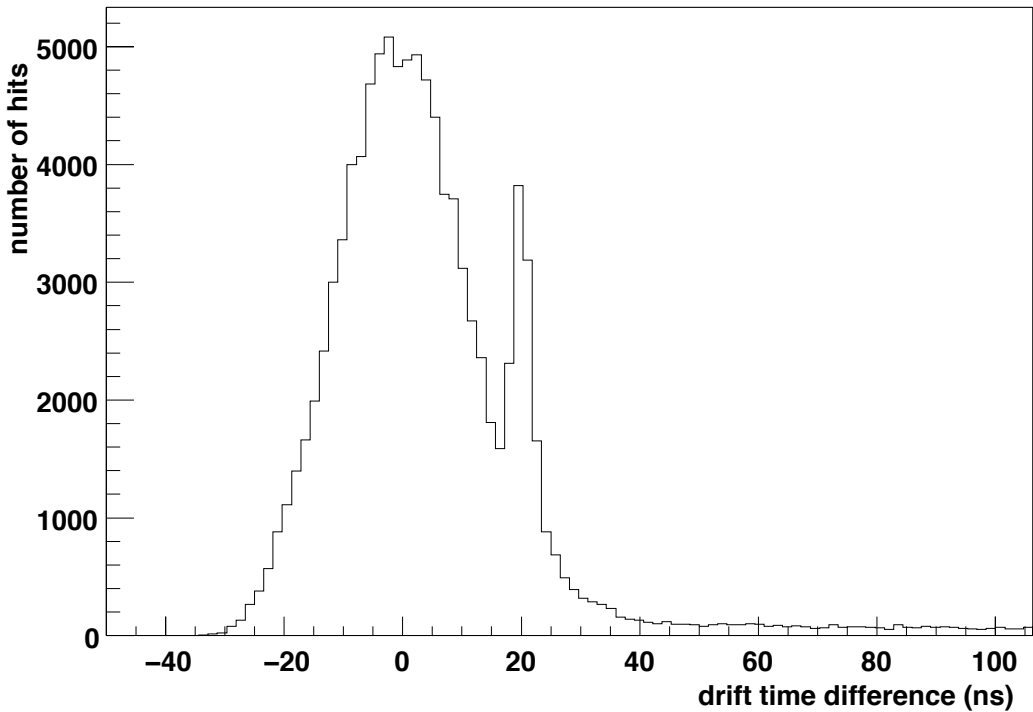


Figure 4.15: Drift time difference of cross talk hits w.r.t. signal hits in the 5 mm straw tubes of module 6032.

4.7 Noise and cross-talk

Various effects can cause a hit to be registered even if no particle crossed the detection cell. Possible sources of these noise hits are internal reflections within a drift cell, cross talk between cells, pick-up from external electrical sources and reflections or cross-talk within the readout electronics.

To make a quantitative estimate of the noise level in the prototypes all hits that are *measured* but not *predicted* are defined as noise hits. To make sure that these hits are not caused by other tracks only those events are used in this study which have one reconstructed track. The cross talk level is defined as the average number of noise hits per event in a layer.

In the 1998 and 1999 tests of modules 6030-6034 some layers showed a high cross talk level ($> 15\%$). The drift time difference of the cross talk hits w.r.t. the signal hit provided an interesting structure as indicated in figure 4.15. It shows a ~ 40 ns wide distribution around zero with a narrow peak, superimposed on this distribution at $+20$ ns and a long flat tail towards large positive values. The peak at 20 ns indicates the presence of time delayed cross talk. Further study shows that the correlation only occurs between channels within the same ASDBLR chip[62]. A dedicated electronics study[66] confirms that for a number of ASDBLR chips extra signals are created on all other 7 channels if the pulse height on a given input is larger than 50 fC (with a 2 fC threshold). In later test beam periods these bad chips were not used and the effect

disappeared.

Figure 4.16 shows the cross talk level as a function of the high voltage for five gas mixtures in the short 5 mm straw tubes of module 6033. In these figures again the arrows indicate the beginning of the efficiency plateau. The cross talk is typically 6 % per mono-layer in these chambers. In table 4.4 the cross talk in these chambers for high voltage settings at the beginning of the efficiency plateau is summarised for the five gas mixtures.

Measurements on the full scale prototype modules 2004 and 0604 show a very large increase of the cross talk level ($> 50\%$ [55]). Extensive lab tests show that this cross talk can be suppressed by shielding the straws with aluminium[56]. Therefore, the full scale prototype module 5 has an outer 25 μm thick aluminium cell layer. Figure 4.17 shows the dependence of the cross talk level on high voltage for module 5 in the gas mixture $\text{Ar}(75)/\text{CF}_4(15)/\text{CO}_2(10)$. An increase in the cross talk level is observed for voltages above the working point. This is explained by the increased signal amplitude resulting from an increase in the operating voltage. At the 1600 V working point the cross talk is 6 %. Figure 4.18 shows the cross talk as a function of position along the tube at this working point. The cross talk is slightly larger towards the centre of the module ($x = 0$), as expected by the previously mentioned larger signal amplitude at this position. Cross talk between the two staggered layers of a half module and between the two half-modules is negligible ($< 0.4\%$) [44].

4.8 Summary and conclusions

This section summarises the results of the prototype tests. Test were performed on short prototype modules and full scale modules. A description of the modules is given in section 3.3. The measurements on short prototype modules were used to study the drift cell behaviour as a function of drift gas, magnetic field and high voltage. The full scale prototypes were used to verify whether the operation of full scale chambers is uniform, especially from the electrical point of view.

mixture $\text{Ar}/\text{CF}_4/\text{CO}_2$	HV (kV)	eff (%)	σ (μm)	t_{\max} (ns)		cross talk
				B=0 T	B=1.37 T	
80 / 0 / 20	1.40	97.2	180	41.2	49.1	6.1 %
75 / 15 / 10	1.55	96.7	196	32.5	40.9	6.0 %
75 / 20 / 5	1.60	95.0	218	31.4	40.8	5.0 %
70 / 20 / 10	1.60	96.2	215	31.4	39.3	5.4 %
65 / 30 / 5	1.70	95.9	221	28.2	36.0	4.9 %

Table 4.4: Parameters of gas mixtures at the beginning of the efficiency plateau in short 5 mm straw tube chambers.

The first short prototype modules, numbered 9002-9005, had 8 mm honeycomb cells. In these modules the measured maximum drift time in an $\text{Ar}/\text{CF}_4/\text{CO}_2$ gas mixture ranges from 45 ns for 30% CF_4 content up to 110 ns when no CF_4 is present. When

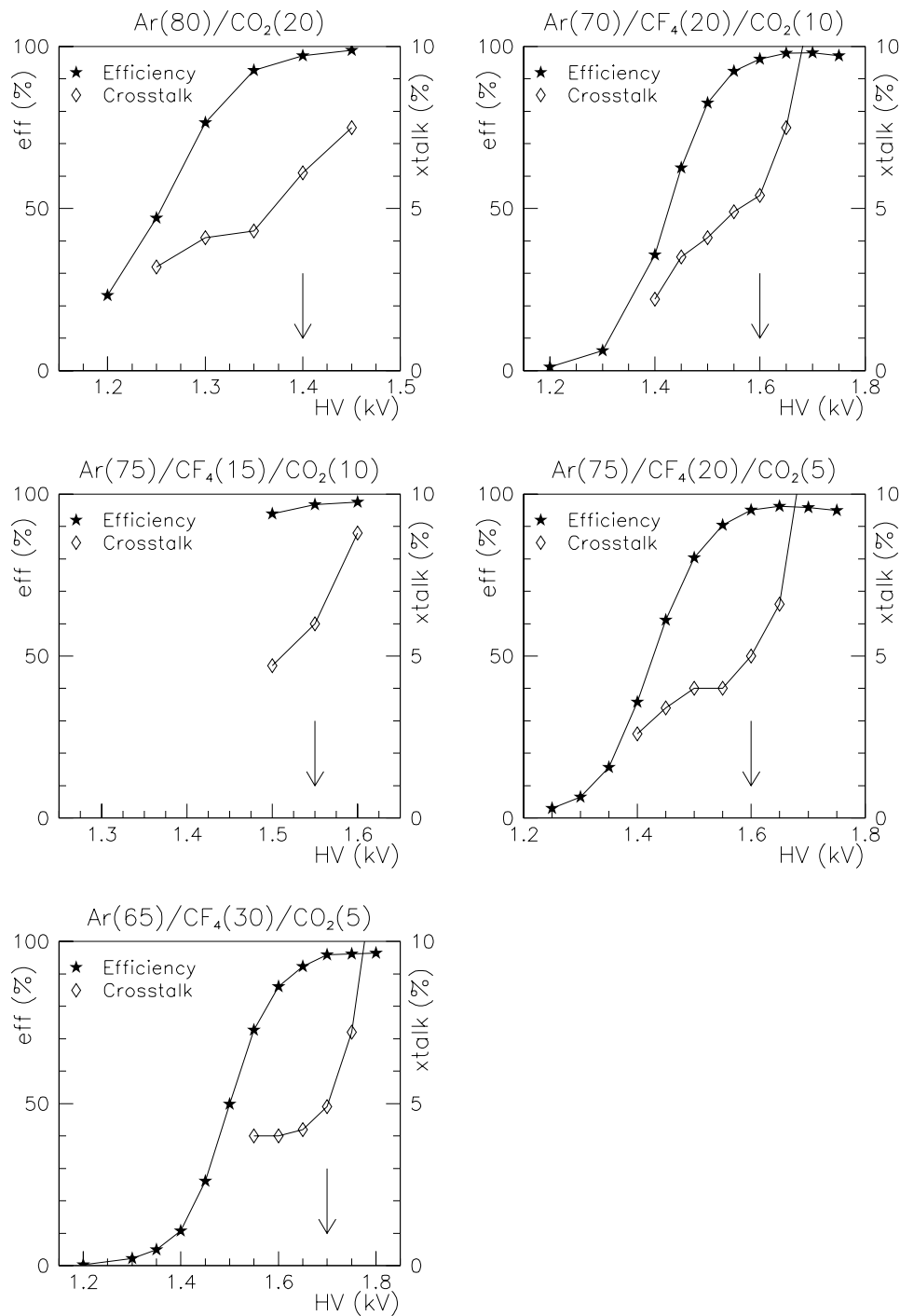


Figure 4.16: Efficiency and cross talk level as a function of high voltage for various gas mixtures in straw tubes of module 6033. The left axis shows the efficiency, the right axis shows the cross talk level.

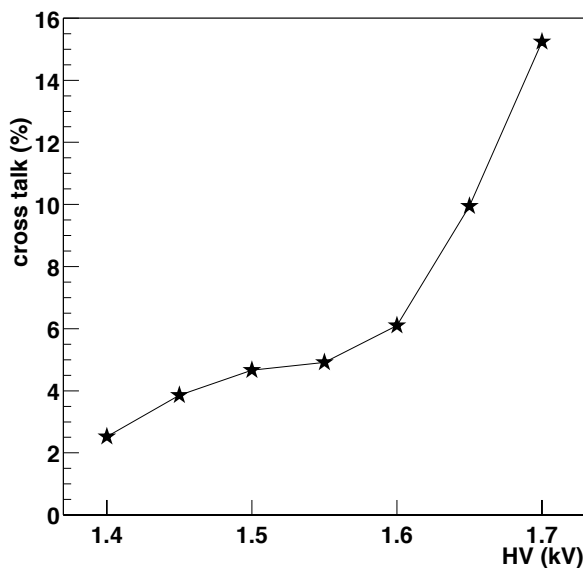


Figure 4.17: Cross talk as a function of high voltage for straw tubes of module 5 in the gas mixtures $Ar(75)/CF_4(15)/CO_2(10)$.

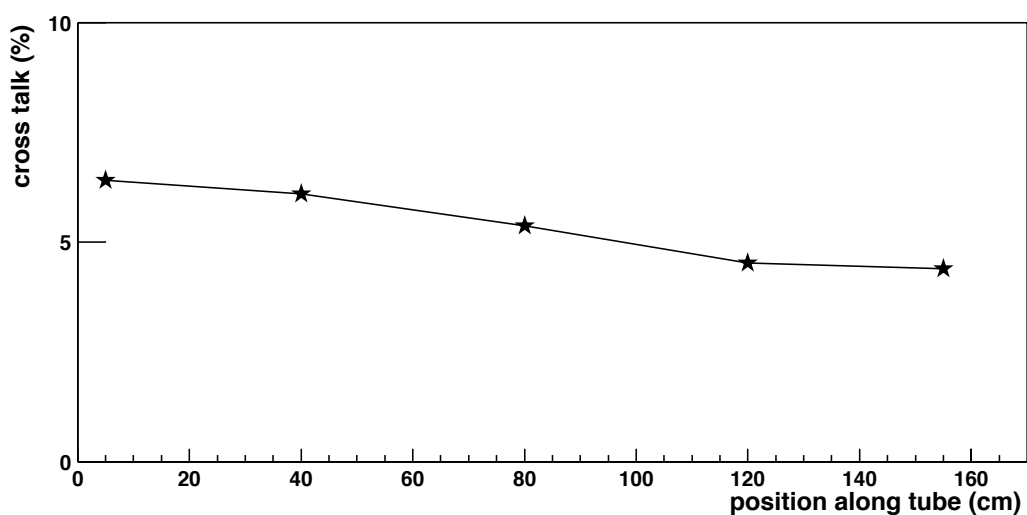


Figure 4.18: Cross talk as a function of position along the straw tubes in one half-module 5 in the gas mixtures $Ar(75)/CF_4(15)/CO_2(10)$.

a magnetic field is applied t_{\max} becomes even significantly larger. In view of the LHC bunch crossing frequency an 8 mm cell diameter is therefore too large and a 5 mm diameter drift tube is chosen instead.

Short 5 mm drift tube modules 6030-6034 were built to test the drift cell behaviour. Measurements on these chambers show that an $Ar/CF_4/CO_2$ gas mixture containing a small fraction (15 %) of CF_4 is fast enough to meet the LHCb timing requirements for all stations whether outside or inside the magnetic field. These measurements are confirmed by simulations with the computer program Garfield. In table 4.4 the measured t_{\max} values for a variety of gas mixtures in the absence of and in a 1.0 T magnetic field are presented.

The single cell efficiency is close to 100% for a large part of the cell volume. Near the cell edges the efficiency drops due to the limited number of ionisation clusters formed in the gas. The efficiency is measured as a function of the high voltage and shows a plateau above a certain voltage value. This leads to a typical average efficiency of 97 % per cell at the plateau.

Table 4.4 shows the measured resolution and cross talk level for a high voltage setting at the beginning of the efficiency plateau. With the gas mixture $Ar(75)/CF_4(15)/CO_2(10)$ a coordinate resolution of 200 μm per drift cell is obtained. The resolution slightly degrades for an increased CF_4 content due to electron attachment. The effect is however small, the CF_4 content can be increased to 30% without a major impact on the resolution.

The cross talk level in these small chambers is found to be about 6% at the start of the efficiency plateaus. It does not have a significant dependence on the CF_4 content. As expected the cross talk level increases with increasing high voltage values.

The first full scale modules 2004 and 0604 show an unacceptable large cross talk level. This has led to a design in which the cells are shielded by a thin aluminium layer. The improved full scale prototype module 5 indeed shows a comparable cross talk performance as the short modules. In the gas mixture $Ar(75)/CF_4(15)/CO_2(10)$ the efficiency plateau for this chamber starts at about 1600 V. At this working point the average efficiency is 97.2 % and the coordinate resolution is 205 μm . The average cross talk within a mono-layer is about 6 %. The cross talk to other layers of a module is negligible. The efficiency, resolution and cross talk level is mostly uniform over the full length of these long modules with a slight deviation towards the centre of the module as can be seen in figures 4.12, 4.14 and 4.18. The deviation is explained by the increased signal amplitude due to the non electrical termination at the wire split. The larger amplitude results in a better efficiency and resolution. The cross talk however becomes worse because of the increase of the signal amplitude at the centre of the module.

These results show that full scale outer tracker modules can be built with good performance. The final outer tracker chamber design presented in section 2.3.3 is similar to that of module 5.

Chapter 5

Track fitting

This chapter describes the procedure to fit trajectories through a set of measurements of the LHCb tracking detectors. The fit makes use of measurements in the inner tracker, outer tracker and VELO system. At a later stage also muon, calorimeter and even RICH information may be included. This chapter only describes the track fitting procedure. The pattern recognition procedure, that assigns individual measurements to their corresponding track, is described in chapter 6. In this chapter it is therefore assumed that the correct measurements on the tracks are known. The results therefore correspond to the assumption of perfect pattern recognition, and can be seen as the best that can be obtained with the LHCb tracker.

The chapter is divided into four sections. Section 5.1 describes the event simulation programs that generate the data used to study track reconstruction. Section 5.2 describes the procedures and algorithms used in the LHCb track fit. Section 5.3 describes the results and performance of the fit. In section 5.4 conclusions are drawn.

5.1 Event simulation

As the LHC is not yet operational no real detector data is available. Therefore, the expected detector output is obtained by computer simulation. The simulation consists of the three sequential steps indicated in figure 5.1, i.e. event generation, particle tracking and detector response.

All reconstruction studies, as presented in chapters 5, 6 and 7 of this thesis, are based on these simulated data. In LHCb we have a simulation program SICBMC[79] and a reconstruction program Brunel[80]. In SICBMC the event generation and the final state particle interaction with the detector is performed. Currently¹ the detector response is included in Brunel and is performed before the event reconstruction takes place. The reconstruction results presented in this thesis are obtained by using SICBMC v247r1, detector description database(DBASE) v240 and Brunel v8.

¹The detector response is in principal a simulation step but is included in Brunel for practical reasons. Once an object oriented version of SICBMC exists the detector response will be included there.

5.1.1 Event generation

In the **event generation** the physics processes in the proton collisions are simulated resulting in a list of four-momenta of particles (“primary” tracks). LHCb uses the Pythia (v6.1) event generator[25] extended with the QQ CLEO Monte-Carlo program[81] to simulate the particle decays. As mentioned in the first chapter (section 1.5) the branching fractions for the B meson decays used to study CP-violation are small. Therefore, apart from generating large samples of minimum bias events (for background studies), the generator is used to produce specific B meson decay samples. Not all bunch crossings contain a single interaction, i.e. a part of the events contain several overlayed interactions. The effects of such a *pile-up* are described in more detail in the next chapter (section 6.1).

5.1.2 Particle tracking

The GEANT[82] program is used to propagate the generated particles through the simulated LHCb detector. The magnetic field map of the LHCb magnet is taken into account in the propagation. Particles with a relatively short lifetime can decay into more stable particles inside the detector. These processes are simulated in GEANT. The particles interact with the detector materials in several ways. In the next paragraphs the most relevant interaction processes for track reconstruction, i.e. multiple scattering and energy loss, are described. The final output of the GEANT simulation step are, for each particle, the positions where the trajectory crosses the active detector components.

A charged particle traversing a medium will be deflected from the original trajectory. This is primarily due to elastic Coulomb scattering from nuclei in the material. The *Rutherford formula* describes the differential scattering cross-section of a particle with momentum p and charge z on a single nucleus of charge Z at an angle θ , i.e. [83]:

$$\frac{d\sigma(\theta)}{d\Omega} = \left(\frac{zZr_e m_e c}{2\beta p \sin^2(\theta/2)} \right)^2 , \quad (5.1)$$

where r_e ($= 2.817 \cdot 10^{-15} \text{ m}$) is the classical electron radius and m_e the electron mass. On a macroscopic scale a particle will encounter many nuclei. These multiple Coulomb interactions cause a “zigzag” movement through the medium of which all individual scattering angles are described by equation 5.1. This process is called *multiple scattering*. The program GEANT follows a theory formulated by Molière to precisely simulate multiple scattering. The description of this theory is beyond the scope of this thesis and the reader is referred to the GEANT manual[82] or the original publications[84, 85, 86].

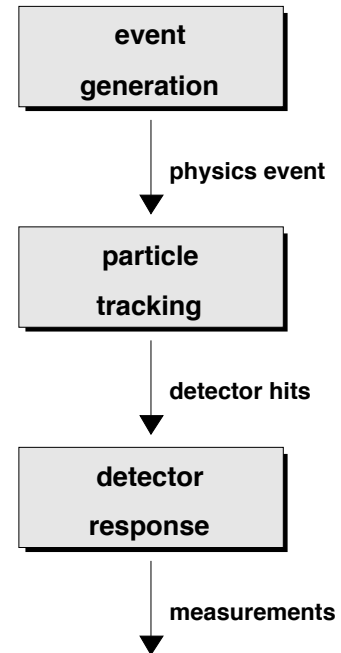


Figure 5.1: Program flow of event simulation.

In addition to multiple scattering, particles will lose energy. The major energy loss is due to inelastic collisions with atomic electrons in the medium. There is a wide variation in the amount of energy transferred from the particle to the electrons. Because a particle will encounter many electrons it is common practice to use the average energy loss per unit path length. The average energy loss per unit length for a charged (charge z) particle, traversing at velocity v , that is heavy in comparison with the electrons it encounters², is given by the *Bethe-Bloch* formula [86, 83]:

$$-\frac{dE}{dx} = 2\pi N_a r_e^2 m_e c^2 \rho \frac{Z}{A} \frac{z^2}{\beta^2} \left[\ln \frac{2m_e c^2 \beta^2 T_{\max}}{(1 - \beta^2) I^2} - 2\beta^2 - \delta \right] . \quad (5.2)$$

Here N_a is Avogadro's number, ρ , Z and A , the density, atomic number and weight of the medium, I the mean excitation potential and T_{\max} the maximum energy transfer in a single collision. The quantity δ is a correction factor for the density effect[87] that plays a role at high energies. GEANT simulates the energy loss such that the average loss follows the Bethe-Bloch formula.

Light charged particles (electrons and positrons) suffer an additional energy loss due to *Bremsstrahlung*. Classically Bremsstrahlung is understood as the acceleration of a particle in the electric field of the nuclei. This process results in the emission of photons. The radiation length X_0 is defined as the distance required in a certain medium to reduce by Bremsstrahlung the mean energy of a high-energy electron by a factor e . The radiation length is a material constant that is determined and tabulated in the literature[88, 89]. The average energy loss due to Bremsstrahlung is thus given by:

$$-\frac{dE}{dx} = \frac{E}{X_0} . \quad (5.3)$$

5.1.3 Detector response

In the final simulation step the **detector response** to the passage of a particle is calculated. In this section the *digitisation* procedure of the detectors used in the track fit (outer tracker, inner tracker and VELO) is briefly described.

The digitisation of the outer tracker straw tube detector consists of three sequential steps[90]:

- First, a “Geometric digitisation” is performed. It consists of calculating the channel number of the hit straw tube and determining the closest distance of approach d of the track to the wire.
- Secondly, the single cell response is simulated, i.e. how a single outer tracker cell responds to the passage of a particle at a distance d . Input to this digitisation step are the prototype results presented in chapter 4. The cell efficiency is taken into account by not creating a detector hit for some particles according to the efficiency profile obtained from test measurements. The distance d is smeared by a Gaussian distribution of 200 μm to simulate the measurement resolution. This distance is converted into a drift-time by applying a $T(d)$ relation.

²In the derivation of equation 5.2 it is assumed that the traversing particle is undeviated from the original trajectory. This holds for particles with a mass significantly exceeding that of an electron.

- Finally, the response of the readout electronics to the created signal is simulated. This step takes into account a 20 ns dead-time (in case a cell would be hit twice closely after each other, only the first measurement will cause a hit) of the electronics. Furthermore, a readout gate of 50 ns is simulated (see section 6.1).

The response of the silicon strip detectors (inner tracker and VELO) is simulated by a digitisation step followed by a hit clustering step[91]. The digitisation consists of three steps

- First, the charge sharing between the strips induced by a traversing particle is calculated.
- Secondly, the detector and amplifier noise on each strip is simulated by means of the addition of a Gaussian distributed value.
- Finally, all strips with a charge above a certain threshold are selected as hit.

The clustering algorithm searches for groups of neighbouring hit strips. The measured coordinate is defined as the weighted average of the strip coordinates of the hits in a cluster.

The digitisations resulting from the above simulation steps are in principle similar to what can be expected from the real experiment. In case of the outer tracker the extra data due to pile-up and *spill-over* (discussed in section 6.1) are taken into account. The digitisations are used as input for the track reconstruction algorithms.

5.2 Track fitting procedure

The track fit determines the best estimate of the track parameters along the particle trajectory. In LHCb the track fit is used to obtain

- the momentum of the particle from the deflection by the B field,
- the position and direction of the track in the vertex region,
- the direction and position at which a particle traverses the RICH detectors,
- the prediction of the particle trajectory when entering the calorimeters and for muons the muon detector.

LHCb is a forward spectrometer setup, with detectors at planes of constant z . For this geometry it is natural to define the track parameters, at reference plane z , as $\mathbf{x} = (x, y, t_x = \frac{dx}{dz}, t_y = \frac{dy}{dz}, \kappa = \frac{q}{p})$. The first two parameters correspond to the position at the reference plane, the third and the forth to the track direction or slope. The last parameter is the ratio of the particle charge q over the momentum p . The track fit also determines the covariance matrix C of the track parameters \mathbf{x} .

The track fit is based on the Kalman filter technique [92]. It is implemented in the TRAIL software package[93] which is part of the reconstruction program Brunel[80]. The use of the Kalman filter in the track fit is described in section 5.2.1. Section 5.2.2

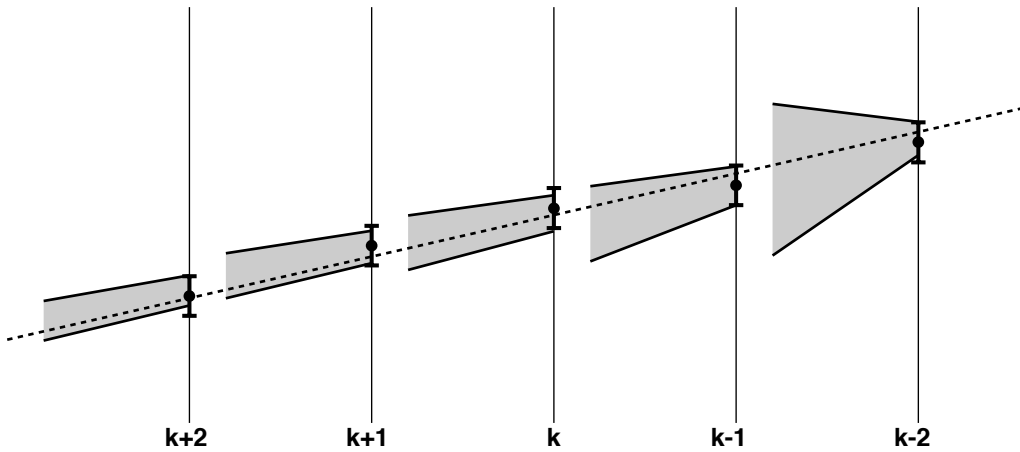


Figure 5.2: Shown is the application of the Kalman filter technique to track fitting. The vertical lines correspond to the detector planes with indicated on it the measurement points and their errors. The cones represent the uncertainty in the reconstructed track parameters. As can be seen the knowledge of the track parameters is step wise updated with each measurement (Kalman filter technique applied from right to left).

describes how the detector measurements are used in the fit. Section 5.2.3 describes the track propagation. Section 5.2.4 describes the modelling of multiple scattering and energy loss. Section 5.2.5 describes the Kalman smoothing procedure.

5.2.1 Kalman filter

The Kalman filter technique was developed in 1960 by Kalman[92] to efficiently update the *state vector* of a dynamic system as a function of time from a set of *measurements* to the system. Mathematically, the Kalman filter is a set of equations that provides an efficient iterative solution of the least-squares method. Since the introduction the filter has been extensively researched and used in areas as diverse as aerospace, marine navigation, nuclear power plant instrumentation, demographic modelling and manufacturing. The technique has also proven to be suited for track (and vertex) fitting in high energy physics experiments[94, 95].

In the case of track fitting, the system state vector is the set of track parameters (i.e. $\mathbf{x} = (x, y, t_x, t_y, \kappa)$ in LHCb). The measurements are defined at the reference detector surfaces. The coordinate system of the detectors can be different from the track parameters. For the measurements in the reference frame of the detectors the symbol m is used. The z -coordinate replaces the role time has in the original formulation of the filter. Contrary to a global track fit, the knowledge of the track parameters is progressively improved by adding the information of the measurements subsequently (see figure 5.2). The Kalman filter applied to track fitting consists of repeating a *prediction* and *filter* step for each measurement. In the prediction step an estimate is made of the track parameters at a given z -position using the measurements of previous detector planes.

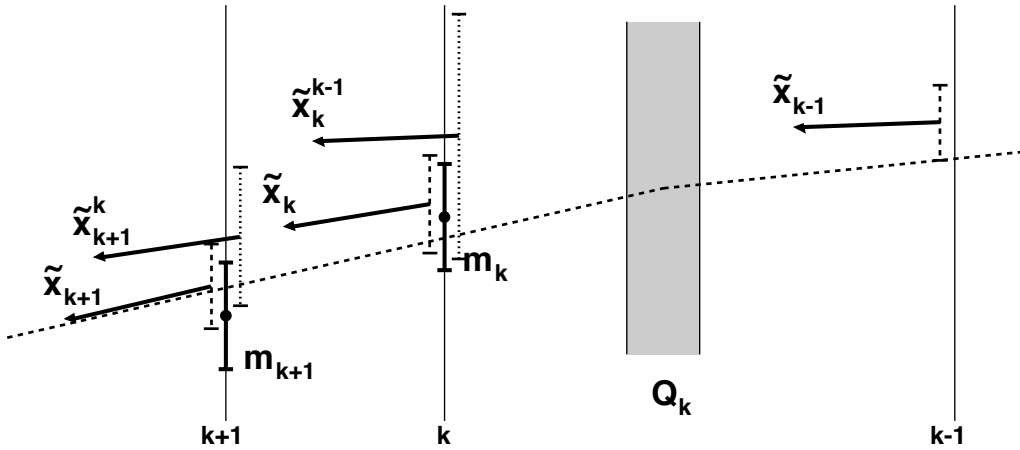


Figure 5.3: Shown is the application of the Kalman filter technique to the measurement at reference planes k . From the track state $\tilde{\mathbf{x}}_{k-1}$ at plane $k-1$ a prediction is made of the track parameters at the measurement plane k , i.e. $\tilde{\mathbf{x}}_k^{k-1}$. The hatched area represents detector material. It is accounted for by increasing the track parameters covariance matrix by the system noise factor Q_k . These predicted track parameters $\tilde{\mathbf{x}}_k^{k-1}$ are updated with the measurement m_k by applying the Kalman filter step. This results in the best estimate of the track parameters $\tilde{\mathbf{x}}_k$.

In the filter step the predicted track parameters are updated with the measurement in the current plane. The filter step is based on calculating the weighted mean of the information of the measurement and the predicted track parameters.

The Kalman filter progresses through the detection planes, at each plane updating the track state vector using all preceding measurements. To initiate the procedure initial track parameters are required. The determination of these initial parameters (seeds) is described in the pattern recognition chapter (section 6.2). The filter is illustrated in figure 5.3. The mathematics of the Kalman filter is presented below.

In the prediction step an estimate is made of the track parameters at the current (k) measurement, i.e. $\tilde{\mathbf{x}}_k^{k-1}$, from the parameters at the previous ($k-1$) measurement, i.e. $\tilde{\mathbf{x}}_{k-1}$ ³. This is done with the prediction relation f_k , i.e.

$$\tilde{\mathbf{x}}_k^{k-1} = f_k(\tilde{\mathbf{x}}_{k-1}) . \quad (5.4)$$

The form of this relation is determined by the track model. When the system is assumed to be linear the relation is approximated by

$$\tilde{\mathbf{x}}_k^{k-1} = F_k \tilde{\mathbf{x}}_{k-1} , \quad (5.5)$$

where $F_k (= \frac{\partial f_k}{\partial \tilde{\mathbf{x}}_k})$ is called the propagation matrix. Note that the track parameters before and after the prediction are defined at different z -positions, hence the (true) parameter values change. The LHCb track model is described in more detail in section 5.2.3.

³The wiggles \sim on top of the track parameters \mathbf{x} indicate it is the best estimate of the parameters obtained from the fit so far.

Propagation of the parameters to the next measurement plane also changes the covariance matrix C of the track parameters. The predicted covariance matrix C_k^{k-1} is given by:

$$C_k^{k-1} = F_k C_{k-1} F_k^T + Q_k \quad . \quad (5.6)$$

The first term corresponds to the prediction due to the track model. The second term Q_k is an optional term to allow for “system noise”. If the particle traverses material, random perturbations on the trajectory (multiple scattering) occur. These perturbations increase the uncertainty on the predicted track parameters and accordingly changes the covariance matrix. The term Q_k allows to take into account such local multiple scattering effects.

In the filter step the track parameters and covariance matrix are updated with a measurement m_k , e.g. the measured drift distance in an outer tracker drift tube. The true track parameters at the measurement plane k can be transformed in a “true” value of this measurement m_k^{true} using a projection relation h_k , i.e.

$$m_k^{\text{true}} = h_k(\mathbf{x}_k) \quad . \quad (5.7)$$

When the projection relation is linear this can be written as:

$$m_k^{\text{true}} = H_k \mathbf{x}_k \quad , \quad (5.8)$$

where $H_k (= \frac{\partial h_k}{\partial \tilde{\mathbf{x}}_k})$ is the *projection matrix* projecting the track parameters into measurement space. All projections for the LHCb tracking detectors are linear or can be approximated as such. They are described in section 5.2.2. The measurement errors are represented by the covariance “matrix” V_k , which for the LHCb detectors used in the track fit is a single number.

The predicted track parameters $\tilde{\mathbf{x}}_k^{k-1}$ as well as the measurement m_k provide information on the true track parameters \mathbf{x}_k at the detector reference surface k . These measurements are combined in a least-squares fit which minimises a χ^2 -function for \mathbf{x}_k using the covariance matrices C_k^{k-1} and V_k . The χ^2 -function is:

$$\begin{aligned} \chi^2 &= (m_k - H_k \mathbf{x}_k)^T V_k^{-1} (m_k - H_k \mathbf{x}_k) + \\ &\quad (\tilde{\mathbf{x}}_k^{k-1} - \mathbf{x}_k)^T (C_k^{k-1})^{-1} (\tilde{\mathbf{x}}_k^{k-1} - \mathbf{x}_k) \quad . \end{aligned} \quad (5.9)$$

The first term corresponds to the measurement m_k . The quantity $r = m_k - H_k \mathbf{x}_k$, i.e. the difference between the actual and true measurement, is called the *residual* of the measurement. It is weighted with V_k . The second term corresponds to the error on the predicted track parameters weighted by C_k^{k-1} .

Minimisation of equation 5.9 shows the best $\tilde{\mathbf{x}}_k$ estimate of the track parameters \mathbf{x}_k to be given by:

$$\tilde{\mathbf{x}}_k = \tilde{\mathbf{x}}_k^{k-1} + K_k (m_k - H_k \tilde{\mathbf{x}}_k^{k-1}) \quad , \quad (5.10)$$

with covariance matrix:

$$C_k = (1 - H_k K_k) C_k^{k-1} \quad , \quad (5.11)$$

where the matrix K_k is given by:

$$K_k = C_k^{k-1} H^T (V_k + H_k C_k^{k-1} H_k^T)^{-1} \quad . \quad (5.12)$$

The filtered state $\tilde{\mathbf{x}}_k$ is equal to the predicted state $\tilde{\mathbf{x}}_k^{k-1}$ corrected by a term proportional to the predicted residual. The magnitude of the correction K_k depends on covariance matrices V_k and C_k^{k-1} . The matrix K_k is often called the *gain matrix*.

The predicted residual before filtering is:

$$r_k^{k-1} = m_k - H_k \quad . \quad (5.13)$$

The quantity R_k^{k-1} is the error on the predicted residual, given by:

$$R_k^{k-1} = V_k + H_k C_k^{k-1} H_k^T \quad . \quad (5.14)$$

After filtering they can be updated to:

$$r_k = (1 - H_k K_k) r_k^{k-1} \quad , \quad R_k = (1 - H_k K_k) R_k^{k-1} \quad . \quad (5.15)$$

These residuals are extensively used in the pattern recognition algorithm described in section 6.3.

The track fitting procedure improves the knowledge of the track parameters by subsequently adding the information of all measurements for the track under consideration using the Kalman filter technique. At the last measurement plane, therefore, the best estimate is obtained of the track parameters. This estimate takes into account the full information of all measurements, multiple scattering and energy losses. In the absence of the multiple scattering terms Q_k (see equation 5.6) the result is mathematically equivalent to a least-squares fit.

The Kalman filter technique used for track fitting has several advantages over a global fit.

- The Kalman filter treats multiple scattering and energy loss locally by including a noise term Q_k . As a consequence the fitted track better follows the true trajectory, even when there are “kinks” due to (large) scatters.
- A global fit requires inversion of a matrix with the dimension of the state vector (i.e. 5×5). The Kalman filter only needs the inversion of a matrix with the dimension of the measurement as can be seen in equation 5.12. For LHCb all measurements are one dimensional, hence m_k and V_k are numbers. This makes the Kalman filter a fast algorithm.
- The fact that measurements are added step by step makes the Kalman filter an ideal technique for finding the measurements on the track as is discussed in chapter 6. A global fit would require a re-fit when a new measurement is added to the track.
- A global track fit in principle yields a best estimate of the track parameters at a single predefined reference surface. Using the Kalman smoother relations (see section 5.2.5) the best estimate is automatically obtained at all measurement positions.

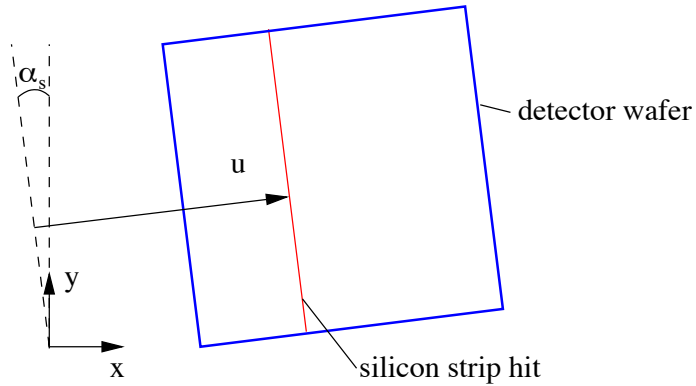


Figure 5.4: Projection of track parameters into the measurement space of an inner tracker.

5.2.2 Measurements

In the current LHCb track fit the measurements of the outer tracker, the inner tracker and the vertex detector are used. The vertex detector comprises two different detector types, R detectors and ϕ detectors. Consequently, measurements from four different detector types are used in the fit.

This section describes the way these measurements are used in the track fit. Projections of the true track parameters into the measurement space of a particular detector provide the “true” measurements m_k^{true} via the projection relation h_k or projection matrix H_k as described in equations 5.7 and 5.8.

inner tracker clusters

The inner tracker silicon strip detector measures the centre of gravity of charges collected in clusters of strips as a consequence of a traversing particle[91]. Part of the inner tracker strips are vertically oriented and hence measure the x -coordinate. The other strips are installed under a small stereo angle α_s . The coordinate u is defined to be perpendicular to the strip as indicated in figure 5.4, i.e.

$$u = x \cos \alpha_s + y \sin \alpha_s . \quad (5.16)$$

The inner tracker detector measures this coordinate, i.e.

$$m = u . \quad (5.17)$$

The projection relation $h(\mathbf{x})$, projecting from the track parameter space \mathbf{x} into the measurement space is defined by:

$$h(\mathbf{x}) = x \cos \alpha_s + y \sin \alpha_s . \quad (5.18)$$

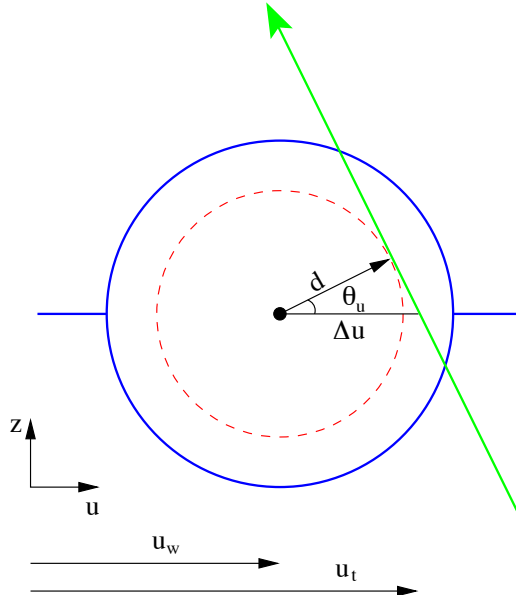


Figure 5.5: Projection of track parameters into the measurement space of an outer tracker straw tube.

Consequently, the track projection matrix H is given by:

$$H = \begin{pmatrix} \cos \alpha_s \\ \sin \alpha_s \\ 0 \\ 0 \\ 0 \end{pmatrix} . \quad (5.19)$$

outer tracker hits

An outer tracker drift tube measures the drift time of the electrons of the ionisation cluster nearest to the wire⁴. The outer tracker, as used in the track fit, therefore measures the **distance** of closest approach of the particle to the wire d . The $D(t)$ -relation (see chapter 4) provides the conversion, i.e.

$$m = d = D(t) . \quad (5.20)$$

As for the inner tracker part of the detectors are placed under a stereo-angle α_s . The same coordinate u as in equation 5.16 is used but now with respect to the wire. The projection relation $h(\mathbf{x})$, projecting the track parameter \mathbf{x} into the measurement space,

⁴In reality the measured time includes a contribution due to the propagation of the signal along the wire. Furthermore, the time depends on the time of flight of the particle. These effects are taken into account in determining the readout-gate described in the digitisation section 5.1.3. However, at present these effects are not included in the track fit.

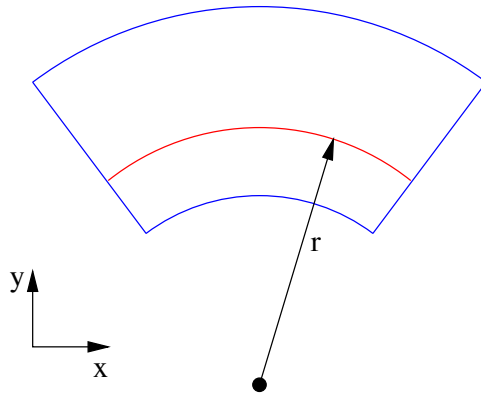


Figure 5.6: Projection of track parameters into the measurement space of a vertex R -detector.

is then defined as:

$$h(\mathbf{x}) = \Delta u \cos \theta_u , \quad (5.21)$$

with

$$\Delta u = u_t - u_w , \quad (5.22)$$

where u_w is the wire ordinate as indicated in figure 5.5. The angle θ_u is the angle the traversing particle projected into the (u, z) -plane makes w.r.t. the z -axis (see figure 5.5), i.e.

$$\tan \theta_u = t_u = t_x \cos \alpha_s + t_y \sin \alpha_s . \quad (5.23)$$

Therefore, combining equations 5.16 and 5.21-5.23, the projection relation $h(\mathbf{x})$ can be written as:

$$h(\mathbf{x}) = (x \cos \alpha_s + y \sin \alpha_s - u_w) \frac{1}{\sqrt{1+t_u^2}} . \quad (5.24)$$

A little algebra shows the projection matrix H is then given by:

$$H = \begin{pmatrix} \partial h / \partial x \\ \partial h / \partial y \\ \partial h / \partial t_x \\ \partial h / \partial t_y \\ \partial h / \partial \kappa \end{pmatrix} = \begin{pmatrix} \frac{\cos \alpha_s}{\sqrt{1+t_u^2}} \\ \frac{\sin \alpha_s}{\sqrt{1+t_u^2}} \\ \frac{-\Delta u t_u \cos \alpha_s}{\sqrt{1+t_u^2}} \\ \frac{-\Delta u t_u \sin \alpha_s}{\sqrt{1+t_u^2}} \\ 0 \end{pmatrix} . \quad (5.25)$$

R clusters

The R -detectors of the vertex detector measure the distance to the origin r (see figure 5.6) corresponding to the centre of gravity of the charges collected in clusters of strips as a consequence of a particle traversing the detector plane. Hence, the measurement m is defined as:

$$m = r , \quad (5.26)$$

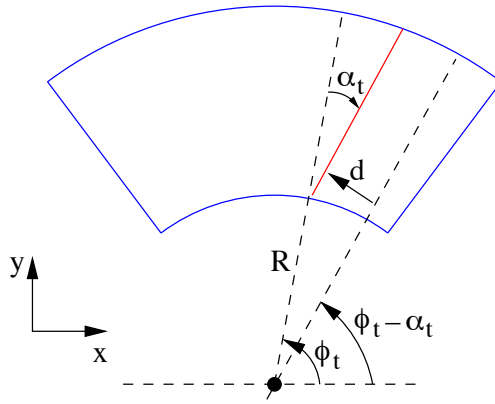


Figure 5.7: Projection of track parameters into the measurement space of a vertex ϕ -detector.

where r is the radial distance of the reconstructed cluster in the vertex detector.

The projection relation in terms of the track state \mathbf{x} is:

$$h(\mathbf{x}) = \sqrt{x^2 + y^2} . \quad (5.27)$$

Consequently, the track projection matrix H is given by:

$$H = \begin{pmatrix} \frac{x}{\sqrt{x^2+y^2}} \\ \frac{y}{\sqrt{x^2+y^2}} \\ 0 \\ 0 \\ 0 \end{pmatrix} . \quad (5.28)$$

ϕ clusters

Vertex detector ϕ -clusters measure the angle ϕ_t or “almost ϕ ” as indicated in figure 5.7. The angle ϕ_t is the ϕ coordinate of the strip that is hit at the inner radius of the silicon wafer. There is a difference between ϕ_t and the azimuthal angle of the strips ϕ as the strips are tilted under an angle α_t ($\phi = \phi_t - \alpha_t$).

Instead of using the angle ϕ_t a distance is used as the measured quantity in the track fit. The vertex ϕ -detector measurement is defined as the shortest distance d to an imaginary strip through the origin under the angle $\phi_t - \alpha_t$. From figure 5.7 it becomes clear that the measurement m then satisfies:

$$m = d = R \sin(\alpha_t) , \quad (5.29)$$

where R is the inner radius of the silicon wafer. At first sight this looks surprising as there is no dependence on the angle ϕ_t , i.e. the measurement value is the same for all clusters. However, the actual measurement does not only correspond to the value d but includes the determination of the strip that is hit and hence the angle ϕ_t .

The projection of the track parameters \mathbf{x} on the strip uses this angle and is given by:

$$h(\mathbf{x}) = -x \sin(\phi_t - \alpha_t) + y \cos(\phi_t - \alpha_t) . \quad (5.30)$$

Consequently, the track projection matrix H is given by:

$$H = \begin{pmatrix} -\sin(\phi_t - \alpha_t) \\ \cos(\phi_t - \alpha_t) \\ 0 \\ 0 \\ 0 \end{pmatrix} . \quad (5.31)$$

Pull distributions

The Kalman filter fit assumes all measurements to be Gaussian distributed (with σ equal to the assigned measurement error) around the true value. A useful monitoring quantity is the *pull* of the measurement, namely the difference between the measured and the Monte Carlo value divided by the calculated error. If all measurements are Gaussian and have been attributed with the correct error the pull distribution should follow a Gaussian distribution centred on zero with unit variance. In figure 5.8 the pull distributions of the four measurement types are presented.

The top left histogram of figure 5.8 shows the pull distribution of the outer tracker hits, i.e. $(d - d_{true})/\varepsilon_d$. The fitted curve is a Gaussian centred at zero with $\sigma = 1.0$, indicating the errors are correctly estimated.

The top right histogram in figure 5.8 shows the pull distribution of the inner tracker clusters, i.e. $(u - u_{true})/\varepsilon_u$. The distribution does not have a Gaussian shape, rather it is block shaped with a RMS of 0.99. The block like shape is explained by the fact that coordinate measurements correspond to the discrete values of the strip positions. Because of the large strip pitch most measurements are due to a single strip causing a block shape. The small deviation from a perfect block is because some clusters consists of 2 strips.

The bottom right histogram in figure 5.8 shows the pull distribution of the ϕ -clusters, i.e. $(d - d_{true})/\varepsilon_d$. This distribution is similar to that of the inner tracker. It has as well an RMS close to one.

The bottom left histogram in figure 5.8 shows the pull distribution of the R -clusters, i.e. $(r - r_{true})/\varepsilon_r$. Again, the coordinate measurements have discrete values causing a non-Gaussian shape. Because the average strip pitch is smaller in this case the shape is different from that of the ϕ -clusters. The distribution has an RMS of 0.99.

The non-Gaussian pull distributions for the inner tracker and the VELO measurements indicate that non-Gaussian effects can be expected in the track fit. The consequences of these effects on the track fit are discussed in more detail in section 5.3.2.

5.2.3 Track parameter propagation

The trajectory of a charged particle in the absence of detector material satisfies the equation of motion given by the *Lorenz force*. In case no magnetic field is present the

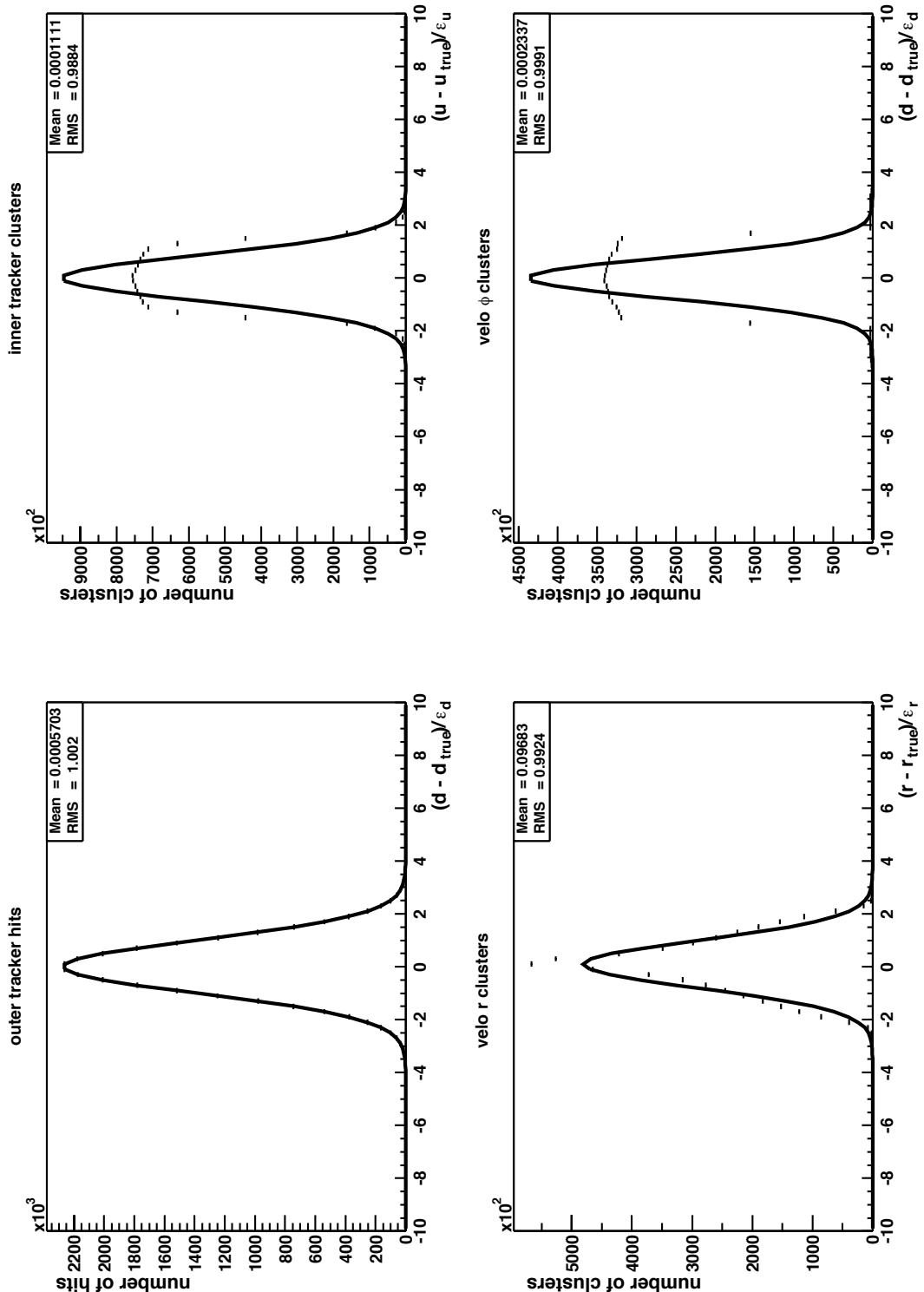


Figure 5.8: Pull distributions of the measurement values of the four measurement types used in the track fit, i.e. $(m - m_{true})/\varepsilon_m$.

particle will move in a straight line. Within a homogeneous magnetic field parallel the particle trajectory becomes a helix. As mentioned in section 2.3.1 the LHCb magnetic field is inhomogeneous and it contains field components along all the coordinate axes. Under these conditions the equation of motion can not be solved analytically and one has to rely on numerical methods. The non-uniformity of the field prescribes the use of the full field map in the track model.

The Kalman filter method allows in an elegant way to take into account external influences on the trajectory like the magnetic field and the detector material. In the track reconstruction a simplified description is used for the detector (with respect to the full GEANT description) by representing the detector components as thin walls of material with the interaction length of these components. This is done to save on the CPU time needed as otherwise a complete navigation is required through the GEANT detector description. The Kalman prediction step of the track parameters and covariance matrix (see equations 5.5 and 5.6), between successive measurements, is divided into a sequence of propagation steps from one material wall to the next. In this section the propagation of track parameters in vacuum is presented. In the next section the interaction with the material is discussed.

Neglecting the interaction with material, the equation of motion for a particle with charge q in a magnetic field \mathbf{B} is:

$$\frac{d\mathbf{p}}{dt} = q\mathbf{v} \times \mathbf{B} . \quad (5.32)$$

Expressing the time in terms of the z -coordinate it can be shown[96] that the equation of motion can be expressed in the following set of differential equations of the track parameters:

$$\frac{d}{dz}\mathbf{x} = \frac{d}{dz} \begin{pmatrix} x \\ y \\ t_x \\ t_y \\ \kappa \end{pmatrix} = \begin{pmatrix} t_x \\ t_y \\ c \cdot \kappa \cdot A_x(t_x, t_y, \mathbf{B}) \\ c \cdot \kappa \cdot A_y(t_x, t_y, \mathbf{B}) \\ 0 \end{pmatrix} = \mathbf{g}(\mathbf{x}) , \quad (5.33)$$

where the functions A_x and A_y are:

$$A_x = \sqrt{1 + t_x^2 + t_y^2} \cdot (t_y \cdot (t_x B_x + B_z) - (1 + t_x^2) B_y) \quad (5.34)$$

$$A_y = \sqrt{1 + t_x^2 + t_y^2} \cdot (-t_x \cdot (t_y B_y + B_z) + (1 + t_y^2) B_x) , \quad (5.35)$$

and with c the velocity of light. The changes in position are proportional to the slopes. The change of the slopes depends on the momentum, the local magnetic field and the slopes itself. Note that because the particle is assumed to move in the vacuum the absolute value of the momentum, and hence the fifth track parameter, does not change.

Because the equation of motion in an inhomogeneous magnetic field can not be solved analytically, a procedure based on a Runge-Kutta interpolation method[97] is used to solve the set of equations $\frac{d\mathbf{x}}{dz} = \mathbf{g}(\mathbf{x})$ numerically. Contrary to other numerical methods to solve a differential equation Runge-Kutta methods do not require differentiations of \mathbf{g} .

Runga-Kutta methods of different order exist. The fourth order Runga-Kutta method is most often used⁵. A fourth order Runga-Kutta method provides a precision that is proportional to the step size to the fifth power. In case the extrapolation distance dz is too large to obtain the required precision the step size can be divided into smaller intervals.

The LHCb parameter propagation is based on code developed for the Hera-B experiment[98]. It uses a fifth order Runga-Kutta method to perform the propagation. This code uses “adaptive step size control” meaning that the step size is automatically adjusted to obtain a given numerical precision. The precision is estimated by performing as well a fourth order Runga-Kutta propagation. The difference between the fifth and fourth order solutions is an estimate of the precision.

The Kalman filter fit requires the linearised propagation matrix F in order to propagate the covariance matrix (see equation 5.6). The matrix is defined by $F_k = \frac{\partial f_k}{\partial \tilde{x}_k}$. It is obtained by numerical differentiation of \tilde{x}_k^{k-1} as function of \tilde{x}_{k-1} , i.e. by numerically determining the change in predicted track parameters for small changes in the starting parameters.

5.2.4 Multiple scattering and energy loss

As mentioned in the previous section, the LHCb detector description used in the track reconstruction is approximated by material walls with a material thickness equivalent to the detector components. In propagating the track through the detector the track parameters and covariance matrix are modified to take into account multiple scattering and energy loss at these material walls.

Multiple scattering is a random process with an average scattering angle of zero. This means that the track parameters remain unchanged. The covariance matrix, however, is increased. In the Kalman filter procedure multiple scattering is incorporated by the system noise term Q_k in equation 5.6.

Multiple scattering is a non-Gaussian effect. The Kalman fit, however, assumes Gaussian errors. As seen from equation 5.1 the cross-section for small angles is large. If the small probability of large angle scattering is neglected and if the number of nuclei encountered is large ($N > 20$) the resulting angle of the multiple scattering follows roughly a Gaussian distribution. It can be shown that the variance of the multiple scattering in a layer of thickness x is then given by[86]:

$$\delta\theta^2 = \left(\frac{13.6}{p}\right)^2 \frac{x}{X_0} \left(1 + 0.038 \ln \frac{x}{X_0}\right)^2 , \quad (5.36)$$

with p the momentum in MeV/c and X_0 the radiation length. To correct for the non-Gaussian tails in the track fit equation 5.36 is corrected by the factor f_{MS}^2 , i.e.

$$\delta\theta^2 = \left(\frac{13.6}{p}\right)^2 \frac{x}{X_0} \left(1 + 0.038 \ln \frac{x}{X_0}\right)^2 \cdot f_{\text{MS}}^2 . \quad (5.37)$$

⁵Geant uses a fourth order Runga-Kutta method to propagate particles through the detector.

The factor is tuned such that the pull distributions of the fitted track parameters have a σ close to one (see section 5.3.2).

Due to the energy loss the momentum of a track is lower on the downstream side of the spectrometer than at the track vertex. In the track reconstruction the average energy loss due to ionisation (see equation 5.2) is approximated by:

$$\left(\frac{dE}{dx} \right)_{ion} = c_{ion}/X_0 , \quad (5.38)$$

where c_{ion} is an average energy loss factor for all detector materials of about 50 MeV. Contrary to the scattering angle, the average energy loss is predictive and hence the track parameter κ is corrected accordingly. The effect on the covariance matrix can be neglected. The tuning of parameter the c_{ion} is also described in section 5.3.2.

For electrons and positrons above a few tens of MeV the energy loss is dominated by Bremsstrahlung. As this is a highly non-Gaussian effect it is difficult to correct for. In the track fit an average correction

$$\left(\frac{dE}{dx} \right)_{rad} = E/X_0 , \quad (5.39)$$

can be switched on[99].

5.2.5 Kalman smoother

After applying the Kalman Filter to all measurements the full information of the particle trajectory is available at the position of the last measurement. The track parameters at previous measurements contain only the information of the measurements up to that point. To get the full information at all measurement positions (e.g. to get the best estimate of the track slopes in the RICH detectors) the information at the last measurement is passed “backwards” to the other measurement positions. The smoothed track parameters are obtained with the *smoother equations*

$$\tilde{\mathbf{x}}_k^n = \tilde{\mathbf{x}}_k + A_k(\tilde{\mathbf{x}}_{k+1}^n - \tilde{\mathbf{x}}_{k+1}^k) , \quad (5.40)$$

with covariance matrix

$$C_k^n = C_k + A_k(C_{k+1}^n - C_{k+1}^k)A_k^T , \quad (5.41)$$

and the smoother gain matrix A_k given by:

$$A_k = C_k F_{k+1}^T (C_{k+1}^k)^{-1} . \quad (5.42)$$

The index n indicates that the smoothed parameters $\tilde{\mathbf{x}}_k^n$ are obtained for a fit containing n measurements.

The smoothed track parameters are especially useful to reject measurements that were incorrectly added to the track during pattern recognition. The smoothed residual of the track parameters w.r.t. a measurement are given by:

$$r_k^n = m_k - H_k \tilde{\mathbf{x}}_k^n , \quad (5.43)$$

with variance

$$R_k^n = R_k - H_k A_k (C_{k+1}^n - C_{k+1}^k) A_k^T H_K^T \quad . \quad (5.44)$$

In case the χ^2 contribution of a measurement is too large it can be removed from the track.

5.3 Track fitting performance

This section reports on the performance of the track fit. As the assignment of the measurements to the track, i.e. the pattern recognition, is assumed perfect, the results on reconstructed track parameter precisions should be considered as the best that can be achieved for the given setup.

Due to the presence of the detector material a large amount of low momentum secondary particles are produced in an event. These particles are usually not directly relevant for the reconstruction of the B decay. Therefore, the following track selection criteria are applied:

- track momentum must be larger than 3 GeV/c,
- the first hit must lie at a position before $z = 1.0$ m,
- the last hit must lie at a position after $z = 9.2$ m.

These criteria select only those tracks that originate from the vertex region and cross the full tracking system of the spectrometer. Tracks satisfying these selection criteria are called *physics tracks*. Furthermore, electrons and positrons at this stage are discarded from the sample. Because of the highly non-Gaussian energy loss processes they require a special track fit approach.

In section 5.3.1 the resolution and pull distributions of the reconstructed track parameters are presented. These results are obtained after tuning various fit model parameters. In section 5.3.2 the tuning of these parameters is discussed. In section 5.3.3 the momentum dependence of the resolutions of the track parameters is discussed.

5.3.1 Resolution and pulls

A measure of the reliability of the fit are the pull distributions of the fitted track parameters. The pull distributions of the track parameters (x, y, t_x, t_y, κ) at the z -position of the track creation vertex are given in figure 5.9. The reconstructed track parameters and covariance matrix at the vertex where the track originates are obtained by propagating the track parameters at the measurement position that is closest to the z -position of the vertex, taking into account the remaining material traversed.

All pulls are centred at zero indicating that there is no systematic shift in the reconstructed track parameter values. Furthermore, the distributions show a Gaussian shape with a tail. This tail is caused by the various non-Gaussian contributions to the fit (see section 5.3.2). The pulls of the coordinate parameters are fitted with a Gaussian. The $1/p$ pull (bottom plot) is fitted with a double Gaussian to take into account the

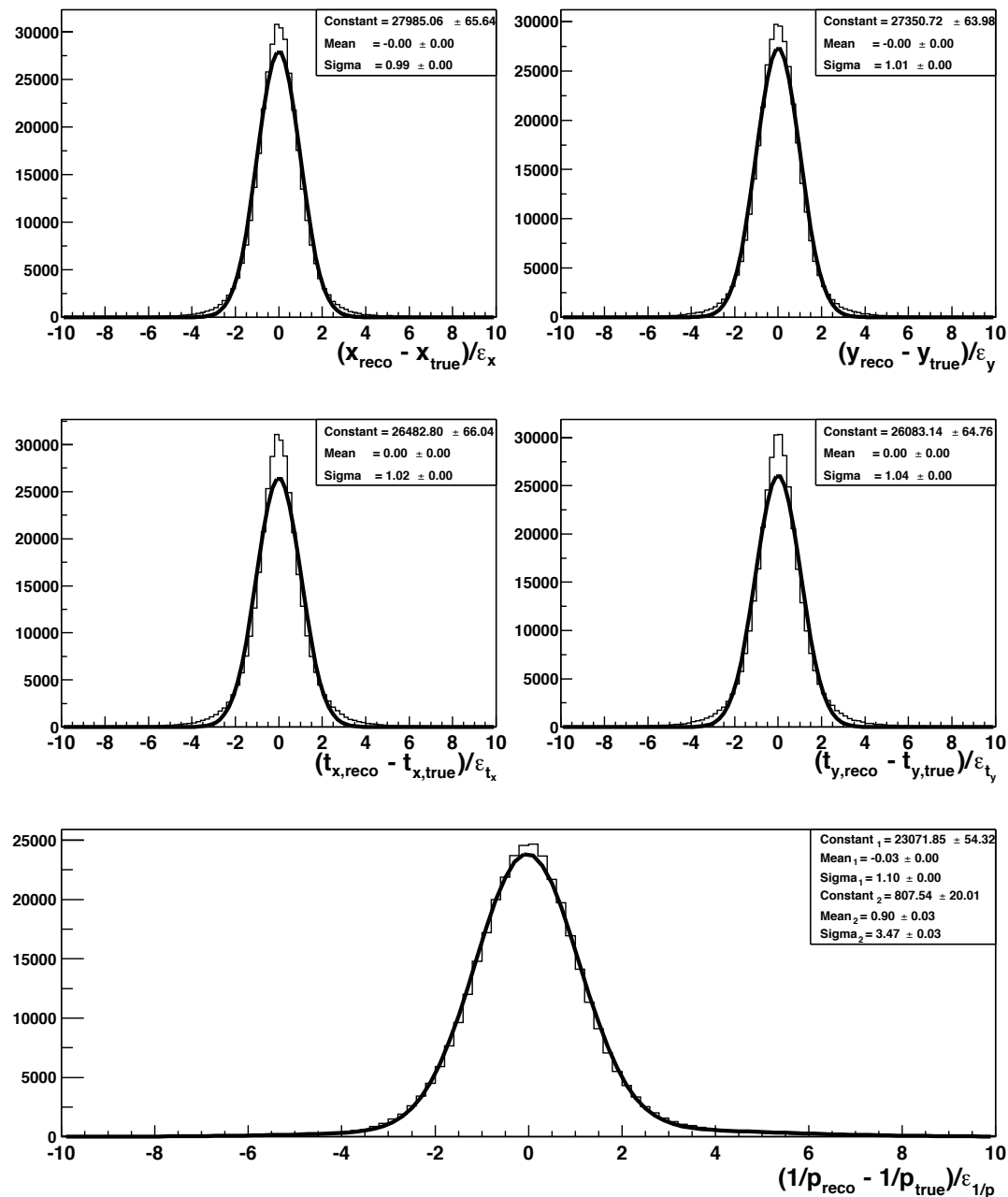


Figure 5.9: Pull distributions of the track parameters at the z -position of the track creation vertex.

parameter	pull	resolution
x	0.99	$27\mu\text{m}$
y	1.01	$28\mu\text{m}$
t_x	1.02	1.8×10^{-4}
t_y	1.04	1.8×10^{-4}
$1/p$	1.10	4.0×10^{-3}

Table 5.1: Pull and resolution value of fitted track parameter distributions at the track generation vertex position. The $1/p$ resolution is defined as $\frac{\delta(1/p)}{1/p}$.

non-Gaussian effects. In table 5.1 the fitted sigma of the (central) Gaussian is shown. The pulls are all within 10 % of one, indicating the errors on the fitted track parameters are understood within 10 %.

The residual distributions on the track parameters at their origin are shown in figure 5.10. The distributions are again centred at zero. They have the shape of a Gaussian with long tails. The curves shown are a double Gaussian fit through the distributions. Taking the σ of the central Gaussian as the resolution the results summarised in table 5.1 are obtained. Note that because $\frac{\delta(1/p)}{1/p} = \frac{\delta p}{p}$ the resolution on κ (bottom plot in figure 5.10) as well represents the momentum resolution. An average momentum resolution ($\delta p/p$) of 0.40 % is obtained. In section 5.3.3 the momentum dependence of the resolutions of the track parameters is discussed.

parameter	RICH 1	RICH 2
x	$73\mu\text{m}$	$66\mu\text{m}$
y	$452\mu\text{m}$	$245\mu\text{m}$
t_x	2.3×10^{-4}	2.8×10^{-4}
t_y	2.5×10^{-4}	2.7×10^{-4}

Table 5.2: Resolution of directions and positions at the RICH detectors as obtained from the track fit.

In a similar manner the resolution on the slopes and the positions is determined at the RICH detectors. In table 5.2 the obtained resolutions are shown. For RICH-1 the resolutions at the upstream edge of station 2 are given. For RICH-2 the resolutions at the downstream edge of station 9 are given.

5.3.2 Tuning the fit

In the track fit several approximations are made. An important one is mentioned in section 5.2.3, i.e. the simplified material description used in the fit to prevent the time consuming lookup of the material crossed by a particle. Another approximation is the assumption that all errors are Gaussian distributed. As shown in section 5.2.2 this is not the case for some of the measurements. Also multiple scattering has non-Gaussian tails (section 5.2.4). From the *central limit theorem* it can be expected that if the number

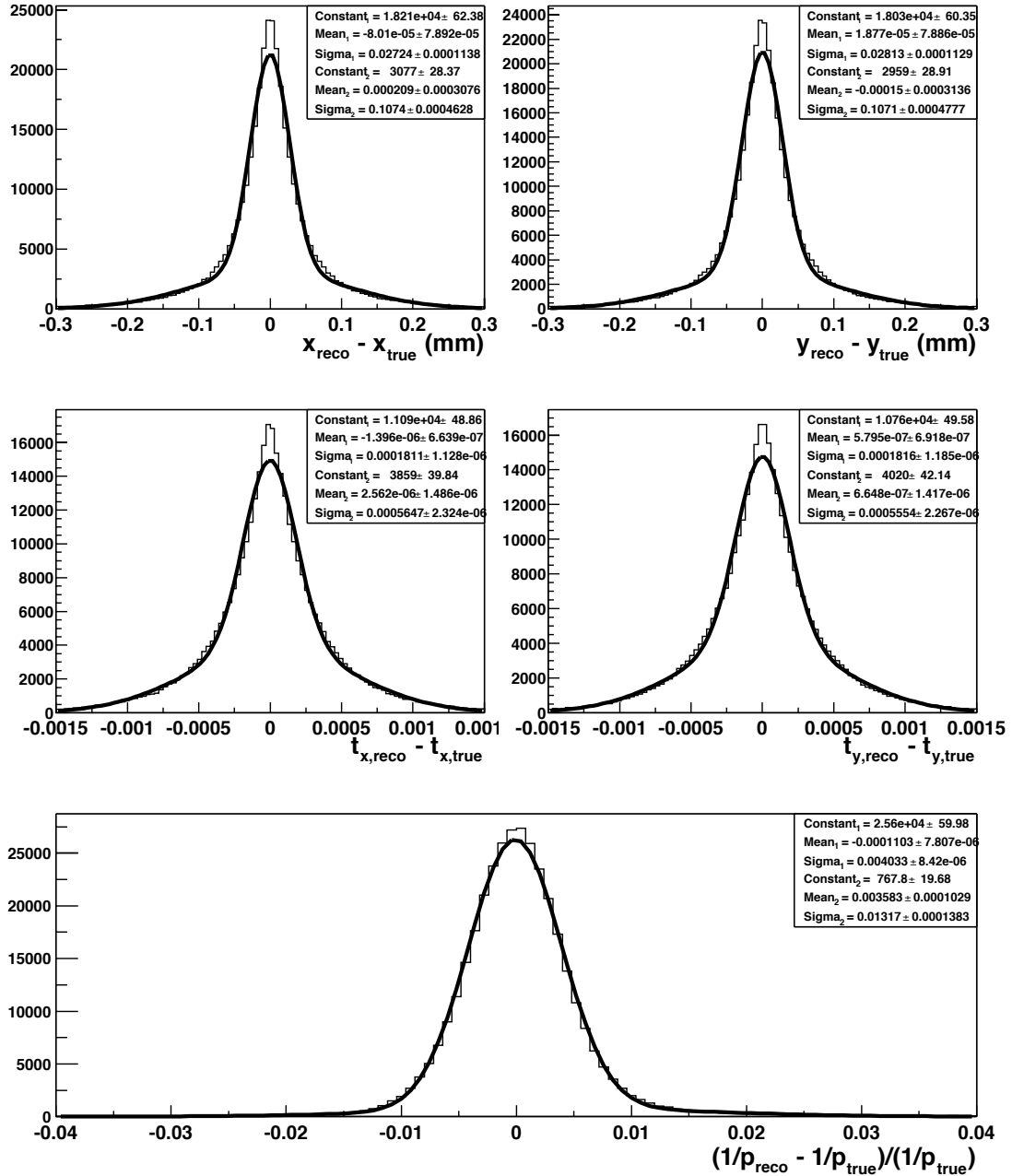


Figure 5.10: Resolution distributions of the track parameters at the z -position of the track creation vertex.

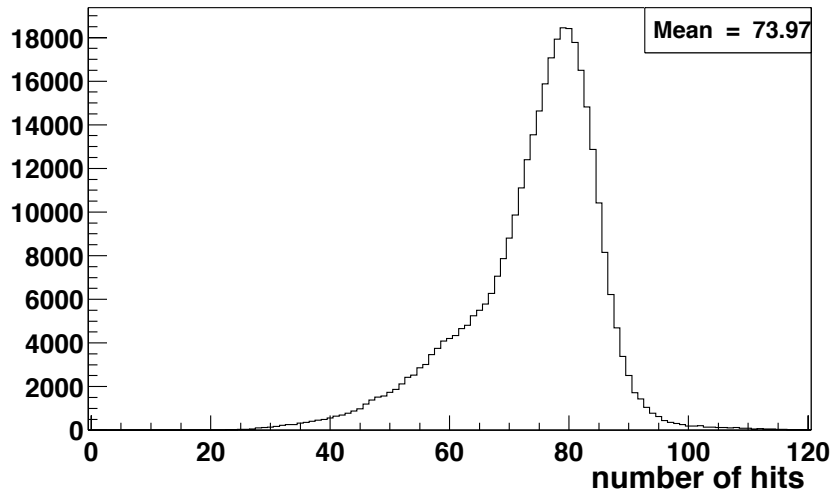


Figure 5.11: Distribution of the total number of hits per track.

f_{MS}	x	y	t_x	t_y	$1/p$
1.2	1.10	1.08	1.15	1.16	1.30
1.3	1.05	1.04	1.09	1.09	1.20
1.4	0.99	1.01	1.02	1.04	1.10
1.5	0.96	0.95	0.98	0.98	1.06

Table 5.3: Pull values at the track creation vertex of the fitted track parameters for 5 GeV/c particles for various values of f_{MS} .

of measurements and material walls is large the fitted track parameters will, at least approximately, be Gaussian distributed. In figure 5.11 it is shown that the average number of hits on a track is indeed large (74).

This section describes the tuning of the parameters f_{MS} and c_{ion} in equations 5.37 and 5.38 to obtain proper pull distributions and a good fit. The results presented in the previous and next section are obtained with the tuned parameters.

The average energy loss factor c_{ion} is tuned by requiring the $1/p$ pull distribution to be centred at zero. In case the energy loss factor is too large the pull is shifted towards negative values, and inversely if it is too small a shift to positive values is obtained. The pull is found to be best centred for $c_{ion} = 40$ MeV, i.e. an average energy loss of 40 MeV/ X_0 in the radiation walls.

The factor f_{MS} is used to correct for the non-Gaussian effects in multiple scattering. In table 5.3 the standard deviation of the fitted Gaussians to the pull distributions of the track parameters⁶ at their origin is given for various values of f_{MS} . For $f_{MS} = 1.4$ all pull distributions are close to one. This value is used in further studies.

⁶The $1/p$ pull is fitted with a double Gaussian.

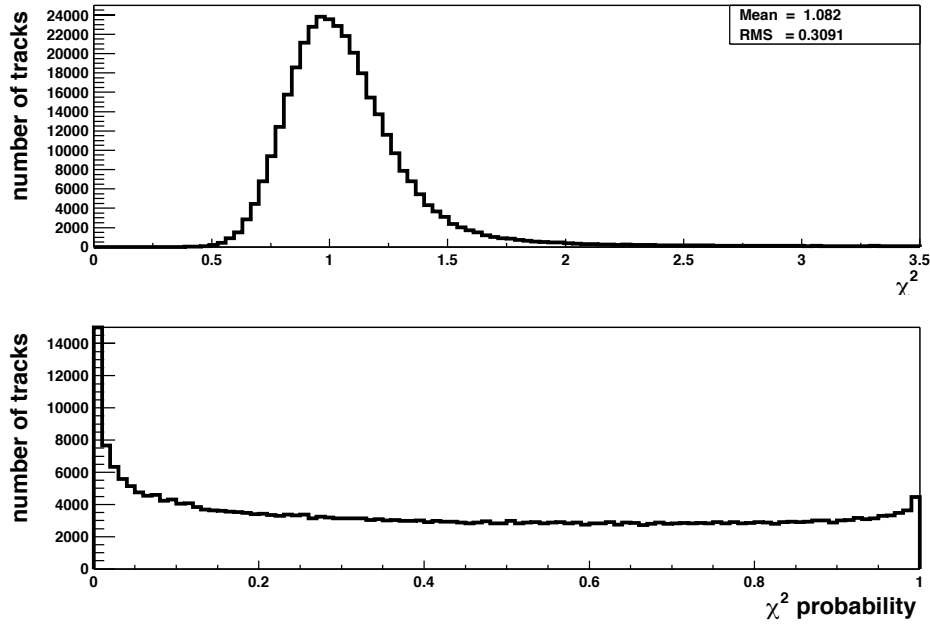


Figure 5.12: Top) The reduced χ^2 distribution in the track fit. Bottom) The distribution of the χ^2 -probability $P(\chi^2 > S)$ in the track fit.

The fit of a trajectory through the measurements (and material) will yield a *total* χ^2 . If all errors would be Gaussian distributed the distribution of *reduced* χ^2 values, i.e. the total χ^2 divided by the number of degrees of freedom, will follow the χ^2 distribution and have an average value of one. The top plot in figure 5.12 shows the reduced χ^2 distribution. As shown the average value is indeed close to one, indicating a good fit.

A better test of the goodness of a fit is the χ^2 probability distribution. The bottom plot in figure 5.12 shows the distribution for the track fit. When the errors are correctly taken into account this distribution is flat. This is the case apart from deviations for small probability values and a peak at zero probability corresponding to large χ^2 values due to some bad fits. These tracks correspond to the tails in the pull distributions, e.g. a particle that experienced a large angle scattering in the material.

5.3.3 Momentum dependence

In table 5.1 the average momentum resolution $\delta p/p$ for reconstructed tracks with $P > 3 \text{ GeV}/c$ is shown to be 0.40 %. It can be shown[96] that there are two main contributions to the momentum resolution:

- The error due to the position measurement is proportional to p , i.e. $\delta p/p \sim p$.
- The error due to multiple scattering is given by $\delta p/p \sim 1/\beta$, which for relativistic particles is almost constant.

The bottom plot in figure 5.13 shows the average momentum resolution as a function of momentum. The resolution is worse for high momentum tracks. This is because the

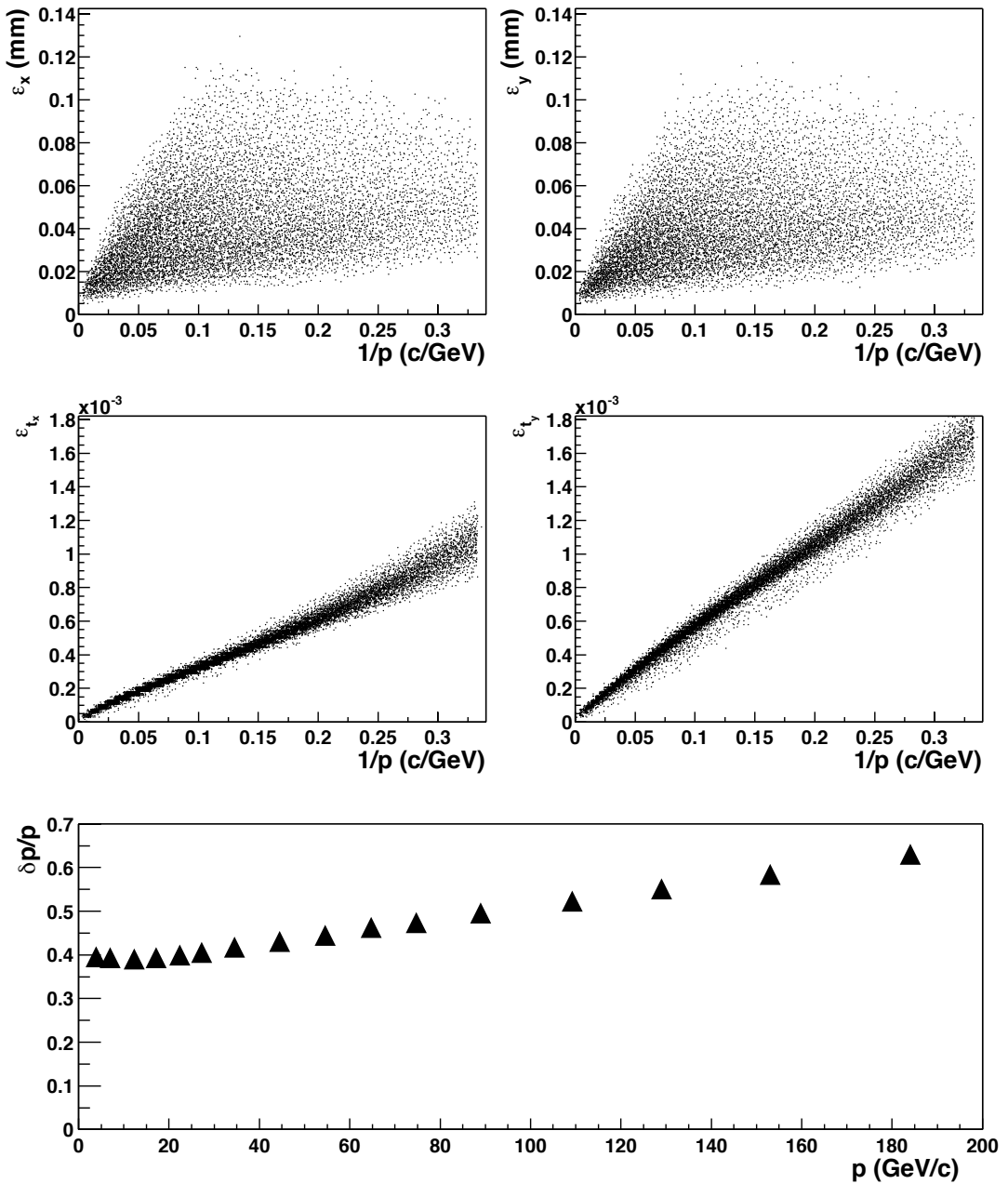


Figure 5.13: Track parameter resolutions as a function of the momentum. The top plots show error distributions of the calculated position at the track vertex, as a function of $1/p$. The middle plots show error distributions of the calculated slope at the downstream edge of station 9, as a function of $1/p$. The bottom plot shows the average momentum resolution as a function of p .

error on the position measurements start to play a dominant role.

As each particle travels a different path it will encounter different amounts of material. Also, the trajectory will be measured by detectors with different coordinate resolution, i.e. inner or outer tracker. Therefore, the average momentum resolution can not easily be understood by one single relation combining the above mentioned contributions.

Because the multiple scattering angle has a $1/p$ dependency (see equation 5.36) the resolution on the track direction is expected to have a similar behaviour. The middle plots of figure 5.13 show the error distribution for the track slopes t_x and t_y at the downstream edge of station 9, as a function of $1/p$. Because the pull distribution of the track slopes are Gaussian with a standard deviation close to unity, the calculated error can be interpreted as the resolution. The figure shows the track slope resolution indeed to roughly have a $1/p$ dependence.

The top plots in figure 5.13 show the error distribution for the track positions x and y at the track origins, as a function of $1/p$. The plots show the position errors also to depend on the momentum. The distributions show that the spread in calculated error on the position for a given momentum is larger than that for the slopes. This is because the resolution on the position depends on the distance between the track creation vertex and the first measurement.

5.4 Conclusions

In this chapter the LHCb track fitting procedure is presented. It is based on the Kalman filter formalism. The following features are included in the fit:

- Four different types of measurements; the outer tracker hits, inner tracker clusters, VELO R clusters and VELO ϕ clusters.
- The energy loss of particles due to detector material.
- The random perturbations on the trajectory due to multiple scattering are locally taken into account. This results in a reconstructed track that follows the true trajectory as close as possible, including the reconstruction of actual *kinks* in the trajectory.
- The presence of an inhomogeneous magnetic field resulting in a complicated track model is taken into account by using a step-wise 5th order Runga-Kutta method for propagating the track parameters.
- The particle trajectory is parameterised by the track parameters $\mathbf{x} = (x, y, t_x, t_y, \kappa)$. The Kalman filter technique allows determining the best estimate of these parameters at all positions along the trajectory. Typical positions are the track vertex (for the reconstruction and analysis of the underlying physics event) and the two RICH detectors (to be able to perform the RICH pattern recognition algorithms).

Results are presented for tracks originating from the vertex region and crossing the full tracking system of the spectrometer. The obtained pull distributions of the track

parameters are shown to be correctly centred at zero. Furthermore, all pulls are within 10 % of unity. This shows that the errors on the track parameters are well understood.

At the track vertex an average position resolution of $\sim 27 \mu\text{m}$ is obtained. The average error on the slopes at the vertex is $\sim 1.8 \times 10^{-4} = 0.18 \text{ mrad}$. At the RICH detectors the error on the slopes is $\sim 0.27 \text{ mrad}$. An average momentum resolution of 0.40 % is obtained. For low momentum tracks this resolution is dominated by multiple scattering. For large momenta the resolution of the measurement devices plays a more important role.

Chapter 6

Pattern recognition

In the description of the track fitting procedure in chapter 5 it is assumed that the association of the detector measurements to the tracks is known. Starting from the set of all measurements provided by the tracking detectors, it is a pattern recognition problem to group these measurements according to individual particle trajectories. This chapter describes pattern recognition algorithms for track reconstruction in the LHCb tracking detectors.

The algorithms are in the first place developed to perform detector optimisation studies and to study the tracking and physics performance of the LHCb detector. Subsequently, they are used as a reference and benchmark for future algorithms.

Section 6.1 gives an overview of the particle fluxes in the LHCb experiment resulting from pp -collisions at a luminosity of $2 \times 10^{32} \text{cm}^{-2}\text{s}^{-1}$ as described in chapters 1 and 2. Section 6.1 also describes the resulting detector occupancies. These numbers set the scale of the pattern recognition problem.

The LHCb detector surface gets larger with increasing z (see figure 2.3), reflected in the fact that the particle flux decreases as a function of z , i.e. moving downstream from the interaction region. In the region before RICH-2 the magnetic field is relatively weak. These conditions make it the most suitable region to start finding tracks. The tracking stations T6-T9 are placed in this region for this purpose. From the track candidates found in these stations a momentum estimate at the percent level is obtained by assuming that the particle originated from the vertex region. The other tracking stations are positioned in such a way that the particle trajectory is measured at enough places to efficiently follow the track from the seeding region all the way to the vertex detector.

The above-mentioned procedure is referred to as “upstream” pattern recognition. An alternative approach is to find the tracks in the vertex detector and follow them downstream. However, since in this case no initial momentum information is available it is hard to propagate these tracks through the magnet. In this thesis “upstream” pattern recognition is studied.

The pattern recognition procedure is split into two sub-tasks, *track seeding* and *track following* (see figure 6.1). The task of track seeding is to find track segments in stations T6-T9. Section 6.2 describes a track seeding algorithm. The task of track following is to follow these tracks towards the vertex region by searching in the tracking stations

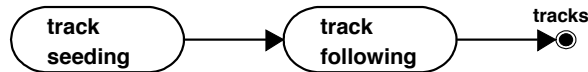


Figure 6.1: Flow diagram of total pattern recognition procedure.

T1-T5 for the measurements corresponding to these tracks. Section 6.3 describes a track following algorithm. Section 6.4 presents the performance of these algorithms.

6.1 Particle rates and detector occupancies

In section 1.5 the expected multiplicities for charged primary particles are presented for single interactions. Figure 1.10 shows that the average number of expected primaries within the LHCb acceptance for a $b\bar{b}$ -production process is 34. The interaction of these primaries with the material of the LHCb detector creates many secondary particles. The total number of particles seen by the detector is therefore significantly larger than the number of primaries.

Figure 6.2 shows the position of the origin of all primary and secondary particles in a sample of 500 $B \rightarrow \pi^+\pi^-$ events. The figure shows a “silhouette” of the position of the material in the detector. Only about 30 % of the particles originate from the primary interaction vertex region. The bottom figure zooms in on the region close to the z-axis. Clearly visible is the conical structure of the beam-pipe. About 30 % of the particles in an average event are created in the beam-pipe material.

Both the number of primaries in the event as well as the number of secondaries generated per primary particle follow statistical distributions with large fluctuations. Therefore, one expects low as well as high track multiplicity events. Figure 6.3 shows the event display of two simulated $B \rightarrow \pi^+\pi^-$ events, one with a low (top plot) and one with a high (bottom plot) track multiplicity. Most tracks are produced in the forward (small angle) direction. Some low momentum particles (mainly electrons) spiral in the magnetic field. All these tracks can create hits in the detectors.

A read-out event is defined as all the data collected in a time window (read-out gate) relative to the bunch-crossing time. For all sub-detectors, except the outer tracker, a time window corresponding to the bunch-crossing interval of 25 ns is used. For the outer tracker a read out gate of 50 ns is used because the signal collection time can exceed the bunch-crossing interval. In addition to the hits generated by a given (B) interaction, there are two types of “background” hits present in a read-out event:

- The first source of background is due to **pile-up** events. As shown in figure 2.2 there is a significant probability for a multiple of pp -interactions to occur in a

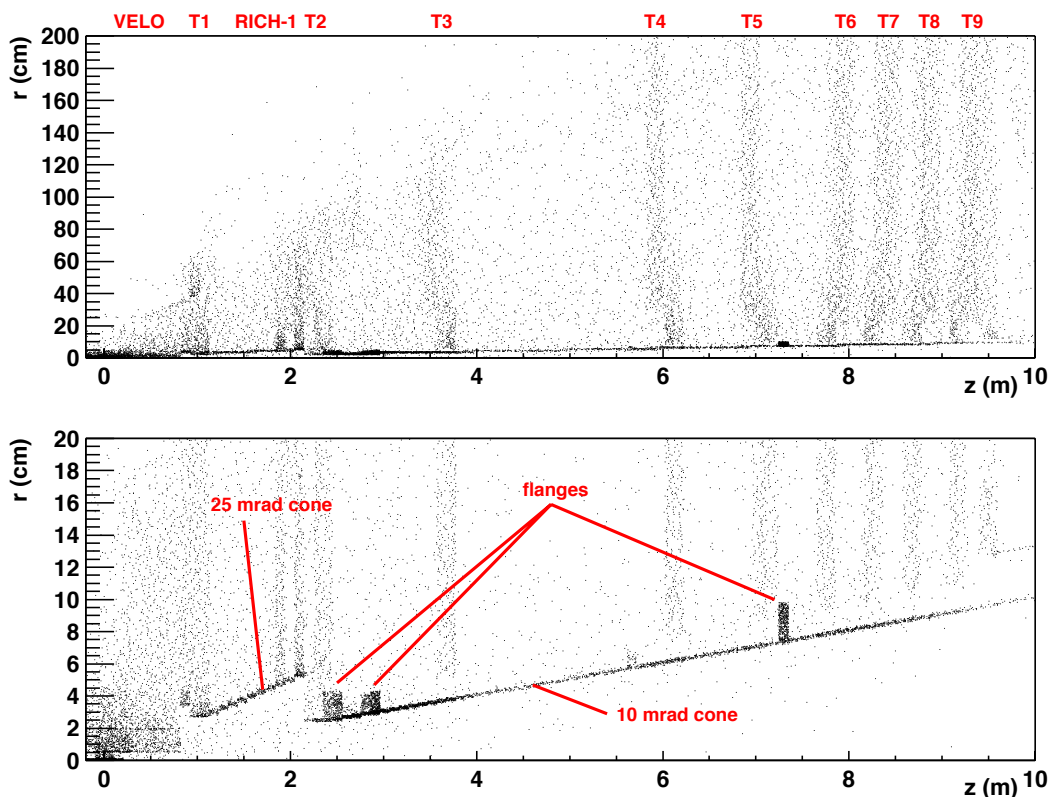


Figure 6.2: Position of the origin of all primary and secondary particles in 500 $B_d \rightarrow \pi^+\pi^-$ events. The top figure shows the vertices for all particles from the VELO up to RICH-2. The bottom figure zooms in on the region close to the beam-pipe. The labels indicate the position of LHCb detector components and the beam-pipe.

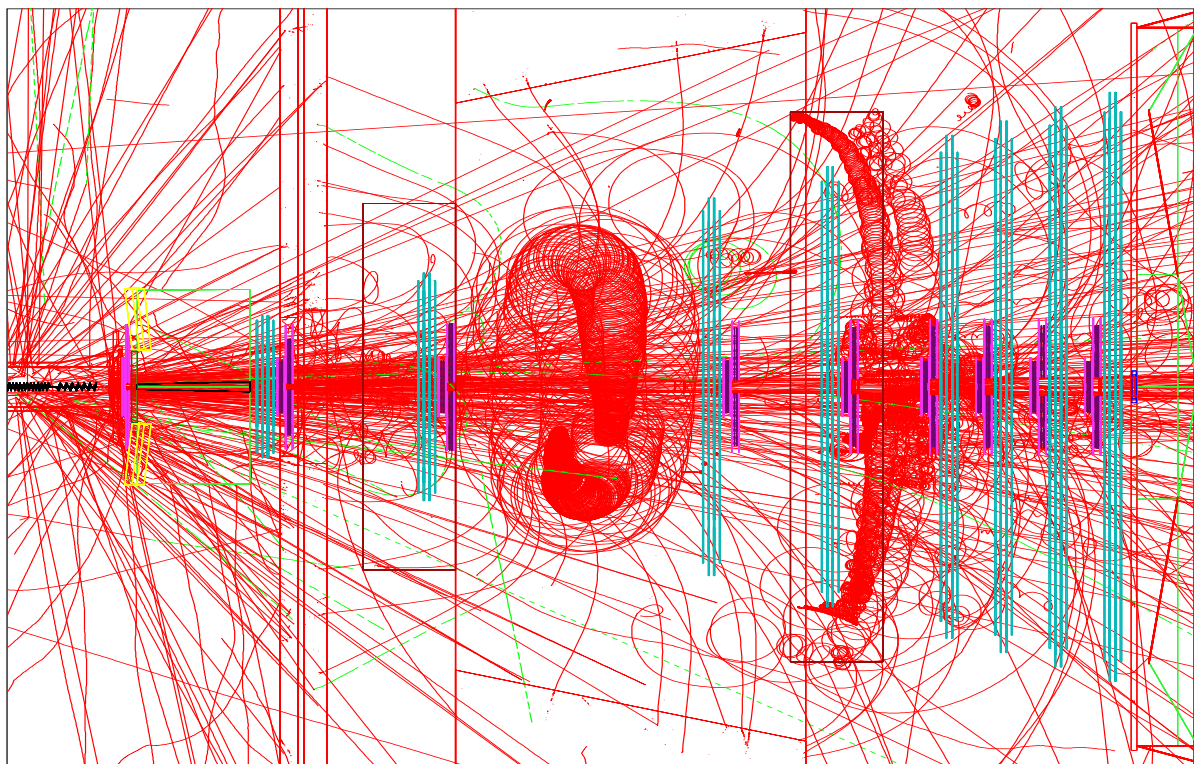
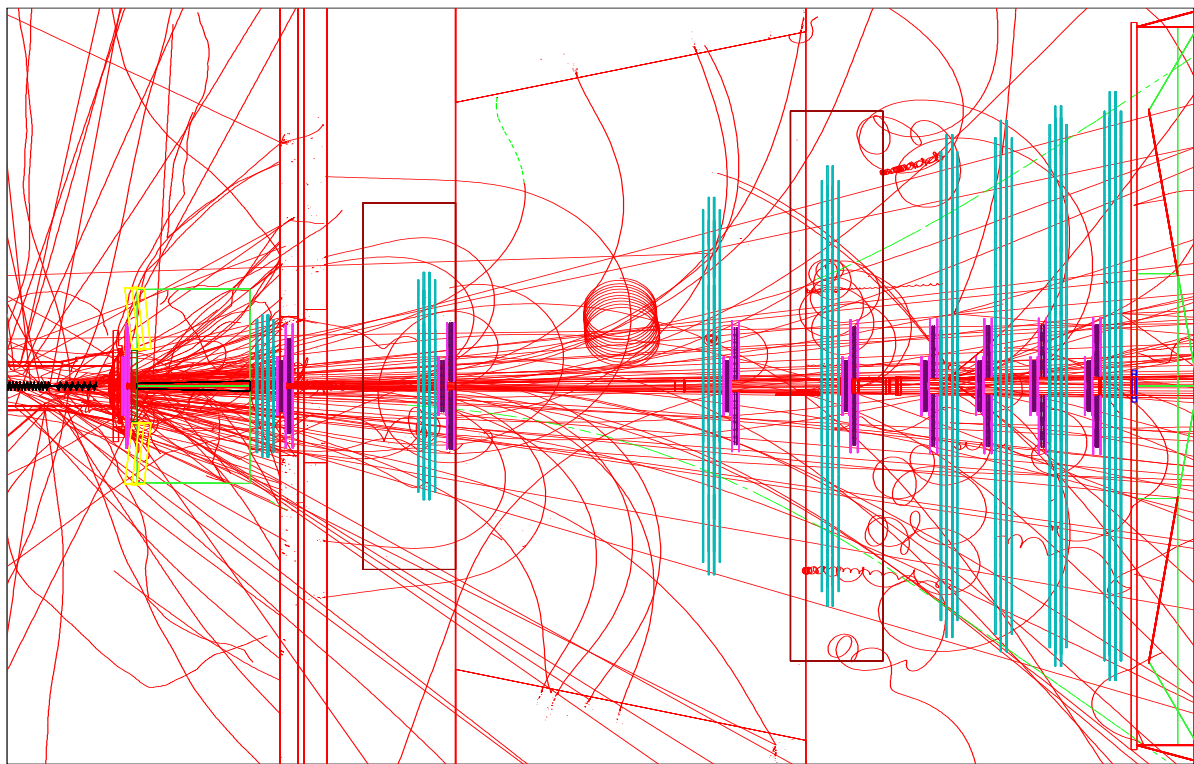


Figure 6.3: Event displays of two simulated $B \rightarrow \pi^+\pi^-$ events. Top) event with low track multiplicity. Bottom) event with high track multiplicity.

single bunch-bunch collision ($10\%^1$ at the nominal luminosity $2 \times 10^{32} \text{cm}^{-2}\text{s}^{-1}$). All interactions will create particles and hence signals in the detectors. Effectively a multiple of events is overlayed.

- The second source of background is due to the **spill-over** from previous bunch-crossings. There are two types of spill over data:
 - As shown in figure 6.3 some low momentum particles spiral in the magnet. The time they spend within the acceptance of the LHCb spectrometer can reach hundreds of nanoseconds. Consequently, the event data can contain hits caused by particles originating from much earlier bunch-crossings. The effect is large in the magnet stations (up to 19 % in T3) and small in the seeding stations (< 4 %)[100].
 - The outer tracker read-out gate corresponds to two bunch-crossings. Hits from a previous bunch-bunch collision with drift times larger than ~ 25 ns will be observed within this time window. Hits from a succeeding bunch-bunch collision with drift times below 25 ns will also be in the time window. Consequently, an event can contain outer tracker hits due to both neighbouring bunch-crossings. These hits will occur in the current read-out event with an apparent drift time offset of 25 ns compared to their true drift time.

The above background hits are taken into account in the simulation. If a detector channel is hit a second time within the (dead) time window only the first hit is used. Both pile-up and spill-over depend on the luminosity. The results reported in this chapter are obtained for the nominal ($2 \times 10^{32} \text{cm}^{-2}\text{s}^{-1}$) luminosity conditions.

An important quantity for the optimisation of the detector and for the pattern recognition performance is the detector *occupancy*. The occupancy is defined as the fraction of channels in a specified detector region that is hit in a read-out event.

The occupancy is defined by both the particle rate and the granularity of the detector. This is the reason why LHCb has chosen to use a high granularity technology for the hot regions close to the beam-pipe, i.e. the inner tracker, and a relatively large cell size for the more quiet outer tracker region. The exact boundary between the outer- and inner tracker results from a study[44] optimising for a low occupancy while keeping the silicon detector surface limited. The outer tracker occupancy was required to be smaller than 10 % for stations T6-T9 and smaller than about 15 % for stations T2-T5.

Figure 6.4 shows the average occupancy as a function of x in one of the outer tracker seeding stations (T7). Clearly visible is the decrease as a function of x due to the decrease in particle rate². The steps at $x = 255$ mm and $x = 596$ mm are due to the cross-shaped geometry of the inner tracker (see section 2.3.2 and figure 6.5). Figure 6.4 also shows that, considering only occupancy, a larger cell size (~ 10 mm) in the outer regions of the acceptance could be envisaged. However, the prototype measurements described in chapter 4) show that even 8 mm diameter drift cells result in a too large signal collection time. Drift tubes with a 6 mm diameter would satisfy the drift time

¹This corresponds to 25 % of the bunch-bunch crossings in which an interaction takes place.

²To first approximation the particle rate scales as $1/r^2$, where r is the distance to the beam axis.

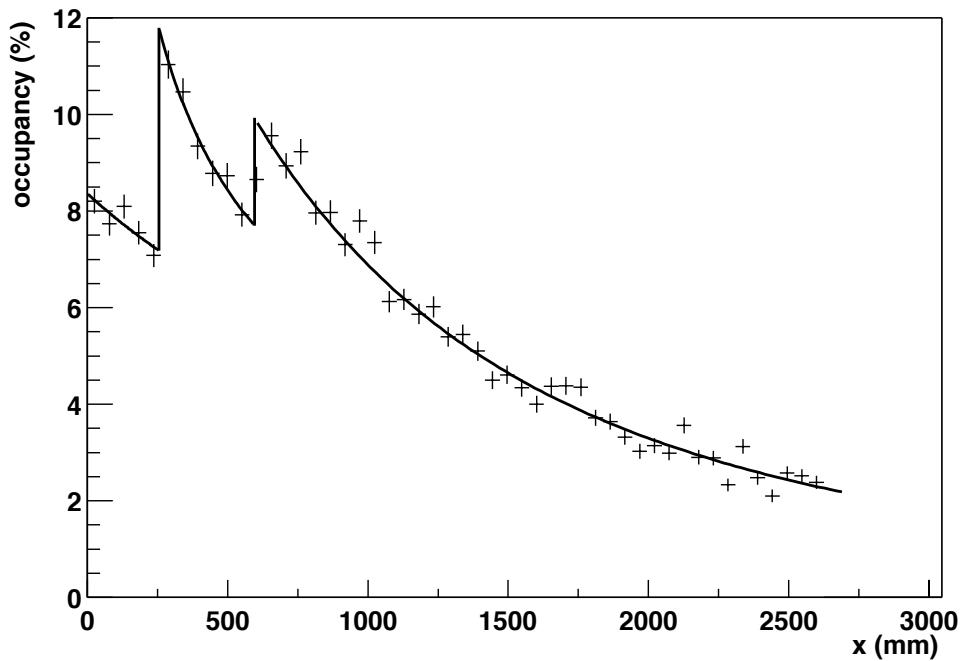


Figure 6.4: Average occupancy as a function of x -position in outer tracker station T7 for nominal luminosity.

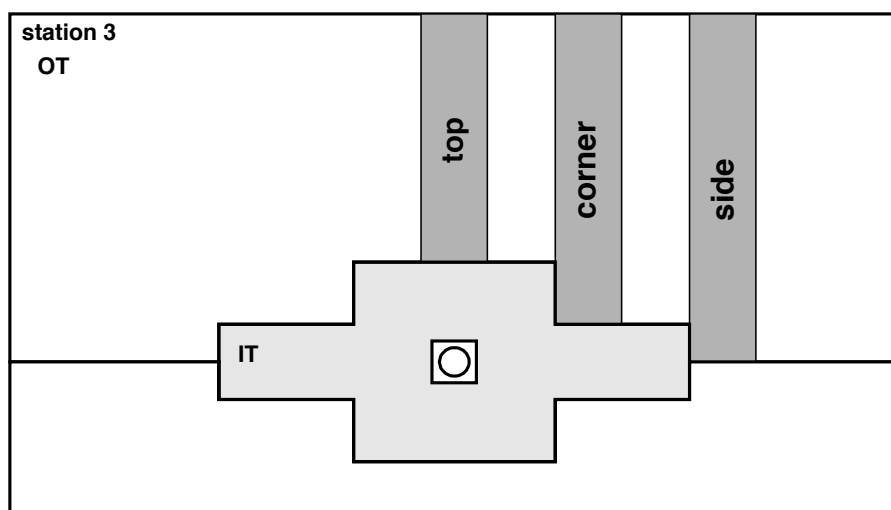


Figure 6.5: The “top”, “side” and “corner” areas of highest outer tracker occupancy.

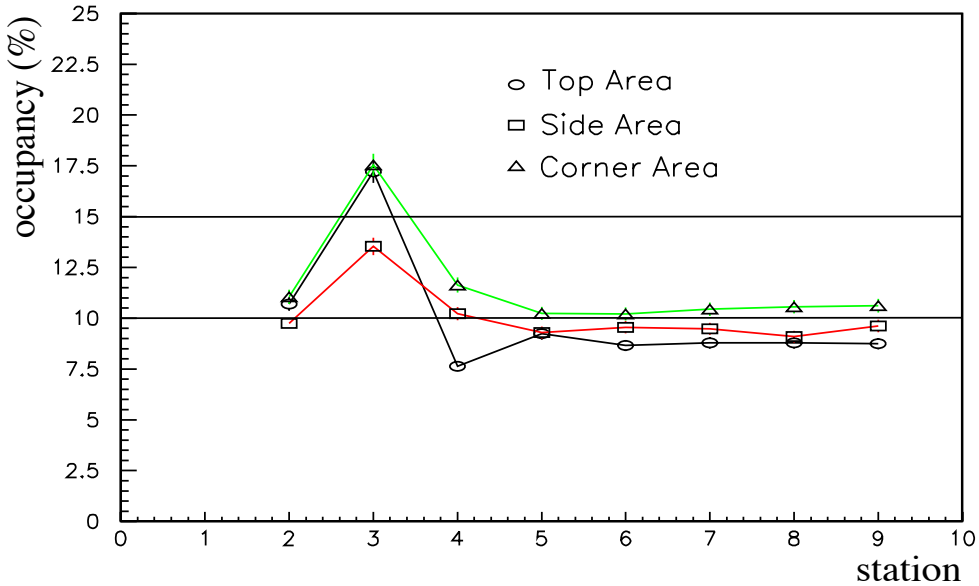


Figure 6.6: Occupancies in the hottest outer tracker areas for each station. The areas are: 1) *above and below* the inner tracker, 2) *aside* of the inner tracker, 3) in the *corner* of the cross.

requirement. However, the reduction in number of channels would not outweigh the implied increase in complexity to produce modules with different cell sizes. Therefore, a uniform cell size of 5 mm is used everywhere.

The inner tracker has a cross-shaped geometry because the particles are relatively more spread along the horizontal axis (see figure 2.11). Due to the cross geometry of the inner tracker each station has three different lengths of outer tracker straw tube modules. The areas indicated in figure 6.5, i.e. *top*, *corner* and *side* area, cover the regions with the highest outer tracker occupancy for these different modules. The exact shape of each inner tracker station is optimised by taking into account the occupancy requirement for each of these areas. Figure 6.6 shows the average occupancies for the areas as a function of the station number. It is seen that the average occupancies are within the requirement for all stations except T3.

The large event-by-event fluctuations in track multiplicities cause also large fluctuations in the occupancy. Figure 6.7 shows the outer tracker occupancy distribution on event basis for the region just above the inner tracker (top area in figure 6.5) in one of the magnet stations (T3). In this region the average occupancy is 17 %, where as an occupancy tail of up to 40 % is observed. Both the trigger electronics and the reconstruction algorithms have to be able to cope with these fluctuations.

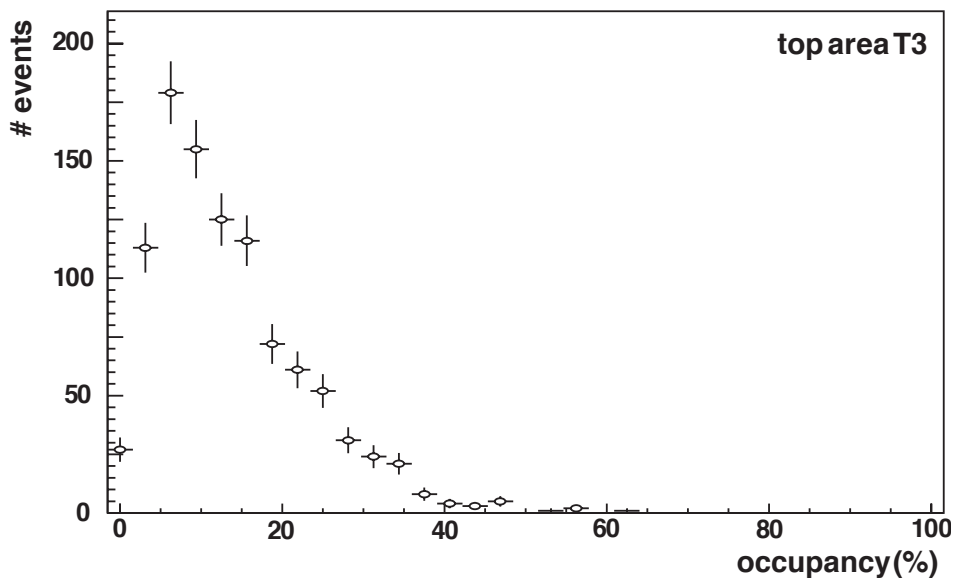


Figure 6.7: Outer tracker occupancy distribution on event-to-event basis in the region just above the inner tracker in station T3.

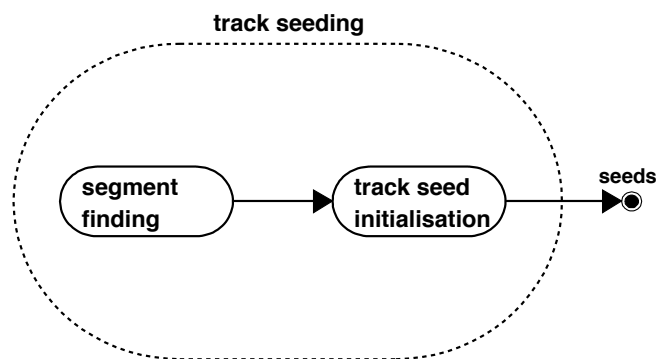


Figure 6.8: Flow diagram track seeding procedure.

6.2 Track seeding

The stations T6-T9 are used to find initial track seeds. To start the Kalman filtering procedure an initial track state, i.e. the track parameters at a certain reference plane is required for each track. The track seeding task is to determine these initial track states, i.e. the *track seeds*.

The current implementation of track seeding contains two components, track segment finding and track seed initialisation (see figure 6.8). In section 6.2.1 an algorithm is described that finds initial track segments in the seeding stations. These segments have information on track position and direction, but only limited information on the particle momentum. Section 6.2.2 describes how a better estimate of the track momentum is obtained. Furthermore, it describes the determination of the initial track seed parameters used in the track following algorithm.

6.2.1 Track segment finding

The track segment finding algorithm consists of three sequential steps. In the first step a search is made for local (i.e. within a station) track segments (so called “stubs”) in the (x, z) -projection. In the second step these stubs are linked together to form 2D-tracks spanning all the seeding stations. In the third step the information of the stereo angle layers is added by searching for straight lines in the (y, z) -projection³. Below a brief outline of these three steps in the algorithm are given. A more detailed description is given elsewhere [101].

2D stub search

In the *first step* of the algorithm track stubs within a station are formed. The search is performed in the (x, z) -projection. Because of the low magnetic field the particle trajectories within a station can be approximated by straight lines.

Pairs of hits are formed from the hits in all⁴ X -layers. The X -layers are located at the upstream and downstream side of each station. The X -measurements thus have a relatively large lever-arm to form a stub. The stub candidates with a slope larger than 1.0 rad are discarded. The remaining pairs are validated by using other hits. This is done differently for the inner and outer tracker:

- For the outer tracker an additional X -layer hit is required to be close (within 0.8 mm) to the line joining the hits of the pair. Because of the double-layer structure of the outer tracker such a hit is likely to exist⁵. In most cases this requirement resolves the left/right ambiguity. In case a hit is found it is added to the stub.

³Tracks are nearly straight lines in the (y, z) -projection as the B-field is predominantly vertically oriented.

⁴To reduce combinatorics the outer tracking stations are divided in an upper and lower part (sector). Only hits within the upper (lower) sector are combined. For the inner tracker layers a similar procedure is followed.

⁵A particle crossing an outer tracker station parallel to the z axis, i.e. $\theta = 0$, causes on average $4 \times 5/5.25 = 3.8$ X -layer hits.

- For the inner tracker no additional X -layer hits exist⁶. Instead the hits in the stereo angle layers U and V are used for validation. Every stereo angle hit is converted into a y -measurement using:

$$y = \frac{u}{\sin \alpha_s} - \frac{x}{\tan \alpha_s} \quad , \quad (6.1)$$

where u is the measured stereo coordinate and x the interpolated coordinate of the stub at the z -position of the stereo layer. The resulting y -coordinate is required to lie within the physical boundary of the inner tracker sector. An inner tracker stub is considered valid if a pair of hits from the U and V layers respectively are found with a resulting track-slope in the (y, z) projection less than 0.3 rad.

Typically a few hundred stubs are found per event[101].

Stub linking

In the *second step* 2D-track segments spanning the seeding stations are obtained by linking the stubs in individual stations together by applying the following procedure:

- Stubs are matched by comparing for every stub the parameters x and t_x with the stubs in the other stations. If the parameters match ($\Delta x < 0.4$ mm and $\Delta t_x < 30$ mrad in the outer tracker) the stubs are linked together forming chains of up to four stubs.
- For every chain a track segment is formed by fitting a parabola through the hits assigned to the stubs⁷.
- A search is made for hits close to the parabola that are not yet assigned to the track segment. If additional hits are found the segment is refitted.
- To avoid “double counting” hits are only allowed to be used by one (the “best”) segment. The selection of the best segment is based on the number of hits in the segment and the χ^2 (< 25) of the fit.

On average about 140 candidates are selected per event[101].

Stereo layer search

In the *third step* a 3D-track segment is made by adding the information of the stereo layer measurements. For every 2D-track segment a search is made for corresponding hits in the (y, z) projection by applying the following procedure:

- All stereo angle hits are converted into y measurements by using equation 6.1 and assuming it originated from the 2D- (x, z) -track segment.

⁶A particle crossing an inner tracker station parallel to the z axis produces only 2 X -layer hits.

⁷Note that still a small magnetic field is present in this region.

p	σ_x	σ_y	σ_{t_x}	σ_{t_y}
< 10 GeV/c	0.18 mm	1.8 mm	1.0×10^{-3}	2.2×10^{-3}
> 10 GeV/c	0.08 mm	0.8 mm	0.4×10^{-3}	0.9×10^{-3}

Table 6.1: Resolution on the track parameters of the reconstructed track seeds at the downstream edge of station T9 for two momenta ranges[101].

- In the (y, z) -plane a search is made for hits that lie on a straight line using an algorithm similar to the one used in the test-beam (see section 4.2.3).
- The best hit combination, i.e. the one with the most hits and lowest χ^2 , in the (y, z) -plane is selected. These stereo hits are added to the 2D-track segment forming a 3D-track.

The final result is a collection of track segments containing hits of both the vertical as well as stereo angle layers. In table 6.1 the obtained position and direction resolutions on the reconstructed track parameters at a reference plane⁸ in the seeding region are given. As can be seen the resolution for high momentum tracks is significantly better than for low momentum tracks. From the fitted parabola to the track segment hits in the (x, z) -plane a momentum resolution $\delta p/p \sim 20\%$ [101] is obtained. A better precision is obtained with the method described in the next section.

6.2.2 Track seed initialisation

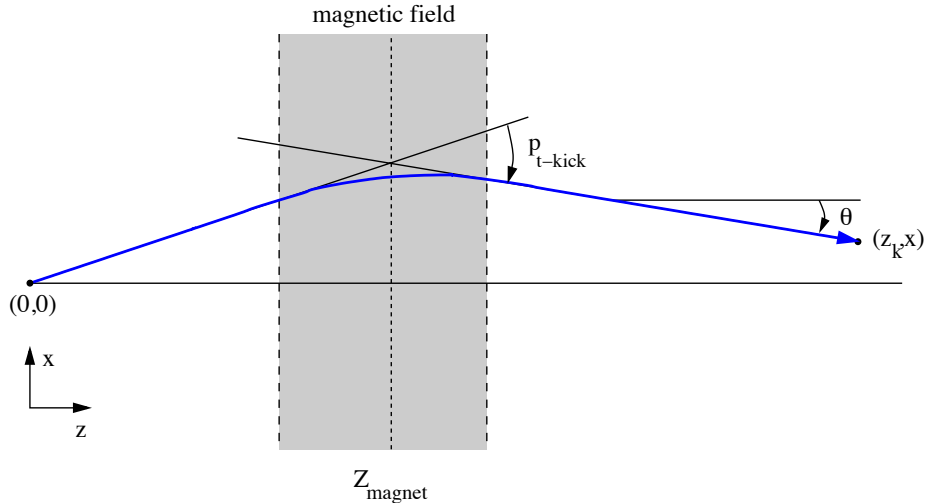


Figure 6.9: A particle experiences a so-called p_t -kick when traversing the magnet.

A momentum estimate can be obtained from a track vector, i.e. position and slope, in the seeding region by assuming the particle originated from the vertex position $(0, 0, 0)$.

⁸The (x, y) plane at z position of the last layer in station T9 is used as reference plane.

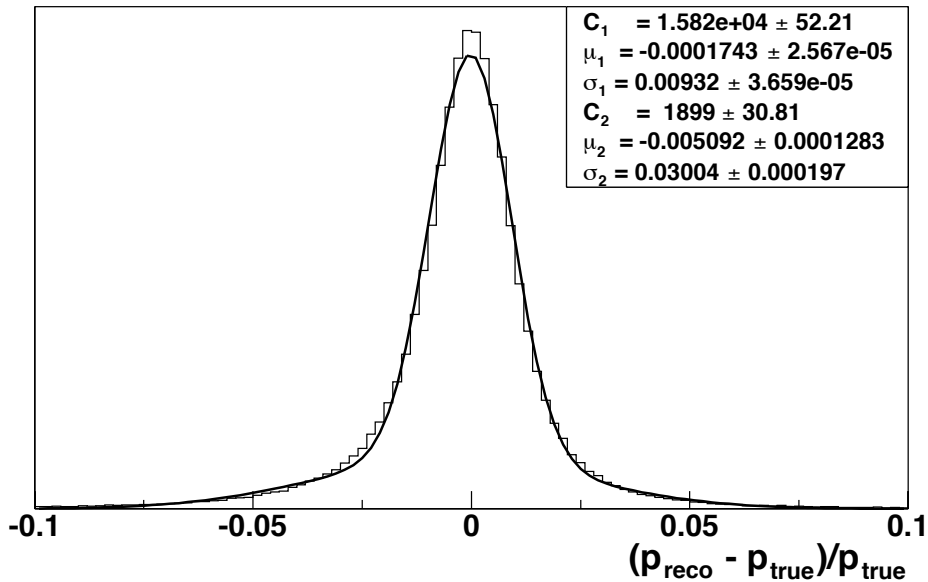


Figure 6.10: Momentum resolution obtained with p_t -kick method.

The magnetic field causes a deflection of the particle trajectory from a straight line (see figure 6.9). The integrated magnetic field $\int B \cdot dl$ the particle experiences can be represented by a deflection at a plane at distance z_{magnet} , i.e. the particle experiences a so called p_t -kick at this plane. Given the position x and direction $\theta (= \arctan t_x)$ of a particle at a reference plane $z = z_k$ downstream of the magnet and assuming it originated from the vertex the momentum of the particle is given by:

$$p = \frac{q \int B \cdot dl}{\sin \theta - 1 / \sqrt{1 + \left(\frac{\tan \theta}{z_{\text{magnet}}} \right)^2 \cdot \left(z_k - z_{\text{magnet}} + \frac{x}{\tan \theta} \right)^2}} , \quad (6.2)$$

where q is the charge of the particle. The plane ($z = z_{\text{magnet}}$) at which the particle experiences the p_t -kick is defined by $\int_{-\infty}^{z_{\text{magnet}}} B \cdot dl \equiv \int_{z_{\text{magnet}}}^{\infty} B \cdot dl$. As the magnetic field is not homogeneous it depends on the particle trajectory. By extrapolating the expected particle trajectory through the magnetic field an estimate of this “centre of the magnetic field” is obtained.

In figure 6.10 the momentum resolution distribution obtained with this method is shown. Fitting a double Gaussian through the distribution results in a resolution of 0.9%. This resolution is sufficient for seeding the Kalman filter in the track following algorithm.

The track segments found with the method described in the previous section are not directly used as an input to the track following. Instead the hits on these segments are refitted with the 3D-track fit presented in chapter 5. This gives a more accurate estimate of the track position and slope. The position and slope, together with the momentum estimate obtained with the p_t -kick method, are used as the input track seed

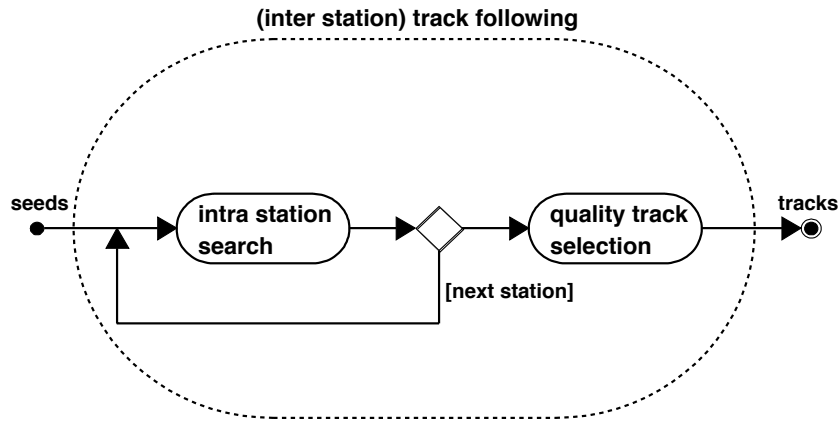


Figure 6.11: Flow diagram track following procedure.

to the track following algorithm of the next section. The errors on the track parameters of the track seed should, in principle, be taken infinitely large because the seed is not an actual measurement. However, for the track following algorithm to work properly, the errors are required to be finite⁹. Therefore, the calculated error on the (re)fitted track parameters increased by a scale factor (3.0) are used as initial track seed errors.

6.3 Track following

The track following procedure consists of two components: *intra-station* pattern recognition, i.e. the search for possible track continuations within a station, and *inter-station* pattern recognition, i.e. linking together, branching and terminating track candidates between the stations (see figure 6.11). The two steps are outlined in section 6.3.1 and section 6.3.2. A more detailed description is given elsewhere[102].

6.3.1 Inter station following

The track following algorithm starts from the initial track candidates found in the track seeding stage. These candidates are extrapolated to the next upstream tracking station. The intra station following algorithm discussed in the next section searches for possible continuations for each track candidate in this station. The hits of the possible continuation are added to the track candidate by applying the Kalman filter. If more than one distinct continuation is found the track branches into a multiple of candidates. All found candidates are extrapolated to the next station. This procedure is repeated looping over all tracking stations as depicted in figure 6.12.

⁹In case the errors are infinitely large the search window (see section 6.3.2) covers the whole station. Furthermore, the cluster selection relies on the track parameter errors.

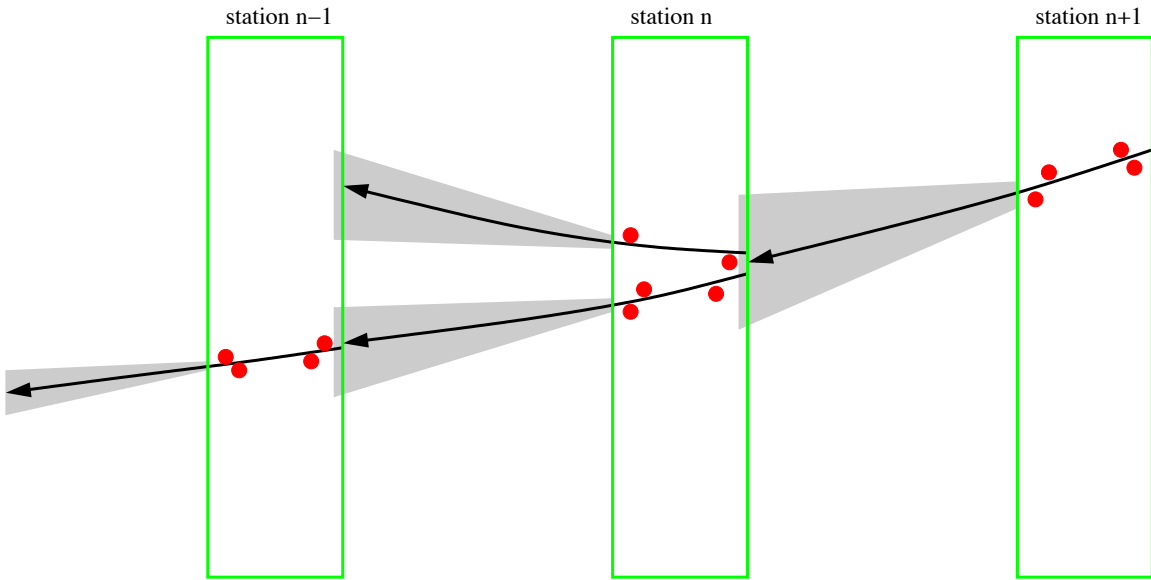


Figure 6.12: Graphical representation of track following procedure.

To be able to compare track candidates a track quality factor Q_{track} is defined by N_{outer} (N_{inner}), i.e. the number of outer (inner) tracker measurements, the χ^2 contribution of all measurements and a weight factor w :

$$Q_{\text{track}} = \left(N_{\text{outer}} - w \sum_{i=0}^{N_{\text{outer}}} \chi_i^2 \right) + 2 \left(N_{\text{inner}} - w \sum_{j=0}^{N_{\text{inner}}} \chi_j^2 \right) . \quad (6.3)$$

The weight factor w is set to 0.1. This implies that a measurement with a χ^2 contribution < 10 (> 10) has a positive (negative) contribution to the quality. The quality factor contains a separate term for the outer and for the inner tracker, with the inner tracker part given a double weight because the maximum expected number of measurements in the inner tracker is half.

To limit the number of track branches after each station two criteria are applied:

- The track parameters of the candidates of each seed are required to be different. Tracks are considered identical if the track parameters (x, y, t_x, t_y) differ less than 10σ . If two candidates are identical only the one with the highest quality, Q_{track} , is kept.
- A maximum of 10 candidates per track seed are allowed. If more candidates are found only those with the highest quality are kept.

In some cases no track continuation is found within a station, e.g. due to a particle passing through an insensitive part of the detector or due to an inefficiency in the intra-station following. Therefore, a track is allowed to skip a whole station, i.e. have no assigned hits in station n but continue in station $n + 1$.

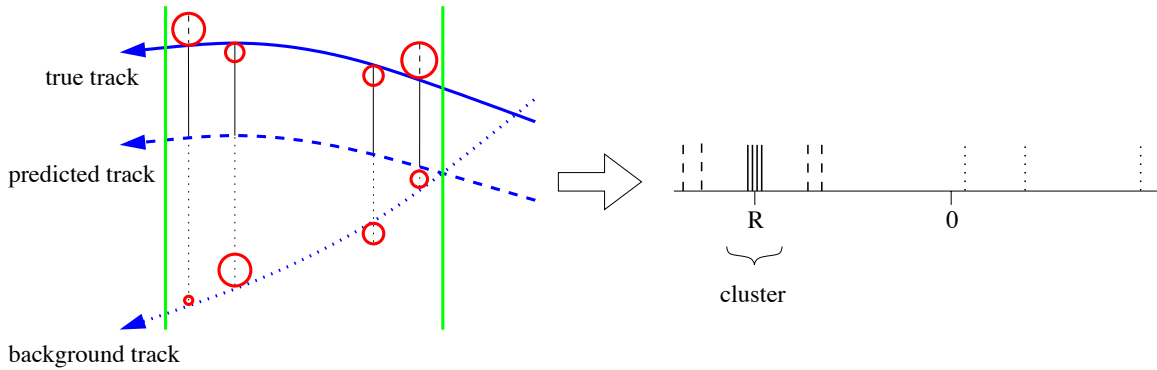


Figure 6.13: Graphical representation of the intra station hit clustering method. The left figure shows the “true” track and the predicted track together with a “background” track. The vertical lines from the measurements (circles) to the predicted track indicate the residuals. As seen in the right figure the residuals corresponding to the correct ambiguity measurements (solid lines) have approximately the same value. The wrong ambiguity residuals (dashed lines) and the background residuals (dotted lines) are spread in residual space.

After applying the algorithm to all tracking stations a collection of track candidates exist. An initial track seed can result in either no track candidate, one track candidate or a multiple of candidates. The reason for finding no candidates can be either an inefficiency in the track-following algorithm or due to the fact that the initial seed was false. In case a multiple of candidates is obtained some of them will be ghost tracks (see section 6.4). To reduce the number of ghost tracks additional selection criteria are applied. For every initial track seed the candidate with the highest quality Q_{best} is selected. For the remaining candidates of the seed to survive they must be

- well reconstructed, i.e. have a quality within 95 % of Q_{best} ,
- different, i.e. have at least 15 % different hits than the selected candidate(s).

6.3.2 Intra station search

Input to the intra station search are all the tracking hits in a station and the track candidates found in the previous stations. The track candidates are extrapolated to the z -position of each of the detection layers (to give a predicted hit position). An intra station search algorithm should, for every candidate, combine those hits that form continuations of the track candidate. There are several ways to do this. The algorithm presented in this section is a so called “global” algorithm, which means that all measurements are treated in the same way. After assigning all consistent measurements to a track candidate the track parameters are updated. This is different with respect to a “local” algorithm in which case each measurement is considered in sequence.

The algorithm uses the fact that measurements caused by the same particle will “cluster” around the (predicted) trajectory. It is therefore a hit-clustering algorithm. For all measurements within a broad window around the predicted trajectory the distance of the predicted track position to the measurement, i.e. the residual, is calculated. When the predicted track would follow the true particle trajectory the residuals of the measurements will all be consistent with zero, within the small error caused by the detector measurement precision. The residuals of measurements caused by other particles will not cluster around zero. This also holds for wrong left/right ambiguity assignments of outer tracker hits. If the predicted track deviates from the true trajectory the residuals of the true measurements will still approximately be the same but shifted from zero. This feature is exploited in the hit clustering method by assuming measurements caused by the same particle to be clustered around the same residual (see figure 6.13 for a graphical representation). The intra station search consists of the following four steps: selecting hits in a region of interest, hit clustering, cluster selection, and track continuation.

Region of interest

To reduce the combinatorics only those hits that are close to the predicted track position in a layer are considered. This Region of Interest (RoI) is defined by a rectangle around the predicted track position with size:

$$RoI_{x,y} = 5\sigma_{x,y} + \text{offset}_{x,y} , \quad (6.4)$$

with $\sigma_{x,y}$ the error on the x, y -position of the trajectory at the measurement layer. In case of Gaussian errors practically all measurements are within the 5σ region. Due to the non-Gaussian effects reported in chapter 5 this is not the case. Therefore, an additional offset is determined for each station with a maximum size of 20 mm.

Clustering

For all hits in the RoI, the residual w.r.t. the predicted track state is calculated, i.e. $r = m - h(\mathbf{x})$, as was defined in section 5.2.1. The hits are then clustered into groups of hits which have approximately the same residual (see figure 6.13). There are two criteria defining a cluster:

- Two hits belong to the same cluster if their difference in residual is smaller than a distance d_{\max} . For all stations $d_{\max} = 0.7$ mm is used.
- A cluster must contain at least N_{\min} hits. A conservative value of $N_{\min} = 3$ is chosen for hits in the outer tracker layers. In case the cluster only contains inner tracker hits $N_{\min} = 2$ is used.

Cluster selection

In the next step a quality factor is calculated for each cluster. The definition of the quality factor incorporates three properties of the cluster:

- The *number of hits*, N , in the cluster.
- The *average (residual) distance*, R , of the cluster to the track prediction;

$$R = \frac{1}{N} \sum_{i=1}^N r_i , \quad (6.5)$$

where r_i is the residual of hit i . The obtained R value is translated into a probability by comparing it to the distribution of R values obtained for clusters formed by true tracks. This is achieved by normalising the distribution of true R values to 1.0, and parameterising this distribution by a double Gaussian function f with standard deviations σ_1 and σ_2 . From this distribution the quantity

$$P(R) = 1 - \int_{-|R|}^{|R|} f(x; \sigma_1, \sigma_2) dx \quad (6.6)$$

is calculated, representing the probability that a cluster shows up at distance R if it was generated by the track.

- The *spread of the residuals* around the average distance R , expressed by the total χ^2 , i.e.

$$\chi^2 = \sum_{i=1}^N \frac{(r_i - R)^2}{\sigma_{r_i}^2} , \quad (6.7)$$

with $\sigma_{r_i}^2$ the error assigned to hit i . From this the χ^2 probability $P(\chi^2)$ is calculated.

Using these three properties the cluster quality is defined:

$$Q_{\text{cluster}} = N \times (P(R) + P(\chi^2)) . \quad (6.8)$$

All clusters for a given track prediction are ordered on quality. The best cluster and all clusters with a quality within 70 % of this best cluster are kept and considered as a track continuation candidate.

Track continuation

The remaining clusters are added to the track with the Kalman filter on a hit by hit basis, rejecting measurements with a large χ^2 . For all candidates associated with the starting candidate the track quality Q_{track} (as in equation 6.3) is calculated using only the measurements in the cluster. The track continuation with the best quality, and all others with a quality within 60 % of the best are accepted as track continuations.

6.4 Pattern recognition performance

All results are obtained from a sample of 8000 $B_d \rightarrow \pi^+ \pi^-$ events overlayed with minimum bias events (pile-up) to the nominal luminosity of $2 \times 10^{32} \text{cm}^{-2}\text{s}^{-1}$. As for the track fit (see section 5.3) only “physics” tracks are considered, i.e. particles satisfying the following track selection criteria:

- track momentum must be larger than 3 GeV/c,
- the first hit must lie at a position before $z = 1.0$ m,
- the last hit must lie at a position after $z = 9.2$ m,
- the track must be in the acceptance of the LHCb tracking system, i.e. traverse the tracking stations T2-T9.

This selects particles originating from the vertex and traversing the tracking stations.

The performance of the algorithms is studied by comparing reconstructed tracks to “true” tracks. The matching criteria used to determine if a track is correctly reconstructed are :

- a hit purity of more than 70 %, i.e. $\frac{n_{\text{good}}}{n_{\text{reco}}} > 0.7$ with n_{reco} the total number of measurements on the reconstructed track and n_{good} the number of measurements correctly assigned to the track,
- a hit efficiency of more than 70%, i.e. $\frac{n_{\text{good}}}{n_{\text{true}}} > 0.7$ with n_{true} the total number of measurements possible on the true track and n_{good} the number of measurements correctly assigned to the reconstructed track,
- the track position reconstructed within 10σ of the true position at the upstream edge of station T2 ($z = 2111$ mm).

The algorithm efficiency is defined as the percentage of physics tracks that are correctly reconstructed. The ghost rate is defined as the percentage of reconstructed tracks that have no hit purity $> 70\%$ for any true track.

6.4.1 Track seeding

To study the performance of the seeding algorithm only the hit purity matching criterium is used, i.e. purity $> 70\%$. Figure 6.14 shows the seeding efficiency as a function of the momentum of these tracks. The average seeding efficiency for these tracks is $96.8 \pm 0.1\%$. The ghost rate is $27.1 \pm 0.1\%$.

The current algorithm is used to perform detector optimisation and performance studies. However, it should not be considered the final algorithm. An improved algorithm is currently under study[103]. Furthermore, different approaches to the task can be studied, e.g. a Hough transform or cellular automa[104] approach.

6.4.2 Track following

The stand-alone performance of the track-following algorithm is tested by assuming ideal performance of the seeding algorithm (i.e. 100 % efficiency and no ghosts). This is achieved by obtaining the true track seeds from Monte Carlo and “smearing” the parameters by Gaussians with the standard deviations as in table 6.2. These are conservative values as is seen by comparison with table 6.1, i.e. the resolutions obtained

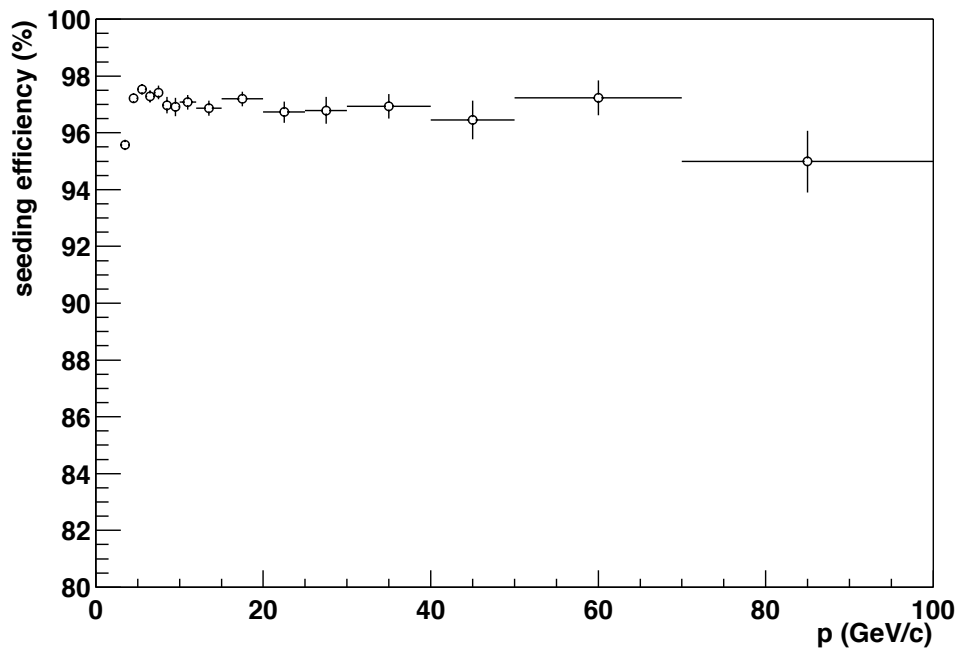


Figure 6.14: Track seeding efficiency as a function of momentum.

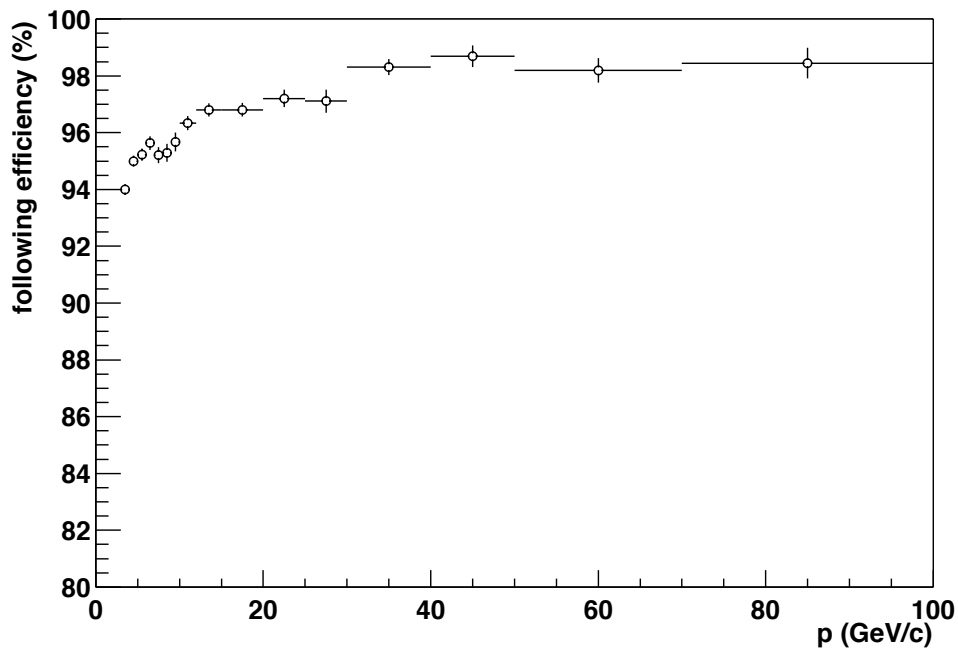


Figure 6.15: Track following efficiency as a function of momentum.

σ_x	σ_y	σ_{t_x}	σ_{t_y}	σ_κ
0.5 mm	1.0 mm	3.0×10^{-3}	3.0×10^{-3}	5.0 %

Table 6.2: Assumed track parameter resolutions obtained from the track seeding for the stand-alone following performance studies.

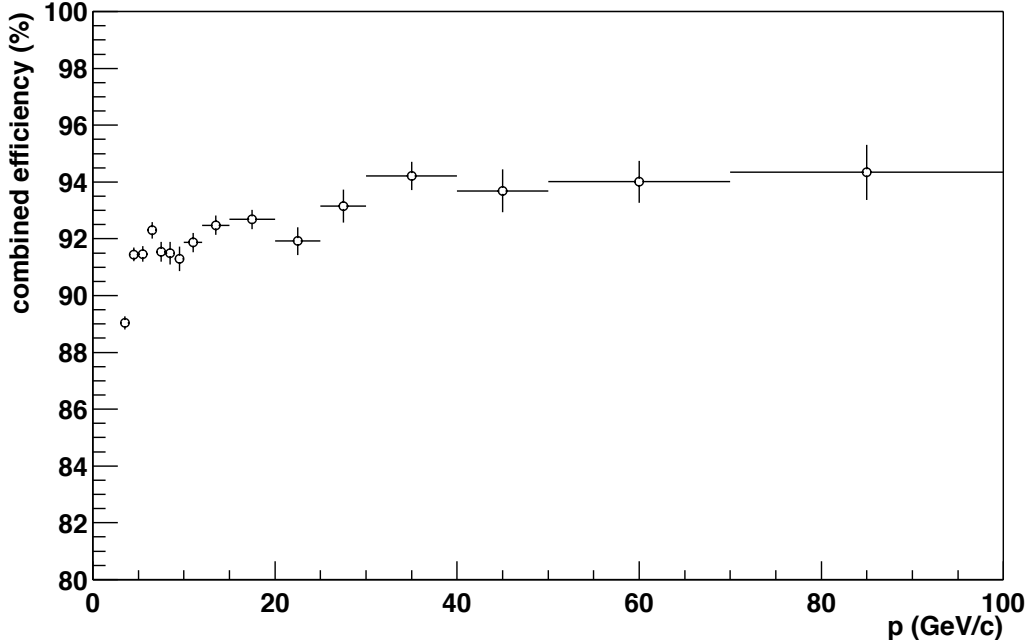


Figure 6.16: Track seeding followed by track following pattern recognition efficiency as a function of momentum.

in the track seeding. These track seeds are followed upstream through the magnet with the track-following algorithm.

Figure 6.15 shows the track following efficiency as a function of momentum for “physics” tracks applying all the matching criteria of page 128. The average track-following efficiency for these tracks is 95.5 ± 0.1 %. The efficiency is lower for low momentum tracks. For tracks with momentum larger than 10 GeV/c the average efficiency is 97.1 ± 0.1 %. The ghost rate is small, i.e. 0.95 ± 0.02 %.

6.4.3 Combined track seeding and following

By using the track segments found in the track seeding in the track-following algorithm a complete pattern recognition chain in the tracking detectors is obtained. Using the same track selection and track matching criteria as for track following an average track reconstruction efficiency of $91.4 \pm 0.1\%$ is found. Figure 6.16 shows the pattern recognition efficiency for tracking as a function of momentum.

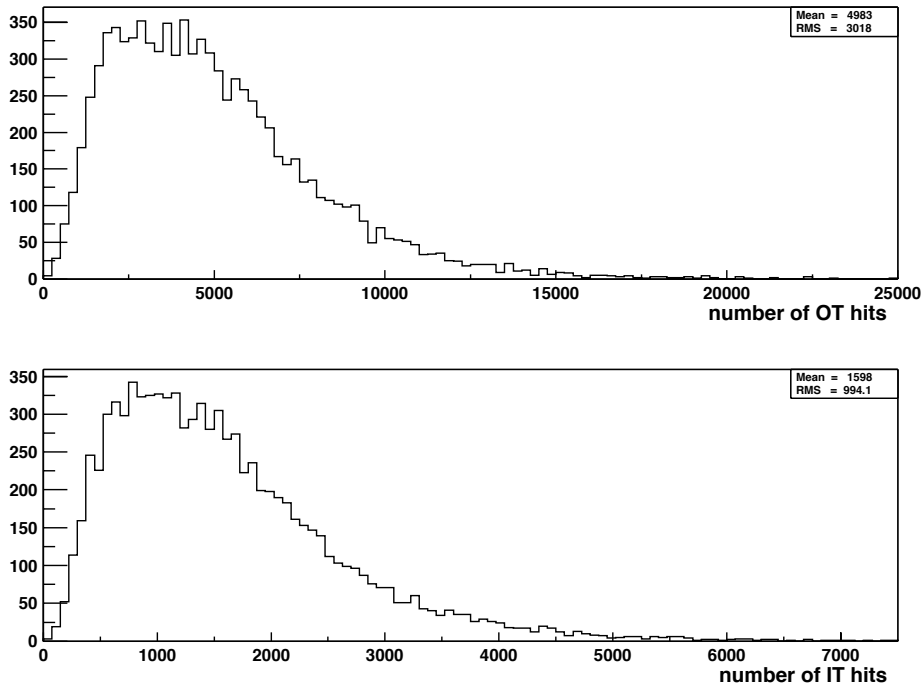


Figure 6.17: Distribution of the total number of hits in the outer tracker (top) and inner tracker (bottom) stations.

The distribution of total number of hits in the outer tracker and inner tracker stations is shown in figure 6.17. Due to the large event-by-event fluctuations mentioned in section 6.1 the total number of hits per event shows a wide distribution. On average an event contains about 5000 outer tracker hits and 1600 inner tracker hits.

The efficiency is expected to depend on the track density due to the fact that the number of combinatorics increases with the track density. Furthermore, the probability for a channel to be hit more than once increases. Channels which are hit more than once will not provide a measurement for all particles, thus effectively decreasing the detection efficiency. Figure 6.18 shows the pattern recognition efficiency as a function of the total number of hits in the outer and inner tracker. Fitting a straight line through the data points results in the parametrisations:

$$\begin{aligned}\varepsilon_{\text{outer}} &= 97.5 \% - 1.0 \times 10^{-3} N_{\text{outer}} \% \\ \varepsilon_{\text{inner}} &= 97.3 \% - 3.0 \times 10^{-3} N_{\text{inner}} \% .\end{aligned}$$

This shows the efficiency for low track densities to be about 97 %. The difference of $\sim 3\%$ with respect to the 100 %, is almost completely due to low momentum tracks.

The total ghost rate for the combined algorithm is $15.6 \pm 0.1\%$. The ghost rate for only track seeding is significantly higher (27 %). This shows that ghost tracks from the seeding get “killed” when searching for track continuations upstream into the detector with the track following algorithm. Figure 6.19 shows the ghost rate as a function of the

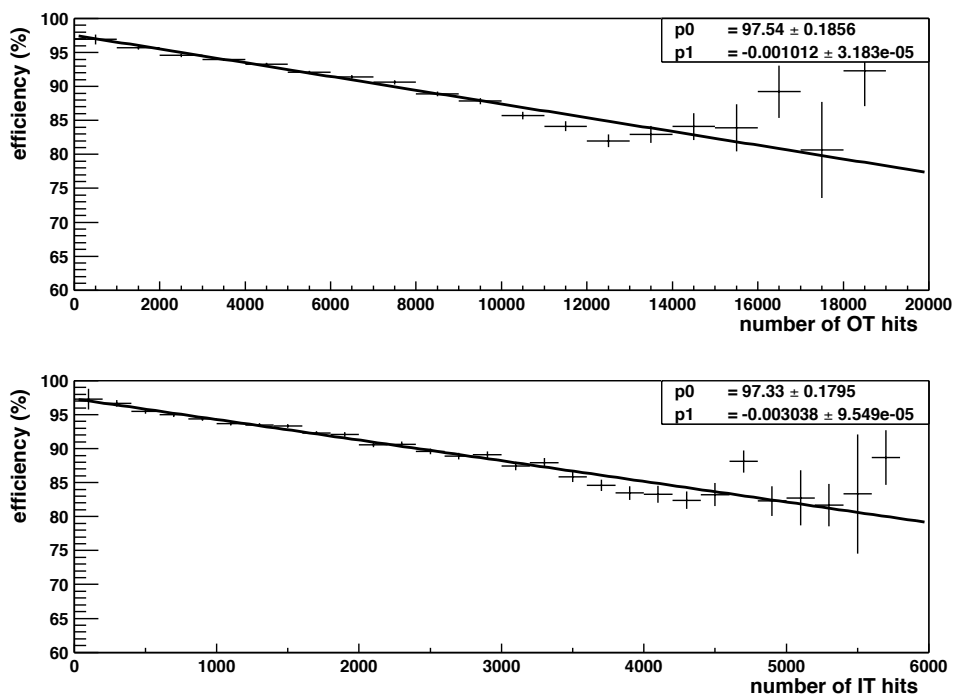


Figure 6.18: Efficiency as a function of the total number of hits in the outer tracker (top) and inner tracker (bottom) stations. The shown lines are straight line fits through the data points.

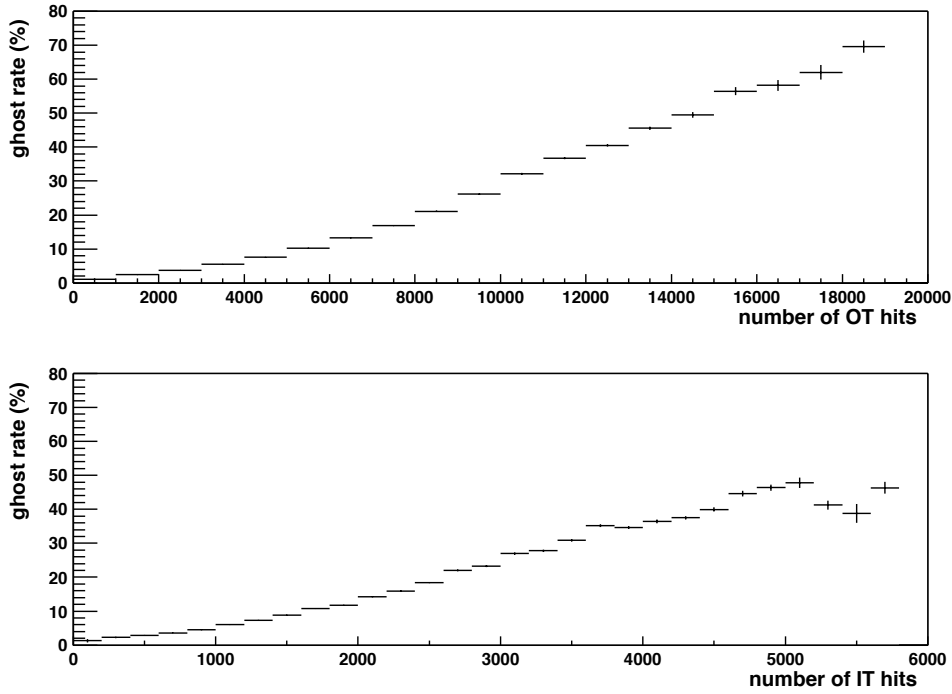


Figure 6.19: Ghost rate as a function of the total number of hits in the outer tracker (top) and inner tracker (bottom) stations.

total number of hits in the outer and inner tracker. As expected the ghost rate increases with the number of hits.

The resolution on the directions and positions at RICH-1 for the efficiently reconstructed tracks are shown in figure 6.20. From these distributions the resolution is determined with the same method as in chapter 5 (i.e. double Gaussian fit). The results are presented in the last column of table 6.3. The first column shows the resolutions obtained for ideal pattern recognition. Comparing these results shows that the resolution obtained with the pattern recognition algorithms described in this chapter is close to ideal.

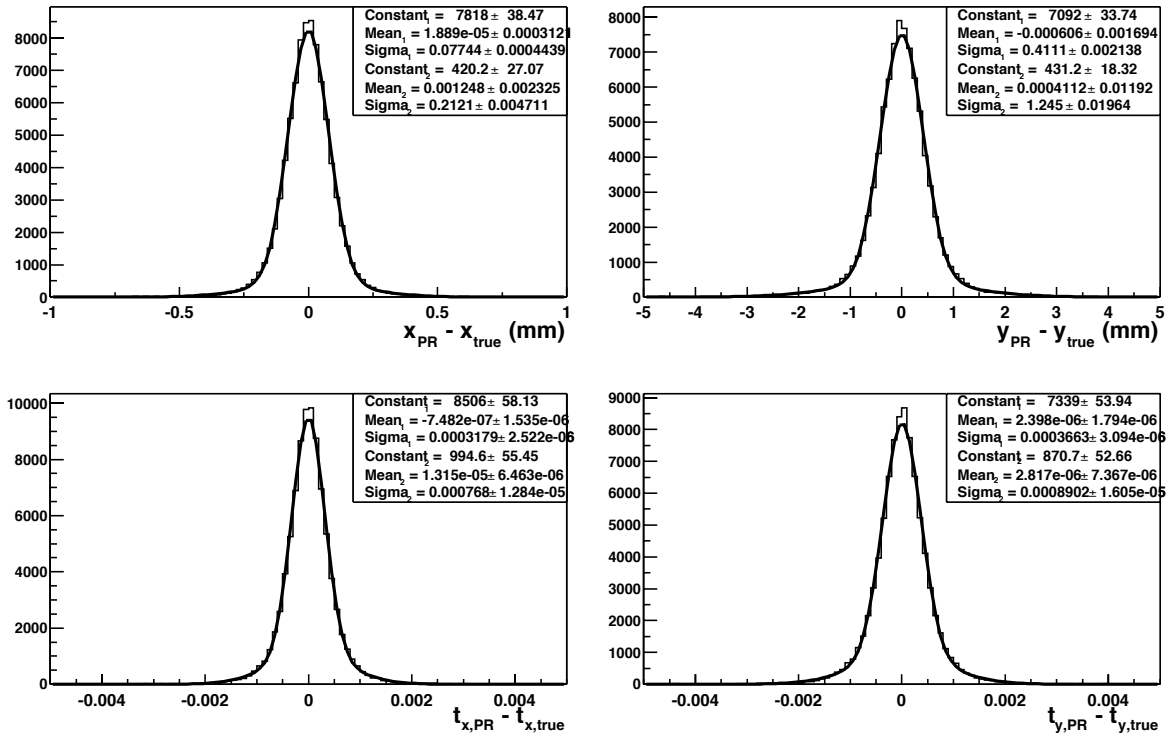


Figure 6.20: Resolution of the fitted position and direction for pattern recognition tracks at the downstream side of RICH-1 (Note: The index “PR” stands for Pattern Recognition).

track parameter	resolution	
	no PR	PR
x	76 μm	77 μm
y	416 μm	411 μm
t _x	3.4 × 10 ⁻⁴	3.2 × 10 ⁻⁴
t _y	3.0 × 10 ⁻⁴	3.7 × 10 ⁻⁴

Table 6.3: Obtained resolution of positions and directions at RICH-1 on perfect pattern recognition tracks (no PR column) and on full pattern recognition tracks (PR column)

Chapter 7

Tracking performance

In this chapter the performance of the LHCb tracking system, in terms of reconstructing interesting B decays and extracting CP violating parameters, is studied. The chapter starts with a summary of the event selection criteria for the two benchmark decay modes discussed in section 1.4, i.e. $B_s \rightarrow D_s^\pm K^\mp$ and $B_d \rightarrow \pi^+\pi^-$. These selection criteria have been optimised in separate studies[7, 105] assuming ideal, i.e. 100% efficient, pattern recognition. In this thesis trajectory reconstruction including *realistic* pattern recognition algorithms are presented. The selection criteria are the same as those used in the LHCb technical proposal[7] in order to allow for a fair comparison of the performance results.

Section 7.1 summarises the event selection criteria, the expected background and the obtained mass resolution for the decay $B_s \rightarrow D_s^\pm K^\mp$. Section 7.2 summarises the event selection criteria and the expected background for the decay $B_d \rightarrow \pi^+\pi^-$. Section 7.3 reports on the (in)efficiency in the reconstruction of B decays with the pattern recognition algorithms discussed in chapter 6. Section 7.4 presents the expected event yields for the benchmark channels per year of data taking. Section 7.5 compares these event yields and the resulting resolutions of the CP violating parameters to the results presented in the technical proposal. In section 7.6 a brief outlook is given on possible algorithm improvements and on a recently started study to re-optimise the LHCb detector.

7.1 $B_s \rightarrow D_s^\pm K^\mp$

7.1.1 Event selection

The event selection criteria are designed to select $B_s \rightarrow D_s^\pm (\rightarrow K^+K^-\pi^\pm)K^\mp$ decays (see section 1.4.2) from the large sample of events produced in LHCb. In LHCb the event selections are performed with the AXSEL[106] analysis package. The main selection criteria of AXSEL are summarised below.

First a set of well measured tracks is selected, i.e. tracks which have:

- at least one hit in the VELO system. This ensures that a high precision measurement of the track is made close to the decay vertices.

- at least 26 hits in the main tracking system. This selects tracks that have enough measurements and traverse the whole magnet thus ensuring that the momentum is well measured.
- the momentum measured with a precision better than 1.5 %, i.e. have $\frac{\delta p}{p} < 1.5 \%$.
- the RICH particle identification compatible with the assumed mass hypothesis. For a kaon the probability is required to be at least 90 % and for a pion larger than 20 %.

From the tracks thus selected, D_s candidate vertices are constructed by combining all oppositely charged kaon tracks with a third track compatible with a pion and requiring these tracks to coincide at a common vertex position. Furthermore, their reconstructed invariant mass should correspond to that of the D_s ($1.969 \text{ GeV}/c^2$). These requirements are verified by performing a mass constrained vertex fit. The χ^2 probability of the fit is required to be better than 0.5 %.

To obtain a B_s decay vertex the reconstructed D_s is combined with all remaining kaons. The invariant mass of the D_s and the kaon is required to be within $30 \text{ MeV}/c^2$ of the B_s mass ($5.369 \text{ GeV}/c^2$). The χ^2 probability of the B_s vertex fit is again required to be greater than 0.5 %.

7.1.2 Background rejection

There are two important sources of background:

- combinatorial background, i.e. events with kaons and pions that “by chance” satisfy the right mass and vertex criteria,
- events containing a real D_s , especially when this D_s belongs to another B decay channel.

To suppress the background events the following additional selection criteria are applied:

- The B_s vertex should be upstream of the D_s vertex.
- The reconstructed B_s momentum vector should point to the primary vertex. This is established by requiring the impact parameter to be smaller than $100 \mu\text{m}$.
- The B_s decay length normalised by the estimated error should be larger than 5.

Distinguishing a B decay containing a D_s is mainly achieved by the B mass cut of section 7.1.1.

An important B_s decay background is the decay $B_s \rightarrow D_s\pi$, which has a branching ratio about a factor 20 larger than $B_s \rightarrow D_s^\pm K^\mp$. The left plot in figure 7.1 shows the mass spectrum of reconstructed $B_s \rightarrow D_s^\pm K^\mp$ candidates using only the information of the tracking detectors. The mass resolution is sufficient to make a mass cut possible at about $5.4 \text{ GeV}/c^2$ rejecting a significant fraction of the $B_s \rightarrow D_s\pi$ candidates. Still the

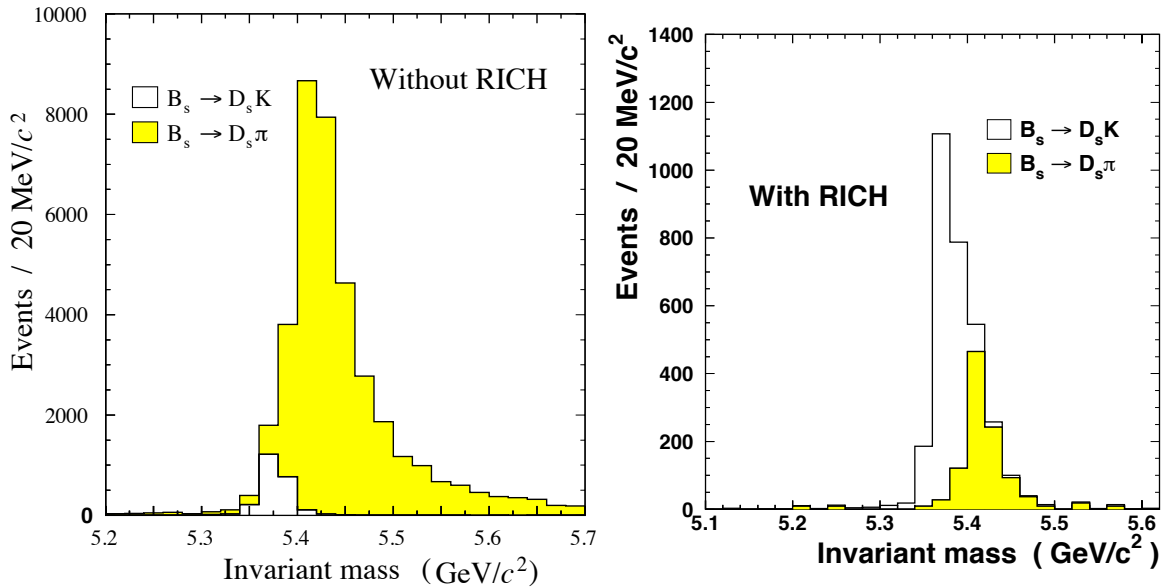


Figure 7.1: Mass spectrum of $B_s \rightarrow D_s^\pm K^\mp$ candidates before particle identification is applied (left), and after using the RICH information (right) [37].

sample of $B_s \rightarrow D_s^\pm K^\mp$ will be severely diluted by $B_s \rightarrow D_s \pi$ events. To improve the separation power LHCb uses two RICH detectors that provide particle identification, i.e. distinguishing pions from kaons. The right plot in figure 7.1 shows the mass spectrum of $B_s \rightarrow D_s^\pm K^\mp$ candidates with use of the RICH detectors.

7.1.3 Mass resolution

A precise mass resolution is important for suppression of background events. The reconstructed B mass resolution depends on the momentum resolution of the individual tracks and on the resolution of the opening angle of the decay particles. The angles are mainly determined by the vertex detector, the momenta by the main tracker. In figure 7.2 the fitted mass resolution of the B_s as well as that of the D_s are shown. A B_s mass resolution of $10.7 \text{ MeV}/c^2$ is obtained.

7.2 $B_d \rightarrow \pi^+\pi^-$

7.2.1 Event selection

As for the $B_s \rightarrow D_s^\pm K^\mp$ decay the selection of $B_d \rightarrow \pi^+\pi^-$ decays is performed with the AXSEL[106] analysis package. The selection criteria are summarised below.

Again only well measured tracks are considered in the event reconstruction. In particular tracks are required to:

- have at least 1 hit in the VELO system, ensuring precision information at the particle position near to the decay vertices.

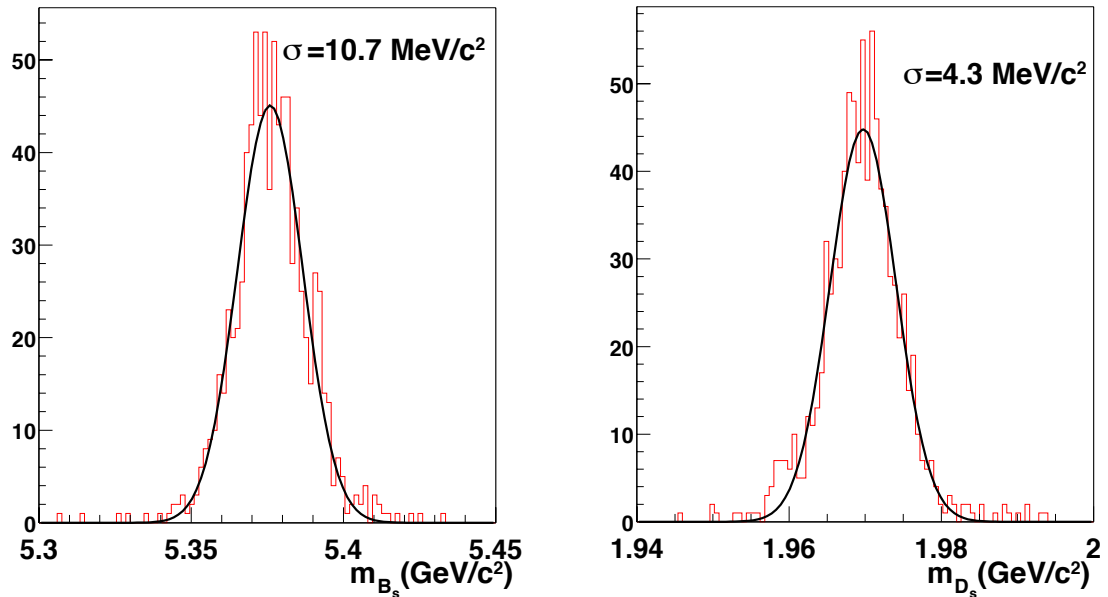


Figure 7.2: Obtained B_s and D_s mass resolution for $B_s \rightarrow D_s^\pm K^\mp$ events after applying all selection criteria (except the mass cut).

- be fitted with a reduced $\chi^2 < 50$. This criterium rejects tracks that are “badly” fitted.
- have an impact parameter d_0 with respect to the primary vertex smaller than 5 mm (upper limit), measured with a precision σ_{d_0} better than 0.5 mm, and a normalised impact parameter $d_0/\sigma_{d_0} > 3$. This criterium selects tracks that are likely to come from a B decay.

All opposite-sign combinations of such tracks are used to form vertices. For a track combination to be selected as a candidate B_d vertex:

- the tracks should be fitted as a vertex with $\chi^2 < 5$.
- the tracks should make up an invariant mass, under the pion hypothesis, within 30 MeV/c² of the B_d mass (5.279 GeV/c²).
- the flight distance, i.e. the distance between the reconstructed vertex and the primary vertex, should be larger than 0.5 mm.

7.2.2 Background rejection

The decay $B_d \rightarrow \pi^+\pi^-$ suffers from two main types of background:

- generic combinatoric background,
- B decays with the same two track topology, e.g. $B_d \rightarrow K^+\pi^-$ or $B_s \rightarrow K^-\pi^+$.

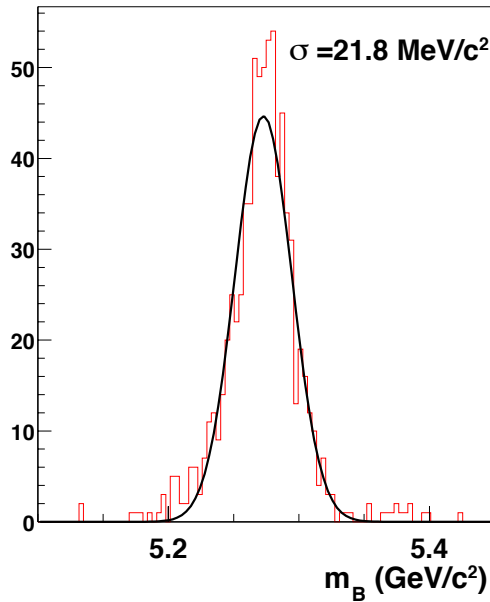


Figure 7.3: Obtained B_d mass resolution for $B_d \rightarrow \pi^+\pi^-$ events after applying all selection criteria (except the mass cut).

The rejection of two body B background events is obtained by applying a mass cut in combination with the particle identification provided by the RICH detector (see section 7.2.1).

A large fraction of the combinatoric background is rejected by requiring a well displaced secondary vertex. This is achieved by applying the following cuts:

- the momentum vector of the combined track should point to the primary vertex. This is achieved by requiring $\cos\theta_B > 0.95$, where θ_B is the angle between the momentum vector and the vector connecting primary and secondary vertex.
- the separation in z between the primary and secondary vertex normalised by the measurement precision should be larger than 3, i.e. $\delta_z/\sigma_{\delta_z} > 3$.

In addition the following kinematic cuts are imposed on the candidate pions and on the reconstructed B meson:

- the helicity angle θ_π of both pions in the B rest-frame should satisfy $|\cos\theta_\pi| < 0.9$,
- the transverse momentum p_t of one pion should be larger than 3 GeV/c. The p_t of the other pion should be at least 1 GeV/c,
- the p_t of the reconstructed B_d should be larger than 3 GeV/c.

Figure 7.3 shows the fitted mass resolution of the B_d after applying all cuts. A mass resolution of $21.8 \text{ MeV}/c^2$ is obtained.

	$B_s \rightarrow D_s^\pm K^\mp$	$B_d \rightarrow \pi^+ \pi^-$
$\epsilon_{\text{signal track}}$	$94.7 \pm 0.9\%$	$96.8 \pm 0.7\%$
$\epsilon_{\text{event}}^{PR}$	$79.3 \pm 3.4\%$	$93.8 \pm 1.5\%$

Table 7.1: Pattern recognition event reconstruction efficiency $\epsilon_{\text{event}}^{PR}$ and the individual signal track reconstruction efficiency $\epsilon_{\text{signal track}}$ for $B_s \rightarrow D_s^\pm K^\mp$ and $B_d \rightarrow \pi^+ \pi^-$ signal events.

7.3 Pattern recognition performance

The event reconstruction inefficiency due to imperfect pattern recognition is a measure of the performance of the LHCb tracking system. The event reconstruction efficiency $\epsilon_{\text{event}}^{PR}$ corresponding to the pattern recognition performance is defined as the actual number of reconstructed B events divided by the number that would be obtained if the pattern recognition were fully efficient for all tracks within the LHCb acceptance. To determine this efficiency the following procedure is followed:

1. Signal B events are generated with SICBMC¹ (see section 5.1).
2. The complete event, i.e. including all sub-detectors, is reconstructed with the Brunel software.
3. The tracks are fitted with the hits correctly assigned to the tracks.
4. By means of the AXSEL routines the event selection criteria of sections 7.1 and 7.2 are applied for the B decay under study.
5. In case the event passes the physics selection cuts all tracks are reconstructed with full pattern recognition. If all stable decay products of the B meson are found in the pattern recognition the event is efficiently reconstructed.

Step 4 results in the number of events N_{select} assuming ideal pattern recognition. Step 5 results in the number of events N_{PR} that also have all stable decay products found in the pattern recognition. The event reconstruction efficiency due to pattern recognition is thus $\epsilon_{\text{event}}^{PR} = N_{\text{PR}}/N_{\text{select}}$.

Table 7.1 shows this event reconstruction efficiency for the benchmark B decay modes $B_s \rightarrow D_s^\pm K^\mp$ and $B_d \rightarrow \pi^+ \pi^-$. Obviously, the first decay mode has a lower efficiency because of the four decay particles that have to be reconstructed. Table 7.1 also shows the individual track reconstruction efficiency $\epsilon_{\text{signal track}}$ for the decay particles of the B meson. These numbers are higher than the average track efficiency of $91.4 \pm 0.1\%$. This is explained by the fact that the momenta as well as transverse momenta(i.e. a large angle θ) of the B decay particles are significantly higher than that of the underlying events (see figure 2.19 and figure 7.4). The track reconstruction efficiency is higher for this type of tracks (see figure 6.16).

¹The events were 'piled up' with minimum bias events corresponding to a luminosity of $5 \times 10^{32} \text{ cm}^{-2}\text{s}^{-1}$, i.e. high luminosity mode.

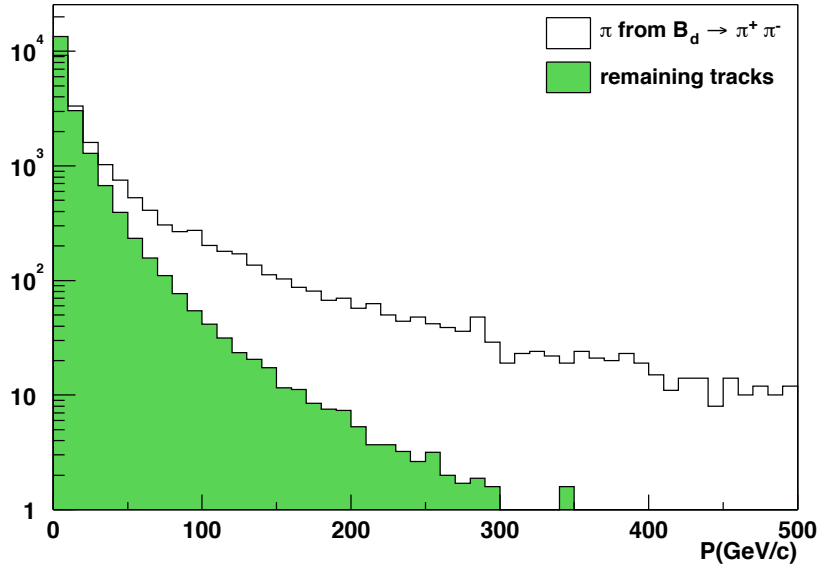


Figure 7.4: The simulated momentum spectrum for the pions from $B_d \rightarrow \pi^+\pi^-$ and the remaining tracks within the LHCb acceptance.

7.4 Event yields

The previous section reports on the track and event reconstruction (in)efficiency due to the pattern recognition algorithms. From a physics point of view the interesting quantity is the total number of fully reconstructed and tagged events that is expected “on tape” after a year (10^7 seconds) of LHCb operation. In this section the event yields taking into account the track reconstruction inefficiencies due to pattern recognition are presented for the two benchmark channels. Note that currently the *input* to AXSEL are the tracks originating from *ideal* pattern recognition. This is necessary because the combined seeding and following of tracks is not yet linked to the measurements from the VELO.

At the nominal luminosity of $2 \times 10^{32} \text{ cm}^{-2} \text{ s}^{-1}$ the expected number of $b\bar{b}$ pairs produced per year in a single interaction is $5.6 \cdot 10^{11}$ (see section 2.1). Taking the production rate ratios of \bar{b} quarks into B_u , B_d and B_s to be 40 %, 40 % and 12 % [7] and assuming the same ratios for the charge conjugate state the number of produced B mesons are:

$$\begin{aligned} B_u X_b + c.c. &: 4.5 \cdot 10^{11} \\ B_d X_b + c.c. &: 4.5 \cdot 10^{11} \\ B_s X_b + c.c. &: 1.3 \cdot 10^{11} . \end{aligned}$$

Here X_b stands for any hadron with a b quark, and *c.c.* for the charge conjugate states.

Only a fraction of the produced B_s and B_d mesons decay via the benchmark channels of sections 7.1 and 7.2. The branching ratio for $B_d \rightarrow \pi^+\pi^-$ is $7.0 \cdot 10^{-6}$ [7], re-

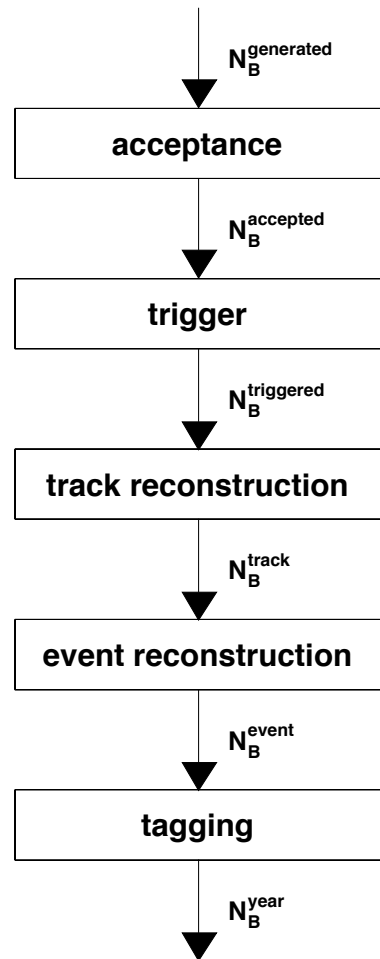


Figure 7.5: Steps in the event reconstruction that reduce the number of produced B events $N_B^{\text{generated}}$ to the number of reconstructed and tagged events on tape N_B^{year} .

sulting in $3.2 \cdot 10^6$ of these decays available in one year of data taking. The branching ratio for $B_s \rightarrow D_s^- K^+$ is $2.0 \cdot 10^{-4}$ and for $B_s \rightarrow D_s^+ K^-$ $3.1 \cdot 10^{-5}$ [7]. Only a fraction of the D_s mesons will decay into $KK\pi$. The visible branching ratio for $B_s \rightarrow D_s^\pm (\rightarrow K^+ K^- \pi^\pm) K^\mp$ is $9.4 \cdot 10^{-6}$. This means $1.2 \cdot 10^6$ of these decay are produced in a year of LHCb data taking.

Not all produced decays are fully reconstructed by LHCb. To get the final number of fully reconstructed and tagged events “on tape” several reduction steps need to be applied. These reduction steps are (see also figure 7.5):

- Only part of the events have all the B decay products decay inside the LHCb spectrometer *acceptance*. If not all B decay products are in the acceptance the event can not be reconstructed. An event is defined to be in the acceptance if all stable particles cross all tracking stations². The fraction of accepted events is defined by the ratio $\frac{N_B^{\text{accepted}}}{N_B^{\text{generated}}}$ with N_B^{accepted} the number of accepted events.
- Not all selected B events pass the *triggers*. The trigger efficiency is defined as $\epsilon_{\text{trigger}} = \frac{N_B^{\text{triggered}}}{N_B^{\text{accepted}}}$ where $N_B^{\text{triggered}}$ is the number of triggered events.
- For those events that pass the triggers the tracks are reconstructed by the reconstruction algorithms including the pattern recognition. The track reconstruction efficiency is defined as $\epsilon_{\text{track}} = \frac{N_B^{\text{track}}}{N_B^{\text{triggered}}}$ where N_B^{track} is the number of events with all stable particles found in the track reconstruction.
- The next step is the reconstruction of the B event. For the two benchmark channels this is achieved by applying the event selection criteria outlined in sections 7.1 and 7.2. The event reconstruction efficiency is defined as $\epsilon_{\text{event}} = \frac{N_B^{\text{event}}}{N_B^{\text{track}}}$ where N_B^{event} is the number of events that pass the selection criteria.
- In order to study neutral B meson decays involving flavour oscillations the initial flavour of the produced B meson needs to be identified. This is achieved by detecting the flavour of the accompanying B hadron from the charge of decay leptons and kaons³. Several *tagging* possibilities exist depending on the specific B decay[7]. Not all events with the B meson decay fully reconstructed will be tagged. The tagging efficiency is the fraction of these events that will be tagged, i.e. $\epsilon_{\text{tag}} = \frac{N_B^{\text{year}}}{N_B^{\text{event}}}$, with N_B^{year} the final number of fully reconstructed and tagged events on tape per year.

The LHCb reconstruction program as described in this thesis is used to determine the *acceptance* and the efficiencies ϵ_{track} and ϵ_{event} for the benchmark channels $B_s \rightarrow D_s^\pm K^\mp$ and $B_d \rightarrow \pi^+ \pi^-$. For the trigger efficiency as well as the tagging efficiency the numbers

²In fact all stable decay products of the B meson are required to be “physics” tracks using the criteria defined in section 6.4.

³Next to using the accompanying B hadron for tagging, also a *same-side tagging* strategy can be applied. In this case the flavour is determined by using the particles produced in association with the B meson.

Mode	acceptance	$\epsilon_{\text{trigger}}$	ϵ_{track}	ϵ_{event}	ϵ_{tag}	N_B^{peryear}
$B_s \rightarrow D_s^\pm K^\mp$	3.3%	16%	77%	42%	40%	823
$B_d \rightarrow \pi^+\pi^-$	8.3%	17%	88%	33%	40%	5212

Table 7.2: Event reduction factors and the final expected LHCb event yield for the channels $B_s \rightarrow D_s^\pm K^\mp$ and $B_d \rightarrow \pi^+\pi^-$ in one year of data taking.

from the technical proposal[7] are used. The efficiency (reduction) factors are indicated in table 7.2. Starting from the number of events produced in a year of LHCb running the expected number of fully reconstructed and tagged events on tape is calculated. The last column in table 7.2 shows that about 800 $B_s \rightarrow D_s^\pm (\rightarrow K^+K^-\pi^\pm)K^\mp$ events and 5200 $B_d \rightarrow \pi^+\pi^-$ events are expected.

7.5 Comparison

The number of reconstructed events determines the precision with which CP violation can be measured by the LHCb experiment. As mentioned in section 1.4 the benchmark decays can be used to measure the unitarity triangle angles α and γ' . In case of the decay $B_d \rightarrow \pi^+\pi^-$ the unitarity angle α is determined by fitting equation 1.21 to the rate asymmetry between the decay of B_d and \bar{B}_d to $\pi^+\pi^-$. In case of the decay $B_s \rightarrow D_s^\pm K^\mp$ the parameters $|\lambda|$ and ϕ ($|\bar{\lambda}|$ and $\bar{\phi}$) are fitted from the rate asymmetry $\mathcal{A}_{D_s^- K^+}(t)$ ($\mathcal{A}_{D_s^+ K^-}(t)$). From the fitted values and using equation 1.23 the angle γ' is determined.

Mode	N_B^{peryear}
$B_s \rightarrow D_s^\pm K^\mp$	2420
$B_d \rightarrow \pi^+\pi^-$	6900

Table 7.3: LHCb event yield presented in the technical proposal[7] for the decays $B_s \rightarrow D_s^\pm K^\mp$ and $B_d \rightarrow \pi^+\pi^-$ in one year of data taking.

In the technical proposal the expected sensitivity on the measurement of these angles is presented. The results were obtained by performing fits of the parameters of the rate asymmetries to rate distributions obtained with stand alone simulation programs[7] simulating the number of fully reconstructed events per year. The event yields for the two benchmark decays presented in the LHCb technical proposal[7] are shown in table 7.3.

The event yields in the technical proposal are higher than those presented in the previous section (table 7.2). In case of the decays $B_s \rightarrow D_s^\pm K^\mp$ the event yield is reduced by a factor $823/2420 = 0.34$. In case of the decays $B_d \rightarrow \pi^+\pi^-$ the event yield is reduced by a factor $5212/6900 = 0.76$. The new results, however, provide a more realistic estimate of the expected event yields because of two reasons. First of all, the LHCb detector description has become more realistic. This has resulted in an increase of the amount of material in the detector and thus in the number of radiation lengths and

α	σ_α		γ'	$\sigma_{\gamma'}$	
	TP	new		TP	new
0°	1.6°	2.7°	0°	7.1°	8.1°
30°	3.4°	5.7°	30°	8.8°	10.1°
			90°	9.3°	10.7°
			120°	8.3°	9.5°
			150°	6.5°	7.5°

Table 7.4: The fitted errors (in the technical proposal ('TP') and in this thesis ('new')) on α (left table) and γ' (right table) from the decays $B_d \rightarrow \pi^+\pi^-$ and $B_s \rightarrow D_s^\pm K^\mp$ for different values of α and γ corresponding to one year of data taking. In case of the γ' fit it is assumed that $\Delta = 30^\circ$ and $x_s = 20$.

number of interaction lengths. The material budget for the VELO system increased from 10% X_0 to 19% X_0 and per outer tracker station increased from 1.6% to 3.0%. The total radiation length up to RICH-2 has increased from 40% X_0 up to 60% X_0 . As a consequence

- of the increase in interaction length more charged hadrons will experience an interaction. Therefore, the probability for a particle to traverse all tracking stations has decreased from 85 – 90% in the technical proposal down to 70 – 80% in the setup described in this thesis.
- of the increase in radiation length minimum ionising particles experience more multiple scattering deflections. Consequently the obtained track parameter resolutions are worse. Moreover, it leads to an increase of photon conversions.
- there are more secondary particles in the detector resulting in more detector hits. Therefore, the detector occupancy has increased resulting in an increase of multiply hit channels. This leads to a loss in track reconstruction efficiency.

Secondly, in the technical proposal the pattern recognition was assumed to be 100% efficient. The results presented in this thesis include realistic track finding and following pattern recognition algorithms in the outer and inner tracker. As mentioned in section 7.3 the pattern recognition event reconstruction efficiency is $\sim 79\%$ for $B_s \rightarrow D_s^\pm K^\mp$ events and $\sim 94\%$ for $B_d \rightarrow \pi^+\pi^-$ events. The fact that for $B_s \rightarrow D_s^\pm K^\mp$ four particles need to be efficiently reconstructed and for $B_d \rightarrow \pi^+\pi^-$ only two explains why the reduction in event yield is larger for $B_s \rightarrow D_s^\pm K^\mp$ events.

The physics simulations of the technical proposal have not been repeated. Also, the event selection criteria have not been re-tuned⁴. However, an estimate of the expected sensitivities is made under the assumption that the errors scale with the \sqrt{N} , with N the number of fully reconstructed tagged events in one year of data taking. In table 7.4 (left) the obtained errors on α for two different values of α as presented in the technical

⁴The 30 MeV/c² B_d mass cut of section 7.2.1 will cut away a fraction of the signal events as can be seen in figure 7.3. This cut has to be re-tuned to cope with the decreased mass resolution because of the effects mentioned above.

proposal are presented⁵. Furthermore, the newly obtained resolutions using the event yields of table 7.2 and applying the scaling with \sqrt{N} are presented. In table 7.4 (right) the obtained errors on γ' for different values of γ' for the technical proposal and the current study are presented for $\Delta = 30^\circ$.

7.6 Outlook

Several improvements can still be made in the reconstruction of the B decays. The current pattern recognition algorithms can be tuned and improved at various points. An improvement can also be made by performing the pattern recognition in several passes, i.e. first finding the “easy” high momentum particles and then another pass for finding the more tough cases discarding the already used hits for the already found tracks. Improved track finding algorithms will be able to reconstruct tracks that do not traverse all tracking stations, i.e. recovering events with some of the B decay products absorbed by the spectrometer. Furthermore, it is envisaged to develop new algorithms.

However, the gain of these improvements is limited. Therefore, recently studies have started to improve the performance of the LHCb experiment by a redesign of the detector. The basic idea is to reduce the amount of material in the detector (resulting in the *LHCb-light* setup). This is achieved by:

- keeping only one tracking station just after RICH-1 and three seeding stations in the field free region before RICH-2 (i.e. the station T1 before RICH-1, the magnet stations T3-T5 and the seeding station T6 are removed),
- reducing the number of stations in the VELO setup and reducing the silicon sensor thickness to $220\mu\text{m}$,
- reducing the material thickness of RICH-1 mirrors and frame,
- removing the magnet shielding plate

Tracking studies for the LHCb-light detector are currently being performed. Preliminary studies show that the track reconstruction efficiencies for “long” tracks, i.e. tracks that traverse the whole spectrometer, are similar to the efficiency with the classic setup. Currently, results on efficiency for the B meson decay reconstruction are not yet available. Therefore, it remains to be seen if this new detector optimisation will result in higher event yields and hence in an improved capability to study CP violation.

⁵These results are obtained assuming no contribution is present from the penguin diagrams.

Bibliography

- [1] E. B. Wilson, *An Introduction to Scientific Research* (McGraw-Hill, 1952).
- [2] A. D. Sakharov, Pisma Zh. Eksp. Teor. Fiz. **5**, 32 (1967).
- [3] J. H. Christenson, J. W. Cronin, V. L. Fitch, and R. Turlay, Phys. Rev. Lett. **13**, 138 (1964).
- [4] D. E. Groom *et al.*, Eur. Phys. J. **C15**, 1 (2000).
- [5] B. Aubert *et al.*, (2002), hep-ex/0203007.
- [6] T. Higuchi, (2002), hep-ex/0205020.
- [7] LHCb, S. Amato *et al.*, *LHCb technical proposal*, CERN-LHCC-98-4, 1998.
- [8] G. Altarelli and M. L. Mangano, editors, *Standard model physics (and more) at the LHC.*, Proceedings workshop, May 25-26, October 14-15, 1999, Geneva, Switzerland, CERN (2000) 529 p.
- [9] G. Branco *et al.*, *CP Violation* (Oxford university press, 1999).
- [10] I. Bigi and A. Sanda, *CP Violation* (Cambridge university press, 2000).
- [11] C. Wu *et al.*, Phys. Rev **105**, 1413 (1957).
- [12] K. Kodama *et al.*, Phys. Lett. **B504**, 218 (2001), hep-ex/0012035.
- [13] S. Glashow, Nucl. Phys. **22**, 579 (1961).
- [14] S. Weinberg, Phys. Rev. Lett. **19**, 1264 (1967).
- [15] A. Salam, Relativistic groups and analyticity, in *Proc. 8th Nobel Symposium Aspenäsgården*, p. 367, Stockholm, 1968, Almquist and Wiksell.
- [16] G. Arnison *et al.*, Phys. Lett. **122B**, 103 (1983).
- [17] G. Arnison *et al.*, Phys. Lett. **126B**, 398 (1983).
- [18] N. Cabibbo, Phys. Rev. Lett. **10**, 531 (1963).
- [19] M. Kobayashi and T. Maskawa, Prog. Theor. Phys. **49**, 652 (1973).

- [20] L. Wolfenstein, Phys. Rev. Lett **51**, 1945 (1983).
- [21] C. Jarlskog, Introduction to cp violation., in *CP Violation*, edited by C. Jarlskog, World Scientific, 1989.
- [22] M. W. N. Isgur, Heavy quark symmetry, in *B decays*, edited by S. Stone, World Scientific, Singapore, 1994.
- [23] I. Siccama, *Measurement of the B_s lifetime*, PhD thesis, Amsterdam University, 1996.
- [24] M. Gronau, D. London, N. Sinha, and R. Sinha, Phys. Lett. **B514**, 315 (2001), hep-ph/0105308.
- [25] T. Sjstrand *et al.*, *High-Energy-Physics Event Generation with Pythia 6.1*, hep-ph/0010017, 2001.
- [26] LHC Study Group, P. Lefvre and T. Pettersson, *The Large Hadron Collider: Conceptual design*, CERN-AC-95-05-LHC, 1995.
- [27] CERN, LEP shuts down after eleven years of forefront research, 2000, <http://press.web.cern.ch/Press/Releases00/PR14.00ELEPstop.html>.
- [28] Alice, *A Large Ion Collider Experiment, Technical Proposal*, CERN-LHCC-1995-71, 1995.
- [29] W. W. Armstrong *et al.*, CERN-LHCC-94-43.
- [30] CMS, *CMS Technical Proposal*, CERN-LHCC-1994-38, 1994.
- [31] CERN, CERN prepares long term plan, 2002, <http://press.web.cern.ch/Press/Releases02/PR04.02EMarchCouncil.html>.
- [32] N. Zaitsev, *Study of the LHCb pile-up trigger and the $B_s \rightarrow J/\psi\phi$ decay*, PhD thesis, Amsterdam University, 2000.
- [33] T. Nakada and O. Schneider, *LHCb Trigger*, writeup for the international workshop on B-physics and CP-violation(BCP4), Ise-Shima, Japan, 2001.
- [34] LHCb, P. B. Marinho *et al.*, *LHCb VELO TDR: Vertex locator. Technical design report*, CERN-LHCC-2001-011, 2001.
- [35] N. van Bakel, M. Ferro-Luzzi, and F. Kroes, *Shielding of the VELO detectors from the LHC beam high-frequency fields: preliminary considerations*, LHCb-2001-081, 2001.
- [36] P. Cherenkov, Phys.Rev. **52** (1937), 378.
- [37] LHCb, S. Amato *et al.*, *LHCb: RICH technical design report*, CERN-LHCC-2000-037, 2000.

- [38] M. Merk, editor, *Minutes Tracking Workshop 27-28 March 2001*, 2001, http://lhcbott.home.cern.ch/lhcbott/tracking/Meetings_Mar_27_2001.ps.
- [39] LHCb, S. Amato *et al.*, *LHCb calorimeters: Technical design report*, CERN-LHCC-2000-036, 2000.
- [40] M. Adinolfi *et al.*, *Proposal for the RPC Muon Detector of LHCb*, LHCb-2000-53, 2000.
- [41] B. Bochin *et al.*, *Wire Pad Chambers and Cathode Pad Chambers for the LHCb Muon System*, LHCb-2000-114, 2000.
- [42] B. Bochin *et al.*, *Wire Pad Chambers for the LHCb Muon System*, LHCb-2000-003, 2000.
- [43] LHCb, P. B. Marinho *et al.*, *LHCb muon system technical design report*, CERN-LHCC-2001-010, 2001.
- [44] LHCb, P. B. Marinho *et al.*, *LHCb Outer Tracker technical design report*, CERN-LHCC-2001-024, 2001.
- [45] LHCb, S. Amato *et al.*, *LHCb magnet: Technical design report*, CERN-LHCC-2000-007, 2000.
- [46] P. Sievers, *The LHCb silicon inner tracker.*, LHCb-2001-108, 2001.
- [47] O. Steinkamp, *Layout of a cross-shaped inner tracker.*, LHCb-2001-114, 2001.
- [48] LHCb, J. Christiansen, *Key parameters and features of LHCb front-end electronics*, <http://lhcb-elec.web.cern.ch/lhcb-elec/html/key-parameters.htm>.
- [49] G. Charpak *et al.*, Nucl. Instr. Meth. **62** (1968), 235.
- [50] F. Sauli, *Principles of operation of multiwire proportional and drift chambers*, CERN-1977-9, 1977.
- [51] H. Tolsma, *The Honeycomb Strip Chamber*, PhD thesis, Twente University, 1996.
- [52] J. Fischer, A. Hrisoho, V. Radeka, and P. Rehak, Nucl. Instr. Meth. **A238**, 249 (1985).
- [53] B. Schmidt, *Drift und diffusion von Elektronen in Methan und Methan-Edelgas-Gemischen*, PhD thesis, Universität Heidelberg, 1986.
- [54] W. Blum and L. Rolandi, *Particle detection with drift chambers* (Springer-Verlag, Berlin, 1993).
- [55] I. Gouz *et al.*, *Beam tests of LHCb Outer Tracker prototypes in 2000*, LHCb-2001-011, 2001.

- [56] V. Gromov and T. Sluijk, *Electrical properties of various types of straw tubes considered for the LHCb Outer Tracker*, LHCb-2001-001, 2001.
- [57] L. Christoprou et al., Nucl. Instr. and Meth. **163**, 141 (1979).
- [58] G. van Apeldoorn, T. Bauer, and J. Steijger, *Aging studies of straw tube chambers*, LHCb-2001-003, 2001.
- [59] E. Hartouni et al., *HERA-B technical design report*, DESY-PRC 95/01, 1995.
- [60] ATLAS, *ATLAS TDR 5, Inner Detector*, CERN-LHCC-97-17, 1997.
- [61] H. Albrecht et al., Nucl.Instr.Meth. (2002), to be published.
- [62] R. van der Eijk, *LHCb Outer Tracker prototypes, October 1998 and June 1999 testbeam data analysis*, LHCb-2000-057, 2000.
- [63] I. Gouz et al., *Beam tests of a full scale prototype of the LHCb outer tracker straw tube modules*, LHCb-2001-098, 2001.
- [64] T. Sluijk et al., *The Beam Test Electronics for the LHCb Outer Tracker*, ETR 2000-02-15, 2000.
- [65] B. Bevensee et al., IEEE Transact ions on Nuclear Science **43** (1996).
- [66] V. Gromov, *Study of operational properties of the ASDBLR chip for the LHCb Outer Tracker*, LHCb-2000-054, 2000.
- [67] J. Schipper and P. Rewiersma, *Datimizer*, <http://www.nikhef.nl/user/jds-datcha/Datimizer.pdf>.
- [68] J. Christiansen, *32 Channel TDC with on chip buffering and trigger matching*, CERN-LHCC-97-60, 1997.
- [69] JTAG Technologies B.V, (2000), <http://www.jtag.com/>.
- [70] H. Groenstege et al., *16 Channel read out driver for the Drift Chambers used in L3+Cosmics project*, <http://www.nikhef.nl/pub/departments/et/L3/cosmics-nimrod/nimrod.pdf>, 1999.
- [71] J. Schipper and P. Rewiersma, *DDAQ version DATIMIZER 980706*, <http://www.nikhef.nl/user/jds/datcha/ddaqtv2.pdf>, 1998.
- [72] R. van Wijk, *DAQFIT a scalable DAQ system*, <http://www.nikhef.nl/user/ruud-HTML/daqfit.html>, 2000.
- [73] R. Brun and F. Rademakers, Nucl. Instr. and Meth. **A389**, 81 (1997), see also <http://root.cern.ch/>.
- [74] R. van der Eijk, *LHCb Outer Tracker Testbeam (Online) Monitoring, Control and Analyses software*, <http://home.cern.ch/lhcbot/software/Index.html>, 1999.

- [75] R. Mankel, *ranger - a Pattern Recognition Algorithm for the HERA-B Main Tracking System*, Hera-B 98-079, 1998.
- [76] R. Veenhof, *Garfield, simulation of gaseous detectors*, CERN, 1999, writeup W5050 (User Guide V6.31).
- [77] R. Veenhof, *Magboltz: Transport of electrons in gas mixtures*, CERN, 2000, CERNLib.
- [78] I. Smirnov, *Interactions of particles with gases*, CERN, 1999, writeup W5060 (User Guide V1.01).
- [79] LHCb collaboration, *SICb - the LHCb Geant3 based simulation program*, <http://lhcb-comp.web.cern.ch/lhcb-comp/SICB/default.htm>.
- [80] M. Cattaneo, *Brunel; The LHCb reconstruction program*, <http://cern.ch/lhcb-comp/Reconstruction>, 2001.
- [81] C. collaboration, *QQ - The CLEO event generator*, <http://www.lns.cornell.edu/public/CLEO/soft/QQ>, 2000.
- [82] CERN, *GEANT 3.21, Detector description and simulation tool*, 1993, writeup W5013.
- [83] W. Leo, *Techniques for nuclear and particle physics experiments* (Springer-Verlag, 1994).
- [84] G. Molière, Z.Naturforsch **2a**, 133 (1947).
- [85] G. Molière, Z.Naturforsch **3a**, 78 (1948).
- [86] H. Bethe, Phys.Rev. **89**, 1256 (1953).
- [87] R. Sternheimer *et al.*, Atomic Data & Nucl. Data Tables **30**, 261 (1984).
- [88] H. Bethe and W. Heitler, Proc. Roy. Soc. **A146**, 83 (1934).
- [89] Y. Tsai, Rev. Mod. Phys **46**, 815 (1974).
- [90] M. Merk *et al.*, *An improved digitization procedure for the outer tracker*, LHCb-2001-55, 2001.
- [91] A. Polouektov, O. Steinkamp, and U. Straumann, *First results from LHCb inner tracker performance studies using new digitization software*, LHCb-2001-118, 2001.
- [92] R. Kalman, Trans. ASME, J. Basic Engineering (1960).
- [93] LHCb tracking task force, *LHCb Tracking web pages*, <http://l.home.cern.ch/l-lhcbott/www/tracking/>.
- [94] P. Billoir, Nucl. Instr. and Meth. **255**, 352 (1984).

- [95] R. Fröhwirth, Nucl. Instr. and Meth. **A262**, 444 (1987).
- [96] R. Bock *et al.*, *Data analysis techniques for high-energy physics experiments* (Cambridge Univ. Press, 1990).
- [97] K. Atkinson, *An introduction to numerical analysis*, 2nd ed. ed. (John Wiley & Sons, 1988).
- [98] A. Spiridonov, *Optimized intergration of the equations of motion of a particle in the HERA-B magnet*, HERA-B 98-133, 1998.
- [99] R. van der Eijk *et al.*, *Performance of the LHCb OO track fitting software*, LHCb-2000-86, 2000.
- [100] M. Merk and M. Needham, *Occupancy results with the new outer tracker simulation.*, LHCb-2001-85, 2001.
- [101] R. Forty, *Track seeding*, LHCb-2001-109, 2001.
- [102] R. Hierck, *Track following for LHCb*, LHCb-2001-112, 2001.
- [103] R. Forty, private communication.
- [104] M. Gardener, Sci. Am. **223**, 120 (1970).
- [105] R. Hierck, *Physics performance of the $B_s \rightarrow D_s^\pm K^\mp$ and $B_s \rightarrow D_s \pi$ decay channels for the technical proposal of the LHCb detector.*, Master's thesis, Amsterdam University, 1998.
- [106] LHCb collaboration, *The AXSEL package*, <http://lhcb-comp.web.cern.ch/lhcb-comp/SICB/html/AXSELECT.html>.

Summary

The LHCb detector will be situated at one of the interaction points of the Large Hadron Collider (LHC), the new proton-proton collider that CERN is presently constructing. LHC will produce B mesons at high rate, which makes it possible to perform detailed studies of CP violation in the B meson systems. The LHCb detector is designed to maximally exploit this possibility. This thesis reports on research done on the reconstruction of trajectories of charged particles in the LHCb detector and the effect of reconstruction inefficiencies on the measurement of CP violation parameters.

The thesis starts with a brief review of CP violation and how it is incorporated in the Standard Model of particle physics. The existence of CP violation was already demonstrated in the mixing of neutral kaons in 1964. It is argued that much larger CP asymmetries are expected to occur in decays of neutral B mesons. This is confirmed by the recent measurements of the BaBar and Belle experiments showing a large asymmetry in B_d mesons decays as represented by the CP violation parameter $\sin 2\beta \sim 0.78$. Since the theoretical uncertainties in calculations involving b quarks are smaller than for the much lighter s quarks, the neutral B meson decays is an interesting topic to test the internal consistency of the Standard Model and, possibly, to look for physics beyond this model.

The LHC is a circular collider of about 27 km circumference in which two proton beams are brought in collision at a centre of mass energy of $\sqrt{s} = 14$ TeV. The bunch crossing frequency is 40 MHz. B events can be distinguished by the existence of a secondary B decay vertex. At the LHC design luminosity of $10^{34}\text{cm}^{-2}\text{s}^{-1}$ on average about 27 interactions will occur per beam crossing. Because matching secondary decay-vertices to the corresponding primary interaction vertices becomes difficult under these circumstances LHCb has chosen to run at the lower luminosity of $2 \times 10^{32}\text{cm}^{-2}\text{s}^{-1}$ and will accept only single interaction events.

A simulation shows that both B hadrons are predominantly produced in the same forward cone. This feature is exploited in the layout of the LHCb detector, which is a single arm forward spectrometer with a polar angular coverage from 10 mrad to 300(250) mrad in the horizontal(vertical) plane. The main tracking detectors provide the measurements to reconstruct the trajectories of charged particles and their momenta as the particles are deflected by a magnetic field provided by a large dipole magnet. In addition to the tracking system the LHCb detector comprises a vertex detector measuring the particle trajectories close to the interaction region, two Ring Imaging Cherenkov (RICH) detectors providing particle identification, an electromagnetic and hadronic calorimeter for measuring the energy of electrons, photons and hadrons and a muon detector to identify and trigger on the muons in the events.

The main tracking system consists of nine stations of tracking chambers (T1-T9). The particle rate near the beam-pipe is much higher than for larger polar angles. Therefore, to cover the full angular acceptance LHCb has chosen to use two tracking detector technologies. The regions of high track density are covered by an inner tracker based on a silicon technology. The outer tracker covers the remaining part of the acceptance. It is built out of gas filled drift tubes.

In this thesis the (prototype) tests and the design considerations that have led to the outer tracker design as presented in the outer tracker technical design report are presented. After a brief review of the operation principle of gas filled drift tubes, the selection of the drift gas mixture is discussed. The main component of the gas mixture is argon with CO_2 as a quencher. To obtain a sufficiently fast drift gas CF_4 is added. Extensive aging tests have been performed on various cathode materials of the drift tubes. These measurements show the polymer Kapton-XC to be sufficiently radiation hard. Studies on the electrical properties of the drift tubes show that the addition of an aluminium layer significantly improves conductivity and reduces cross talk.

Several outer tracker prototype modules, with different properties are constructed. From 1998 until 2001 some of these prototypes were tested in a particle beam. The measurements of various drift cell properties as a function of varying drift gas composition, high voltage and magnetic field settings are described. Measurements as well as computer simulations point to the use of 5 mm diameter straws as tube geometry. A final full scale (2×1.6 m) prototype module shows an average cell efficiency of 97.2 %, a position resolution of about $200 \mu m$ and a cross talk level below 6%. Furthermore, the maximum drift time in these drift cells in a 0.0(1.4) T magnetic field is measured to be 32.5(40.9) ns. These properties satisfy the requirements for the outer tracker very well.

The remaining part of this thesis is devoted to track reconstruction procedures developed for LHCb. Based on simulated data, the momentum, position and direction of particles are reconstructed at several important positions in the LHCb spectrometer. To fit these track parameters the Kalman Filter formalism is used. It includes four different measurement types; the outer tracker hits, the inner tracker clusters and the two types of vertex detector clusters. The Kalman filter treats multiple scattering and energy loss locally. Therefore, the fitted track will follow the true trajectory as closely as possible. The presence of an inhomogeneous magnetic field results in a complicated track model. Therefore a step-wise 5th order Runga-Kutta method is used to propagate the track parameters.

To be able to check the track fit the expected detector output is simulated. A comparison of the fitted error on track parameters with the true error (by means of pull-distributions) shows that the errors in these simulations are well understood. At the track creation vertex average resolutions of $\sim 27 \mu m$ on the position and 0.18 mrad on the directions are obtained. The momentum resolution is about 0.40 %.

Before fitting a trajectory the detector measurements have to be assigned to the corresponding particle. In this thesis a set of pattern recognition algorithms are presented that solve this problem. The pattern recognition procedure is performed "upstream", i.e. opposite to the particle flow direction. It is split into two sub-tasks; *track seeding* and *track following*. The task of the track seeding is to *find* track segments in the tracking stations T6-T9. The task of track following is to *follow* these tracks towards the

vertex region by searching in the stations T1-T5 for the measurements corresponding to these tracks.

The performance of the pattern recognition algorithms is studied for particles originating from the vertex region and traversing the whole spectrometer. The presented track seeding algorithm has an average efficiency of $96.8 \pm 0.1\%$. The ghost rate, i.e. the percentage of reconstructed tracks that is not associated to a real particle, is $27.1 \pm 0.1\%$. The average track following efficiency is $95.5 \pm 0.1\%$. The ghost rate is only 1%. The combined algorithms give an average efficiency of $91.4 \pm 0.1\%$ and a ghost rate of $15.6 \pm 0.1\%$.

The thesis continues with a study of the LHCb performance in reconstructing two benchmark B meson decay modes that are relevant for measuring CP violation. A low track multiplicity decay $B_d \rightarrow \pi^+ \pi^-$ and a high track multiplicity decay $B_s \rightarrow D_s^\pm K^\mp$ followed by $D_s^\pm \rightarrow K^+ K^- \pi^\pm$ are considered. The B_d in the decay $B_d \rightarrow \pi^+ \pi^-$ is reconstructed by the LHCb tracking system with a mass resolution of $10.7 \text{ MeV}/c^2$. The B_s in the decay $B_s \rightarrow D_s^\pm K^\mp$ is reconstructed with a mass resolution of $21.8 \text{ MeV}/c^2$. The event reconstruction inefficiency due to the pattern recognition algorithms is shown by comparing it with ideal, i.e. 100% efficient, pattern recognition. The event reconstruction efficiency for the two body decay $B_d \rightarrow \pi^+ \pi^-$ is about 94%. The decay $B_s \rightarrow D_s^\pm K^\mp$ with four stable decay products has an event reconstruction efficiency of about 79% showing the importance of a high track reconstruction efficiency.

At the LHCb nominal luminosity of $2 \times 10^{32} \text{ cm}^{-2} \text{s}^{-1}$ the expected number of $b\bar{b}$ pairs produced in single interaction bunch crossings in one year of LHCb operation is $5 \cdot 10^{11}$. Only a fraction of the B hadrons will decay in one of the benchmark channels. Furthermore, not all produced decays are fully reconstructed by LHCb because of acceptance effects, trigger inefficiencies and track and event reconstruction inefficiencies. Taking all these effects into account it is expected that about 800 $B_s \rightarrow D_s^\pm K^\mp$ events and 5200 $B_d \rightarrow \pi^+ \pi^-$ events will be observed in one year of data taking. The number of reconstructed events determines the precision with which CP violation can be measured with the LHCb experiment. The obtained results are compared with an earlier study on the LHCb performance. The thesis is concluded with a brief outlook on possible algorithm and detector improvements.

Samenvatting

De LHCb-detector zal worden geplaatst bij een van de botsingspunten van de *Large Hadron Collider* (LHC), de nieuwe protonenversneller die momenteel wordt gebouwd op het CERN. De LHC zal met een hoge frequentie B -mesonen produceren. Dit maakt het mogelijk om gedetailleerde studies te doen naar CP -schending bij B -mesonen. De LHCb-detector is ontworpen om optimaal gebruik te maken van deze mogelijkheid. Dit proefschrift is het verslag van onderzoek dat is verricht naar het reconstrueren van de sporen van geladen deeltjes in de LHCb-detector en naar het effect van inefficiënties in deze reconstructie op de meting van CP -schendingsparameters.

Het eerste deel van dit proefschrift geeft een kort overzicht van CP -schending en hoe het is opgenomen in het Standaardmodel van de deeltjesfysica. Het bestaan van CP -schending is reeds in 1964 aangetoond bij het verval van neutrale kaonen. De verwachting is dat bij het verval van neutrale B -mesonen een veel grotere CP -asymmetrie optreedt. Recente metingen in de Babar en Belle experimenten bevestigen dit in de meting van de CP -schendingsparameter $\sin 2\beta \sim 0.78$. Het feit dat de theoretische onzekerheid in berekeningen met de b -quarks kleiner is dan met de veel lichtere s -quarks, maakt neutrale B -mesonen een interessant gebied om de interne consistentie van het Standaardmodel te testen en om mogelijke fysische processen te vinden die buiten dit model vallen.

De LHC is een cirkelvormige deeltjesversneller met een omtrek van ongeveer 27 kilometer waarin men twee protonenbundels met een frequentie van 40 MHz op elkaar laat botsen met een massamiddelpuntsenergie van 14 TeV. Een B -meson gebeurtenis onderscheidt zich door het bestaan van een tweede vervalpunt. Bij de geplande LHC luminositeit van $10^{34} \text{ cm}^{-2} \text{s}^{-1}$ zullen gemiddeld 27 interacties plaats vinden per botsing. Omdat het bij dergelijke omstandigheden moeilijk is om de interacties te onderscheiden heeft LHCb-er voor gekozen om te opereren met een luminositeit van $2 \times 10^{32} \text{ cm}^{-2} \text{s}^{-1}$ en om alleen enkelvoudige botsingen toe te laten.

B -mesonen worden altijd paarsgewijs geproduceerd. Uit simulatie blijkt dat beide B -mesonen meestal worden geproduceerd onder dezelfde kleine openingshoek (t.o.v. de bundelas). In het ontwerp van de LHCb-detector is hiermee rekening gehouden door deze uit te voeren als enkelzijdige voorwaartse spectrometer. De primaire positiedetectoren leveren de gegevens waarmee de banen van de geladen deeltjes gereconstrueerd kunnen worden. De impuls van de deeltjes wordt bepaald door meting van de kromming van de deeltjesbanen in het magnetisch veld van een grote dipoolmagneet. Verder bestaat de LHCb-detector uit een vertexdetector die de banen van deeltjes vlak bij het interactiepunt meet, twee Ring Imaging Cherenkov (RICH) detectoren die de deeltjes identificeren, een calorimeter om de energie van elektronen, fotonen, en hadronen te meten, en tenslotte een muondetector om muonen te identificeren.

Het primaire positiedetectiesysteem is opgebouwd uit negen *tracking stations* (T1-T9). De deeltjesintensiteit nabij de bundelas is veel hoger dan onder een grote openingshoek. Dit is de reden waarom LHCb-gebruikt maakt van twee verschillende detectietechnologieën. De *inner tracker* (binnenste detector) is gebaseerd op siliciumtechnologie en meet in het gebied waar de deeltjes intensiteit het hoogst is. De *outer tracker* (buitenste detector) is opgebouwd uit strootjes gevuld met een *driftgas* en beslaat het overige gebied.

Het tweede deel van dit proefschrift geeft een verslag van de tests en ontwerpkeuzes die hebben geleid tot het ontwerp van de outer tracker zoals gepresenteerd in het *LHCb-outer tracker design report*. Na een kort overzicht van de werking van *driftgas*-detectoren wordt de keuze van het gasmengsel bediscussieerd. Het hoofdbestanddeel van het gasmengsel is argon en CO_2 wordt gebruikt als *quencher*. Om het gas voldoende snel te maken wordt er CF_4 toegevoegd. Om een geschikt kathodemateriaal te vinden zijn er uitgebreide verouderingstests verricht voor diverse materialen. De metingen wezen uit dat het polymeer Kapton-XC voldoende stralingsbestendig is. Onderzoek van de elektrische eigenschappen laat zien dat de toevoeging van een aluminiumlaag op de kathode de elektrische geleiding significant verbetert en de overspraak (*cross talk*) verminderd.

Gedurende het onderzoek zijn er diverse prototype detectoren, met verschillende eigenschappen, gebouwd. In de periode van 1998 tot 2001 zijn enkele van deze prototypes getest in een deeltjesbundel. De meetresultaten voor diverse eigenschappen van de detectoren bij verschillende soorten gasmengsel, hoogspanning en magnetisch veld worden beschreven. Metingen en computersimulaties tonen aan dat de geometrie van de buizen moet bestaan uit strootjes met een doorsnede van 5 mm. Voor een prototype op ware grootte (2×1.6 m) is een gemiddelde cel-efficiëntie van 97.2%, een positieresolutie van ongeveer $200 \mu\text{m}$ en een overspraakniveau van minder dan 6% gemeten. Verder is gemeten dat de maximale drifttijd in deze detectoren 32.5(40.9) ns is bij een magnetisch veld van 0.0(1.4) T. Deze eigenschappen voldoen ruimschoots aan de eisen die gesteld zijn aan de outer tracker.

Het derde deel van dit proefschrift is gewijd aan methoden om de deeltjesbanen in de LHCb-detector te reconstrueren. Met behulp van gesimuleerde detectordata wordt de impuls, de positie en de richting van deeltjes op diverse belangrijke plaatsen in de LHCb-spectrometer bepaald. Er wordt gebruik gemaakt van vier verschillende detec-tormetingen: de inner tracker clusters, the outer tracker *hits* en twee type vertex detector clusters. De berekeningen maken gebruik van het Kalman Filter formalisme. Het inhomogene magneetveld leidt tot een complex model voor het deeltjesspoor. Daarom is gebruik gemaakt van een stapsgewijze 5e-orde Runga-Kutta methode om de baanparameters te propageren.

Om de precisie van het reconstructieformalisme te bepalen worden de baanparameters vergeleken met de gesimuleerde deeltjes. Een vergelijking van de berekende fout met de werkelijke afwijking leert ons dat de fouten in de reconstructie goed onder controle zijn. Op het punt waar het spoor ontstaat wordt een gemiddelde resolutie van $\sim 27\mu\text{m}$ voor de positie gehaald en 0.18 mrad voor de richting. De impulsresolutie is ongeveer 0.40%.

Voordat een spoor berekend wordt moeten de metingen van de detector toegewezen worden aan het bijbehorende deeltje. In dit proefschrift zijn een aantal algoritmes

voor patroonherkenning behandeld die dit probleem oplossen. Het uitvoeren van de patroonherkenning gebeurt *stroomopwaarts*, dat wil zeggen tegengesteld aan de richting waarin de deeltjes zich bewegen. De procedure is opgesplitst in twee subtaken; *track seeding* en *track following*. Bij track seeding is het de taak om delen van het spoor te vinden in de stations T6-T9. Bij track following is het de taak om het spoor terug te volgen naar het botsingsgebied door in de stations T1-T5 te zoeken naar metingen die overeenkomen met het deeltje.

De prestatie van de patroonherkenningsalgoritmen is bestudeerd voor deeltjes die starten in het botsingsgebied en de gehele spectrometer door gaan. Het track seeding algoritme heeft een gemiddelde efficiëntie van $96.8 \pm 0.1\%$. De *ghost rate*, het percentage van gereconstrueerde banen dat niet gekoppeld kan worden aan een echt deeltje, bedraagt $27.1 \pm 0.1\%$. De gemiddelde efficiëntie van het track following algoritme is $95.5 \pm 0.1\%$ en de ghost rate slechts 1%. De algoritmen achter elkaar uitgevoerd levert een gemiddelde efficiëntie van $91.4 \pm 0.1\%$ en een ghost rate van $15.6 \pm 0.1\%$.

Het vierde en laatste deel van het proefschrift is gewijd aan de volledige reconstructie van twee referentie B -meson vervalkanalen die relevant zijn voor de meting van CP schending. Een verval met een laag ($B_d \rightarrow \pi^+ \pi^-$) en met een hoog ($B_s \rightarrow D_s^\pm K^\mp$ gevuld door $D_s^\pm \rightarrow K^+ K^- \pi^\pm$) aantal vervalproducten is bestudeerd. Het B_d -meson in het verval $B_d \rightarrow \pi^+ \pi^-$ is gereconstrueerd door het LHCb tracking systeem met een massaresolutie van $10.7 \text{ MeV}/c^2$. Het B_s -meson in het verval $B_s \rightarrow D_s^\pm K^\mp$ is gereconstrueerd met een massa resolutie van $21.8 \text{ MeV}/c^2$. De trackreconstructie-inefficiëntie als gevolg van de patroonherkenningsalgoritmen is bepaald door deze te vergelijken met een ideaal (100% efficiënt) algoritme. De reconstructie-efficiëntie van het gehele $B_d \rightarrow \pi^+ \pi^-$ verval is ongeveer 94%. Het verval $B_s \rightarrow D_s^\pm K^\mp$, dat vier vervalproducten heeft, wordt in zijn geheel gereconstrueerd met een efficiëntie van 79%. Dit laat het belang zien van een hoge spoorreconstructie-efficiëntie.

Bij de nominale LHCb luminositeit van $2 \times 10^{32} \text{ cm}^{-2} \text{s}^{-1}$ is het verwachte aantal geproduceerde $b\bar{b}$ paren per jaar in een enkelvoudige interactie $5 \cdot 10^{11}$. Slechts een fractie van de B -hadronen zal vervallen in een van de referentiekanalen. Ook wordt niet elk verval volledig gereconstrueerd als gevolg van de beperkte LHCb *acceptance*, *trigger*-inefficiëntie en inefficiëntie bij het reconstrueren van de gebeurtenissen. Al deze effecten in overweging nemend wordt verwacht dat ongeveer 800 $B_s \rightarrow D_s^\pm K^\mp$ gebeurtenissen en 5200 $B_d \rightarrow \pi^+ \pi^-$ gebeurtenissen per jaar volledig worden gereconstrueerd. Het aantal gereconstrueerde gebeurtenissen bepaalt de precisie waarmee *CP*-schending gemeten kan worden met het LHCb-experiment. De verkregen resultaten zijn vergeleken met een eerdere studie naar de prestatie van LHCb. Het proefschrift wordt afgesloten met een korte vooruitblik op mogelijke verbeteringen van de algoritmen en de detector.

Acknowledgement

Finally, I am writing the last section of my thesis. I can now see the consequences of the scientific method. Indeed, all previous text is made as objective as possible. A consequence is, however, that it seems that no people are involved. This is surely not the case. The studies have been performed inside of the context of the LHCb experiment, which is an effort of hundreds of people. Furthermore, more personally, I could not have written this thesis without the support of a lot of people in my life. Thank you all for your contribution! Below I especially want to express my gratitude to some of you.

I start where it all began and that is 29 years ago. Janneke, thank you for always being there for me, for your love and for raising me to the person I am now. Huno, thank you for providing me the brain-power to get my PhD in physics. Thank you for your commitment and integrity towards your son. Jaco, thank you for being a friend. Especially the last year you showed me the value of having a brother.

At NIKHEF I, first of all, want to thank my supervisor Marcel for all his feedback and corrections on the draft versions that have led to this thesis. Thank you for motivating me when I sometimes didn't see the point of it all. I appreciate the valuable time my promoter Walter spend on providing me with the final corrections on this thesis. I thank Werner for giving me the opportunity to work in the *B-fysica* group. Bert, thank you for taking over his supervision when he passed away so suddenly.

I enjoyed working in the *B-fysica* group. In particular I want to thank Matthew Needham for the period at CERN, where we together build the foundation of the current LHCb track reconstruction framework. I am grateful to Iouri Gouz for providing me with input and feedback on the test-beam chapter. The pattern recognition studies of Rutger Hierck (and Roger Forty) resulted in the necessary tools to perform the track reconstruction performance studies. Rutger, I wish you the best in finishing your thesis. Jeroen, good luck with the endless LHCb software struggle. Bart, as my office mate you have provided the necessary relieve in this intense year. I had a lot fun: thanks!

Of course I met lots of other fellow (PhD)-students. Thank you for the inspiring and intriguing and “round-table” discussions. In particular, the PVDD (Ernst-Jan, Ivo, Maarten, Niels, Wouter) made sure I did not forget the relevant things happening in the world. Jaap, thanks for the pizzas and dinners we had.

I owe to my dearest friends (Frenk, Henriette, Jeroen, Sander, Sasja, Tjarda, ...) for not giving upon me. I promise to never write a thesis again. Sander, thank you for providing the *samenvatting*. I hope you soon finish your thesis. Cor, bedankt voor de nodige geestelijke ontspanning d.m.v. de hard nodige lichamelijke inspanning elke dinsdag *stipt* om 20:00.

Without the support of the Amsterdam Landmark Course Supervisors I would have

not finished my thesis. We are really an amazing group of people. Your stand for me made it happen. John, the conversations we had last year have had a major impact on who I was being while writing my thesis. Thank you Sanne for your love, courage and contribution. You will probably never get that you are really special. Marijke, thank you for being my buddy, your listening for me made me grow and discover who I really am.

Als elke Amsterdammer zo zou zijn als Tonnie dan is er inderdaad geen reden om in de provincie te gaan wonen. Tonnie bedankt voor je gastvrijheid! I had the best time of my life living at Ferme de l'Espeneux in Crozet. Ans, Dirk, Gilles, Martin, Robert and Thomas every time I think of the farm I miss you.

Myriam, I acknowledge you for all the things you did (and did not) do to support me in finishing my thesis. Thank you for your love and generosity. I am looking forward to our future together. Soon I shall marry my friend, the one I laugh with, live for and dream with.

Love,

Rutger.

Amsterdam, July, 2002.

